Boîtes quantiques de semi-conducteurs nitrures pour des applications aux capteurs opto-chimiques

Aparna Das

UNIVERSITÉ DE GRENOBLE

THÈSE

Pour obtenir le grade de

DOCTEUR DE L'UNIVERSITÉ DE GRENOBLE

Spécialité : **Physique / Nanophysique**

Arrêté ministériel : 7 août 2006

Présentée par

Aparna DAS

Thèse dirigée par **Eva MONROY**

préparée au sein du **Laboratoire Nanophysique et Semi-Conducteurs (CEA / INAC / SP2M)**
dans **l'École Doctorale de Physique**

Boîtes quantiques de semi-conducteurs nitrures pour des applications aux capteurs opto-chimiques

Thèse soutenue publiquement le **13 juin 2012**
devant le jury composé de :

Mme Chantal FONTAINE
Rapporteur
M Nikos T. PELEKANOS
Rapporteur
M Henri MARIETTE
Président
M Bernard GIL
Membre
Mme Philomela KOMNINOU
Membre
Mme Eva MONROY
Membre
M Fernando B. NARANJO
Membre

Université Joseph Fourier / Université Pierre Mendès France / Université Stendhal / Université de Savoie / Grenoble INP

Acknowledgement

My thesis work would not have been possible without the guidance and the help of various people who in one way or another contributed and extended their valuable assistance in the preparation and completion of this study. It is a pleasant task to express my thanks to all those who contributed to the success of this study.

First and foremost, my utmost gratitude to my thesis advisor Dr. Eva Monroy, without her guidance, support and encouragement this work would not have been possible. She taught me everything, from A to Z, and I strongly believe that, I am one of the luckiest PhD students in the word to have a thesis advisor like her. Her prodigious knowledge, promptness to everything, composed nature made me to grow more and my work interesting, my deepest gratitude to my mentor.

My sincere thanks go to Prof. Henri Mariette, Director of the group Nanophysics and semiconductors Prof. Jean-Michel Gerard, Director of the division on physics of materials and microstructures of INAC, for their able leadership has created a positive and learning environment for all the members of the lab. Special thanks to Prof. Henri Mariette for being the president of jury.

I convey my thanks to the members of the jury: Referees Dr. Chantal Fontaine (LAAS-CNRS), and Prof. Nikos T. Pelekanos (University of Crete, Greece), Examinators Prof. Bernard Gil (CNRS, Montpellier), Prof. Philomela Komninou (Aristotle University of Thessaloniki, Greece), Ass. Prof. Fernando B. Naranjo (Universidad de Alcalá, Spain) for accepting to serve in the jury, despite of their busy schedule.

Concerning the external collaborations, I would like to thank Prof. Ph. Komninou and her group at Aristotle University of Thessaloniki, for helping me for microscopic analysis of my samples and providing us high quality TEM data. I also would like to thank Dr. K. Lorenz at Instituto Tecnológico e Nuclear, Portugal for the RBS measurements. I take this opportunity to thank Prof. M. Eickhoff and his group at Justus-Liebig-Universität Giessen, Germany and Dr. A. Helwig and his group at EADS,

Germany for chemical analysis and for design of our sensor system. I am grateful to Prof. Pierre Ruterana (ENSICAEN-CNRS) and Dr. Eirini Sarigiannidou (INPG) for their support in microscopic analysis. Thanks are due to G. Nataf and Ph. De Mierry from CHREA-CNRS for providing semipolar GaN templates, and to DOWA for polar AlN templates.

Many thanks to Joel Bleuse and Bruno Gayral for helping me with the optical characterization of samples. I would also acknowledge Edith Bellet-Almaric for her support in diffraction experiments. My special thanks go to the technicians of our lab Yoann Cure, Yann Genuist and Jean Dussaud for supporting us with their MBE expertise regularly. Special acknowledgements to Carmelo and Cécile, for their indispensable help related with administrative work.

I would like to acknowledge Lise and Prem for their support to learn about MBE machine. I am deeply indebted to Yulia for her support and entertainment. Yulia, thanks for sharing the office with me and scolding me when I came late in the office. Very special thanks to Fernando and Sirona for their comments and encouragement during rehearsal. Sirona, thanks for the Spanish sweet, my parents will really love that. Fernando, I learned a lot from you and thanks for helping me with the origin graphs and mental support during my defense.

Words are short to express my deep sense of gratitude towards my friends, Kannan, Nitin, Sandeep, Rajeev, Siddharth, Veeresh, Anna, Karine, Diane for their support.

I am gratefully acknowledges the financial support from the EU FP7 project DOTSENSE (STREP 224212) and the French National Research Agency project COSNI (BLAN08-1_323691).

Lastly, and most importantly, I wish to thank my family and the special person who made all this possible.

Résumé

Ce travail de thèse a porté sur la synthèse de boîtes quantiques (BQs) de semi-conducteurs nitrures orientés (11-22) ou (0001) par épitaxie par jets moléculaires à plasma d'azote, pour des applications aux capteurs chimiques pour la détection du niveau de pH, d'hydrogène ou des hydrocarbures dans des environnements gazeux ou liquides.

Les trois premiers chapitres sont généraux. Le premier chapitre présente l'état du domaine et précise les objectifs de la thèse. En particulière il y est expliqué comment une polarisation piézoélectrique et spontanée est présente dans les couches nitrures du fait de leur structure wurtzite. Pour empêcher cette propriété très gênante pour les applications optoélectroniques, une proposition consiste à changer l'orientation cristalline des couches. Dans le cadre de cette thèse, la possibilité d'utiliser la croissance de structures dans des directions semipolaires (de polarité faiblement marquée) a été visée, ces dernières pouvant assurer un bon compromis si la qualité structurale des matériaux est meilleure que celle obtenue pour les matériaux d'orientation non polaire, contenant une grande densité de défauts. Enfin, il a été choisi d'exploiter les structures à boîtes quantiques GaInN car elles devraient minimiser l'effet des recombinaisons non-radiatives, qui s'avèrent très néfastes pour les puits quantiques. Aussi dans ce premier chapitre, j'explique le cadre applicatif de mon travail. Le domaine des capteurs, qui est en pleine explosion, a jusqu'ici reposé sur la technologie silicium. Or les nitrures possèdent des propriétés qui correspondent au cahier des charges de ces applications et aussi à certains de leurs besoins, en particulier pour les capteurs chimiques.

Le second chapitre précise les propriétés des nitrures du groupe III. Ce chapitre rappelle tout d'abord les différentes formes cristallines que peuvent prendre ces semiconducteurs, notamment la forme wurtzite qui est la plus stable, et explicite le problème de polarité, qui conduit à la présence du champ piézoélectrique interne spontané, et sa relation à l'orientation cristalline. Je commente ensuite la structure de bande de ces matériaux et leur dépendance à la température, ainsi que les valeurs de masse effectives publiées pour les électrons et les trous. Les propriétés élastiques sont ensuite précisées et utilisées pour évaluer les déformations attendues dans les

matériaux contraints pour les orientations polaire (0001) et semi-polaire (11-22). Les polarisations engendrées par les piézoélectricités spontanée et induite par les déformations sont enfin précisées et leur effet sur la structure de bande des puits quantiques rappelée.

Le troisième chapitre décrit les techniques expérimentales sollicitées dans ces travaux. Je discute d'abord de la technique d'épitaxie qu'elle a utilisée, la technique d'épitaxie par jets moléculaires (MBE). Après en avoir rappelé brièvement les principes généraux, le bâti utilisé est décrit. Le principe de la technique de diffraction électronique en incidence rasante (RHEED) est ensuite présentée, ainsi que les informations qui peuvent en être tirées sur l'évolution du paramètre de maille du matériau en croissance, l'arrangement atomique de sa surface et la vitesse de croissance. Le choix du substrat de saphir est alors précisé, ainsi que les relations d'épitaxie entre le GaN et le saphir, de structure rhomboédrique, qui dépendent bien sûr de son orientation. Les défauts ponctuels et les dislocations qui sont présents dans les couches sont discutés. Le chapitre se termine par une présentation des techniques de caractérisation, diffraction de rayons X, microscopie à force atomique et spectroscopie de luminescence, mises en jeu dans ces travaux. A la fin de ce chapitre, les informations nécessaires à la compréhension de l'étude menée sur l'élaboration des multicouches à puits et boîtes quantiques et leur caractérisation ont été données.

Les trois derniers chapitres concernent ma contribution personnelle. L'épitaxie par jets moléculaires de couches (11-22) semipolaires est traitée dans le quatrième chapitre successivement pour les matériaux AlN, GaN , GaInN et InN. Dans les deux premiers cas, le but était de mieux comprendre l'origine des défauts rencontrés dans les travaux précédents de l'équipe. Ainsi, pour AlN, il s'est agi de préciser l'origine du polycristal formé pendant la croissance, constitué de grains orientés (11-22) et (10-10), dont la densité tend à diminuer quand le rapport III/V diminue. Mon étude a montré que ces grains se forment dès les premiers stades de la germination d'AlN dans le cadre d'une collaboration avec l'Université de Thessalonique, par une étude couplée de microscopie en transmission (MET), RHEED et AFM. L'existence de ces zones parasites a été reliée à la présence de nanofacettes localement formées à la surface du saphir, par réaction avec l'AlN, en particulier lors du départ de l'épitaxie sous flux d'azote. L'optimisation de ce matériau est importante car il va être utilisé comme

tampon pour le GaN. En effet, dans le cas du GaN (11-22), l'épitaxie directe sur saphir conduit à la présence de deux orientations, mais l'utilisation d'un tampon AlN permet d'obtenir uniquement l'orientation visée. J'ai trouvé que l'optimisation du matériau orienté (11-22) consistait à contrôler le léger excès de gallium imposé pendant l'épitaxie car il conduisait plus rapidement à l'accumulation de Ga que pour l'orientation (0001).

Je me suis ensuite intéressée à la réalisation de couches dopées de GaN dopées. Des couches épaisses de GaN:Mg ont pu être réalisées avec des dopages élevés ($1,6 \times 10^{20}$ cm^{-3}), sans y observer les défauts identifiés pour l'orientation (0001) par microscopie ou sur les spectres de photoluminescence. Le dopage N du GaN (11-22) par le silicium a pu être réalisé sans ennui, les conditions trouvées étant les mêmes que celles de couches non dopées.

De la même façon, l'épitaxie de couches d'AlGaN de bonne qualité peut être réalisée, mais en utilisant un rapport III/V plus faible que pour (0001). Le problème est plus complexe pour le ternaire GaInN. Aussi, j'ai étudié la désorption d'indium d'une surface GaN (11-22) en la comparant au cas de référence (0001). J'ai pour cela exploité les variations temporelles d'intensité du RHEED. J'ai utilisé ces données pour étalonner la température de croissance, puis pour préciser la quantité d'excès d'indium optimal, qu'elle a à nouveau trouvé égal à 2 monocouches pour cette surface (même si l'arrangement atomique de ces deux surfaces diffèrent). Les couches épaisses réalisées sous ces conditions conduisent cependant à des surfaces facettées. La présence de dislocations dans les couches a été identifiée par MET comme origine de ces facettes. Un autre résultat important identifié est que l'incorporation de l'indium y est cinq fois plus faible que pour (0001). Ce résultat, en contradiction avec la théorie et les matériaux MOVPE, est bien confirmé par les spectres de luminescence de ces couches.

La fin de ce chapitre est consacrée à l'étude menée par A. DAS sur l'épitaxie d'InN orienté (0001) et (11-22). Cette croissance est difficile car elle doit être réalisée dans certains cas à température beaucoup plus faible (450°C au lieu de 600-700°C pour InGaN), pour laquelle la désorption de l'InN est plus rapide que celle de l'indium. Pour l'orientation (0001), cette propriété a été exploitée pour connaitre le rapport optimal de flux III/V par RHEED. Des couches de InN(11-22) ont été réalisées

conjointement. Les propriétés de luminescence de ces matériaux indiquent des déviations par rapport aux prévisions, en particulier pour l'InN (11-22) dont l'émission ne suit pas la loi en température de Varshni, alors que la recombinaison non radiative y est toutefois moins forte que pour l'orientation (0001).

Le cinquième chapitre porte sur la réalisation de structures à plans empilés de boîtes quantiques (In)GaN/AlN (QDs). Je rappelle d'abord les résultats obtenus sur les QDS de GaN/AlN (0001). Je précise les techniques utilisables pour leur obtention, croissance en condition riche N, ou en condition Ga avec arrêt, avec une moins grande densité dans le second cas, qui sera la technique qu'elle utilisera. Je rappelle finalement l'intérêt de ces nanostructures qui conduisent à une grande stabilité en luminescence en température, avec une efficacité interne quantique beaucoup plus élevée, mais à des spectres plus larges que pour les multi-puits quantiques (MQW) du même type.

La forme des QDs GaN/AlN (11-22) obtenus en condition riche Ga avec arrêt de croissance a été identifiée par MET à Thessalonique, et présente deux variantes: rectangle ou trapèze. Les propriétés de luminescence des QDs sont celles attendues pour ces nanostructures, mais comparées au cas (0001), on remarque que la réduction du champ piézoélectrique modifie leur gamme d'émission, d'énergie plus resserrée mais plus élevée que le gap du GaN, et diminue d'un ordre de grandeur le temps de déclin de luminescence. Dans le cas des QDs InGaN/AlN, pour (0001), des MQW et QDs ont été réalisés. La MET met en évidence une certaine interdiffusion aux interfaces supérieures des MQW et l'absence de défauts d'empilement dans les QDs. La spectroscopie de luminescence indique que la température de croissance conduit à une diminution de la longueur d'onde d'émission, reliée logiquement à une augmentation en In dans les MQW, alors que la tendance est moins nette pour les boites quantiques. J’explique ce résultat en considérant que dans ce cas, la forme des QD évolue avec la concentration en In. Quand l'indium est augmenté, non seulement l'énergie de leur émission de luminescence diminue mais la largeur à mi-hauteur augmente, certainement du fait de leur plus grande dispersion. De plus, les effets de localisation de porteurs dus à des fluctuations de potentiel observés quand on augmente la température deviennent plus prononcés. Pour les QW, la dépendance en température indiquent des fluctuations de contenu en indium. Il serait logique que les

fluctuations rencontrées dans les QDs soient du même type. La situation s'avère plus complexe pour les QD orientées selon (11-22). Dans un premier temps, une température qui permet la désorption de l'indium est utilisée, mais les observations MET indiquent que les boîtes s'épitaxient en partie sur des plans inclinés, du fait de la contrainte qui courbe la surface, et éventuellement à la présence de défauts d'empilement, à la proximité desquels elles se forment apparemment préférentiellement. Ceci peut effectivement s'expliquer par le fait que la formation de ces défauts linéaires, qui précèdent celle des QD, peut aussi être due aux contraintes, d'autant plus qu'une composante de cisaillement est autorisée pour cette orientation, et que ces défauts contiennent des dislocations à leur extrémité. Cela pourrait permettre une relaxation des contraintes au sein des boîtes. Réalisée à basse température où la désorption d'indium est négligeable, l'épitaxie de QDs conduit à la présence à une forte distorsion de la surface par une grande densité de ST multiples. Elles restent toutefois bien identifiables sur la coupe transversale de MET alors que ce n'est pas le cas pour les QDs (0001), qui contiennent une densité très forte de SFM. La comparaison de la photoluminescence des structures réalisées à différentes températures est menée. Alors que pour les températures plus élevées (650-690°C), l'énergie d'émission des boites indique que l'incorporation d'indium est beaucoup faible même pour les QDs (0001) faible, ce d'autant plus que la température est élevée, cette énergie diminue drastiquement pour les basses températures d'épitaxie. Le confinement 3D est confirmé en comparant leur évolution en température avec celles de QW. Pour les QDS épitaxiées à haute température, les recombinaisons non radiatives y sont plus présentes que pour l'orientation polaire, alors qu'elles diminuent quand la longueur d'onde d'émission des QD augmente (plus faible température d'élaboration). Il n'y a plus de luminescence des QDS (0001), sinon une émission constante, qui serait due à la présence de poches cubiques liées aux SFM. Ce chapitre se conclut sur les mesures de contraintes par MET menées à Thessalonique. Les tendances données par ces résultats confirment les observations précédentes.

Enfin, le sixième chapitre présente les résultats obtenus par nos partenaires de contrat sur les composants que j’ai a réalisés. Des capteurs à base de QDS et MQW GaN/AlN ont été épitaxiés et processés. Les caractéristiques de photoluminescence sous polarisation électrique indiquent une bonne sensibilité. Toutefois, un courant

tunnel parasite participe à la génération de porteurs si les barrières AlN des QD sont trop fines. La réponse du capteur à la présence d'hydrogène est très contrastée. Le signal est toutefois saturé dès que l'hydrogène excède 10% de concentration sans courant tunnel, et 500 ppm en présence de courant tunnel. La conclusion tirée est que seuls les plans de QD supérieurs sont affectés par l'hydrogène et effectivement le contraste du composant est meilleur pour un composant à un seul plan de QD. Ces résultats ont été obtenus pour les QDs (0001).

En effet, l'utilisation des QDs (11-22) a conduit à des émissions de luminescence d'énergie supérieure au gap, donc non utilisables, d'où la nécessité d'ajouter de l'indium à ces QDs. Des composants à base de GaInN/GaN (0001) et (11-22) ont alors été réalisés. Seules les structures (0001) ont donné des émissions de photoluminescence à température ambiante. Les premières demandent encore une optimisation plus poussée pour réaliser les composants entiers qui comprennent des empilements complexes des différents nitrures. Les composants à QDs (0001) se sont en revanche révélés excellents, leur réponse à la tension externe étant extrêmement sensible. Ainsi, des capteurs ont permis de mesurer le pH de l'eau de 0 à 7 d'une manière très efficace. A la suite de cette validation, j’ai conclu mes travaux en dressant un cahier des charges pour la réalisation de ces composants.

Contents

Chapter 1

Introduction and targets

1.1 Historical introduction of III-nitride semiconductors

Group III-nitride semiconductors (GaN, AlN and InN) are currently the materials of choice for ultraviolet/blue/green light emitters and high power electronics. The electronic band structure for each of the nitride materials possesses a direct transition with a band gap energy ranging from 0.64 eV ([Wu09] and references therein) for InN to 3.4 eV for GaN, and to 6.2 eV for AlN, as illustrated in Figure 1.1. Thus, these semiconductors and its alloys could cover most of the solar spectrum range. Besides this, characteristics such as high mobility, high breakdown voltage, high electron saturation velocity, high thermal conductivity, chemical inertness, and mechanical stability make them well suited for designing and fabricating high-power, high-frequency and high-temperature electronic devices [Dec08, Pea99].

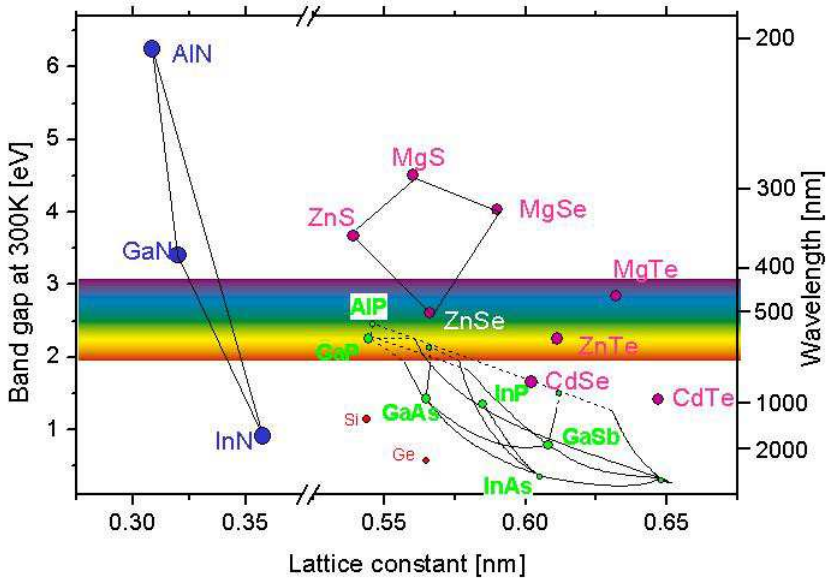

Figure 1.1: Bandgap energy versus lattice constant of the most common semiconductors.

The first studies of the growth of polycrystalline III-nitrides go back to 1907, when Fichter et al. [Fic07] reported the synthesis of AlN when aluminum is burned in the air or heated in nitrogen to a high temperature. Following that, Johnson et al. [Joh32] reported the synthesis of GaN in 1932, and Juza and Hahn [Juz38] demonstrated the growth of InN. The first important breakthrough in the research history of group III nitrides occurred when a number of workers began applying hetero-epitaxial growth on sapphire substrates to produce GaN films with reasonable crystalline quality, in 1969 by hydride vapor phase epitaxy (HVPE) [Mar69], in 1971 by metal-organic vapor phase epitaxy (MOVPE) [Man71] and in 1975 by molecular beam epitaxy (MBE) [Yos75].

All the GaN made at that time was very conducting n-type even when not deliberately doped. The lack of p-type conductivity coupled with somewhat poor crystalline quality blocked the development of nitride-based devices for several years. Another major breakthrough was the first successful production of p-type GaN using Mg, in 1989, by Amano et al., [Ama89], which later resulted in the first fabrication of highly efficient blue light emitting diodes (LEDs) (1994) and laser diodes (LDs) (1996) by Nakamura et al. [Nak94, Nak96]. Since 1994, the research activities on these materials increased rapidly because of their commercial applications.

Several techniques are currently used for the epitaxial growth of III-V nitride semiconductors. Among these techniques, MBE and MOCVD (Metal-organic chemical vapor deposition) are the most popular, due to their capability to produce films and heterostructures with the crystalline quality required for short-wavelength optoelectronic devices, and high-power high-frequency electronic devices. In the early years, MBE growth had faced some difficulties to prepare nitride epilayers, due to the lack of a proper nitrogen source, and at that time it has been surpassed by MOCVD. Thanks to the developments in the nitrogen plasma sources, MBE grown materials can now compete well with MOCVD in terms of material quality, but not in terms of surface and production throughput. Nevertheless, MBE keep several advantages over MOVPE for nanostructure fabrication. For example, the low growth temperature makes it possible to achieve chemically sharper interfaces, it is particularly adequate for the growth of InN and high-In content alloys, it offset a wide flexibility for the growth of three-dimensional (3D) nanostructures like quantum dots

(QDs) and nanowires (NWs), no post-growth activation of Mg dopants is required and Mg memory effects are reduced, which leads to sharper Mg doping profiles.

Many of the major problems that have hindered the progress in III-nitride related semiconductors can be traced back to the lack of native substrates for epitaxial growth. Most of the III-nitride-based devices are grown on foreign substrates such as sapphire or silicon carbide. Due to the destitution of the substrate with similar lattice parameters and thermal expansion coefficients, the III-nitride epitaxial layers usually contain numerous crystalline defects. The defect densities in nitride epilayers (10^7-10^{10} cm^{-2}) are much higher than those of other III-V semiconductors (e.g., for arsenide or phosphide materials, 10^2-10^4 cm^{-2}). In addition, the mismatch of thermal expansion coefficients induces thermal stress in the film and substrate during cooling down to room temperature, which can lead to bowing and even cracking of the epitaxial films. It is expected that the performance of the nitride devices will be improved with native substrates, in part due to the elimination of lattice and thermal expansion mismatch between the device layers and the substrate. Nowadays the researchers are using conductive free-standing GaN substrates created via HVPE [Kel99], since the growth of bulk GaN crystals is a challenge due to their high melting temperature, very high equilibrium nitrogen vapor pressure at moderate temperatures, and low solubility in acids, bases and most other inorganic elements and compounds. However, free-standing GaN substrates are much more expensive than the sapphire substrates used commercially as a base for nitride growth.

Another main problem with nitride semiconductors is related to the polar nature of the material. Because of their crystalline structure, III-nitride semiconductors exhibit strong spontaneous and piezoelectric polarization along their growth axis, the *c*-axis [Ber97], which leads to strong internal fields of the order of some MV/cm in quantum wells (QWs) and heterostructures [Mar96, Ler98]. Even though this large internal electric field has potential applications in piezoelectric sensors and high electron mobility transistors (HEMT) [Gas97], it has deleterious effect on the performance of optoelectronic devices, where they lead to the quantum confined Stark effect (QCSE) and reduce the radiative recombination rate within the heterostructures.

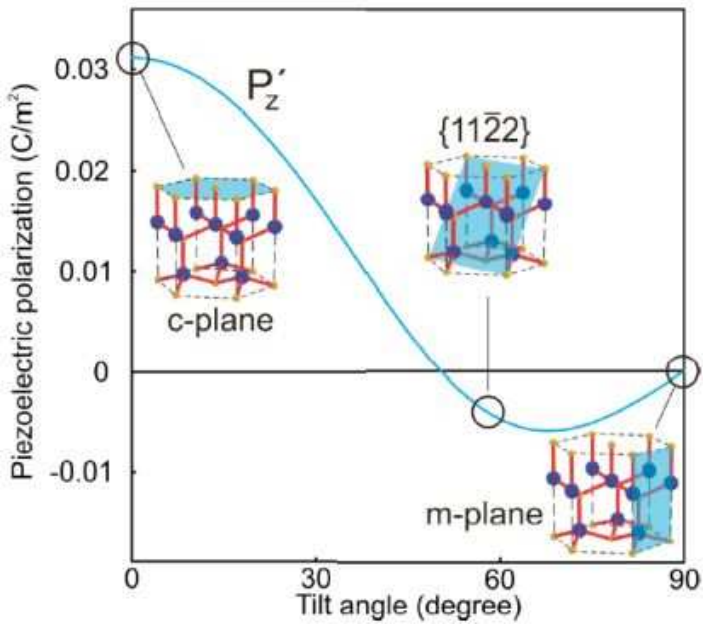

Figure 1.2: Piezoelectric polarization of an $In_xGa_{1-x}N$ quantum well as a function of the growth direction.

In order to overcome these polarization-related problems, nitride heterostructures need to be grown along crystallographic directions where the internal electric field is small or zero, that is, on semipolar planes (tilted in the range of 0° to 90° with respect to *c*-plane) or on nonpolar planes (tilted 90° with respect to *c*-plane). Figure 1.2 shows the piezoelectric polarization of an $In_xGa_{1-x}N$ QW grown pseudomorphically between relaxed GaN barriers [Par99]. Here P'_z is the polarization perpendicular to the growth plane and the lattice planes of particular polar, semipolar, and nonpolar orientations are shown as insets.

Around the year 2000 the research field of non-polar III-nitrides started to emerge in an effort to eliminate the QCSE in the heterostructures and thus achieve higher internal quantum efficiency. Waltereit et al. first demonstrated the absence of the piezoelectric field in *m*-plane GaN/AlGaN QWs grown on LiAlO2 substrates [Wal00]. A reduction of the electric field has also been observed in QDs grown in nonpolar orientations [Fou05, Ams07]. However, nonpolar nitride growth remains challenging due to the strong anisotropy of their surface properties, which leads to epitaxial layers with a high density of crystalline defects.

Another approach is the growth of the heterostructures in semipolar directions. Semipolar crystallographic orientation in the growth direction can have the potential

to reduce the polarization-induced internal electric field in the nitride structures and are subject of intense investigation in the last three years as preferred growth orientation for green/yellow light emitting diodes and lasers. Benefits like reduction in piezoelectric field strength has been experimentally verified for nitride heterostructures grown along (10-1-1), (10-1-3), and (11-22) semipolar directions [Cha05, Nis04]. Furthermore, epitaxial growth along semipolar directions appears easier to control, semipolar-grown films also incorporate indium — a crucial element in the LED — more efficiently, and have a wider growth window than nonpolar films. However, growth on alternative crystallographic orientations, like semipolar orientations, implies new defect structures, due to the enhanced probability of stacking fault formation and availability of gliding planes [Tya09], which results in an enhancement of the nonradiative recombination rate.

An advantage of QDs is that excitons trapped in these objects are expected to be much more insensitive to nonradiative recombination than other semiconductor structures, such as QWs, due to the 3D electronic confinement [Ger96]. Thus, QDs in these semipolar orientation are believed to be capable of avoiding the carrier migration to nonradiative recombination centers, and thereby the possibility of enhanced internal quantum efficiency.

1.2 Wide bandgap semiconductors for chemical sensors

Key innovations in the field of chemically-sensitive field-effect structures are due to the pioneering work of Lundström [Lun75], Bergveld [Ber70] and their coworkers. These researchers demonstrated in the nineteen-seventies that hydrogen-sensitive field-effect devices and ion-sensitive field-effect transistors could be formed using silicon-based semiconductor technology. Research along these lines remained a subject of intense interest up to the present days. Whereas in the first two decades, various kinds of gas- and ion-sensitive metal-oxide-semiconductor (MOS) capacitors and field-effect transistors were realized using the standard silicon-technology, the range of applications of chemically-sensitive field-effect devices was significantly

extended by two follow-on innovations: the first was applying SiC as a substrate material for enabling high-temperature applications, such as exhaust gas sensors required for novel kinds of exhaust gas after-treatment [Llo97]. The second innovation relates to the scanning light-pulse technique (SLPT), which allows for a spatially resolved detection of chemically induced variations in the surface potential [Lun91], and which has recently enabled developments such as computer screen-assisted remote diagnostics [Fil05]. In SLPT, the achievable spatial resolution is limited by the minority carrier diffusion length. As far as bioelectronic applications in liquid environments are concerned, the development has culminated in highly-integrated, Si-based solution-gate field-effect transistor arrays for the spatially-resolved electronic detection of neuron activity and neural signal transmission [Eve03].

More recently, other wide-bandgap semiconductors, such as diamond or the group III-nitride system, have been shown to bear promising material properties for the application in chemical and biochemical sensors. Besides their capability of high-temperature operation, which allows the realization of high-temperature gas sensors as for instance Pt:GaN Schottky diodes [Lut99, Sch02] or AlGaN/GaN field effect transistors [Sch02b], the high electrochemical surface stability of these compound semiconductors also enables novel biochemical sensor applications in liquid electrolytes [Ste03, Bau06]. Using such materials, a largely improved stability is attained with regard to conventional silicon devices.

1.3 Motivation and targets

Besides their unique optoelectronic properties, III-nitride semiconductors also exhibit material characteristics favorable for the realization of chemical sensors: high chemical and thermal stability [Eic03], and a high pH-sensitivity in liquid solutions [Ste03]. Furthermore, this material system and sapphire as the respective substrate material offer the unique advantage of being transparent to visible light, which enables transducer integration into setups for opto-chemical analyses (e.g. fluorescence spectroscopy [Ste03b]).

These concepts were the motivation of the 7th European Framework Project DOTSENSE (STREP 224212) which ran between 2008 and 2011 and set the basis of this PhD work. In this project we proposed to combine the optical properties of III-nitrides (transparency, direct bandgap, efficient luminescence) with their chemical surface properties in order to develop novel kinds of opto-chemical sensor systems. There, chemically-induced variations in the surface potential are detected by induced changes in the luminescence of III-nitride nanostructures, namely (In)GaN self-assembled QDs (Figure 1.3). This detector design allows exploiting the capability of III-nitride materials for operation under harsh environment conditions (high pressure, explosive media), as neither electrical feedthroughs nor a deterministic current are necessary for the sensor signal read-out. Furthermore, the progress in nitride technology opens up the possibility to integrate these transducers with commercially-available light emitters and detectors to form novel integrated opto-chemical sensor system architectures.

The requirement on the transducers of providing intense room-temperature photoluminescence (PL) is satisfied by the introduction of QD structures as optically active media. As described above, the 3D confinement in these nanostructures suppresses thermally activated non-radiative recombination processes. The development of III-nitride technology allows achieving QD ensembles emitting in a range of wavelengths extending from the UV to the green region. Within this range, efficient room-temperature PL can be observed, even in the case of a single QD layer. To take advantage of commercial III-nitride emitters and detectors, the sensor system should operate in the blue-green spectral range. Finally, we decided to assess the growth of QDs on non-polar or semipolar orientations in order to enhance the sensitivity of the transducers.

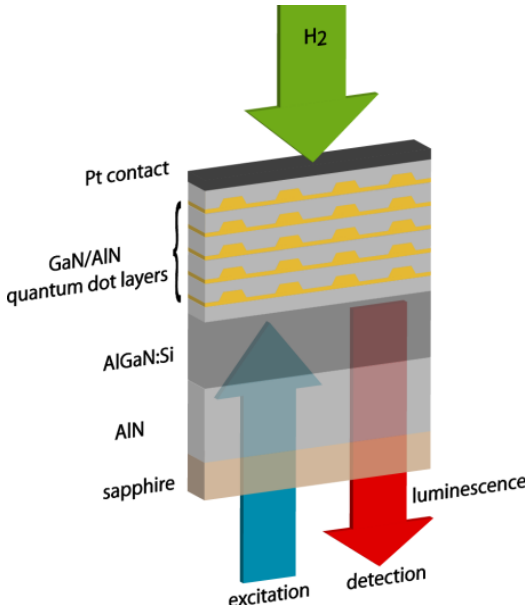

Figure 1.3: Group III-nitride QD test structures. The Si-doped AlGaN layer serves as a back contact for applying a defined potential difference across the QD stack. A bare (oxidized) surface is used in case of pH detection in liquids, a catalytic Pt-top contact is used for hydrogen detection.

Therefore, my thesis work has focused on the PAMBE growth of (In)GaN-based QD structures, grown in both polar and semipolar crystallographic orientations, for application as optical transducers for chemical sensors for detection of pH levels, and hydrogen or hydrocarbon concentrations in gas or liquid environments. With this purpose, I have first scrutinized the indium kinetics during the PAMBE growth of polar (0001) and semipolar InGaN layers, and I have applied the results to elaborate and investigate polar and semipolar InGaN/GaN QD structures. In parallel, I have studied also the growth conditions for the synthesis of semipolar (11-22)-oriented two-dimensional (2D) layers (AlGaN, InGaN, InN), including the grow of quantum well (QW) structures (InGaN/GaN QWs or InGaN/InN QWs) and the effect of Mg doping on the growth kinetics of semipolar GaN(11-22) layers. The work on semipolar material was also partially supported by the French National Research Agency Project COSNI (BLAN08-1_323691, 2008-2012).

In this project work, I have used plasma-assisted molecular beam epitaxy (PAMBE) as the growth technique to obtain III-nitride based 2D layers and nanostructures. I have applied various characterization tools to investigate the morphological, structural, and optical properties of the grown samples. In particular, I

have used reflection high energy electron diffraction (RHEED), which is an *in situ* non destructive method, to obtain structural and morphological information during the growth and *ex situ* characterization of samples by X-ray diffraction (XRD), atomic force microscopy (AFM) and photoluminescence (PL). Additional data on the structural quality of the layers was provided by transmission electron microscopy (TEM), performed by our collaborators at Aristotle University of Thessaloniki, Greece (Prof. Ph. Komninou). Furthermore, the thickness and depth profile of the chemical composition have been characterized by Rutherford backscattering spectroscopy (RBS) at Instituto Tecnológico e Nuclear, Portugal (Dr. K. Lorenz). Chemical studies of the QDs and sensor structures, as well as characterization of the QD stacks under bias, were performed by our collaborators at Justus-Liebig-Universität Giessen, Germany (Prof. M. Eickhoff) and the final integrated sensor system was designed and tested by EADS (Dr. A. Helwig).

1.4 Organization of the manuscript

The thesis starts with this first chapter that presents a historical introduction to III-nitrides and to wide bandgap semiconductor sensors. The motivation, target and methods of the work are described and the chapter finishes with the description of this document.

The second chapter presents a comprehensive overview of fundamental properties of III-nitride semiconductors, starting with the description of the crystalline structure, then presenting the band structure and finishing with the discussion of the origin of the polarization and the internal electric field in nitride heterostructures.

The purpose of the third chapter is to provide the information about the different techniques used for the experiments described in this work. The first part of this chapter deals with the thermodynamics and growth kinetics of GaN, AlN, AlGaN and InGaN, after a short introduction about epitaxial growth, while the latter sections describe the characterization tools I used to determine structural and optical properties of the nitride structures.

In chapter four, I present my contribution to the domain of PAMBE of 2D semipolar layers. The first sections deal with the synthesis of binary AlN and GaN alloys and the effect of doping on the growth of semipolar GaN. The chapter finishes with the discussion of the growth details and properties of the ternary AlGaN and InGaN alloys, and finally the results of the synthesis of semipolar InN.

The fifth chapter starts with the description of the growth and characterization of polar and semipolar GaN/AlN QDs. Then I present my contribution to the domain of InGaN/GaN QDs, starting with the description of the synthesis and optical performance of the polar InGaN/GaN QDs in comparison with polar InGaN/GaN QWs. After that, I will discuss the particularities of the growth and properties of semipolar InGaN/GaN QDs.

The last chapter, chapter six, begins by introducing different opto-chemical transducer structures, including the polar and semipolar GaN/AlN and InGaN/GaN QD transducers. Then, I describe the fabrication of the QD transducer structures and its characterization. Details of the integrated chemical sensor based on InGaN/GaN QDs transducer is presented at the end of this chapter.

Bibliography

[Ama89] H. Amano, M. Kito, K. Hiramatsu, and I. Akasaki, *P-type conduction in Mg-doped GaN treated with low-energy electron beam irradiation (LEEBI)*. Japanese Journal of Applied Physics 28, L2112 (1989).

[Ams07] B. Amstatt, J. Renard, C. Bougerol, E. Bellet-Amalric, B. Gayral, and B. Daudin, *Growth of m-plane GaN quantum wires and quantum dots on m-plane 6H-SiC*. Journal of Applied Physics 102, 074913 (2007).

[Bau06] B. Baur, J. Howgate, H.-G. von Ribbeck, Y. Gawlina, V. Bandalo, G. Steinhoff, M. Stutzmann, and M. Eickhoff, *Catalytic activity of enzymes immobilized on AlGaN/GaN solution gate field-effect transistors.* Applied Physics Letters 89, 183901 (2006).

[Ber70] P. Bergveld, *Development of an Ion-Sensitive Solid State Device for Neurophysiological Measurements*. *IEEE Transactions on Biomedical Engineering* 17, 70 (1970).

[Ber97] F. Bernardini, V. Fiorentin, and D. Vanderbilt, *Spontaneous polarization and piezoelectric constants of III-V nitrides*. Physical Review B 56(16), R10024 (1997).

[Cha05] A. Chakraborty, T. J. Baker, B. A. Haskell, F. Wu, J. S. Speck, S. P. Den-Baars, S. Nakamura, and U. K. Mishra, *Miliwatt power blue InGaN/GaN Light-emitting diodes on semipolar GaN templates*. Japanese Journal of Applied Physics 44, L954 (2005).

[Dec08] E. A. DeCuir, Jr., M. O. Manasreh, Elena Tschumak, J. Schörmann, D. J. As, and K. Lischka, *Cubic GaN/AlN multiple quantum well photodetectors.* Applied Physics Letter 92, 201910 (2008).

[Eic03] M. Eickhoff, J. Schalwig, G. Steinhoff, O. Weidemann, L. Görgens, R. Neuberger, M. Hermann, B. Baur, G. Müller, O. Ambacher, and M. Stutzmann, *Electronics and sensors based on pyroelectric AlGaN/GaN heterostructures* physica status solidi (c) 0, 1908 (2003).

[Eve03] B. Eversmann, M. Jenkner, F. Hofmann, C. Paulus, R. Brederlow, B. Holzapfl, P. Fromherz, M. Merz, M. Brenner, M. Schreiter, R. Gabl, K. Plehnert, M. Steinhauser, G. Eckstein, D. S. Landsiedel and R. Thewes, *A 128×128 CMOS Biosensor Array for Extracellular Recording of Neural Activity*. IEEE Journal of Solid-State Circuits 38, 2306 (2003)

[Fic07] F. Fichter, *Über Aluminiumnitrid. Z. Anorg. Chem.* 54, 322 (1907).

[Fil05] D. Filippini and I. Lundström, *Adaptive illumination in computer screen assisted spectral fingerprinting.* Applied Physics Letters 86, 084101 (2005).

[Fou05] S. Founta, F. Rol, E. Bellet-Amalric, J. Bleuse, B. Daudin, B. Gayral, H. Mariette, and C. Moisson, *Optical properties of GaN quantum dots grown on nonpolar (11-20) SiC by molecular-beam epitaxy*. Applied Physics Letters 86, 171901 (2005).

[Gas97] R. Gaska, J. W. Yang, A. Osinski, A. D. Bykhovski, and M. S. Shur, *Piezoeffect and gate current in AlGaN/GaN high electron mobility transistors.* Applied Physics Letters 71, 3673 (1997).

[Ger96] J. M. Gérard, O. Cabrol, and B. Sermage, *InAs quantum boxes: Highly efficient radiative traps for light emitting devices on Si.* Applied Physics Letters 68, 3123 (1996).

[Joh32] W. C. Johnson, J. B. Parsons, and M. C. Crew, *Nitrogen compounds of Gallium III.Gallic Nitride*. Journal of Physical Chemistry 36, 2651 (1932).

[Juz38] R. Juza and H. Hahn, *Über die Kristallstrukturen von Cu_3N, GaN und InN Metallamide und Metallnitride.* Z. Anorg. Allg. Chem. 239, 282 (1938).

[Kel99] M. K. Kelly, R. P. Vaudo**,** V. M. Phanse, L. Görgens, O. Ambacher and M. Stutzmann, *Large Free-Standing GaN Substrates by Hydride Vapor Phase Epitaxy and Laser-Induced Liftoff*. Japanese Journal of Applied Physics 38, L217 (1999).

[Ler98] M. Leroux, N. Grandjean, M. Laügt, J. Massies, B. Gil, P. Lefebvre, and P. Bigenwald, *Quantum confined Stark effect due to built-in internal polarization fields in (Al,Ga)N/GaN quantum wells.* Physical Review B 58, 13371 (1998).

[Llo97] A. Lloyd Spetz, A. Baranzahi, P. Tobias, and I. Lundström, *High temperature sensors based on metal- insulator- silicon carbide devices. Physica Status Solidi (a)* 162, 493 (1997)

[Lun75] I. Lundström, S. Shivaraman, C. Svensson, and L. Lundkvist, *A hydrogen−sensitive MOS field−effect transistor*. Applied Physics Letter 26, 55 (1975).

[Lun91] I. Lundström, R. Erlandsson, U. Frykman, E. Hedborg, A. Spetz, H. Sundgren, S. Welin and F. Winquist, *Artificial 'olfactory' images from a chemical sensor using a light-pulse technique.* Nature 352, 47 (1991).

[Lut99] B. P. Luther, S. D. Wolter, S. E. Mohney, *High temperature Pt Schottky diode gas sensors on n-type GaN.* Sensors and Actuators B 56, 164 (1999).

[Man71] H.M. Manasevit, F.M. Erdmann, and W.I. Simpson, *The use of metalorganics in the preparation of semicondutor materials*. Journal of Electrochemistry Society 118, 1864 (1971).

[Mar69] H. P. Maruska and J. J. Tietjen, *The preparation and properties of vapordeposited single-crystalline GaN*. Applied Physics Letter 15, 327 (1969).

[Mar96] G. Martin, A. Botchkarev, A. Rockett, and H. Morkoç, *Valenceband discontinuities of wurtzite GaN, AlN, and InN heterojunctions measured by xray photoemission spectroscopy.* Applied Physics Letters 68, 2541 (1996).

[Nak94] S. Nakamura, T. Mukai, and M. Senoh, *Candela-class high-brightness InGaN/AlGaN double-heterostructure blue-light-emitting diodes.* Applied Physics Letter 64, 1687 (1994).

[Nak96] S. Nakamura, M. Senoh, S. Nagahama, N. Iwasa, T. Yamada, T. Matsushita, Y. Sugimoto, and H. Kiyoku , *Room-temperature continuous-wave operation of*

InGaN multi-quantum-well structure laser diodes. Applied Physics Letter 69, 4056 (1996).

[Nis04] K. Nishizuka, M. Funato, Y. Kawakami, S. Fujita, Y. Narukawa, and T. Mukai, *Efficient radiative recombination from (11-22) -oriented $In_xGa_{1-x}N$ multiple quantum wells fabricated by the regrowth technique.* Applied Physics Letters 85, 3122 (2004).

[Par99] S.-H. Park and S.-L. Chuang, *Crystal-orientation effects on the piezoelectric field and electronic properties of strained wurtzite semiconductors.* Physical Review B 59, 4725 (1999).

[Pea99] S. J. Pearton, J. C. Zolper, R. J. Shul, and F. Ren, *GaN: Processing, defects, and devices.* Journal of Applied Physics 86,1 (1999).

[Sch02] J. Schalwig, G. Müller, U. Karrer, M. Eickhoff, O. Ambacher, M. Stutzmann, L. Görgens, and G. Dollinger, *Hydrogen response mechanism of Pt–GaN Schottky diodes.* Applied Physics Letters 80, 1222 (2002).

[Sch02b] J. Schalwig, G. Muller, M. Eickhoff, O. Ambacher and M. Stutzmann, *Gas sensitive GaN/AlGaN-heterostructures.* Sensors and Actuators B 87, 425 (2002).

[Ste03] G. Steinhoff, M. Hermann, W. J. Schaff, L. F. Eastman, M. Stutzmann, and M. Eickhoff, *pH response of GaN surfaces and its application for pH-sensitive field-effect transistors*. Applied Physics Letters 83, 177 (2003).

[Ste03b] G. Steinhoff, O. Purrucker, M. Tanaka, M. Stutzmann and M. Eickoff, *$Al_xGa_{1-x}N$ - A new material system for biosensors.* Advanced Functional Materials 13, 841 (2003).

[Tya09] A. Tyagi, F. Wu, E. C. Young, A. Chakraborty, H. Ohta; R. Bhat, K. Fujito; S. P. DenBaars, S. Nakamura, and J. S. Speck, *Partial strain relaxation via misfit dislocation generation at heterointerfaces in (Al,In)GaN epitaxial layers grown on semipolar (11-2 2) GaN free standing substrates.* Applied Physics Letters 95, 251905 (2009).

[Wal00] P.Waltereit, O. Brandt, A. Trampert, H. T. Grahn, J.Menniger, M. Ramsteiner, M. Reiche, and K. H. Ploog, *Nitride semiconductors free of electrostatic fields for efficient white light-emitting diodes*. Nature 406, 865 (2000).

[Wu09] J. Wu, *When group-III nitrides go infrared: New properties and perspectives.* Journal of Applied Physics 106, 1 (2009).

[Yos75] S. Yoshida, S. Misawa, and A. Itoh, *Epitaxial growth of aluminium nitride films on sapphire by reactive evaporation*. Applied Physics Letter 26, 461 (1975).

Chapter 2

Properties of III-nitride semiconductors

A brief summary of the basic physical and electronic properties of group III nitrides will be introduced in the present chapter. It starts with the description of the crystalline structure, then presenting the band structure and finishing with the discussion about the origin of the polarization and the internal electric field in nitride heterostructures.

2.1 Crystalline structure

2.1.1 Crystal symmetry and lattice parameters

Group III nitrides (GaN, AlN, InN and their alloys) share three common crystal structures: the wurtzite (α-phase), the zinc-blend (β-phase) and the rocksalt (γ-phase). While the wurtzite structure is the thermodynamically more stable one, group-III nitrides can also be grown, by epitaxy, in the metastable zinc-blende structure. The rocksalt structure appears only at very high pressures and cannot be stabilized by the epitaxial growth.

The wurtzite structure shows hexagonal symmetry with the associated space group $P6_3mc$ (C^4_{6v}). It consists of two hexagonal compact sublattices of metal (Ga, Al or In) and nitrogen (N) atoms, which are shifted with respect to each other ideally by 3/8[0001], as shown in figure 2.1(a). By contrast, the zinc-blend structure also called sphalerite shows a cubic symmetry with the associated space group F43m (T^2_d). It consists of two interpenetrating face-centered cubic sublattices, the second shifted by ¼[111] with respect to the first (Figure 2.1 (b)), with both metal and nitrogen atoms occupying appropriate sites.

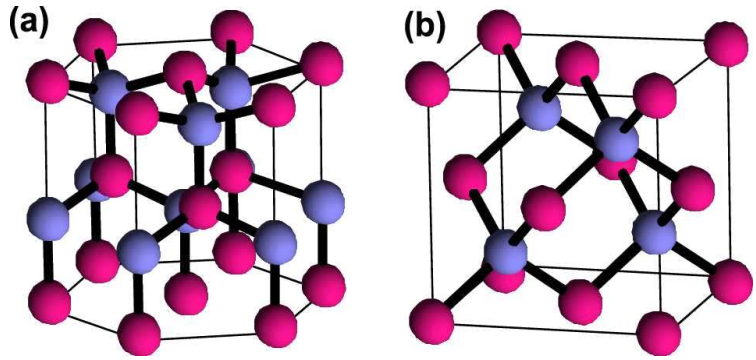

Figure 2.1: Schematic representation of (a) the Wurtzite and (b) zinc-blende structure. The red and blue spheres indicate metal and N atoms, respectively.

In both wurtzite and zinc-blend structures, each atom is tetrahedrally coordinated. The group III metal and nitrogen tetrahedrons are differently oriented for the two structures, one structure can be locally transformed into the other by a rotation of 60^0 around the [111] axis of the zinc-blende structure or the equivalent [0001] axis of the wurtzite structure. That is, both structures differ only by the stacking sequence of close-packed III-N planes, and the energy difference between the two structures is within ±10 meV/atom [Yeh92]. The stacking periodicity along the [0001] axis is ABABA… for the wurtzite phase and it is ABCABCA... along the [111] axis for the zinc-blend phase (Figure 2.2). Changing the sequence during growth produces defects such as stacking faults. This work focuses on wurtzite type nitrides, and the following chapters will only address the intrinsic properties of wurtzite materials.

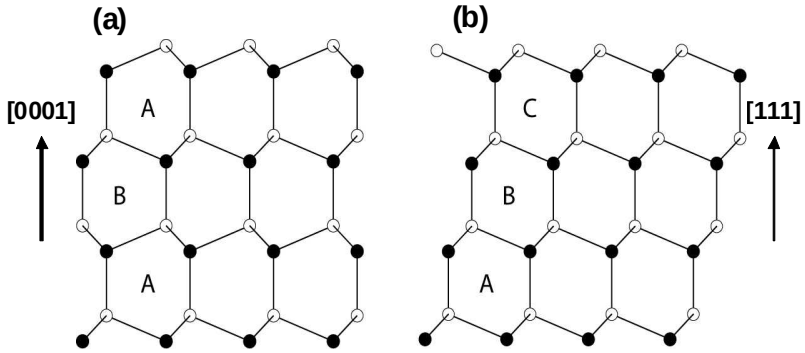

Figure 2.2: Stacking sequence for (a) (0001) planes in wurtzite ([11-20] azimuth), and (b) (111) planes in zinc-blende ([1-10] azimuth).

Figure 2.3 shows the three parameters that define the wurtzite unit cell. These are the edge length of the basal hexagon (*a*), the height of the hexagonal lattice cell

(*c*), and the anion-cation bond length (*u*) along the [0001] direction. In an ideal wurtzite crystal, the *c/a* ratio and *u/c* ratio are 1.633 and 0.375, respectively. Because of the different metal cations, the bond lengths and the resultant *c*/*a* ratios of AlN, GaN, and InN are different. Table 2.1 shows an overview of these lattice parameters of wurtzite III-nitrides at 300 K. The experimental values for GaN and InN are close to the ideal ones, whereas those of AlN deviate slightly, which indicates that the AlN lattice is distorted with respect to a pure wurtzite structure. This fact is very important because the degree of non-ideality is a significant factor in determining the strength of polarization in III-nitrides.

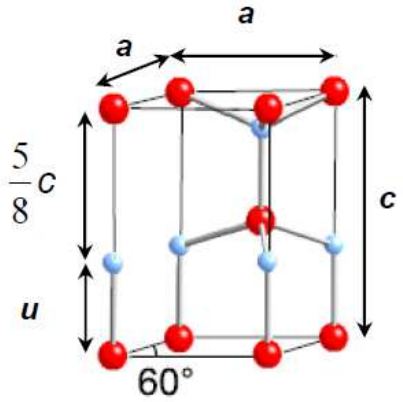

Figure 2.3: Wurtzite unit cell, where c and a are the lattice constants and u is the anion-cation bond length.

The lattice parameters of ternary alloys, like $A_xB_{1-x}N$, are usually investigated based on the Vegard's law, i.e., assuming that the lattice constant of a ternary alloy can be expressed as a linear combination of the lattice constants of the two forming binary alloys:

$$a_{AB} = x\, a_A + (1 - x)\, a_B \;\; ; \;\; c_{AB} = x\, c_A + (1 - x)\, c_B \qquad (2.1)$$

	InN	**GaN**	**AlN**
***c* (Å)**	5.703	5.185	4.982
***a* (Å)**	3.545	3.189	3.112
c/a	1.608	1.626	1.6
u/c	0.377	0.377	0.382
References	[Vur03]	[Mor94] [Vur03]	[Mor94] [Vur03]

Table 2.1: Lattice parameters of bulk InN, GaN and AlN.

Crystal planes in hexagonal unit cells are commonly identified by using four indices called *Miller-Bravais indices*, which are denoted by the letters *h*, *k*, *i*, and *l* and are enclosed in parentheses as (*hkil*). These four-digit hexagonal indices are based on a coordinate system with four axes, as shown in figure 2.4. There are three basal axes, a_1, a_2, and a_3, which make 120° with each other. The fourth axis or *c* axis is the vertical axis of the hexahedron. The reciprocals of the intercepts that a crystal plane makes with the a_1, a_2, and a_3 axes give the *h*, *k*, and *i* indices, while the reciprocal of the intercept with the *c* axis gives the *l* index. Note that the sum of the first three indices is necessarily zero: $i = -(h + k)$

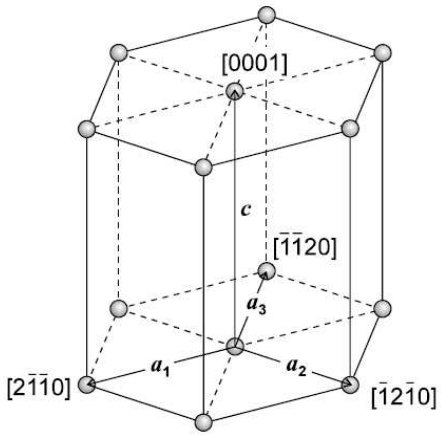

Figure 2.4: Hexagonal unit cell with representations for the base vectors a_1, a_2, a_3 and c.

The crystallographic directions in hexagonal unit cells are also usually indicated by four indices *u*, *v*, *t*, and *w* enclosed by square brackets as [*uvtw*]. The *u*, *v*, and *t* indices are lattice vectors in the a_1, a_2, and a_3 directions, respectively (Figure 2.4), and the *w* index is a lattice vector in the *c* direction.

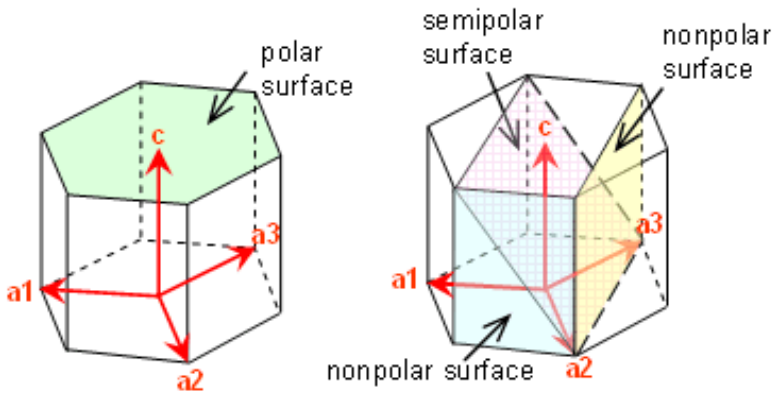

Figure 2.5: Schematic views of the polar plane, the nonpolar planes and a semipolar plane.

In a wurtzite system, the [0001] direction is called polar direction, and using it as a reference we can distinguish three types of crystal planes. The {0001} planes are commonly referred to as polar plane and it has only group III or nitrogen atoms on the top layer. Other planes are either perpendicular or inclined to the (0001) polar plane. Schematic views of such wurzite crystal planes are shown in figure 2.5. There are two surfaces parallel to the c axis, which have equal number of group III and nitrogen atoms in the top surface layer, and are called nonopolar surfaces: the {11-20} *a*-plane and the {1-100} *m*-plane. Inclined surfaces, such as {10-1-3}, {10-1-1}, and {11-22}, are often denominated semipolar surfaces. In this thesis work, the semipolar (11-22) plane has an important role.

2.1.2 Crystal polarity

Due to the lack of inversion symmetry of the wurtzite structure, the [0001] and the [000-1] directions are not equivalent. The axis sign is determined by the direction of the vector associated to the metal-nitrogen bond along the <0001> axis. The [0001] axis is considered positive when this vector points from the metal atom to the nitrogen atom. We arbitrarily denote the material as metal-polar if grown along the [0001] or as nitrogen-polar if grown along [000-1] (see figure 2.6). The corresponding metal-polar (0001) and nitrogen-polar (000-1) faces can be terminated by either metal atoms or nitrogen atoms.

The polarity can drastically affect the surface properties. Polarity in GaN films is important for the design and fabrication of many electronic devices. To determine the polarity of GaN films, there are many analytical tools used- X-ray photoemission spectroscopy (XPS) [Sas88], Auger spectroscopy [Asi93], X-ray photoelectron diffraction (XPD) [See97], convergent beam electron diffraction (CBED) [Pon96] and ion channeling techniques [Dau97]. Also chemical etching using KOH or NaOH solution is a destructive method of polarity determination, that is, N polar orientation is easily etched while the Ga- polar face is chemically inert.

The polarity of GaN depends the nature of the substrate and on the growth conditions. By molecular beam epitaxy, Ga polar GaN can be grown on an AlN buffer layer on (0001) sapphire while N-polar GaN can be obtained by nucleating GaN

buffer layer directly on (0001) sapphire under heavily Ga-rich conditions. In 1999, Ramachandran et al, determined that polarity inversion of Ga polar GaN to N polar can occur through Mg doping [Ram99]. All growths conducted in this research were metal-polar.

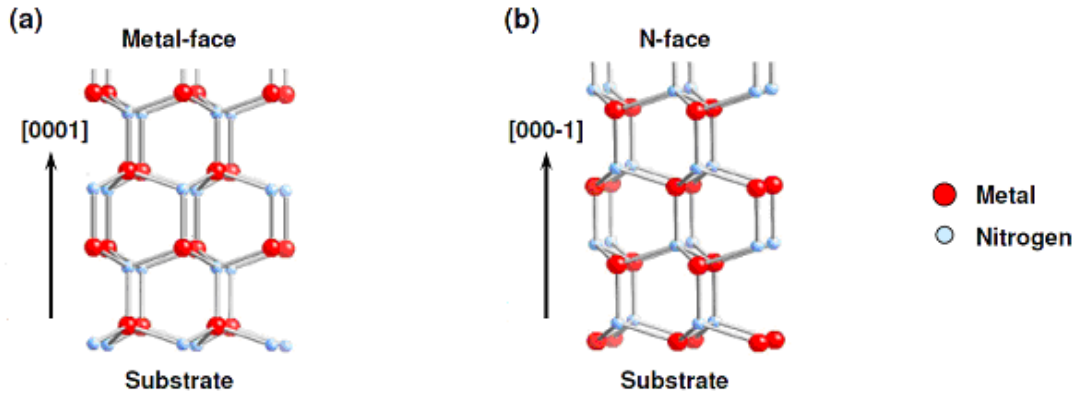

Figure 2.6: Polarity in GaN: (a) Ga-polar along [0001], (b) N-polar for [000-1].

2.2 Electronic properties

2.2.1 Band structure

Group III nitrides are direct band gap semiconductors. The conduction band minimum is located at the centre of the Brillouin zone (Γ-point, k=0). The calculated band structures of GaN and AlN are depicted in figure 2.7.

At the Γ point, the valence band of the wurtzite structure of III nitrides consists of three subbands which are split as a result of the crystal-field interaction (Δ_{CR}) and spin-orbit coupling (Δ_{SO}). The three subbands are the heavy hole band (A band, with Γ_9 symetry), the light hole band (B band, with Γ_7 symmetry) and the spin-orbit band (C band with Γ_7 symmetry) [Figure 2.7]. This band structure leads to three different excitons formed between electrons of the conduction band and holes of the corresponding valence subband, usually named A, B and C. In the case of GaN, the energy difference between the valence band subbands is given by $\Delta E_{AB} = 6$ meV, $\Delta E_{CB} = 37$ meV, with the values of degeneracy by the crystal-field and spin-orbit $\Delta_{CR} = 10$ meV and $\Delta_{SO} = 17$ meV respectively [Vur01], as shown in figure 2.8. In the

case of AlN, Δ_{CR} = -169 meV, [Vur01], i.e. the top of the C subband is at higher energy than the A or B subbands.

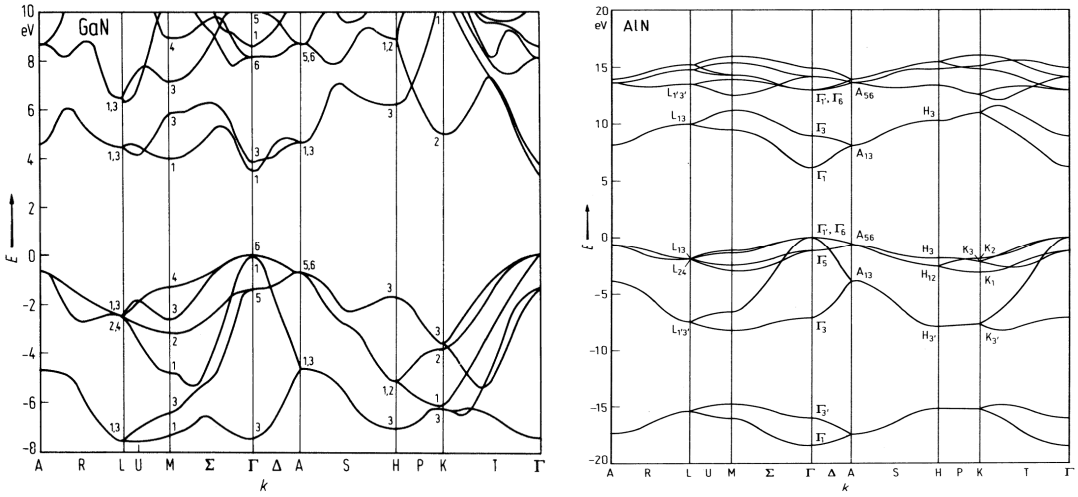

Figure 2.7: Calculated band structure of GaN and AlN (from [Rem99]).

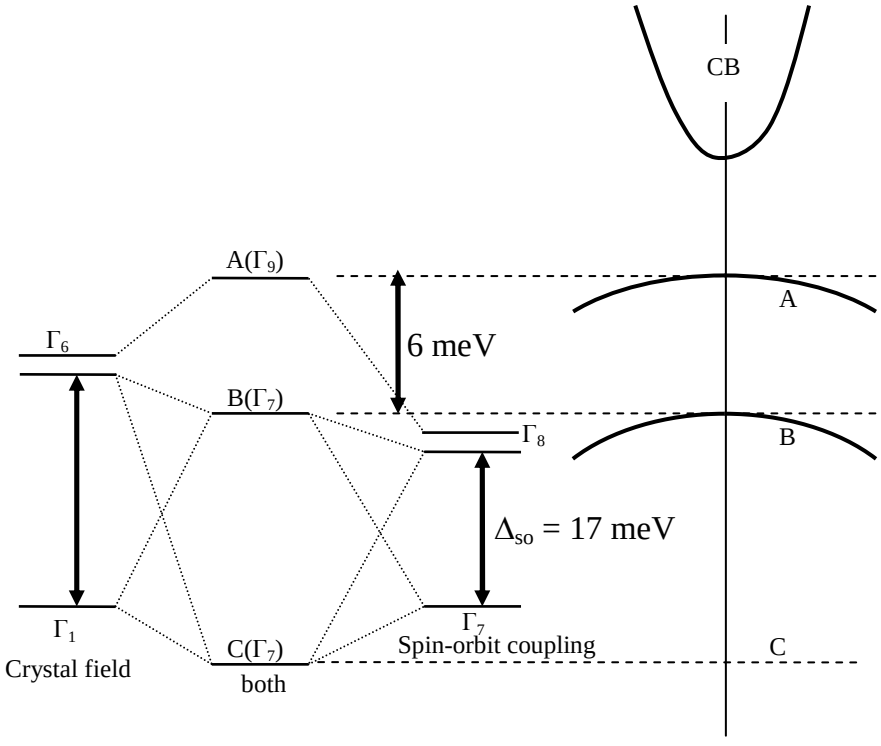

Figure 2.8: Schematic representation of the valence band splitting in wurtzite GaN.

The band parameters for GaN, AlN and InN have been summarized below, in Table 2.2.

	$E_g(T = 0\ K)$ (eV)	$E_g(T = 300\ K)$ (eV)	α (meV/K)	β (K)	References
GaN	3.47 3.492	3.411 3.426	0.59 0.531	600 432	[Li97] [Tri99]
AlN	6.126	6.03	1.799	1462	[Guo94]
InN	0.69	0.641	0.414	454	[Wal04]

Table 2.2: Band parameters of GaN, AlN and InN.

In ternary compounds, the band gap dependence on the alloy composition is modeled using a quadratic polynomial whose nonlinear coefficient is called the bowing parameter. Therefore, the band gap of $A_xB_{1-x}N$ ternary alloys as a function of alloy composition is generally parametrized by:

$$E_g^{(AB)} = xE_g^{(A)} + (1 - x)E_g^{(B)} - x(1 - x)b \qquad (2.2)$$

where b is the bowing parameter. Some values of bowing parameters reported for the III-nitrides are given in Table 2.3.

	b (eV)	References
$Al_xGa_{1-x}N$	0.62 ± 0.45 0 1.33 0.353 ± 0.024 -0.82 0.341 ± 0.035 0.351 ± 0.043	[Och99] [Lee99] [Sha98] [Kuo02] [Onu04] [Lio05] [Lio05]
$In_xGa_{1-x}N$	1.21 ± 0.03 1.782 ± 0.076 1.916 ± 0.068 1.44*	[Kuo01] [Lio05] [Lio05] [Cae07]

*Table 2.3: Values of the bowing parameter for AlGaN and InGaN alloys.*Value used in this work.*

2.2.2 Temperature dependence of the fundamental band gap

The temperature dependence of the fundamental energy gap is mainly caused by the changes of band structure induced by the lattice thermal expansion and electron-phonon interaction. An analytical expression, which has been frequently used during the past 30 years for numerical fittings of temperature dependences reported

for various semiconductor materials, was first suggested by Varshni in the simple form [Var67]:

$$E_g(T) = E_g(T=0) - \frac{\alpha T^2}{\beta + T} \tag{2.3}$$

where $E_g(T)$ is the gap at a temperature T, and α and β are known as Varshni thermal coefficients. There is widespread values reported in the literature and some of those are recorded in Table 2.2.

2.2.3 Effective masses

Several techniques were used in order to determine the effective masses of GaN and AlN. Barker et al. used infrared reflectivity and absorption measurements on single-crystal epitaxial GaN and obtained a value of $m_e = (0.22 \pm 0.03)m_0$ for the electron effective mass [Bar73]. This value was confirmed by using cyclotron resonance experiments on unintentionally doped GaN films, and most of the experimental results showed that, for GaN and AlN, the electron effective mass is approximately constant along all the crystallographic directions. For the effective hole mass the scenario is different, theoretical calculations predict that the effective mass of holes should be strongly anisotropic, since they have a strong dependence on the k-direction (Figure 2.9). Experimental values of the effective mass of electrons and holes for wurtzite type GaN, AlN and InN are summarized in Table 2.4.

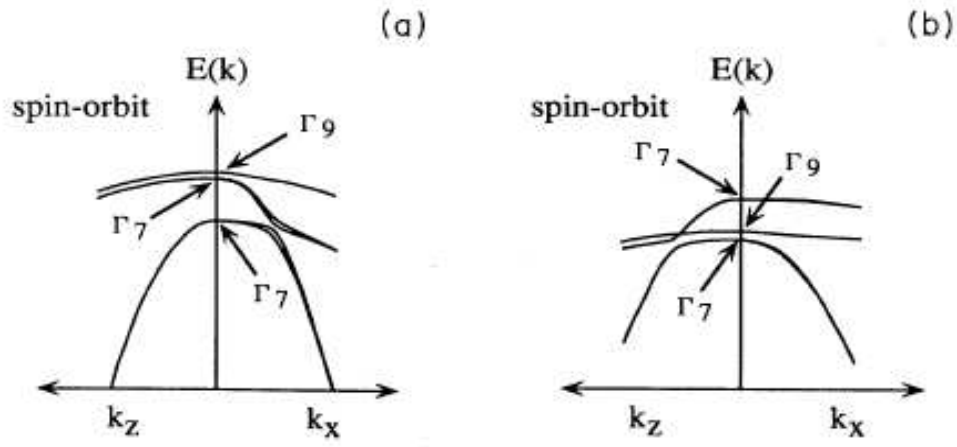

Figure 2.9: Valence band structure of (a) GaN (b) AlN, indicating the anisotropy.

	Electron effective mass	Hole effective mass
GaN	0.2 m_0 [Per96, Dre95]	0.3 m_0 [Sal95] 2.2 m_0 [Im97] 0.54 m_0 [Mer96] 0.8 m_0 [Pan75] 1 m_0 [Vur01]
AlN	0.32 m_0 [Vur01, Dre95]	1.41 m_0 [Kim97]
InN	0.11 m_0 [Tya77]	1.63 m_0 [Xu93]

Table 2.4: Effective masses of wurtzite GaN and AlN.

2.3 Elastic properties

Nitrides are mainly synthesized on substrates as sapphire, SiC or Si, by heteroepitaxy. The lattice and thermal mismatch between the substrate and the epitaxial layer induces strain during growth. The effects of the strain introduced by lattice constant and thermal expansion mismatch are difficult to separate and they are dealt with as an overall effect. This strain has a profound effect on the optical properties, electrical properties and also on the band gap properties of the III nitrides. When a GaN layer is grown on a sapphire substrate, it experiences a compressive biaxial stress which will increase the fundamental band gap compared to the unstrained GaN layer. However, using a Si(111) or a silicon carbide (SiC) substrate will introduce a biaxial tensile stress and it will reduce the band gap. This effect can be confirmed by the energy position of the excitonic transitions.

2.3.1 Strain and stress

In the framework of linear elasticity, the stress (σ_{ij}) of a material is related to the strain (ε_{kl}) by Hooke's law:

$$\sigma_{ij} = \sum C_{ijkl}\ \varepsilon_{kl} \tag{2.4}$$

where (C_{ijkl}) is the fourth-order elastic tensor.

To simplify the notation especially that of the fourth-order tensor C_{ijkl} – we introduce the indices {1,2,3,4,5,6}, which replace the pairs of indices {xx,yy,zz,yz,zx,xy}:

$$\varepsilon_1 = \varepsilon_{xx} \qquad \sigma_1 = \sigma_{xx}$$

$$\varepsilon_2 = \varepsilon_{yy} \qquad \sigma_2 = \sigma_{yy}$$

$$\varepsilon_3 = \varepsilon_{zz} \qquad \sigma_3 = \sigma_{zz}$$

$$\varepsilon_4 = \varepsilon_{yz}\,,\ \varepsilon_{zy} \qquad \sigma_4 = \sigma_{yz}\,,\ \sigma_{zy}$$

$$\varepsilon_5 = \varepsilon_{zx}\,,\ \varepsilon_{xz} \qquad \sigma_5 = \sigma_{zx}\,,\ \sigma_{xz}$$

$$\varepsilon_6 = \varepsilon_{xy}\,,\ \varepsilon_{yx} \qquad \sigma_6 = \sigma_{xy}\,,\ \sigma_{yx}$$

Then, the elastic module can be represented by a matrix (a second-order tensor). For a crystal of hexagonal symmetry, this matrix contains six elastic modules, of which five are independent [$C_{66} = (C_{11}\text{-}C_{12})/2$], as given in equation (2.5):

$$C_{ij} = \begin{pmatrix} C_{11} & C_{12} & C_{13} & 0 & 0 & 0 \\ C_{12} & C_{11} & C_{13} & 0 & 0 & 0 \\ C_{13} & C_{13} & C_{33} & 0 & 0 & 0 \\ 0 & 0 & 0 & C_{44} & 0 & 0 \\ 0 & 0 & 0 & 0 & C_{44} & 0 \\ 0 & 0 & 0 & 0 & 0 & \frac{1}{2}(C_{11} - C_{12}) \end{pmatrix} \tag{2.5}$$

Calculated and experimental values of the parameters C_{ij} for InN, GaN and AlN are summarized in Table 2.5.

	C_{11}	C_{12}	C_{13}	C_{33}	C_{44}	**References**
InN	271	124	94	200	46	[Kim96] theory
	223	115	92	224	48	[Wri97] theory
GaN	374	106	70	379	101	[Tak96] exp.
	390	145	106	398	105	[Pol97] exp.
	365	135	114	381	109	[Yam97] exp.
	370	145	110	390	90	[Deg98] exp.
	396	144	100	392	91	[Kim96] theory
	367	135	103	405	95	[Wri97] theory
AlN	411	149	99	389	125	[McN93] exp.
	410	140	100	390	120	[Deg98] exp.
	398	140	127	382	96	[Kim96] theory
	396	137	108	373	116	[Wri97] theory

Table 2.5: Experimental and theoretical stiffness constants of InN, GaN and AlN in GPa.

2.3.2 Biaxial stress in a (0001)-oriented hexagonal system

During heteroepitaxy of III-nitrides on the (0001) plane, the in-plane stress is uniform ($\sigma_{11} = \sigma_{22} = \sigma$) and there is no stress along the *c* axis or shear stress. In that particular case (biaxial stress configuration), the Hooke law is simplified as in equation 2.6:

$$\begin{pmatrix} \sigma \\ \sigma \\ 0 \end{pmatrix} = \begin{pmatrix} C_{11} & C_{12} & C_{13} \\ C_{12} & C_{11} & C_{13} \\ C_{13} & C_{13} & C_{33} \end{pmatrix} \cdot \begin{pmatrix} \varepsilon_1 \\ \varepsilon_2 \\ \varepsilon_3 \end{pmatrix} \tag{2.6}$$

Here the growth is carried out on a (0001) plane and the strain components ε_1 and ε_2 are equal:

$$\varepsilon_1 = \varepsilon_2 = \varepsilon_{xx} = -(a_{epi} - a_{sub})/a_{sub} \tag{2.7}$$

where a_{epi} and a_{sub} are the lattice constants of the epilayer and the substrate, respectively. Consequently, the biaxial strain induces a strain ε_3 of opposite sign along the [0001] axis perpendicular to the surface, which is given by:

$$\varepsilon_3 = \varepsilon_{zz} = -2(C_{13}/C_{33})\varepsilon_{xx} \tag{2.8}$$

2.3.3 Strain in semipolar layers under biaxial stress

To describe the strain state in III-nitride semipolar layers it is convenient to use two coordinate systems *xyz* (natural) and *x*'*y*'*z*' (primed), as shown in figure 2.10. In this case, the *z*' axis is in the direction of the template surface normal and the two other axes (*x*' and *y*') are in the template's surface plane with the *x*' axis coincident with the *x* axis. In general, the misfits along *x*' and *y*' directions (ε_{m1} and ε_{m2} , respectively) are different and the elastic strain depend on these crystal lattice mismatch parameters.

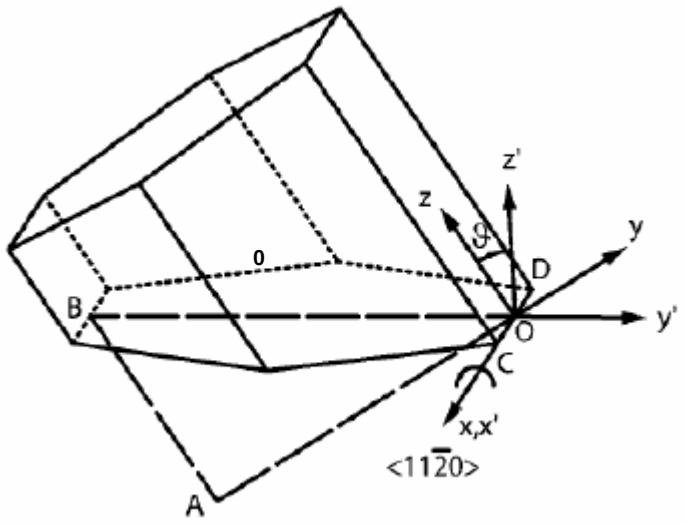

Figure 2.10: Schematic for calculating in-plane misfit strains of semipolar planes.

The crystal lattice mismatch is determined by the crystal lattice parameters a_L, c_L of the film (layer) and a_T, c_T of the substrate (template):

$$\varepsilon_{m1} = (a_T - a_L)/a_L$$

$$\varepsilon_{m2} = \left(a_T c_T - \sqrt{(a_L c_T)^2 \cos^2\vartheta + (a_T c_L)^2 \sin^2\vartheta} \right) / \sqrt{(a_L c_T)^2 \cos^2\vartheta + (a_T c_L)^2 \sin^2\vartheta}$$

Since the out- of plane direction is free, the layer is under zero traction stress ($\sigma_{z'z'}$) and the absence of shear stress gives $\sigma_{x'z'} = \sigma_{y'z'} = 0$ together with a zero in-plane shear mismatch $\varepsilon_{x'y'} = 0$.

In the primed-coordinate system the nonzero components of strain tensor are [Rom06]:

$$\varepsilon_{x'x'} = \varepsilon_{m1}$$

$$\varepsilon_{y'y'} = \varepsilon_{m2}$$

$$\varepsilon_{z'z} = [(B_{41}\,\varepsilon_{m1} + B_{42}\,\varepsilon_{m2})\,A_{32} - (B_{31}\,\varepsilon_{m1} + B_{32}\,\varepsilon_{m2})\,A_{42}] / (A_{31}A_{42} - A_{32}\,A_{41})$$

$$\varepsilon_{y'z'} = [(B_{31}\,\varepsilon_{m1} + B_{32}\,\varepsilon_{m2})\,A_{41} - (B_{41}\,\varepsilon_{m1} + B_{42}\,\varepsilon_{m2})\,A_{31}] / (A_{31}A_{42} - A_{32}\,A_{41})$$

where

$$A_{31} = C_{11}\sin^4\vartheta + (\tfrac{1}{2}C_{13} + C_{44})\sin^2(2\vartheta) + C_{33}\cos^4\vartheta$$

$$A_{32} = [C_{11}\sin^2\vartheta + (C_{13} + 2C_{44})\cos(2\vartheta) - C_{33}\cos^2\vartheta]\sin(2\vartheta)$$

$$A_{41} = \tfrac{1}{2}[(C_{11} - C_{13})\sin^2\vartheta + 2C_{44}\cos(2\vartheta) + (C_{13} - C_{33})\cos^2\vartheta]\sin(2\vartheta)$$

$$A_{42} = [(C_{11} + C_{33})/2 - C_{13}]\sin^2(2\vartheta) + 2C_{44}\cos^2(2\vartheta)$$

$$B_{31} = C_{12}\sin^2\vartheta + C_{13}\cos^2\vartheta$$

$$B_{32} = C_{13}(\sin^4\vartheta + \cos^4\vartheta) + [(C_{11} + C_{33})/4 - C_{44}]\sin^2 2\vartheta$$

$$B_{41} = \frac{C_{12} - C_{13}}{2}\sin(2\vartheta)$$

$$B_{42} = \tfrac{1}{2}[C_{11}\cos^2\vartheta - (C_{13} + 2C_{44})\cos(2\vartheta) - C_{33}\sin^2\vartheta]\sin(2\vartheta)$$

The values of the parameters A_{ij} and B_{ij}, calculated for both AlN(11-22) and GaN(11-22), are given in Table 2.6.

Parameters (GPa)	**AlN(11-22)**	**GaN(11-22)**
A_{31}	371	340
A_{32}	27.9	20.5
A_{41}	13.9	10.2
A_{42}	268	264
B_{31}	129	126
B_{32}	126	140
B_{41}	13	14.3
B_{42}	-3.60	-27.2

Table 2.6: Values of the parameters A_{ij} and B_{ij} calculated for AlN(11-22) and GaN(11-22), from [Rom06].

In the natural-coordinate system nonzero strains can be determined from the values of strain tensor in the primed-coordinate system by applying the appropriate tensor transformation as follows:

$$\varepsilon_{xx} = \varepsilon_{x'x'}$$

$$\varepsilon_{yy} = \varepsilon_{y'y'}\cos^2\vartheta + \varepsilon_{z'z'}\sin^2\vartheta + \varepsilon_{y'z'}\sin(2\vartheta)$$

$$\varepsilon_{zz} = \varepsilon_{y'y'}\sin^2\vartheta + \varepsilon_{z'z'}\cos^2\vartheta - \varepsilon_{y'z'}\sin(2\vartheta)$$

$$\varepsilon_{yz} = \tfrac{1}{2}(\varepsilon_{z'z'} - \varepsilon_{y'y'})\sin(2\vartheta) + \varepsilon_{y'z'}\cos(2\vartheta)$$

Table 2.7 gives the misfit components ε_{ij} calculated for AlN(11-22) and GaN(11-22) grown on sapphire (1-100), and GaN(11-22) grown on AlN(11-22).

Templates	sapphire(1-100) template		AlN(11-22)
Layers	AlN(11-22)	GaN(11-22)	GaN(11-22)
$\boldsymbol{\varepsilon_{xx}}$	-0.116	-0.137	0.024
$\boldsymbol{\varepsilon_{yy}}$	0.168	0.606	0.035
$\boldsymbol{\varepsilon_{zz}}$	-0.063	-0.540	-0.0002
$\boldsymbol{\varepsilon_{yz}}$	-0.115	-0.327	-0.688

Table 2.7: Values of ε_{ij} calculated for AlN(11-22) and GaN(11-22) grown on sapphire(1-100), and GaN(11-22) grown on AlN(11-22).

2.4 Spontaneous polarization and piezoelectricity

A relevant feature observed in group III nitrides is the presence of strong polarization, which influences dramatically the optical and electrical properties of heterostructures. The polarization presents two components: (1) spontaneous, which is inherent to the material, and (2) strain-induced piezoelectricity.

Since nitrogen atoms are more electronegative than metal atoms, cation-N bonds can be considered as an electrostatic dipole. Along the [0001] direction, this charge distribution is not fully compensated, which leads to spontaneous polarization $P_{sp.}$. The values of spontaneous polarization calculated by Bernardini et al. are presented in the Table 2.8 [Ber97]:

	GaN	**AlN**	**InN**
$\mathbf{P_{sp}\,(C/m^2)}$	-0.029	-0.081	-0.032

Table 2.8: Calculated spontaneous polarization for wurtzite type GaN, AlN and InN.

If stress is applied to the III - nitride lattice, the ideal lattice parameters *c* and *a* of the crystal structure will be changed to accommodate the stress. Thus the polarization strength will be changed. This additional polarization in strained III-nitride crystals is called piezoelectric polarization. The piezoelectric polarization in wurtzite III nitrides can be calculated with the following equation [Rom06].

$$\vec{P}_{PZ} = \begin{pmatrix} 0 & 0 & 0 & 0 & e_{15} & 0 \\ 0 & 0 & 0 & e_{15} & 0 & 0 \\ e_{31} & e_{31} & e_{33} & 0 & 0 & 0 \end{pmatrix} \times \begin{pmatrix} \varepsilon_{xx} \\ \varepsilon_{yy} \\ \varepsilon_{zz} \\ \varepsilon_{yz} \\ \varepsilon_{xz} \\ \varepsilon_{xy} \end{pmatrix} \tag{2.9}$$

where e_{ij} are the piezoelectric coefficient of the material and ε_j is the stress tensor.

For growth along polar direction with layers under in-plane biaxial stretching or contraction, the piezoelectric polarization is:

$$\vec{P}_{PZ} = 2\varepsilon_{xx}\left(e_{31} - e_{33}\frac{C_{13}}{C_{33}}\right) \tag{2.10}$$

The piezoelectric polarization constants for InN, GaN and AlN are indicated in Table 2.9. We observe that the magnitude of piezoelectric constants is ten times higher than for GaAs (e_{33} = -0.12 C/m^2, e_{31} = 0.06 C/m^2), or CdTe (e_{33} = 0.03 C/m^2, e_{31} = -0.061 C/m^2) compounds, due to the strong ionic character of the III-N bond [Ber97].

	e_{33} (C/m^2)	e_{31} (C/m^2)	e_{15} (C/m^2)
InN	0.97	-0.57	-
GaN	0.73	-0.49	-0.30
AlN	1.46	-0.60	-0.48
Ref.	[Ber97]	[Ber97]	[Amb00]

Table 2.9: Calculated piezoelectric constants for InN, GaN and AlN.

In semipolar growth case, the piezoelectric polarization is related to strain as:

$$\vec{P}_{PZ} = \begin{pmatrix} e_{15}\varepsilon_{xz} \\ e_{15}\varepsilon_{yz} \\ e_{31}(\varepsilon_{xx}+\varepsilon_{yy})+e_{33}\varepsilon_{zz} \end{pmatrix} \quad (2.11)$$

2.4.1 Polarization effects in heterostructures

The vector sum of the spontaneous and the piezoelectric polarization gives the overall polarization in the crystal. Discontinuities of the polarization vector at heterointerfaces lead to charge accumulation, which in turn generates internal electric fields in nanostructures. The amount of charges at the interface depends on the strain and material composition.

The large polarization fields (on the order of MV/cm) in III-nitride semiconductors affect the electronic properties of the layered structures in many ways. As mentioned in the chapter 1, the polarization induced electrical field is beneficial for the formation of a 2D electron gas in HEMTs without the need of doping. However, the built-in electric field created within (0001) oriented QWs leads to a band bending as illustrated in figure 2.11(a), and, as a consequence, to a spatial separation of electron and hole wavefunctions.

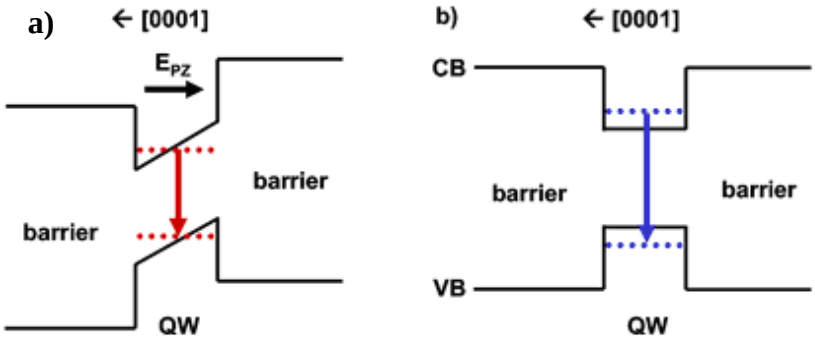

Figure 2.11. Band structure of a single QW (a) with and (b) without internal electric field.

Such a band structure leads to the QCSE and the consequences of this effect are decreased recombination efficiency, and red-shift of the emission. Thus, the polarization of wurtzite nitrides can have deleterious effects on the performance of optoelectronic devices. A promising mean of reducing internal field effects in the nitrides is through the growth of wurtzite device structures with semipolar crystallographic orientations. The energy-band diagrams illustrating the separation of the electron and hole wavefunctions for AlN/GaN QWs in a superlatice grown on the (0001) polar plane and on the (11-22) semipolar plane are presented in the figure 2.12. In both cases the band diagram deviates from the square QW model, but the distortion is significantly smaller in semipolar case.

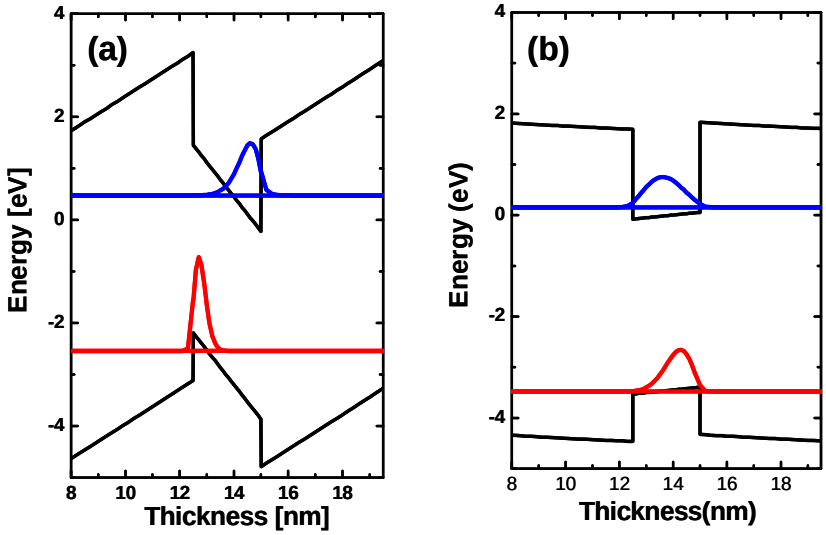

Figure 2.12: A comparison of band diagram between (a) polar c-plane GaN/AlN QW in the presence of polarization electric field and (b) semipolar (11-22) GaN/AlN QW in the presence of field (band diagrams calculated using the nextnano[3] software assuming the material strained on AlN).

Bibliography

[Amb00] O. Ambacher, B. Foutz, J. Smart, J. R. Shealy, N. G. Weimann, K. Chu, M. Murphy, A. J. Sierakowski, W. J. Schaff, L. F. Eastman, R. Dimitrov, A. Mitchell, and M. Stutzmann, *Two dimensional electron gases induced by spontaneous and piezoelectric polarization in undoped and doped AlGaN/GaN heterostructures*. Journal of Applied Physics 87, 334 (2000).

[Asi93] M. AsifKhan, J. N. Kuznia, D. T. Olson, and R. Kaplan, *Deposition and surface characterization of high quality single crystal GaN layers*. Journal of Applied Physics 73, 3108 (1993).

[Bar73] A. S. Barker, Jr. and M. Ilegems, *Infrared Lattice Vibrations and Free-Electron Dispersion in GaN*. Physical Review B 7, 743 (1973).

[Ber97] F. Bernardini, V. Fiorentin, and D. Vanderbilt, *Spontaneous polarization and piezoelectric constants of III-V nitrides*. Physical Review B 56(16), R10024 (1997).

[Cae07] C. Caetano, L. K. Teles, M. Marques, A. D. Pino, and L. G. Ferreira, *Theoretical support for the smaller band gap bowing in wurtzite InGaN alloys*. AIP Conference Proceeding 893, 257 (2007).

[Dau97] B. Daudin, J. L. Rouviere, and M. Arlery, *The key role of polarity in the growth process of (0001) nitrides.* Materials Science Engineering: B 43, 157 (1997).

[Deg98] C. Deger, E. Born, H. Angerer, O. Ambacher, M. Stutzmann, J. Hornsteiner, E. Riha, and G. Fischerauer, *Sound velocity of* AlxGa1−xN *thin films obtained by surface acousticwave measurements*. Applied Physics Letter 72(19), 2400 (1998).

[Dre95] M. Drechsler, D. M. Hoffman, B. K. Meyer, T. Detchprohm, H. Amano, and I. Akasaki, *Determination of the conduction band electron effective mass in hexagonal GaN*. Japanese Journal of Applied Physics Part 2 34(9B), 1178 (1995).

[Guo94] Q. Guo and A. Yoshida, *Temperature dependence of band gap change in InN and AlN*. Japanese Journal of Applied Physics 33, 2453 (1994).

[Im97] J. S. Im, A. Moritz, F. Steuber, V. Haerle, F. Scholtz, and A. Hangleiter, *Radiative carrier lifetime, momentum matrix element and hole effective mass in GaN*. Applied Physics Letter 70(5), 631 (1997).

[Kim96] K. Kim, W. R. L. Lambrecht, and B. Segall, *Elastic constants and related properties of tetrahedrally bonded BN, AlN, GaN, and InN*. Physical Review B 53(24), 16310 (1996).

[Kim97] K. Kim, W. R. L. Lambrecht, B. Segall, and M. V. Schilfgaarde, *Effective masses and valence band splittings in GaN and AlN*. Physical Review B 56(12), 7363 (1997).

[Kuo01] Y.-K. Kuo, W.-W. Lin, and J. Lin, *Band-Gap Bowing Parameter of the InxGa1−xN Derived From Theoretical Simulation*. Japanese Journal of Applied Physics 40(Part 1, No. 5A), 3157 (2001).

[Kuo02] Y.-K. Kuo andW.-W. Lin, *Band-Gap Bowing Parameter of the Al*x*In*1−x*N Derived from Theoretical Simulation*. Japanese Journal of Applied Physics 41(Part 1, No. 9), 5557 (2002).

[Lee99] S. R. Lee, A. F. Wright, M. H. Crawford, G. A. Petersen, J. Han, R. M. Han, and R. M. Biefeld, *The band-gap bowing of* AlxGa1−x,N *alloys*. Applied Physics Letter 74, 3344 (1999).

[Li97] Y. Li, Y. Lu, H. Shen, M.Wraback, M. G. Brown, M. Schurman, L. Koszi, and R. A. Stall, *Temperature dependence of energy band gap in GaN thin film studied by thermomodulation*. Applied Physics Letter 70, 2458 (1997).

[Lio05] B.-T. Liou, S.-H. Yen, Y.-K. Kuo, J. quan Yao, Y. J. Chen, and S. Lee, *Vegard's law deviation in band gaps and bowing parameters of the wurtzite III-nitride ternary alloys*. Semiconductor Lasers and Applications II 5628(1), 296 (2005).

[McN93] L. E. McNeil, M. Grimsditch, , and R. H. French, *Vibrational spectroscopy of aluminium nitride*. Journal of American Ceramic Society 76(5), 1132 (1993).

[Mer96] C. Merz, M. Kunzer, U. Kaufmann, I. Akasaki, and H. Amano, *Free and bound excitons in thin wurtzite GaN layers on sapphire*. Semiconductor Science Technology 11(5), 712 (1996).

[Mor94] H. Morko¸c, S. Strite, G. B. Gao, M. E. Lin, B. Sverdlov, and M. Burns, *Large-band- gap SiC, III-V nitride, and II-VI ZnSe-based semiconductor device technologies*. Journal of Applied Physics 76(3), 1363 (1994).

[Och99] T. J. Ochalski, B. Gil, P. Lefebvre, N. Grandjean, J. Massies, S. Nakamura, and H. Morko¸c, *Photoreflectance investigations of the bowing parameter in AlGaN allows lattice-matched to GaN*. Applied Physics Letter 74, 3353 (1999).

[Onu04] T. Onuma, S. F. Chichibu, , A. Uedono, T. Sota, P. Cantu, T. M. Katona, J. F. Keading, S. Keller, U. K. Mishra, S. Nakamura, and S. P. DenBaars, *Radiative and nonradiative processes in strain-free Al*x*In*1−x*N films studied by time-resolved photoluminescence and positron annihilation techniques*. Journal of Applied Physics 95(5), 2495 (2004).

[Pan75] J. L. Pankove, S. Bloom, and G. Harbeke, *Optical properties of GaN*. RCA Review 36, 163 (1975).

[Per96] P. Perlin, E. Litwin-Staszewska, B. Suchanek, W. Knap, J. Camassel, T. Suski, R. Piotrzkowski, S. Grzegory, E. Porowski, E. Kaminska, and J. C. Chervin, *Determination of the effective mass of GaN from infrared reflectivity and Hall effect*. Applied Physics Letter 68(8), 1114 (1996).

[Pol97] A. Polian, M. Grimsditch, and I. Grzegory, *Elastic constants of gallium nitride* Journal of Applied Physics 79, 3343 (1996)

[Pon96] F. A. Ponce, D. P. Bour, W. T. Young, M. Saunders, and J. W. Steeds, *Determination of lattice polarity for growth of GaN bulk single crystals and epitaxial layers.* Applied Physics Letters 69, 337 (1996).

[Ram99] V. Ramachandran, R. M. Feenstra, W. L. Sarney, L. Salamanca-Riba, J. E. Northrup, L. T. Romano and D. W. Greve, *Inversion of wurtzite GaN(0001) by exposure to Magnesium.* Applied Physics Letters 75, 808 (1999).

[Rem99] I. N. Remediakis and E. Kaxiras, *Band-structure calculations for semiconductors within generalized-density-functional theory.* Physical Review B 59, 5536 (1999).

[Rom06] A. E. Romanov, T. J. Baker, S. Nakamura, and J. S. Speck, *Strain-induced polarization in wurtzite III-nitride semipolar layers*. Journal of Applied Physics 100, 023522 (2006).

[Sal95] A. Salvador, G. Liu, W. Kim, O. Aktas, A. Botchakarev, and H. Morkoç, *Properties of a Si-doped GaN/AlGaN quantum well*. Applied Physics Letter 67, 3322 (1995).

[Sas88] T. Sasaki and T. Matsuoka, *Substrate-polarity dependence of metal-organic vapor-phase epitaxy-grown GaN on SiC.* Journal of Applied Physics 64, 4531 (1988).

[See97] M. Seelmann-Eggebert, J. L. Weyher, H. Obloh, H. Zimmermann, A. Rar, and S. Porowski, *Polarity of (00.1) GaN epilayers grown on a (00.1) sapphire*. Applied Physics Letters 71, 2635 (1997).

[Sha98] W. Shan, J. W. A. III, K. M. Wu, W. Walukiewicz, E. E. Haller, M. C. Martin, W. R. McKinney, and W. Yang, *Dependence of the fundamental band gap of* AlxGa1−x,N *on alloy composition and pressure*. Applied Physics Letter 84, 4452 (1998).

[Tak96] Y. Takagi, M. Ahart, T. Azuhato, T. Sota, K. Suzuki, and S. Nakamura, *Brillouin scattering study in the GaN epitaxial layer.* Physica B 219, 547 (1996).

[Tri99] S. Tripathy, R. K. Soni, H. Asahi, K. Iwata, R. Kuroiwa, K. Asami, and S. Gonda, *Optical properties of GaN layers grown on C-, A-, R-, and M- plane sapphire substrates by gas source molecular beam epitaxy*. Journal of Applied Physics 85(12), 8386 (1999).

[Tya77] V.A Tyagai, A.M Evstigneev, A.N Krasiko, A.F Andreeva and V.Ya Malakhov, *Optical properties of Indium Nitride films.* Sov. Phys. Semicond 11, 1257 (1977).

[Var67] Y. P. Varshni, *Temperature dependence of the energy gap in semiconductors*, Physica 34, 149 (1967).

[Vur01] I. Vurgaftman, J. R. Meyer, L. R. Ram-Mohan, *Band parameters for III–V compound semiconductors and their alloys.* Journal of Applied Physics 89 (11), 5815 (2001)

[Vur03] I. Vurgaftman and J. R. Meyer, *Band parameters for nitrogen-containing semiconductors*. Journal of Applied Physics 94, 3675 (2003).

[Wal04] W. Walukievicz, S. X. Li, J. Wu, K. M. Yu, J. W. Ager, E. E. Haller, H. Lu, and W. J. Schaff, *Optical properties and electronic structure of InN and In-rich group III-nitride alloys*. Journal of Crystal Growth 269, 119 (2004).

[Wri97] A. F. Wright, *Elastic properties of zinc-blende and wurtzite AlN, GaN and InN*. Journal of Applied Physics 82, 6 (1997).

[Xu93] Y.-N.Xu and W.Y.Ching, *Electronic, optical, and structural properties of some wurtzite crystals.* Physical Review B 48, 4335 (1993).

[Yam97] M. Yamaguchi, T. Yagi, T. Azuhata, T. Sota, K. Suzuki, S. Chichibu, and S. Nakamura, *Brillouin scattering study of gallium nitride: elastic stiffness constants*. Journal of Physics D: Condensed MatterMatter 9(1), 241 (1997).

[Yeh92] C.-Y. Yeh, Z. W. Lu, S. Froyen and A. Zunger, *Predictions and systematizations of the zinc-blende–wurtzite structural energies in binary octet compounds.* Physical Review B 45, R12130 (1992).

Chapter 3

Experimental techniques

The purpose of this chapter is to provide the information about the different techniques used for the experiments described in this work. The first part of this chapter deals with the thermodynamics and growth kinetics of GaN, AlN, AlGaN and InGaN, including a description of the structural defects that can be generated during growth. The latter sections describe the characterization tools which I used to determine structural and optical properties of the nitride structures.

3.1 Epitaxial growth

The term '*epitaxy*' is applied to a film grown over a crystalline substrate in such a way that the atomic arrangement of the film bears a defined crystallographic relationship to the atomic arrangement of the substrate. When a material is grown epitaxially upon a substrate of the same material, the process is called homoepitaxy. If the layer is grown upon a chemically different substrate the process is termed as heteroepitaxy.

The epitaxial growth process depends not only on the thermodynamical properties of the surface but also on the adatom kinetics [Vil95, Sai96, Mar95, Bar95, Pol00]. The substrate temperature is a key parameter which activates the kinetic processes occurring at the growing surface.

A series of surface processes takes place during the epitaxial growth which is schematically summarized in figure 3.1. The impinging fluxes can be adsorbed at the surface by chemisorption (if chemical bonds are created via a transfer of electrons between impinging atoms and atoms from the surface) or physisorption (if the atoms are adsorbed via Van der Waals forces). At a given substrate temperature and concentration, the atoms have a certain mobility. Some of the species will diffuse and be desorbed without being incorporated to the layer, whereas the others will incorporate either by step-edge growth forming atomic terraces, or by cluster nucleation.

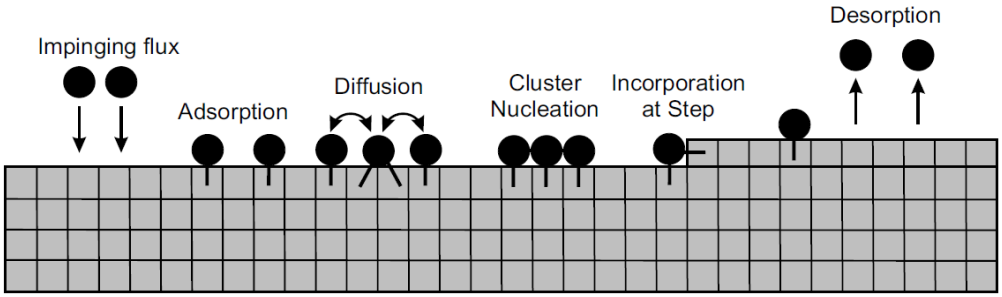

Figure 3.1: Basic atomic processes during growth.

When considering heteroepitaxy, three growth modes can be observed, depending on the lattice mismatch between the materials and surface free energy. They are the Volmer-Weber mode, Frank-van der Merwe mode and Stranski-Krastanov mode (Figure 3.2.). The growth mode characterizes the nucleation and growth processes, and there is a direct correspondence between the growth mode and the film morphology.

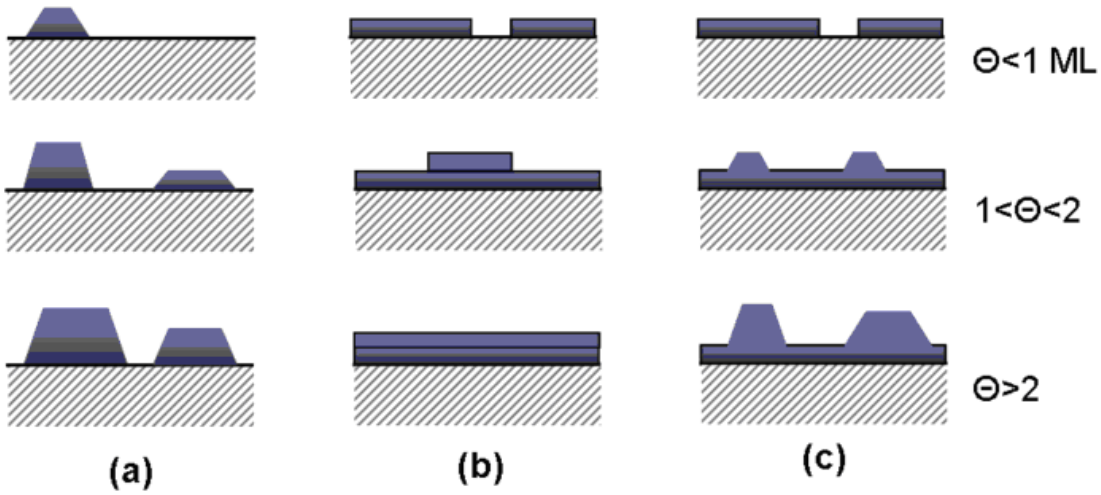

Figure 3.2: Growth mode of thin films: morphology of a growing film for (a)Volmer-Weber growth, (b) Frank-van der Merwe growth and (c) Stranski-Krastanov growth, upon increasing coverage in monolayers (ML).Each mode is shown for several different amounts of surface coverage,Θ.

- *Volmer-Weber growth* [Vol26]: In this growth mode adatom-adatom interactions are stronger than those of the adatom with the surface, leading to the formation of three-dimensional adatom clusters or islands.
- *Frank van der Merwe* growth [Fra49]: Here, adatoms attach preferentially to surface sites resulting in atomically smooth, fully formed layers. This layer-

by-layer growth is two dimensional, indicating that complete films form prior to growth of subsequent layers.

- *Stranski-Krastanov* growth [Str38]: An intermediary process characterized by both two-dimensional (2D) layer and three-dimensional (3D) island growth. Transition from the layer-by-layer to island-based growth occurs at a critical layer thickness which is highly dependent on the chemical and physical properties, such as surface energies and lattice parameters, of the substrate and film.

Many growth techniques have been successfully developed for epitaxial growth. Some of the most common techniques include: Metalorganic Vapor Phase Epitaxy (MOVPE), Liquid Phase Epitaxy (LPE), Hydride Vapor Phase Epitaxy (HVPE), and Molecular Beam Epitaxy (MBE). All epitaxial growth for our work was performed in a plasma-assisted MBE (PAMBE) system.

3.2 Plasma-assisted molecular beam epitaxy

MBE was developed during the 1970s for the growth of III-V semiconducting compounds (principally GaAs) [Art68,Cho75] and rapidly became established as a technique for producing thin films of high purity and well defined thickness for a wide variety of device structures. It came particularly into its own in the 1980s with the development of low dimensional structures which requires atomic layer precision in the deposition of multi-layers. MBE is characterized by growth under ultra-high vacuum (UHV) conditions and the ready availability of an *in situ* monitoring method in the form of Reflection High Energy Electron Diffraction (RHEED). During the growth process, elemental sources are heated and evaporated at controlled rate onto a heated substrate under UHV conditions ~ 10^{-10} – 10^{-11} Torr. UHV is necessary in order to prevent the interference of impurities with the growth, and to guarantee a minimal interaction of the molecular beams with residual background molecules. In other words, the UHV ensures the beam nature of the mass flow towards the substrate, i.e. the mean free path is much longer than the distance between the source cells and the substrate. Under these conditions, the crystal growth is far from thermodynamic equilibrium, and is mostly governed by the kinetics of the surface processes.

Figure 3.3 is an illustration of the PAMBE system I used. It consists of three chambers, each one with its own pumping system. They are separated by gate valves which can only be opened once the pressure at both sides is in the same range.

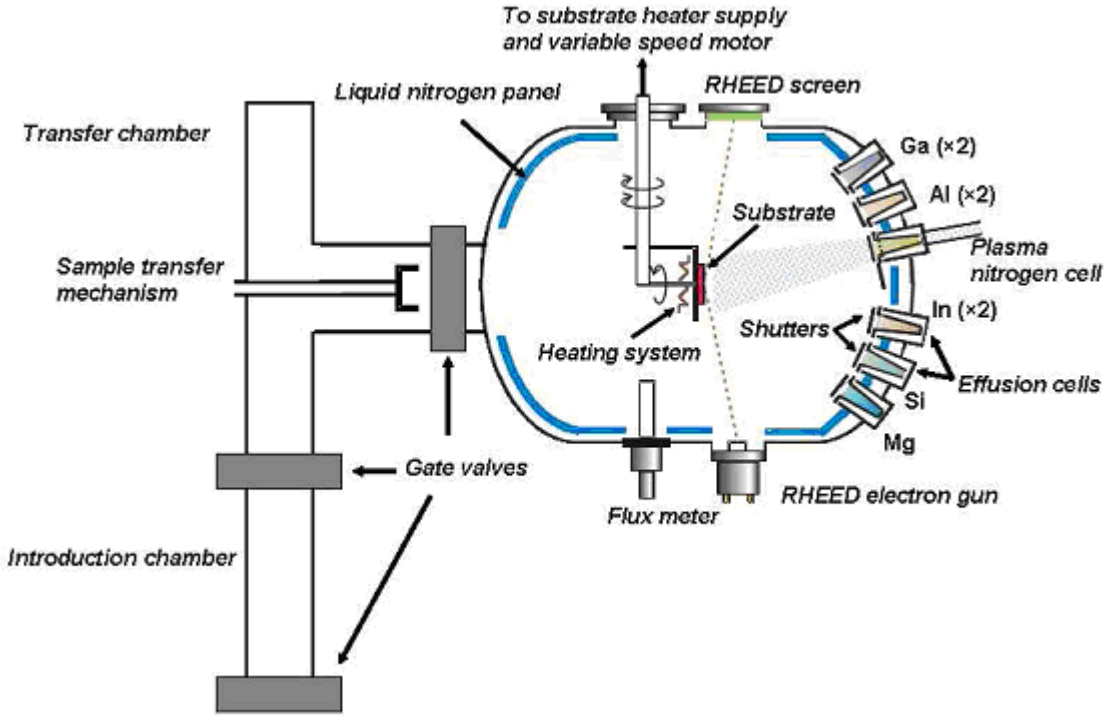

Figure 3.3: Schematic of the PAMBE used in this thesis.

The introduction chamber is the chamber through which the substrates are entered in the machine. It is pumped thanks to a turbomolecular pump reaching $\approx 10^{-8}$ Torr. The chamber is only opened under nitrogen overpressure in order to limit air pollution. The substrates are indium-glued on a 2 inch molybdenum sample holder (molyblock) and introduced in the machine onto a cart which can contain several molyblocks. The cart is brought from the introduction chamber to the transfer chamber, passing through a gate valve. With an ionic pumping system, the transfer chamber pressure is $\approx 10^{-10}$ Torr. Virgin substrates are stocked in this chamber before the growth and the transfer arm allows us to select and enter a new molyblock into the growth chamber.

The growth chamber is the main body of the machine. It is continuously under both cryogenic pumping and liquid-nitrogen cooling on the walls so that the pressure in the chamber can be kept in the range of 10^{-11} Torr. As schematized in figure 3.3,

the molyblock entered in the center of the chamber is mounted onto the manipulator, which can be rotated from transfer position to growth position. In growth position, the substrate is facing the effusion cells providing the elements for the epitaxial growth. The substrate is heated by a hot filament and its temperature is controlled using a thermocouple in mechanical contact with the molyblock. To insure a homogeneous deposition, the molyblock is in-plane rotating during the growth. The growth chamber is equipped with a mass spectrometer and a RHEED system.

Impinging metal elements (Ga, Al, In, Mg and Si) are provided by effusion cells oriented towards the center of the growth chamber. Our chamber is equipped with 2 cells of each group III element (Ga, Al, and In) and one cell for each dopant (Si and Mg). Figure 3.4 shows a typical effusion cell used in our MBE system. The solid charge of the material is placed into a cylindrical or conical crucible heated by a filament, whose current is controlled using a thermocouple in contact with the backside of the crucible.

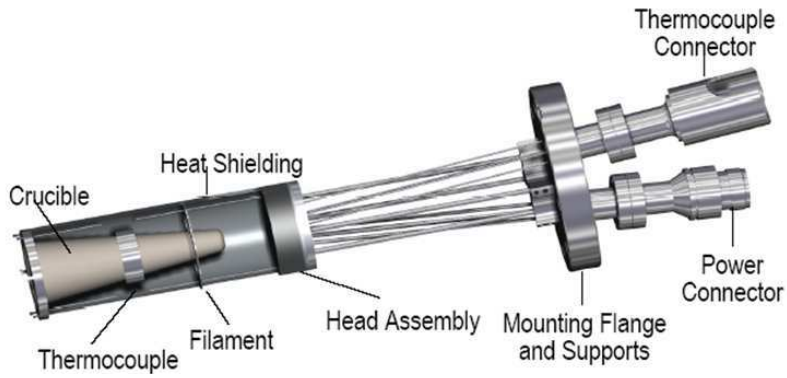

Figure 3.4: Description of a typical effusion cell.

Active nitrogen is provided by a plasma cell, whose operating principle is illustrated in figure 3.5. Our system is equipped with a radiofrenquency (RF) plasma cell HD-25 from Oxford Applied Research. Nitrogen molecules coming into the cell are resonantly excited and dissociated by a 13.56 MHz RF electromagnetic wave. To adjust the growth rate, the N flux can be varied from 0.2 sccm to 2 sccm and the excitation power from 250 W to 500 W. For our experiments, the nitrogen-limited growth rate was ≈ 0.27 - 0.34 monolayers per second (ML/s).

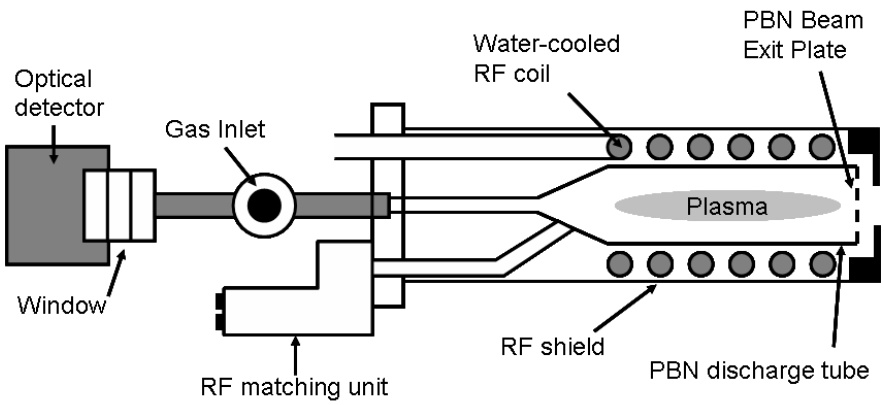

Figure 3.5: Schematic of the RF plasma cell mounted in our PAMBE system.

3.3 Reflection high-energy electron diffraction (RHEED)

RHEED is perhaps the most useful surface analytical tool in the MBE growth chamber for *in situ* studies of surface crystallography and kinetics. In RHEED, a collimated monoenergetic electron beam is directed towards the surface at a grazing angle of about 2^{o}, see figure 3.6. In our system, the electrons are emitted by a hot filament excited by a 1.5 A current and accelerated under high voltage (typically 32 kV). The penetration depth of the incident electron beam is limited to only the first few atomic layers, as a result, a smooth crystal surface acts as a two-dimensional grating which diffracts the incident electron beam. A fluorescent screen placed diametrically opposite the electron gun records the diffraction pattern. In this configuration the growing surface can be continuously monitored.

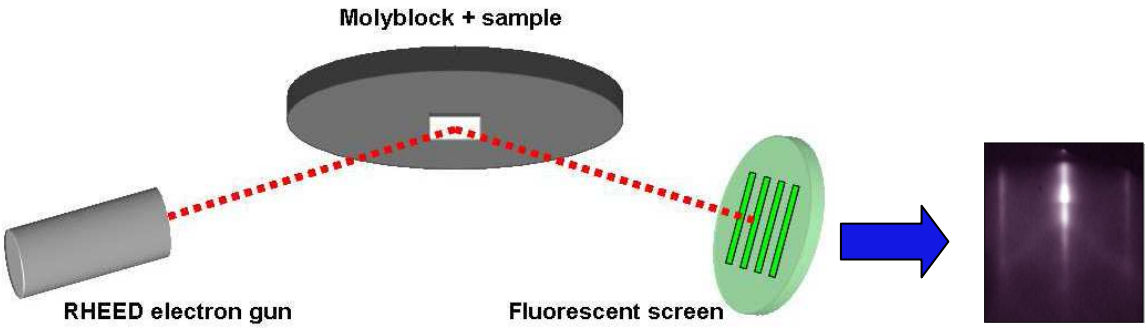

Figure 3.6: Schematic description of the RHEED measurement setup.

The RHEED pattern immediately reveals the character of the growing surface: streaks indicate an atomically flat surface, spots that move with sample rotation indicate atomic flatness with large terrace size, stationary spots indicate 3D growth, and concentric rings indicate polycrystalline growth. Other than this, from the analysis of the diffraction pattern, we can extract the following information:

- *Determination of the in-plane lattice constant.* As illustrated in figure 3.7, the interplanar distance d_u is defined as follows

$$d_u = L\lambda_0/t \tag{3.1}$$

where L is the distance between the surface normal and the screen, λ_0 is the electron wavelength, and t is the distance between two streaks observed in the screen. Therefore d_u is inversely proportional to t, which has been used to analyze the in-plane strain relaxation during the growth of heterostructures.

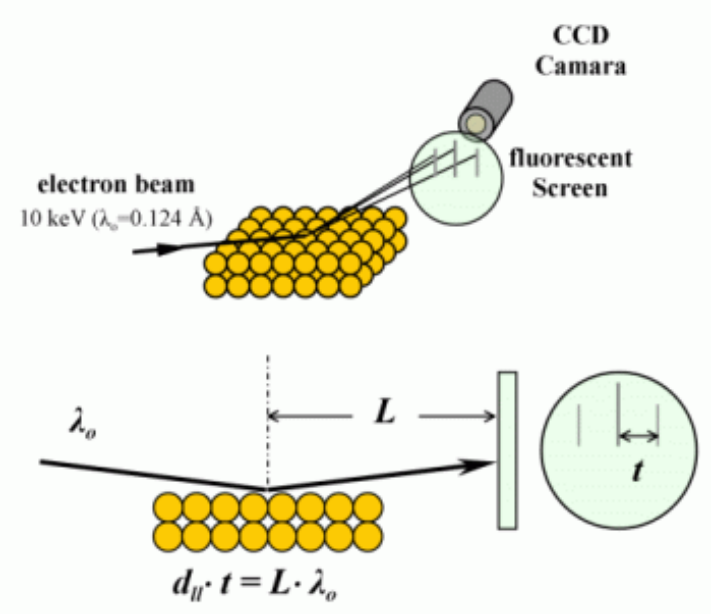

Figure 3.7: Schematic description of the procedure to determine the in-plane lattice constant.

- *Surface reconstructions.* RHEED is also able to identify the presence of surface superstructure known as a surface reconstruction, which generates additional features in the RHEED pattern.

- *Determination of the growth rate.* The intensity depends on the surface roughness during the layer formation process due to change in density of the atoms. In the case of a flat surface, when the coverage is $\theta = 0$ the RHEED intensity is maximum. Once the coverage increases reaching $\theta = 0.5$, the roughness is maximum and the intensity is at its lowest. At $\theta = 0.75$ the intensity recovers as the space in-between the nucleating sites gets filled and the surface flattens completely at $\theta = 1$, reaching again a maximum RHEED intensity. This sequence is illustrated in figure 3.8.

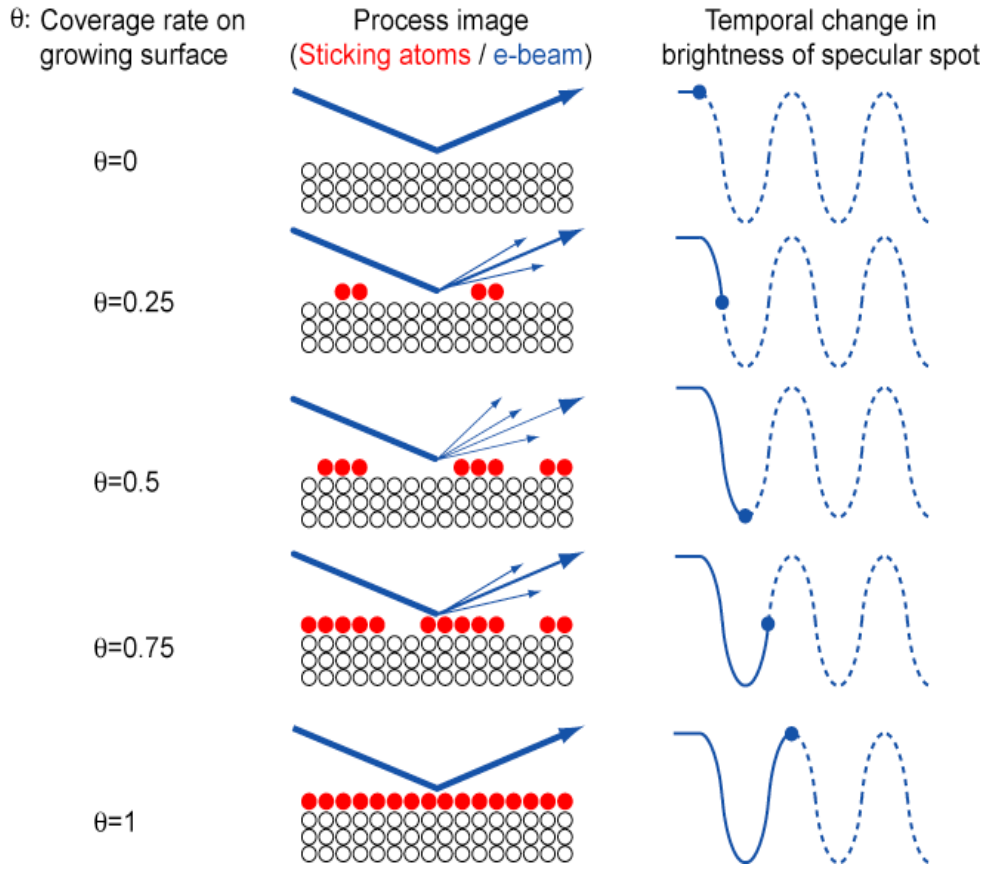

Figure 3.8: Schematic description of the procedure to determine the growth rate from the variation of the RHEED intensity.

3.4 PAMBE of III-nitrides

The PAMBE growth of III-nitrides is performed under constant nitrogen flux which imposes the growth rate. The key parameters which control the crystalline quality and growth kinetics are the substrate temperature, which determines the adatoms kinetics, and the metallic flux, *i.e.* the III/V ratio. The appropriate growth

conditions to obtain a 2D layer depend on the nature (composition, orientation) of the growing surface, and can be influenced by the presence of dopants or pollutants.

3.4.1 Growth of GaN (0001)

The growth of GaN (0001) by PAMBE requires a precise control of the metal-to-nitrogen (III/V) flux ratio [Ade03, Neu03, Hey00]. GaN deposition under N-rich conditions (III/V<1) proceeds in a layer-by-layer mode that starts with RHEED oscillations that attenuate as the surface roughness increases (Figure 3.9). After a few nanometers, the RHEED becomes spotty and the samples are facetted with a high surface roughness due to reduced adatom mobility.

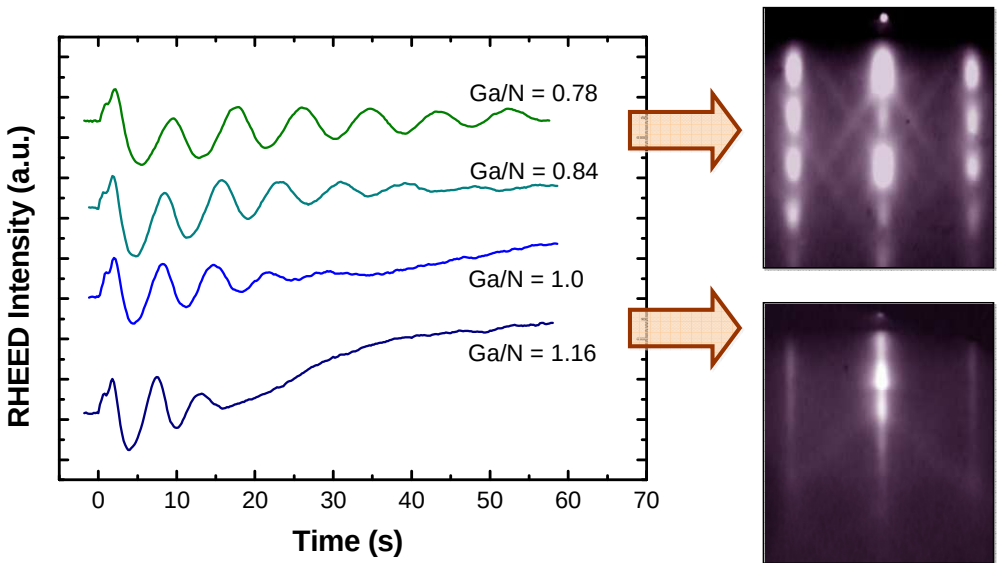

Figure 3.9: RHEED intensity oscillations and pattern at different III/V ratios.

Deposition of 2D GaN layers requires Ga-rich conditions. However, very high Ga flux (III/V>>1) forms metal droplets on the surface which is detrimental to layer quality. Hence it is necessary to study the Ga wetting of the GaN surface to determine the appropriate growth conditions for 2D layers.

The Ga excess can be quantified in situ and in real time by RHEED measurements. With this purpose, the GaN surface is exposed to a certain Ga flux, and we study the desorption of Ga under vacuum after stopping the exposure. The RHEED transient duration depends on the amount of Ga which was on the surface [Ade03]. From the measurements of the desorption transient as a function of the

impinging Ga flux, it is possible to calculate the Ga coverage on GaN which is depicted in figure 3.10. Four regimes can be distinguished:

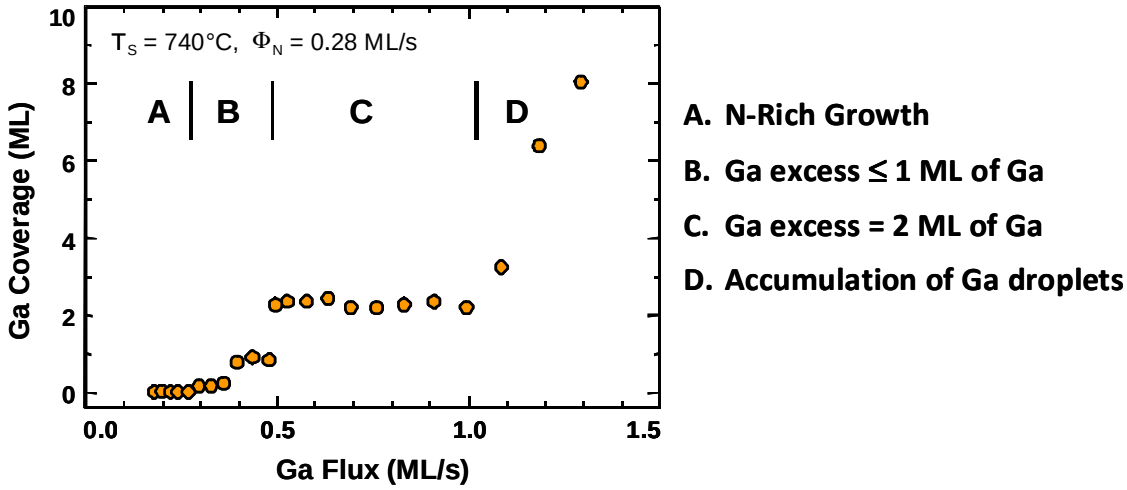

Figure 3.10: Ga coverage on top of the GaN(0001) surface as a function of the Ga flux, measured at a substrate temperature T_S = 740°C and under a N flux Φ_N = 0.28 ML/s.

- **A**: There is a very small coverage of Ga on the surface of less than 1 ML (Φ_{Ga} < 0.3 ML/s).
- **B**: The GaN surface is covered with about 1 ML of Ga (0.3 ML/s < Φ_{Ga} < 0.5 ML/s).
- **C**: A self-regulated Ga bilayer is formed on top of the GaN surface (0.5 ML/s < Φ_{Ga} < 1 ML/s).
- **D**: Ga accumulates on the GaN surface forming Ga droplets (Φ_{Ga} > 1 ML/s).

The dependence of Ga coverage as a function of both Ga flux and substrate temperature is presented in figure 3.11, together with typical AFM images of the surface of GaN layers grown in regimes A, B, and C.

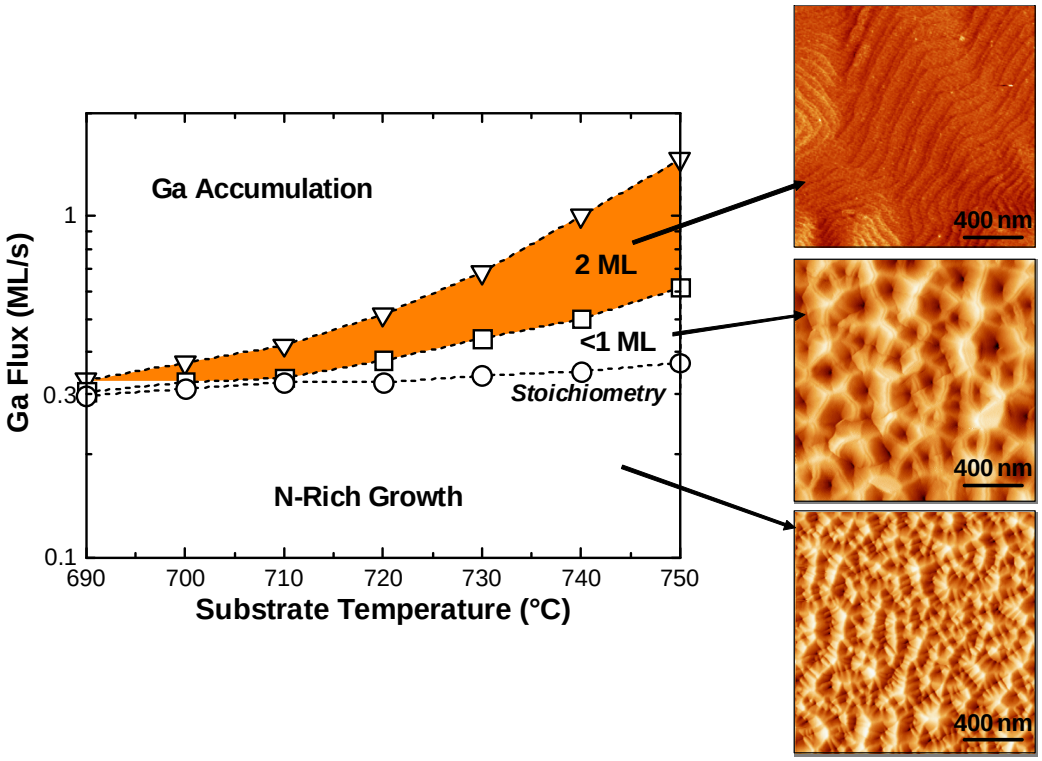

Figure 3.11: Ga coverage regimes as a function of both substrate temperature and impinging Ga flux. On the right side, AFM images of the surface of GaN layers grown at different values of Ga flux.

Adelmann *et al.* have shown that the morphology of the GaN surface strongly depends on the Ga coverage [Ade02]. The AFM images in figure 3.11 show that if GaN is grown with Ga coverage < 2 ML, it presents a rough surface, whereas atomic steps can be seen of GaN deposited under Ga excess (regime C). This regime is characterized by the formation of a Ga bilayer, as schematized in figure 3.12, which consists of two Ga layers adsorbed on top of the Ga-terminated GaN(0001) surface [Neu03, Fee02, Nor00]. This Ga bilayer allows reduction of the (0001) surface energy by at least 25 meV/A^2, favoring 2D growth. It is observed that the demand for Ga flux to attain the bilayer conditions increases with the substrate temperature, T_s, due to the thermal enhancement of Ga desorption.

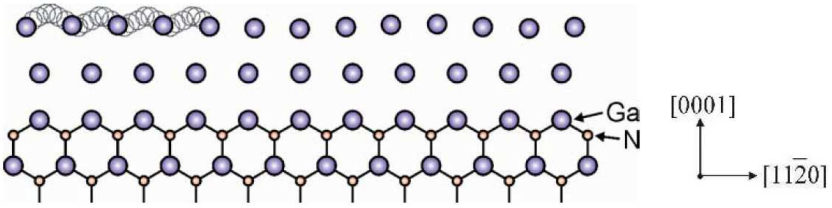

Figure 3.12: Schematic view of the laterally-contracted Ga bilayer model [Nor00].

3.4.2 Growth of AlN (0001)

The bond strength of AlN is significantly higher than that of GaN and thus we can expect that the surface structures and their temperature dependence may differ between the two materials. In the case of AlN growth, Al starts to desorb and the growth is optimized with a self-regulated Al coverage on the AlN surface only at higher temperatures ($T \geq 800^{o}C$) [Kob03]. Since such high temperatures can not be reached in our MBE system, AlN (0001) grown under Al excess presents Al droplets which are periodically consumed by exposure to nitrogen flux. Therefore, to identify suitable growth condition for AlN, we deposit 20 min of AlN with excess Al at Ga desorption temperatures. The excess Al on the surface is observed as extra line or shadow in the RHEED pattern taken along the <11-20> azimuth shown in figure 3.13(a), this line is the evidence of the reduced lattice constant of metal Al. Next, the surface is exposed to N to consume excess Al. By noting the time required to consume excess Al we can calculate the III/N ratio. This data can be used to tune the Al cell temperature to attain the required stoichiometric growth condition.

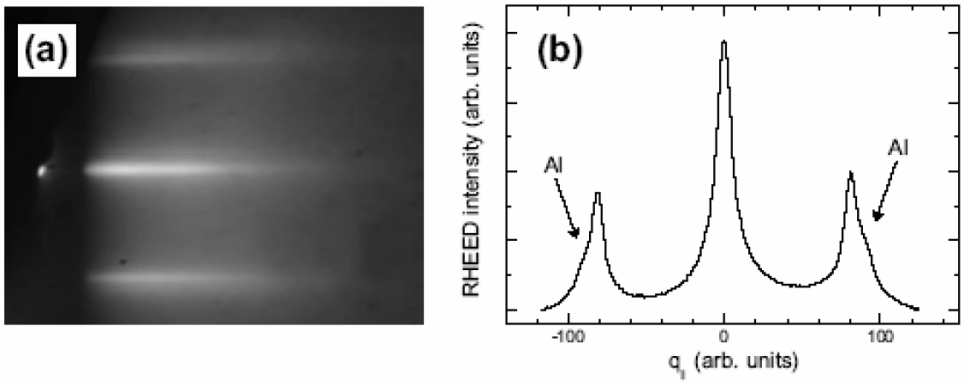

Figure 3.13: (a) RHEED image of an Al-rich AlN surface (azimuth <11-20>). (b) Intensity profile along the <11-20> direction. The extra streaks due to the Al excess are indicated by the arrows.

3.4.3 Growth of polar (0001) AlGaN

The growth of AlGaN poses some additional difficulties, due to the difference in Ga-N and Al-N binding energy and the different mobility of Ga and Al adatoms on the growing surface. The stronger Al-N bond allows reaction between them irrespective of presence of species like Ga or In in the surroundings [lli02, Mon03]. Therefore, as a first step, the Al flux required to be incorporated in the AlGaN is fixed

to a percentage of the N flux corresponding to the targeted Al mole fraction. Then, Ga is used in excess, to obtain a surfactant effect that favors 2D growth. This procedure works for low Al content material valid up to Al ~ 40%. For Al contents above 40%, it is necessary to decrease T_S to maintain 2D growth, and In can be used as a surfactant to stabilize the surface [Mon03].

3.4.4 Growth of polar (0001) InGaN

The growth of InGaN alloys has proven to be relatively more difficult, particularly for In mole fractions higher than 10%. The difficulties in growing high-quality InGaN materials can be attributed to a number of problems: for instance, the large difference in interatomic spacing between InN and GaN results in a solid phase miscibility gap [Ho96] and the relatively high vapor pressure of InN as compared to the vapor pressure of GaN leading to low indium incorporation in the InGaN alloy [Nag89]; in addition, the difference in formation enthalpies for InN and GaN causes a strong indium surface segregation on the growth front [Yos91]. These problems, however, can be minimized by optimizing the growth parameters, such as the use of relatively low growth temperatures, high V/III flux ratio, low growth rate and low growth pressure.

3.5 Substrates

The production of bulk GaN crystals is difficult because of the high melting point of GaN (2,600K) and the extremely high nitrogen pressures involved in their growth. AlN has been produced using relatively straightforward physical vapor transport (sublimation), but it is difficult to grow in large diameter with low-defects. To date, no one has produced bulk crystal InN. Because of the lack of the native, single crystal nitride substrates, the entire nitride technology is developed by heteroepitaxial growth on a variety of substrates, such as sapphire (Al_2O_3), silicon carbide (SiC), silicon (Si), GaAs, ZnO, MgO and lithium gallium oxide ($LiGaO_2$, LGO). A wise choice of substrate for heteroepitaxy should be made by considering lattice constant, thermal expansion coefficient, and requirement of crystal orientation, defect density, purity and surface morphology.

Among the mentioned substrates, Si remains one of the desirable options due to its well-established growth, availability in large substrate size and low cost. However, Si has dissimilarities in crystal structure and physical properties to III-nitrides and exhibits 17% lattice mismatch with GaN. SiC on the other hand offers a lattice mismatch of only 3.5% with GaN, but SiC wafers are significantly more expensive compared to other alternative substrates. Sapphire presents a good compromise between Si and SiC and thus remains one of the most popular substrate for nitrides owing to its low price, hexagonal symmetry, ease of handling and pregrowth cleaning, availability of large area crystals of high quality, transparent nature and high temperature stability. Even though sapphire is not the best choice in terms of lattice mismatch (~ 13.9% mismatch with GaN), good quality epilayers can be produced using sapphire as a substrate. The detrimental effects of performing heteroepitaxy on a foreign substrate with huge lattice mismatch can be reduced by sophisticated processing steps like surface treatment followed by nitridation and low temperature buffer layers.

3.5.1 Sapphire-based substrates

Sapphire (α-Al_2O_3) has a rhombohedral structure and it can be described either by a rhombohedral unit cell or by a hexagonal unit cell. In this latter case, the lattice parameters are $a = 4.765$ Å and $c = 12.982$ Å at 300 K. Various commercially available sapphire orientations are shown in figure 3.14. To date, four orientations of sapphire have been commonly used as nitride substrates: (10-10) or *m*-plane, (0001) or *c*-plane, (1-102) or *r*-plane, and (11-20) or *a*-plane (Figure 3.14).

- GaN or AlN epitaxy on *c*-plane sapphire results in *c*-plane oriented films, but with in-plane rotation of 30° with respect to sapphire (0001). The 30° rotation of the (0001) nitride plane with respect to the sapphire (0001) occurs to reduce the lattice mismatch to 13.9%.
- GaN films grown on *a*-plane sapphire are also oriented in the [0001] direction [Nak96, Ale99]. Although the lattice mismatch for *c*-GaN films on *a*-plane sapphire is less (2%) than on *c*-plane sapphire (13.9%), no significant differences in GaN film quality have been reported between these two substrates.

– For either GaN or AlN epitaxy on *r*-plane (1-102) sapphire, *a*-plane (11-20)-oriented nitride films are produced [Edd93].

– Nitride growth on (10-10) *m*-plane sapphire can result in (10-10), (10-13) or (11-22)-oriented nitride layers, depending on the growth technique and growth conditions [Iwa97, Bak06, Kap07].

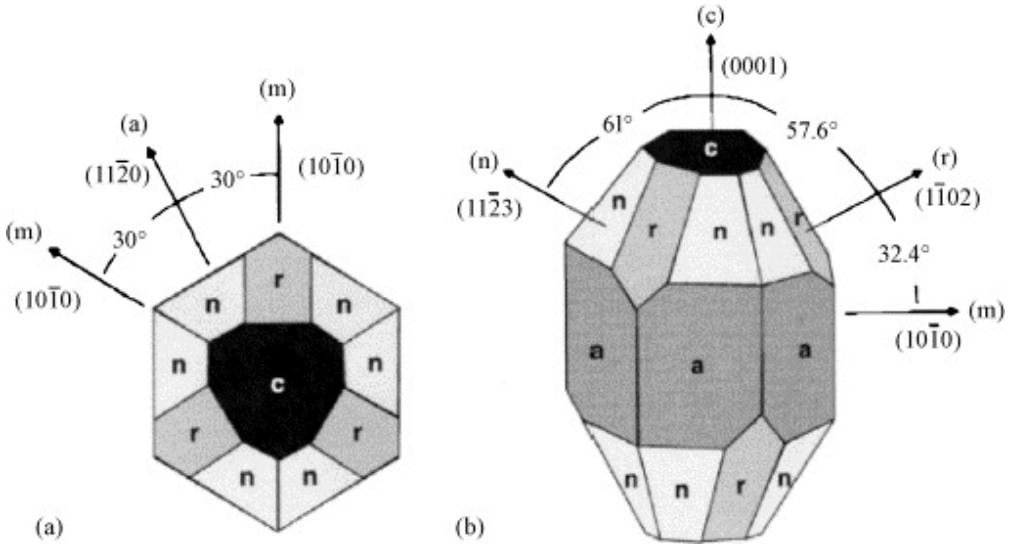

Figure 3.14: Rhombohedral structure of sapphires: (a) structure viewed along the [0001] direction (b) surface planes [Liu02].

Most of the work contained in this thesis was performed using sapphire-based templates as substrates. The templates consist of a thin III-nitride film deposited by MOVPE on the sapphire substrate. The various templates that were used in this work, for making nitride structures in polar and semipolar orientations, are listed below:

- Commercial GaN(0001)-on-sapphire templates supplied by LUMILOG. The template consists of ~ 4-µm-thick GaN on *c*-sapphire, with threading dislocation density in the range of 10^8 cm^{-2}.
- Commercial AlN(0001)-on-sapphire templates procured from DOWA, consisting of 1.0±0.3 µm thick AlN deposited on *c*-sapphire with a dislocation density is ~ 10^9 cm^{-2}.
- Commercial AlGaN(0001)-on-sapphire templates from TDI-Oxford Instruments, consisting of a 1 µm thick Si doped $Al_{0.4}Ga_{0.6}N$ layer on *c*-sapphire.

- GaN(11-22)-on-sapphire templates from CRHEA, fabricated by G. Nataf and Ph. De Mierry [Mie09]. The template consists of 1 µm thick GaN epitaxial layer deposited by MOVPE on *m*-sapphire.

Therefore, we used three different templates for polar growth, and the atomic force microscopy (AFM) images of the template surfaces are presented in figure 3.15.

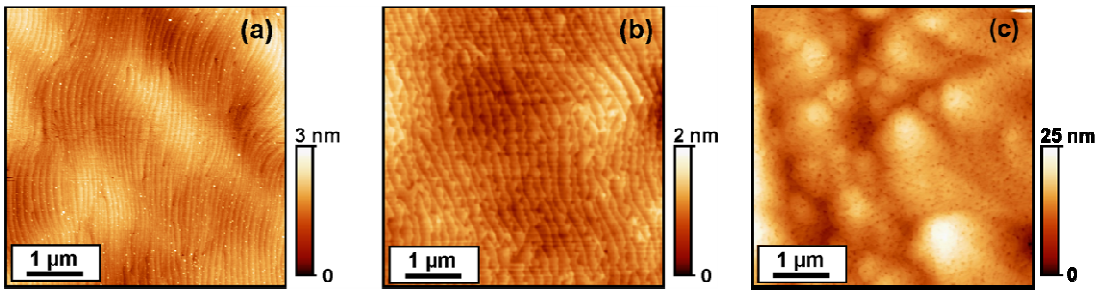

Figure 3.15: AFM images of (a) the GaN-on-sapphire, (b) the AlN-on-sapphire and (c) the AlGaN-on-sapphire templates used in this work

Semipolar (11-22) structures were grown either directly on *m*-plane sapphire (Kyocera corporation) as well as on GaN (11-22)-on-sapphire templates deposited by MOVPE [Mie09]. The AFM images from these substrates are pictured in figure 3.16.

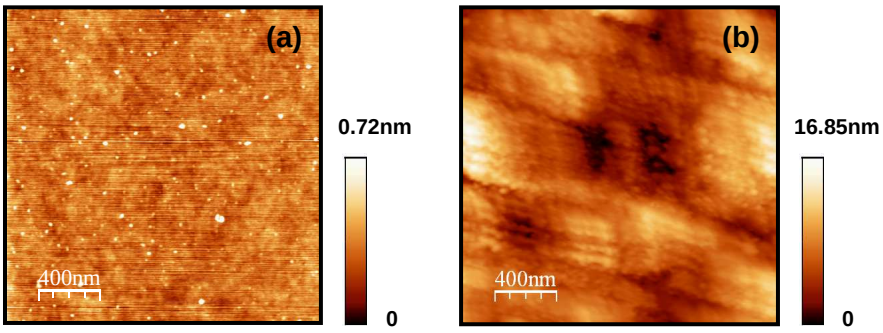

Figure 3.16: AFM images from (a) the m-sapphire substrate and (b) the GaN (11-22)-on-sapphire template.

3.6 Defects observed in III-nitrides

This section lists and describes various defects that can be found in III-nitride structures grown by epitaxy on non-coherent substrates. The structural defects are divided into point defects, line defects (dislocations) and planar (stacking faults and domain boundaries) defects.

3.6.1. Point defects

Point defects are where an atom is missing or is in an irregular place in the lattice structure. Point defects include vacancies, self interstitial atoms, interstitial impurity atoms and substitutional atoms. Vacancies are empty spaces where an atom should be, but is missing (eg. Ga- or N-vacancy in GaN). They are common, especially at high temperatures when atoms are frequently and randomly change their positions leaving behind empty lattice sites. Due to the fact that vacancies do not involve foreign atoms they are called intrinsic or native defects. Their concentration cannot be determined by chemical analysis of mass spectrometry; however, positron annihilation is an effective tool for studying vacancy-type defects in semiconductors [Pus94]. Interstitial atoms are the ones which are not situated in well defined lattice positions; instead they are placed in-between the atoms forming the periodic crystal structure. Substitutional atoms on the other hand are atoms which do not occupy their own position in the crystal. Both kinds of defects can be either intrinsic or extrinsic. There are two reasons for foreign atoms to be found in III-N layers, those are: intentional doping which is meant to change the electrical properties of the sample making it either n- or p-type; or unintentional doping which is a result is a result of impurity incorporation during the growth process.

3.6.2. Line defects

When we use foreign substrate for epitaxial growth of III-nitrides structures, it introduces a large number of various defects into the crystal structure. Some of them might be of a grown-in type, i.e. generated during growth due to the lattice mismatch, others might result from post-growth stressed due to difference in expansion coefficients between substrate material and layer. That is, line defects such as dislocations are caused by the differences in lattice constants and thermal expansion coefficients between epilayer and the substrate. Dislocations emerging during the growth due to the difference of lattice parameters between the substrate and the epilayer are called “misfit dislocations”. The most common dislocation type in wurtzite systems are threading dislocations (TDs) [Kap95, Chi96] which are going through the whole film, from the interface with the substrate to the surface of the layer.

The line defects include mostly dislocations of the edge, screw or mixed type, and inversion domains (ID). Edge-type dislocations are formed by adding an extra partial plane of atoms to the crystal (see figure 3.17), while the material suffers a linear distortion. In such a case, the adjacent planes are not straight, but instead bend around the edge of the terminating plane so that the crystal structure is perfectly ordered on both sides. The position of the dislocation line is marked by the symbols ⊥ and ⊤ indicating the involvement of extra planes from the top (positive sign) and bottom (negative sign) of the crystal, respectively. The vertical line of the symbol ⊥ points in the direction of the dislocation line in the extra partial plane. The dislocation line is a region of high energy than the rest of the crystal and the lattice above the dislocation line is in a state of compression.

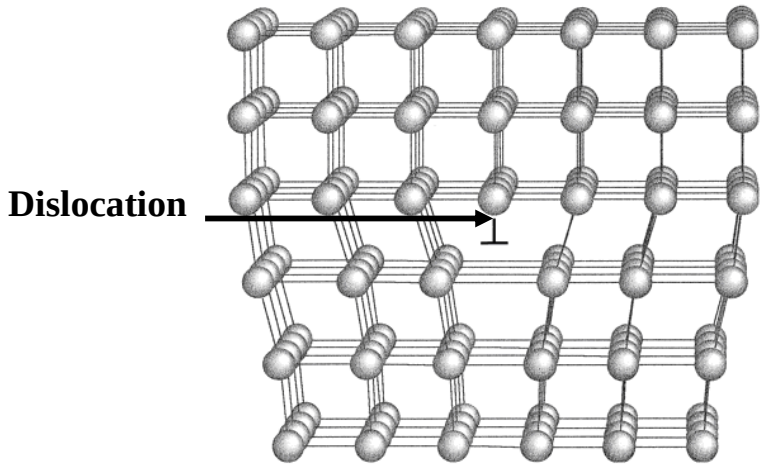

Figure 3.17: schematic representation of an edge type dislocation in a cubic lattice. The dislocation line terminates the extra half-plane (⊥).

The technical definition of a dislocation is by means of Burgers vector. It is defined as a vector equal to the difference between Burgers circuit made around a dislocation line and one made around an equivalent undisturbed crystal. That is, Burgers vector (*b*) represents the magnitude and the direction of the main lattice distortion caused by a dislocation. Figure 3.18 shows that Burgers circuit is simply a closed path taken from atom to atom around a certain area. The Burgers vector of an edge dislocation is perpendicular to the line of the dislocation.

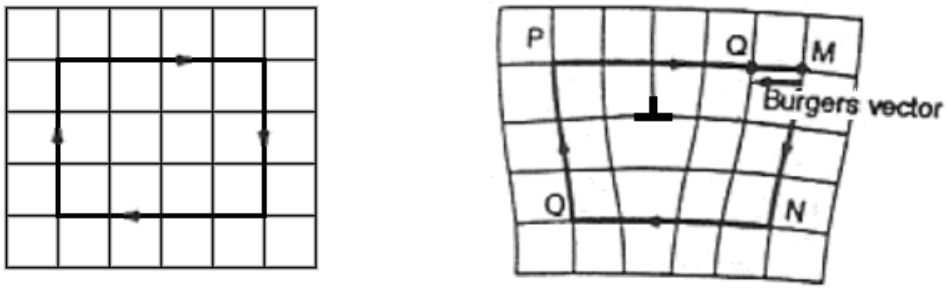

Figure 3.18: (a) Burgers circuit in a perfect crystal and (b) the same circuit around an edge dislocation.

Screw-type dislocations present a dislocation line parallel to the Burgers vector. The defect is due to the collinear shift of the two regions separated by the dislocation line. That is, here the atoms are displaced in two separate plane perpendicular to each other and the distortion follows a helical or screw path, both right hand and left hand screw are possible. Figure 3.19 represents the gliding plane and the lattice deformation due to a screw dislocation.

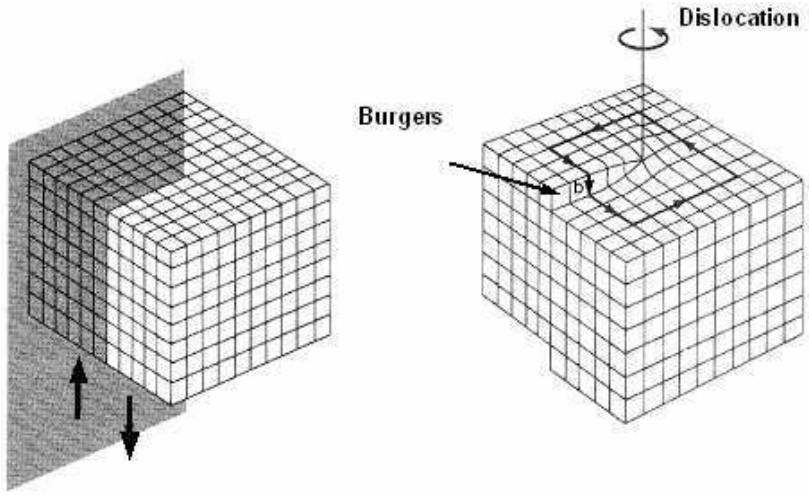

Figure 3.19: Screw-type dislocation: Burgers vector b is parallel to the dislocation line.

If Burgers vector is forming an angle different from 0^o or 90^o with the dislocation line, it is called a mixed dislocation. Most of such dislocations can be decomposed into an edge-type and a screw-type dislocation. An example is shown in figure 3.20.

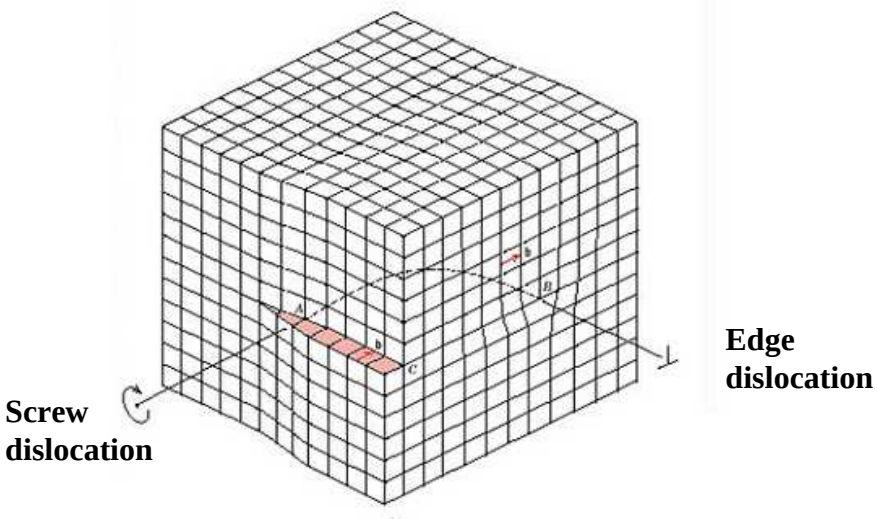

Figure 3.20: Mixed dislocation showing a screw component and an edge component.

In III-Nitrides which have in general wurtzite type structure the geometry is not as simple as for cubic lattices. The smallest translation vectors in the wurtzite structures are: *a*-type 1/3<-12-10> and *c*-type <0001>. They are also the Burgers vectors of the simplest threading dislocations, i.e. dislocations parallel to the c-axis which penetrate through the thickness of the layer. These simple dislocations are: an edge dislocation with Burgers vector $b = a$ and a screw dislocation with $b = c$. A mixed dislocation is a linear combination of edge and screw dislocations, eg. a dislocation in the [-1-101] [Wu96].

$$1/3\langle 11\text{-}20\rangle + [0001] \rightarrow 1/3\ \langle 11\text{-}23\rangle$$

$$\text{Edge} \quad + \quad \text{screw} \rightarrow \quad \text{mixed}$$

In most of the case, the edge-type TDs are situated within (1-100) planes and their line is along the [0001] direction. Their Burgers vector is typically 1/3 <1-210>, 1/3 <11-20>, or 1/3 <2-1-10> [Wu96]. Edge-type TDs are mainly generated at the first stages of the growth, when the islands coalesce [Hir91, Hey96].

3.6.3 Planar defects

Planar defects such as stacking faults (SF) are errors in the stacking sequence of atomic planes when the perfect order of atomic planes of the crystal is disturbed. The original stacking sequence in the (0001) direction for wurtzite III-nitride is

…ABABABAB…. There are four types of stacking faults possible in such case [Sta98]:

- Type-I stacking fault (also called I_1) contains one violation of the stacking rule and is commonly expected to have the lowest formation energy. For this type of fault two stacking sequences can be considered: …ABCBCB… and …ABACAC… But they are equivalent and have the same energy.
- Type-II stacking fault (I_2) containing two violations of the stacking rule: …ABABCACA…
- Type-III stacking fault is an intrinsic fault in which one of the A or B layers occupies the wrong C position, eg. …ABACABAB…, which according to theoretical predictions has the second lowest formation energy.
- Extrinsic (E) stacking fault where an extra planes is added between normal atomic layers, eg. …ABCABABA….

Stacking fault do not generate interface levels in the bandgap, but since they can be regarded as an insertion of zinc-blende phase into wurtzite lattice there is a bandgap difference to be expected.

3.7 Characterization methods

3.7.1 X-ray diffraction

X-ray diffraction (XRD) is a versatile non-destructive structural characterization tool for analyzing a wide range of materials. Now XRD has become an indispensable method to determine identity, composition, crystalline orientation, strain state, grain size, and crystalline quality of the sample.

X-ray diffraction is based on constructive interference of monochromatic X-rays diffracted by a crystalline sample. These X-rays are generated by a cathode ray tube, filtered to produce monochromatic radiation, collimated to a concentrated beam, and directed toward the sample. The interaction of the incident x-rays with the sample produces constructive interference of the diffracted x-rays only at certain angles that satisfy Bragg's Law given by:

$$2d \sin \theta = n\lambda \qquad (3.2)$$

where *n* (an integer) is the order of reflection, λ is the wavelength of the x-rays, *d* is the interplanar spacing of the reflecting planes and θ is the angle of incidence (Figure 3.21). For any angle other than θ the scattered x-rays undergo destructive interference and hence no signal is perceived by the detector. Therefore, determination of θ reveals the interplanar spacing of the crystal phase, and in turn the lattice parameter.

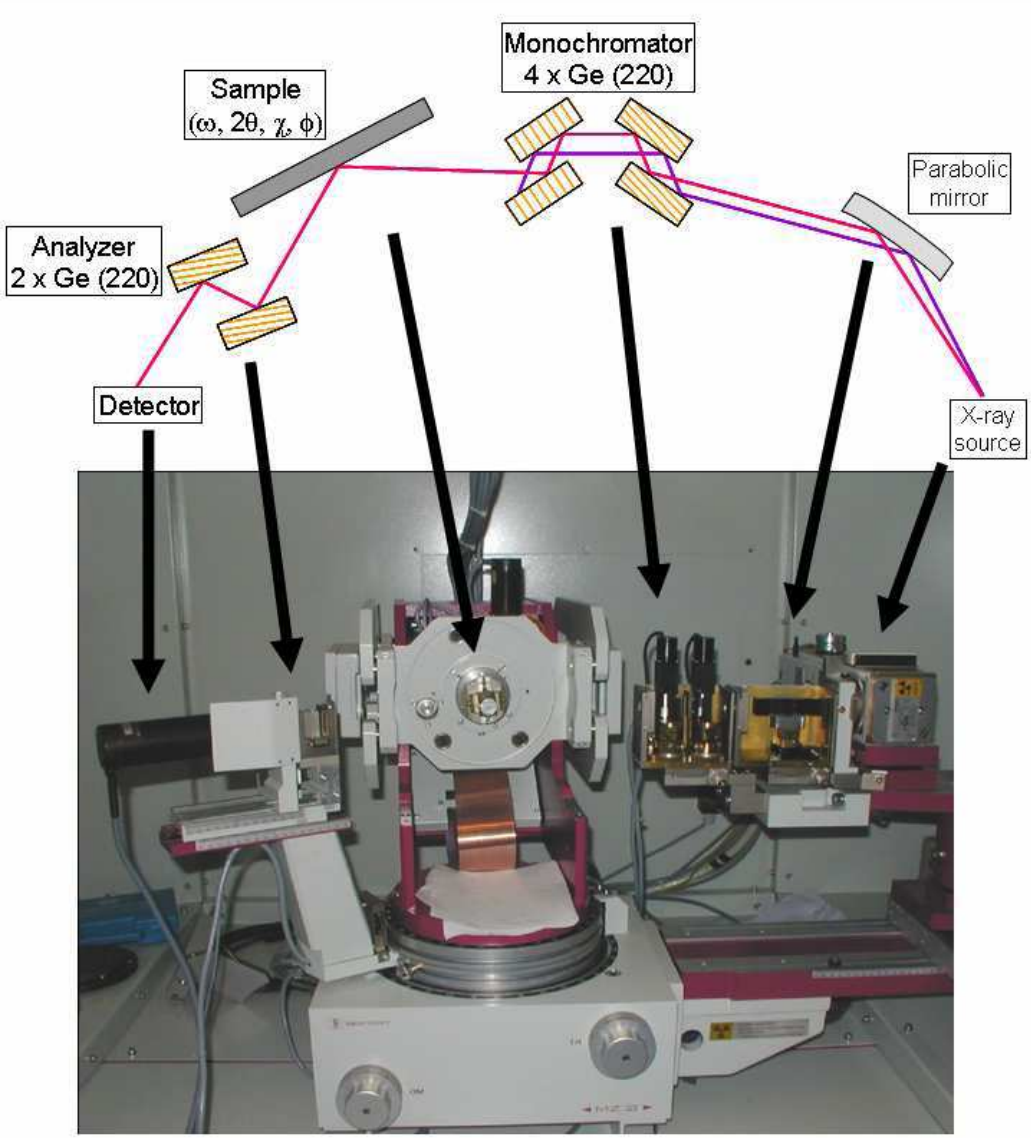

Figure 3.21: Photograph and illustration of the X-ray diffraction system used in this work.

X-ray diffractometers consist of three main parts: a beam generator, a sample holder (goniometer), and an X-ray detector. X-rays can be generated by an X-ray tube, a vacuum tube that uses a high voltage, typically 15-60 kV, to accelerate

the electrons released by a hot cathode to a high velocity. The high velocity electrons collide with a metal target, the anode, creating the X-rays. In this study, XRD measurements were performed on a *Seifert XRD 3003 PTS* system (photographed on figure 3.21) which uses the Cu $K_{\alpha 1}$ wavelength, *i.e.* $\lambda = 0.154056$ nm. The Cu X-ray beam generated by the tube is transformed into a parallel beam (0.01° divergent) by reflection onto a parabolic mirror with a parameter gradient, which additionally increases its intensity by a factor of 10.

This diffractometer is equipped with two monochromators, each of them consisting of two Ge(220) monocrystals, are mounted in the so-called "4-crystal" scheme (-n, +n, +n, -n) (Figure 3.22(c)) [Bow]. This configuration is important for reducing the angular (Figure 3.22(a)) and wavelength (Figure 3.22(b)) divergences of the beam. The resolution is improved by the diffraction of the beam by the crystals. Generally, the Ge(220) plane family is placed in diffraction condition, which leads to $\Delta\theta = 0.0033\circ$ and $\Delta\lambda/\lambda = 1.4 \times 10^{-4}$.

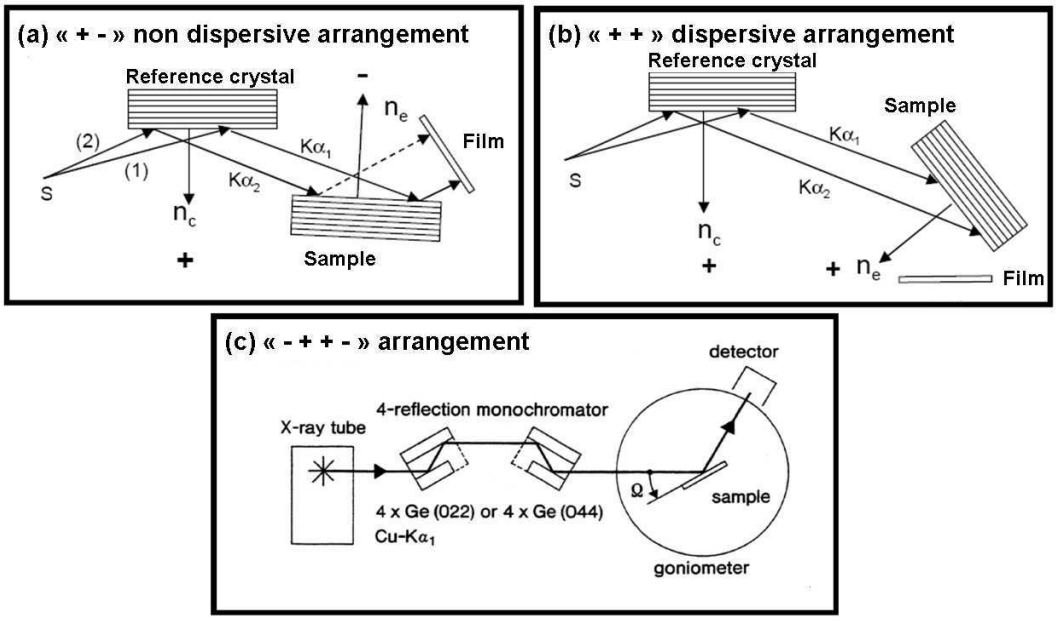

Figure 3.22: Illustration of the effect of Ge monocrystals on the beam path.

Another important part of the diffractometer is goniometer, the mechanical assembly that makes up the sample holder, detector arm and associated gearing is referred to as goniometer. The goniometer allows selecting the plane family in diffraction condition by changing the orientation of the sample. It is called "4-circle"

goniometer because it is possible to rotate independently the 4 angles, (ω, 2θ, φ, χ), which determine the sample position (Figure 3.23). The angle ω is the incident angle of the beam with the surface, 2θ the angle between the ingoing and outgoing beams, φ and χ the rotations around the normal of the sample (*z*-axis) and *x*-axis, respectively. Another part of the goniometer is dedicated to the movement along *x*, *y* and *z* axis, to center the sample. Two additional angles, χ_1 and χ_2, can be rotated around the *x*-axis and the *y*-axis, independently from the goniometer, in order to put the normal to the planes exactly along *z*-axis without using the χ angle. For each reflection, we can measure ω, 2θ or ω−2θ scans. It is also possible to make a two-dimensional scan around a reflection, *i.e.* draw a local mapping of the reciprocal space, by moving both ω and 2θ angles.

The detector has an aperture of 2^o which can be reduced by inserting slits in order to improve the resolution of the diffracted beam. For high-resolution x-ray diffraction (HRXRD) measurements, an analyzer (two Ge (220) monocrystals) is placed between the sample and the diffracted beam to improve the angular precision of the diffracted beam ($\leq 0.001^\circ$).

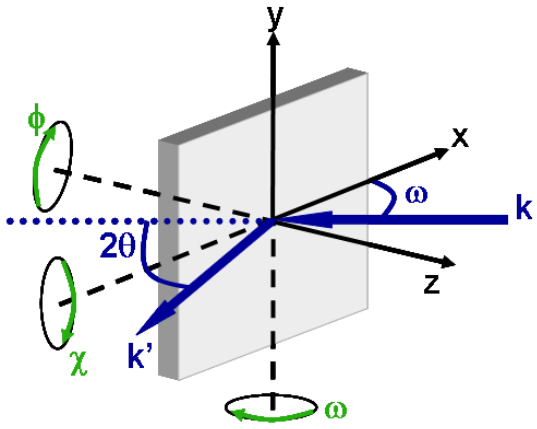

Figure 3.23: *Schematic representation of the angles and axis which allow to position the sample.*

3.7.2 Atomic-force microscopy (AFM)

AFM is one of a family of techniques known as scanning probe microscopies (SPM) in which the lateral position of a probe is scanned across a surface and the probe-sample interaction or interactions are monitored. The AFM probe has a very sharp tip, usually a couple of microns long and often less than 100 Å diameter, at the

end of a small cantilever (that is 100 to 200 μm long). AFM tips and cantilevers are microfabricated from Si or Si_3N_4. The short-range interaction between the sample and the probe is directly the force between the two [Bin86]. As this force usually depends on the distance between the sample and the probe, via Hook's law, this can be used to measure the probe-sample distance and thus the sample morphology. Schematic of an AFM measurement setup is shown in figure 3.24. As no current need flow, this technique effectively remedies one of the limitations of scanning tunneling microscopy (STM): it can be used to characterize insulators. AFM can image conductors, semiconductors and insulators in vacuum, atmosphere as well as in liquid.

Depending on the needs, the AFM can be operated in various modes. The three common modes are contact, non-contact and tapping mode. Figure 3.25 shows schematically the difference.

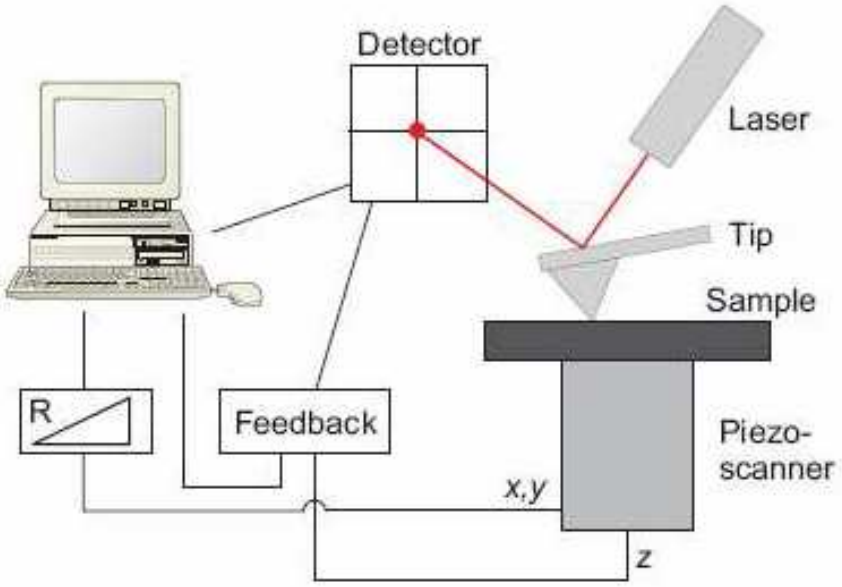

Figure 3.24: Schematics of an AFM: The bending of the cantilever is measured by the deviation of a laser beam using a 4-sector detector. The bending will be proportional to the force on the cantilever and is kept constant in a feeback circuit. This can be achieved by changing the tip-sample distance using a piezoelectric actuator. The same piezoelectric actuator is used to generate the lateral scanning movement.

In the contact mode, the cantilever is held less than a few angstroms from the sample surface, and the interatomic force between the cantilever and the sample is repulsive. This mode scans the sample surface by using feedback to keep the repulsive force constant. Unfortunately, contact mode imaging is heavily influenced by

frictional and adhesive forces which can damage samples and distort image data. In the non-contact mode, the cantilever is held on the order of tens to hundreds of angstroms from the sample surface, and the interatomic force between the cantilever and sample is attractive Van der Waals forces. In this method, the cantilever is oscillated at large amplitudes and at frequencies close to or at its resonance frequency (~kHz). It measures changes in the oscillation amplitude at a fixed driving frequency and the probe-sample interactions can be obtained from the change in the amplitude of oscillation. Non-contact imaging generally provides low resolution and can also be hampered by the contaminant layer which can interfere with oscillation.

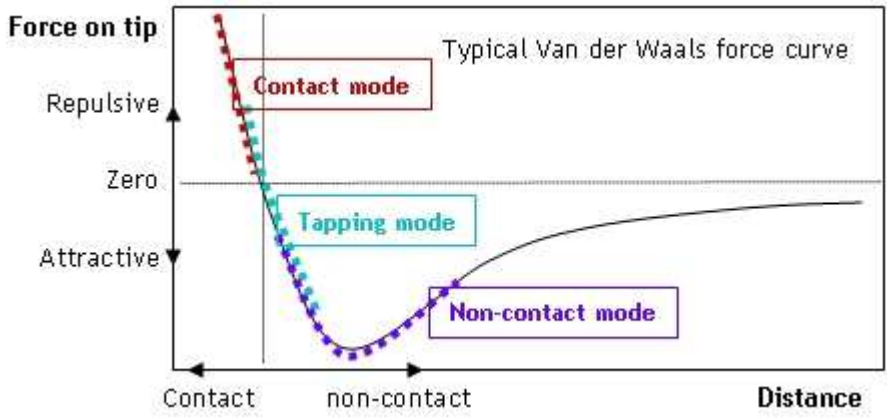

Figure 3.25: Force vs. tip-to-sample distance in AFM operation. Far from the sample, the cantilever is not affected by interatomic forces and is in its free equilibrium position. But when brought closer to the surface, attractive forces act upon the tip to bend the cantilever towards the sample. When the tip is in contact with the surface, repulsive forces dominate, deflecting the cantilever backwards.

Tapping mode is a key advance in AFM and it is a combination of the two previous modes. It overcomes problems associated with friction, adhesion, electrostatic forces, and other difficulties that can plague conventional AFM scanning methods by alternately placing the tip in contact with the surface to provide high resolution and then lifting the tip off the surface to avoid dragging the tip across the surface. In this work, the AFM measurements were performed in the tapping mode.

In intermittent or tapping mode operation the probe is oscillated at or near its resonant frequency ω_0 (Eq.3.3) with a certain amplitude.

$$\omega_0 = \sqrt{k/m} \tag{3.3}$$

A high resonance frequency ($\omega_0 >> 1$ kHz) is generally advantageous, since it allows to decouple the cantilever oscillations from low-frequency noise induced by vibrations of the microscope or the building.

When the oscillating tip is close enough to the surface (less than 10 nm), it is exposed to a Van der Waals interaction gradient. This force gradient leads to a shift of the resonance frequency of the tip:

$$\omega = \omega_0 \sqrt{1 - \frac{1}{k}\frac{\partial F}{\partial z}} \tag{3.4}$$

In addition to this effect, the oscillation amplitude is also damped by increasing interaction between the probe and the surface. So in this mode, to measure the surface morphology, the oscillating amplitude is kept constant using a piezoelectric actuator and a PID regulator to control the tip-sample distance. Maintaining a constant oscillation amplitude or phase shift results in a constant tip-sample force gradient. The minimal detectable force gradient is given by [Wie94]:

$$\frac{\partial F}{\partial z} = \frac{1}{A}\sqrt{\frac{4Bk k_B T}{\omega_0 Q}} \tag{3.5}$$

where A is the rms (root mean square) oscillation amplitude, B the detection bandwidth, and $Q = \Delta\omega/\omega$ the quality factor of the resonance. Hence, there are four main parameters to optimize the sensitivity:

- The force constant k should be small and the resonance frequency ω_0 should be high. This requires minimization of the cantilever mass.
- The quality factor of the resonance $Q = \Delta\omega/\omega$ should be high. Size minimizations of the cantilever generally increase Q. Another way to increase Q is to work under vacuum.
- If possible low temperatures are preferred.
- The oscillation amplitude A should be sufficiently large. However, the oscillation amplitude is generally limited by the experimental setup.

So basically, tapping mode AFM was developed as a method to achieve high resolution without inducing destructive frictional forces both in air and fluid. With the tapping mode technique, the very soft and fragile samples can be imaged successfully.

The AFM can be used to study a wide variety of samples (i.e. plastic, metals, glasses, semiconductors, and biological samples such as the walls of cells and bacteria). However there are some issues influencing atomic resolution in AFM scanning. In AFM the spatial resolution depends on the shape and size of the tip, as well as the separation between the tip and sample.

The physical probe used in AFM imaging is not ideally sharp. As a consequence, an AFM image does not reflect the true sample topography, but rather represents the interaction of the probe with the sample surface. This is called tip convolution. Tip convolution occurs when the radius of curvature of the tip is comparable with, or greater than, the size of the feature that is imaged. Figure 3.26 illustrates this problem; as the tip scans over the specimen, the sides of the tip make contact before the apex, and the feedback mechanism begins responding to the feature.

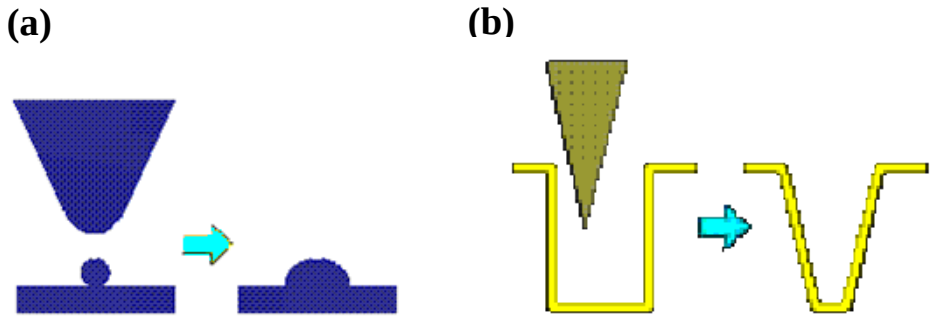

Figure 3.26: Examples of tip-sample convolution:(a) an overestimated convex surface feature, and (b) an underestimated concave feature.

The effective tip shape may change during an image, as the tip may pick up impurities as it contacts the surface, this can cause a change in the effective resolution. Tips with multiple asperities at the apex can result in multiple superposed images of surface features, if these are sufficiently close, the resolution is degraded. Other factors influencing resolution are non-linear response of the piezo materials used in the AFM scanner and environmental noise (vibration and electrical interference).

3.7.3 Photoluminescence spectroscopy

Photoluminescence (PL) spectroscopy is a contactless, nondestructive method of probing the electronic structure of materials. Light is directed onto a sample, where it is absorbed and imparts excess energy into the material in a process called photo-excitation. One way this excess energy can be dissipated by the sample is through the emission of light, or luminescence. The intensity and spectral content of the PL is a direct measure of various important material properties.

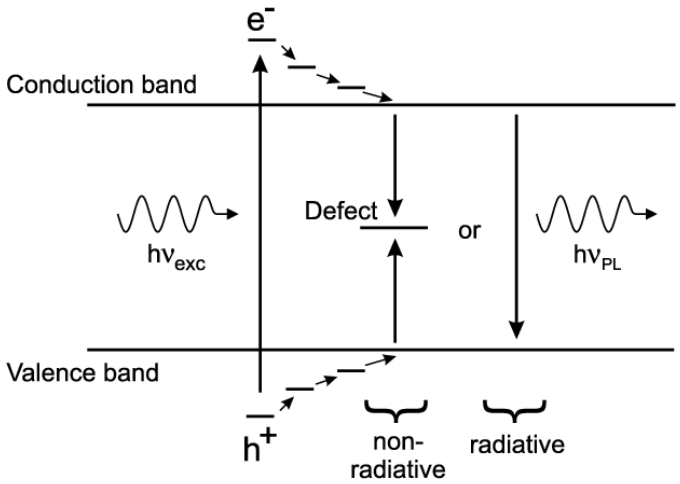

Figure 3.27: PL mechanism in semiconductors: an incoming photon of sufficiently high energy $h\nu_{exc}$ is absorbed by the material creating an electron-hole pair (h^+e^-). These carriers quickly thermalize to the limits of the conduction and valence bands. They can recombine either non-radiatively on defects or radiatively by emitting a PL photon with an energy close to that of the band gap.

The general mechanism of PL in solids is described in figure 3.27. When a photon of energy higher than the so-called band gap of the material is absorbed, an electron-hole pair is created. On a very short timescale the energy is thermalized so that the energy separation between the electron and the hole becomes approximately equal to the energy of the gap. Then the pair can radiatively recombine, giving rise to the emission of a photon (luminescence). As a result, the peak position of the photoluminescence roughly reflects the band gap of the material. In general, the yield of PL is governed by a competition between radiative and non-radiative recombination. The sources of non-radiative recombination are defects in the material (for example impurities and disorder sites in a crystal or dangling bonds on the surface). Therefore, the defects are said to quench the photoluminescence.

Figure 3.28 illustrates the setup used in this work. The excitation source was a frequency-doubled continuous-wave Ar+ laser (λ = 488/2 = 244 nm). The signal was collected into a 45-cm-focal-length Jobin-Yvon monochromator and detected by an ultraviolet-enhanced charge-coupled device (CCD).

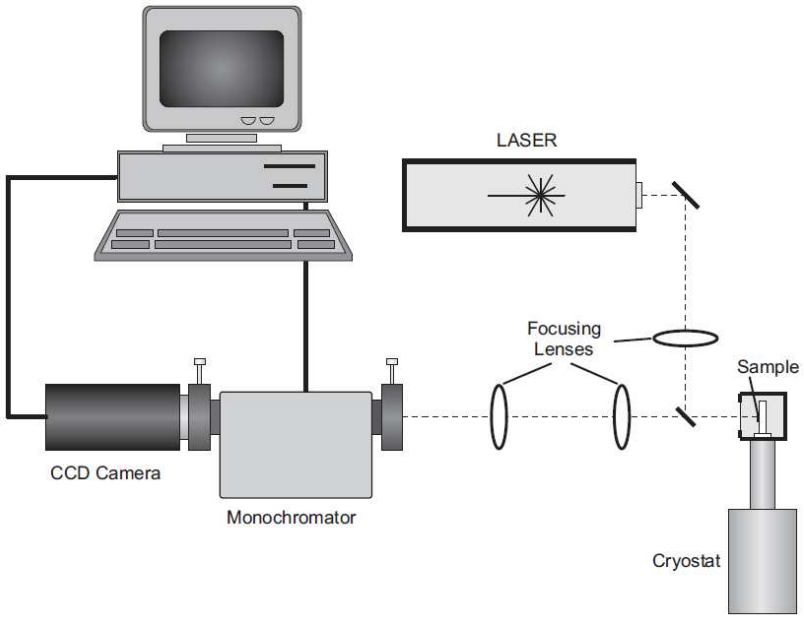

Figure 3.28: *Photoluminescence setup.*

Time-resolved photoluminescence (TRPL) has been used to study the carrier relaxation processes. The principle is to excite the sample with laser pulses and record the evolution of the emission intensity. The measured decay times provide information about the nature of the transition involved. The excitation source was a pulsed frequency-tripled Ti-sapphire laser (λ = 270 nm) with a pulse width around 200 fs. The repetition rate of the laser could be adjusted from 76 MHz (13 ns period) down to 0.9 MHz (1.1 μs period) by the use of a cavity dumper. Thus, the effective system resolution depends on the time window used for the analysis. For the shorter pulse periods (13 ns), the signal was analyzed with a 2 ns window, giving a system response of about 10 ps. In the case of longer periods (1.1 μs), we used a 20 ns window, providing a system response of about 500 ps. In this TRPL setup, the monochromator had a focal length of 32 cm. In both PL and TRPL experiments the samples were mounted in a cold finger He cryostat and the diameter of the laser spot was about 50 μm.

Bibliography

[Ade02] C. Adelmann, *Growth and strain relaxation mechanisms of group III nitride heterostructures*. Ph.D. thesis, Universit´e Joseph Fourier – Grenoble 1 (2002).

[Ade03] C. Adelmann, J. Brault, G. Mula, B. Daudin, L. Lymperakis, and J. Neugebauer, *Gallium adsorption on (0001) GaN surfaces.* Physical Review B 67, 165419 (2003).

[Ale99] A. Alemu, M. Julier, J. Campo, B. Gil, D. Scalbert, J.-P. Lascaray, S. Nakamura, *Optical anisotropy in GaN grown onto A–plane sapphire.* Materials Science and Engineering B 59, 159 (1999).

[Art68] J. R. Arthur, *Interaction of Ga and* As2 *molecular beams with GaAs surfaces*. Journal of Applied Physics 39, 4032 (1968).

[Bak06] T. J. Baker, B. A. Haskell, F. Wu, J. S. Speck, and S. Nakamura, *Characterization of Planar Semipolar Gallium Nitride Films on Sapphire Substrates.* Japanese Journal of Applied Physics 45, L154 (2006).

[Bar95] A.-L. Barabási and H. E. Stanley, *Fractal Concepts in Surface Growth* (Cambridge University Press, Cambridge, 1995)

[Bin86] G. Binnig, C. Quate, and C. Gerber, *Atomic force microscope*. Physical Review Letter 56, 930 (1986).

[Bow] K. Bowen and B. K. Tanner, *High resolution X-ray diffractometry and topography.*

[Chi96] F. R. Chien, X. J. Ning, S. Stemmer, P. Pirouz, M. D. Bremser, and R. F. Davis, *Growth defects in GaN films on 6H–SiC substrates*. Applied Physics Letters 68, 2678 (1996).

[Cho75] A. Y. Cho and J. R. Arthur, *Molecular beam epitaxy*. Progress in Solid State Chemistry 10, 157 (1975).

[Edd93] C.R. Eddy, Jr., T.D. Moustakas and J. Scanlon, *Growth of gallium nitride thin films by electron cyclotron resonance microwave plasma-assisted molecular beam epitaxy*. Journal of Applied Physics 73, 448 (1993).

[Fee02] R. M. Feenstra, J. E. Northrup, and J. Neugebauer, *Review of Structure of Bare and Adsorbate-Covered GaN(0001) Surfaces*. MRS Internet Journal of Nitride Semiconductor Research 7, 3 (2002).

[Fra49] F. C. Frank and J. H. van der Merwe, *One-dimensional dislocations. II. Misfitting monolayers and oriented overgrowth*. Proceedings of the Royal Society of London. Series A, Mathematical and Physical Sciences198, 216 (1949).

[Hey00] B. Heying, R. Averbeck, L. F. Chen, E. Haus, H. Riechert, and J. S. Speck, *Control of GaN surface morphologies using plasma-assisted molecular beam epitaxy*. Journal of Applied Physics 88, 1885 (2000).

[Hey96] B. Heying, X. H. Wu, S. Keller, Y. Li, D. Kapolnek, B. P. Keller, S. P. D. Baars, and J. S. Speck, *Role of threading dislocation structure on the xray diffraction peak widths in epitaxial GaN films*. Applied Physics Letter 68, 643 (1996).

[Hir91] K. Hiramatsu, S. Itoh, H. Amano, I. Akasaki, N. Kuwano, T. Shiraishi, and K. Oki, *Growh mechanism of GaN grown on sapphire with AlN buffer layer by MOVPE*. Journal of Crystal Growth 115, 628 (1991).

[Ho96] I. Ho and G.B. Stringfellow, *Solid phase immiscibility in GaInN.* Applied Physics Letters 69, 2701 (1996).

[Ili02] E. Iliopoulos and T. D. Moustakas, *Growth kinetics of AlGaN films by plasma-assisted molecular-beam epitaxy.* Applied Physics Letters 81, 295 (2002)

[Iwa97] K. Iwata, H. Asahi, K. Asami, R. Kuroiwa, and S. Gonda, *Gas Source Molecular Beam Epitaxy Growth of GaN on C-, A-, R- and M-Plane Sapphire and Silica Glass Substrates.* Japanese Journal of Applied Physics 36, L661 (1997).

[Kap07] M. J. Kappers, J. L. Hollander, C. McAleese, C. F. Johnston, R. F. Broom, J. S. Barnard, M. E. Vickers, and C. J. Humphreys, *Growth and characterisation of semi-polar (1 l-22) InGaN/GaN MQW structures*. Journal of Crystal Growth 300, 155 (2007).

[Kap95] D. Kapolnek, X. H. Wu, B. Heying, S. Keller, B. P. Keller, U. K. Mishra, S. P. DenBaars, and J. S. Speck, *Structural evolution in epitaxial metalorganic chemical vapor deposition grown GaN films on sapphire*. Applied Physics Letters 67, 1541 (1995).

[Kob03] G. Koblmueller, R. Averbeck, L. Geelhaar, H. Riechert, W. Hosler, and P. Pongratz, *Growth diagram and morphologies of AlN thin films grown by molecular beam epitaxy*. Journal of Applied Physics 93, 9591 (2003).

[Liu02] L. Liu and J. H. Edgar, *Substrates for gallium nitride epitaxy*. Materials Science and Engineering R 37, 61 (2002).

[Mar95] I. V. Markov, *Crystal Growth for Beginners* (World Scientific, Singapore, 1995)

[Mie09] P. De Mierry, T. Guehne, M. Nemoz, S. Chenot, E. Beraudo, and G. Nataf, *Comparison between Polar (0001) and Semipolar (11-22) Nitride Blue–Green Light-Emitting Diodes Grown on c- and m-Plane Sapphire Substrates*.Japanese Journal of Applied Physics 48, 031002 (2009).

[Mon03] E. Monroy, B. Daudin, E. Bellet-Amalric, N. Gogneau, D. Jalabert, F. Enjalbert, J. Brault, J. Barjon, and Le Si Dang, *Surfactant effect of In for AlGaN growth by plasma-assisted molecular beam epitaxy*. Journal of Applied Physics 93, 1550 (2003)

[Nag89] T. Nagatomo, T. Kuboyama, H. Minamino and O. Omoto, *Properties of* $Ga_{1-x}In_xN$ *films prepared by MOVPE.* Japanese Journal of Applied Physics 28, L1334 (1989).

[Nak96] S. Nakamura, M. Senoh, S. Nagahama, N. Iwasa, T. Yamada, T. Matsushita, H. Kiyoku, and Y. Sugimoto, *InGaN Multi-Quantum-Well-Structure Laser Diodes with Cleaved Mirror Cavity Facets.* Japanese Journal of Applied Physics 35, 217 (1996).

[Neu03] J. Neugebauer, T. Zywietz, M. Scheffler, J. E. Northrup, H. Chen, and R. M. Feenstra, *Adatom Kinetics On and Below the Surface: The Existence of a New Diffusion Channel*. Physical Review Letter 90, 056101 (2003).

[Nor00] J. E. Northrup, J. Neugebauer, R. M. Feenstra, and A. R. Smith, *Study of GaN(0001): the laterally contracted Ga bilayer*. Physical Review B 51, 9932 (2000).

[Pol00] P. Politi, G. Grenet, A. Marty, A. Ponchet, and J. Villain. *Instabilities in crystal growth by atomic or molecular beams.* Physics Reports 324, 271 (2000)

[Pus94] M.J. Puska and R.M.Nieminen, *Theory of positrons in solids and on solid surfaces.* Reviews of Modern Physics 66, 841(1994).

[Sai96] Y. Saito, *Statistical Physics of Crystal Growth* (World Scientific, Singapore, 1996)

[Sta98] C.Stampfl and C.G. Van de Walle, *Energetics and electronic structure of stacking faults in AlN, GaN, and InN.* Physical Review B 57, R15052 (1998).

[Str38] I. N. Stranski and L. V. Krastanow, *Zur Theorie der orientation Ausscheidung von Ionenkristallen aufeinander*. Math.-Naturwiss. K1 Abt. IIb 146, 797 (1938).

[Vil95] J. Villain and A. Pimpinelli, *Physique de la Croissance Cristalline* (Eyrolles, Paris, 1995)

[Vol26] M. Volmer and A.Weber, *Keimbildung in übersättigten Gebilden* (Nucleation of supersaturated structures). Zeitschrift für Physikalische Chemie 119, 277 (1926).

[Wie94] R. Wiesendanger, *Scanning probe microscopy and spectroscopy* (Cambridge Univ.Press, 1994).

[Wu96] X. H. Wu, L. M. Brown, D. Kapolnek, S. Keller, S. P. DenBaars, and J. S. Speck, Defect structure of metal-organic chemical vapor deposition-grown epitaxial (0001) GaN/Al_2O_3. Journal of Applied Physics 80, 3228 (1996)

[Yos91] N. Yoshimoto, T. Matsuoka, T. Sasaki and A. Katsui, *Photoluminescence of InGaN films grown at high temperature by metalorganic vapor phase epitaxy*. *Applied Physics Letters* 59, 2251 (1991).

Chapter 4

Plasma-assisted MBE of semipolar (11-22)-oriented 2D layers

This chapter presents my contribution to the PAMBE of 2D semipolar layers. The first sections deal with the synthesis of binary AlN and GaN alloys and the effect of doping on the growth of semipolar GaN. The chapter finishes with the discussion of the growth details and properties of the ternary AlGaN and InGaN alloys, and finally the results of the synthesis of semipolar InN.

4.1 Introduction

The growth of nitrides on planes other than the *c*-plane has been explored to reduce the negative effects of polarization. The semipolar nitride field garnered scientific interest very recently and most of the research efforts on the semipolar III-nitrides were based on the HVPE and MOVPE techniques. PAMBE presents advantages for certain device structures, particularly in terms of dopant incorporation and nanoscale design. So in the present chapter, we will step into the growth kinetics of semipolar (11-22) 2D layers by PAMBE. However, it is very difficult to grow semipolar epilayers on sapphire compared to polar (in the preceding chapter, I discussed about polar growth) due to the anisotropy of the growing surface.

4.2 Semipolar (11-22) AlN

The synthesis of semipolar AlN on *m*-sapphire was extensively studied in the PhD work of Dr. Lise Lahourcade [Lah07, Lah09b], with the results that I summarize in section 4.2.1. During my PhD, I have studied the early stages of growth, trying to find the origin of the nucleation sites of parasitic crystallographic phases. This work is described in section 4.2.2.

4.2.1 Growth of single-phase (11-22) AlN

During the growth of AlN layers on *m*-sapphire, the RHEED patterns reveal a different behavior as a function of the III/V ratio. The samples grown under Al-rich conditions present the superimposition of two RHEED patterns with different period

(indicated with continuous and dashed lines in figures 4.1(a) and (b)), which points out the coexistence of two AlN orientations. In the case slightly N-rich conditions (III/V = 0.92), the RHEED pattern at the beginning of the growth presents also reflections corresponding to two AlN orientations, but after the growth of about 250 nm only one crystallographic orientation is observed (Figure 4.1(c) and (d)). Finally, under very N-rich conditions (III/V< 0.8), we observe a ring-shaped RHEED pattern as shown in figure 4.1(e), consistent with polycrystalline growth.

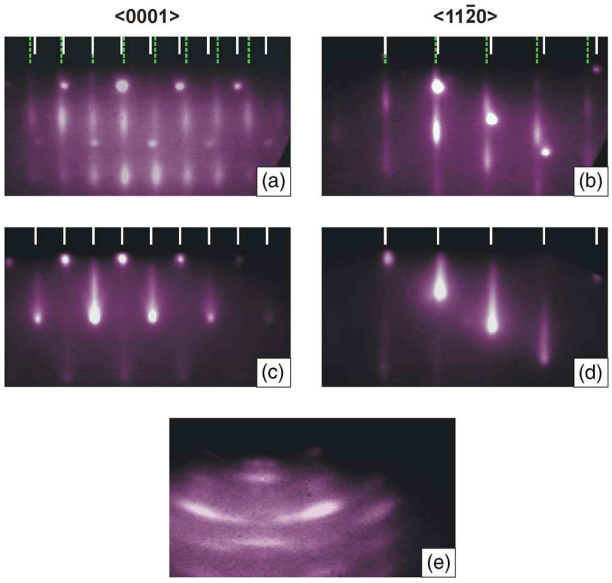

Figure 4.1: RHEED patterns of AlN layers grown at T_s = 730 ^{o}C with III/V=1.15 [(a) and (b)], III/V=0.92 [(c) and (d)] and III/V=0.77 (e), as viewed along the <0001> and<11-20> azimuths of the m-sapphire substrate [Lah07].

AlN layers grown at relatively low temperatures ($T_S \sim 600^oC$) showed polycrystalline growth with RHEED patterns similar to figure 4.1(e) regardless the III/V ratio. On the contrary, an increase of the substrate temperature up to 870 °C does not induce qualitative changes in the crystalline structure.

XRD measurements were applied to determine the crystallographic orientations involved and the obtained diffractograms are shown in figure 4.2. The main diffraction peak corresponds to the (3-300) reflection of the sapphire substrate. The reflection around $2\theta = 71.25^o$ is attributed to AlN(11-22), whereas the reflection at $2\theta = 69.72°$ reveals the presence of AlN(10-10) domains in samples with III/V ratio of 1.15, 1.02 and 0.92. Additionally, a weak signal at $2\theta = 65.87°$ points out the presence of AlN(10-13) domains in the samples grown under Al-rich conditions, but

in negligible concentration in comparison with AlN(11-22) and AlN(10-10). When the III/V ratio decreases, the (10-10)- and (10-13)-oriented domains tend to disappear, which points to moderate N-rich growth conditions (III/V ~ 0.85) as the optimum conditions to achieve high-quality AlN(11-22) layers.

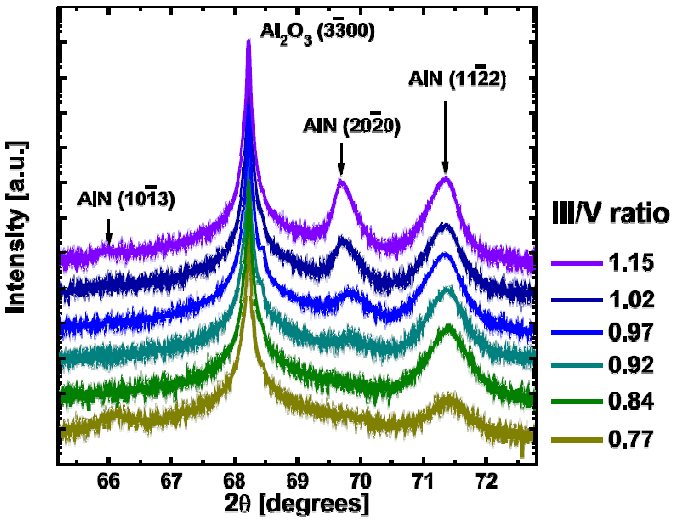

Figure 4.2: X-ray diffraction θ - 2θ scan of AlN layers grown on m-sapphire with different III/V ratio [Lah07].

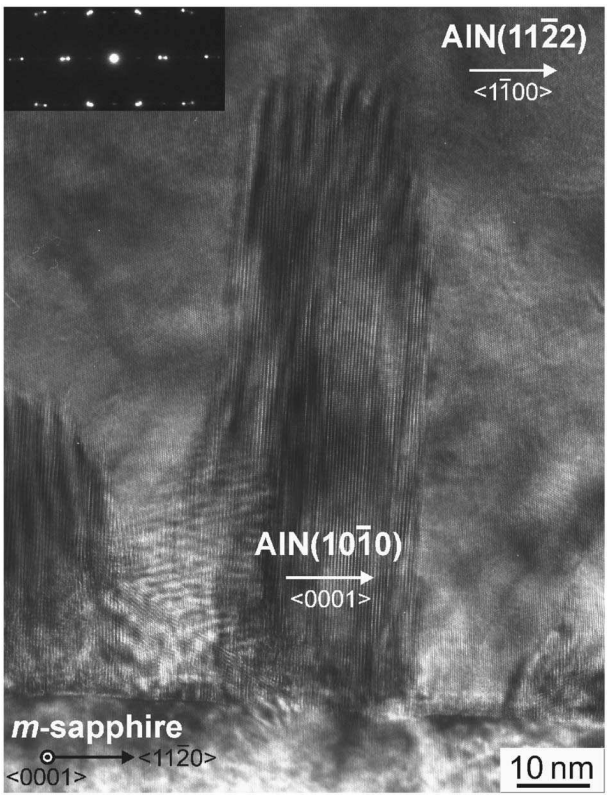

Figure 4.3: High-resolution transmission electron microscopy (HRTEM) image of an AlN (11-22) grown with a III/V ratio of 0.92[Lah07].

HRTEM studies (see figure 4.3) performed by the group of P. Ruterana at ENSICAEN-CNRS confirm that the AlN(10-10) domains are mostly confined close to the interface with the substrate, in agreement with RHEED observations.

4.2.2 AlN nucleation on *m*-sapphire substrate

High-resolution TEM studies performed by the group of Ph. Komninou in the Aristotle University of Thessaloniki tried to identify the nucleation sites associated to the AlN(1-100) parasitic crystallographic phase. With this purpose, I grew samples with and without substrate nitridation. Figure 4.4(a) is a weak-beam TEM image of the $<0001>_{sapphire}$ zone axis recorded on AlN (11-22) sample, grown directly on *m*-sapphire. This sample exhibits a polycrystalline interface with the substrate, with ≈ 30nm-high grains. On the other hand figure 4.4(b), which presents an AlN sample grown after the nitridation of the substrate, shows the presence of nonpolar domains higher than 50 nm and often exceeding 100 nm in other zones.

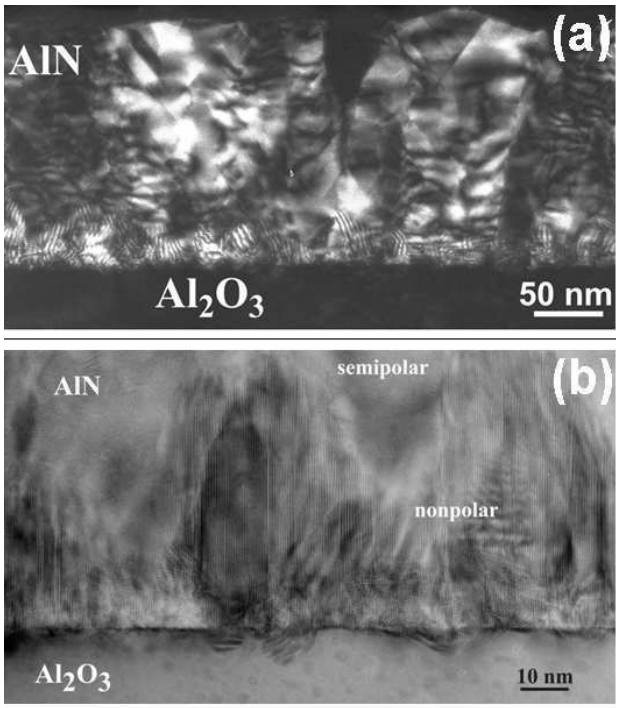

Figure 4.4: (a) Weak-beam g/3g dark-field image obtained from AlN (11-22), grown directly on m-sapphire, along the $[11\text{-}2\text{-}3]_{AlN}/[0001]_{sapphire}$ zone axis with g = [-1100], and it illustrates the nanocrystalline region, manifested by moire´ fringes at the sapphire interface. (b)Cross-sectional HRTEM image of an AlN (11-22) sample grown on nitridated sapphire recorded along the $[11\text{-}2\text{-}3]_{AlN}/[0001]_{sapphire}$. It shows large nonpolar crystallites and a distorted heteroepitaxial interface.

Figures 4.5(a) and (b) present the RHEED patterns of *m*-sapphire along $<0001>_{sapphire}$ and $<11\text{-}20>_{sapphire}$ azimuths, respectively. Additionally, the RHEED images of the nitridated substrate are presented in figures 4.5(c) and (d), recorded after 15 min of nitridation, and in figures 4.5(e) and (f) after 30 min of nitridation. After nitridation, the RHEED images present the same patterns and periodicity as the RHEED images from AlN(10-10): Figures 4.5(c) and (e) are similar to those of *m*-AlN viewed along $<11\text{-}20>_{AlN}$ azimuth in figure 4.5(g), whereas figures 4.5(d) and (f) are similar to figure 4.5(h). We can therefore conclude that the nitridation induces the formation of an AlN(10-10) layer at the *m*-sapphire surface.

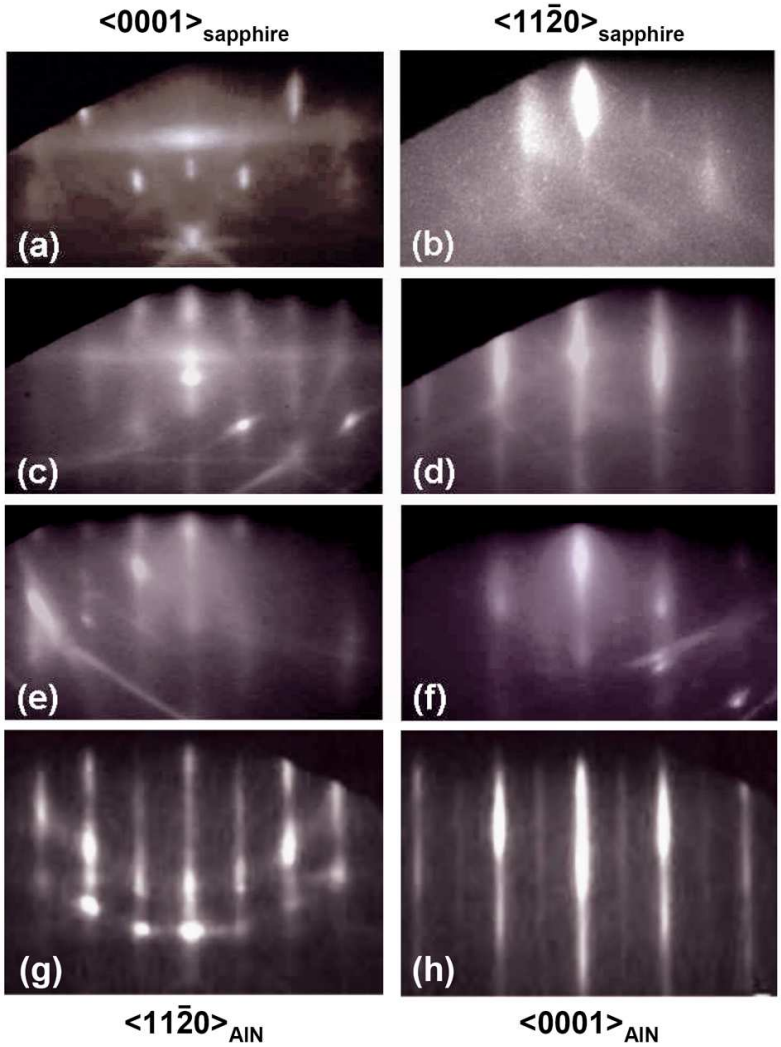

Figure 4.5: RHEED patterns of m-sapphire viewed along (a) $<0001>_{sapphire}$ and (b) $<11\text{-}20>_{sapphire}$, and RHEED images illustrating its evolution [(c), (d)] after 15 min and [(e), (f)] 30 min of nitridation.The RHEED patterns of m-AlN viewed along the (g) <11-20> and (h) <0001> azimuths were included for comparison.

An interesting feature observed in figure 4.4(b) is the presence of v-shaped defects on the sapphire. Same type of defects observed in samples with no nitridation of the substrate (pointed out by the white arrows in figure 4.6). That is, these v-defects exist independently of the nitridation process. In figure 4.6, the v-defects seem to have facets aligned with the (10-14) and (10-12) planes. When viewed along $<0001>_{sapphire}$, the v-defects are also identified (Figure 4.6(b)) and they present (11-20)-oriented facets. We observed that the nonpolar domains are mainly present at the surrounding of the v-defects. This is shown in fact in the HRTEM image of figure 4.7, depicting a nucleus of *m*-plane AlN abutting a sapphire {-12-10} nanofacet. In order to distinguish between the semipolar and nonpolar regions, the geometrical phase analysis (GPA) map of the relative variation of the lattice constants along $[-1-123]_{AlN}$ // $[0001]_{Al2O3}$ has been superimposed on the image. The dislocations at the sapphire-AlN and semipolar-nonpolar interfaces are also clearly discernible by their localized strain fields.

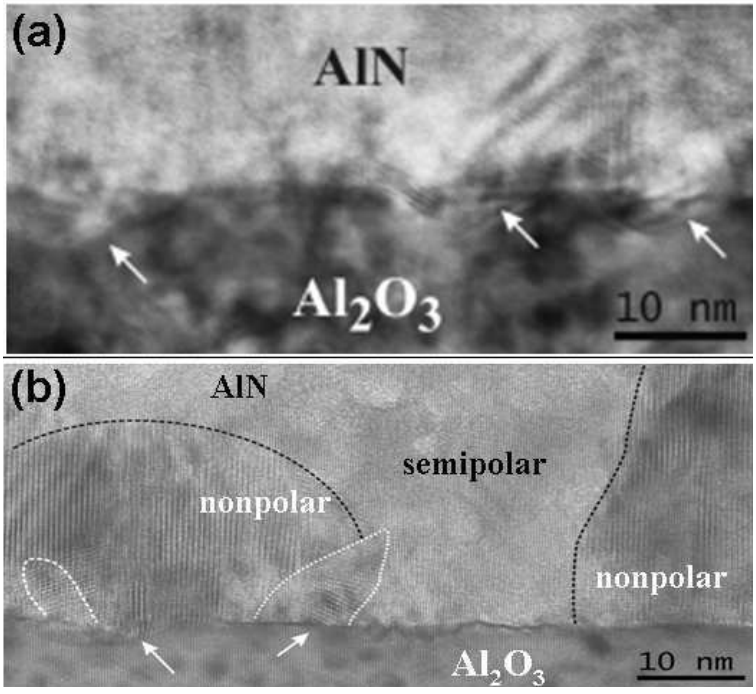

Figure 4.6: Cross-sectional HRTEM images of the interface between AlN and sapphire to show the presence of v-shaped defects on the sapphire surface. (a) Viewed along $<11-20>_{sapphire}$ axis and (b) along $<0001>_{sapphire}$ axis. Both images were recorded on a sample with no nitridation of the substrate before the growth.

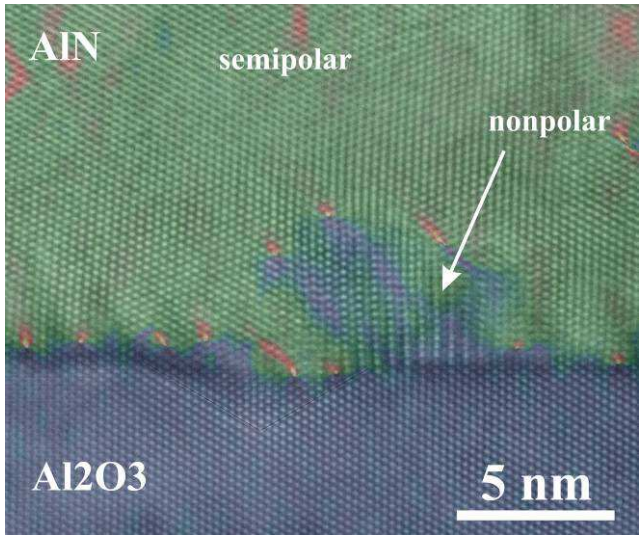

Figure 4.7: Cross sectional HRTEM image of the sapphire interface with semipolar AlN viewed along [-1-123]$_{AlN}$ / [0001]$_{Al2O3}$. The corresponding GPA strain map has been superimposed on the HRTEM image. A nonpolar AlN region is discernible nucleated near a v-pit on the sapphire surface.

In order to identify the origin of these v-defects, I have performed AFM characterization of a series of samples, including:

- An as-received *m*-sapphire substrate.
- An *m*-sapphire substrate after the standard degreasing procedure before introduction to the growth chamber, and 5 min of HF and HCl treatement.
- An m-sapphire substrate after 30 min nitridation at the AlN growth temperature (N flux = 0.3 ML/s, T_S = 720°C). Once extracted from the growth chamber, the substrate was treated with molten KOH for 5 min in order to remove any rest of AlN.
- An *m*-sapphire substrate after deposition of 2 ML of Al at the AlN growth temperature (T_S = 720°C) and Al removal with KOH treatment.
- Substrate with 3 nm of AlN deposited at under stoichiometric conditions, after the deposition of 2 ML of Al and without previous nitridation. Once extracted from the growth chamber, the substrate was treated with molten KOH for 5 min in order to remove any rest of AlN.
- Substrate with 3 nm of AlN deposited at under stoichiometric conditions after nitridation. Once extracted from the growth chamber, the substrate was treated with molten KOH for 5 min in order to remove any rest of AlN.

To be sure of the interpretation of the results, I prepared and analyzed two samples of each kind. The most representative results are summarized in figure 4.8. Figure 4.8(a) shows an AFM image of the bare *m*-sapphire substrate. No modification of this surface morphology is observed after cleaning with organic solvents (trichloroethylene, acetone, methyl alcohol), with HF or HCl for 5 min, by treatment in molten KOH for 5 min, by 30 min nitridation at the growth temperature (N flux = 0.3 ML/s, T_S = 720°C) (Figure 4.8(b)), or by deposition of 2 ML of Al at the growth temperature and Al removal by KOH treatment. However, defects are identified in the case of AlN overgrowth (Figures 4.8(c) and (d)), being larger in diameter in the case of initial nitridation. From these observations, reproduced in two series of samples, we can conclude that the v-defects at the sapphire substrate seem to be related to a reaction with AlN, which is enhanced by starting the growth with N exposure.

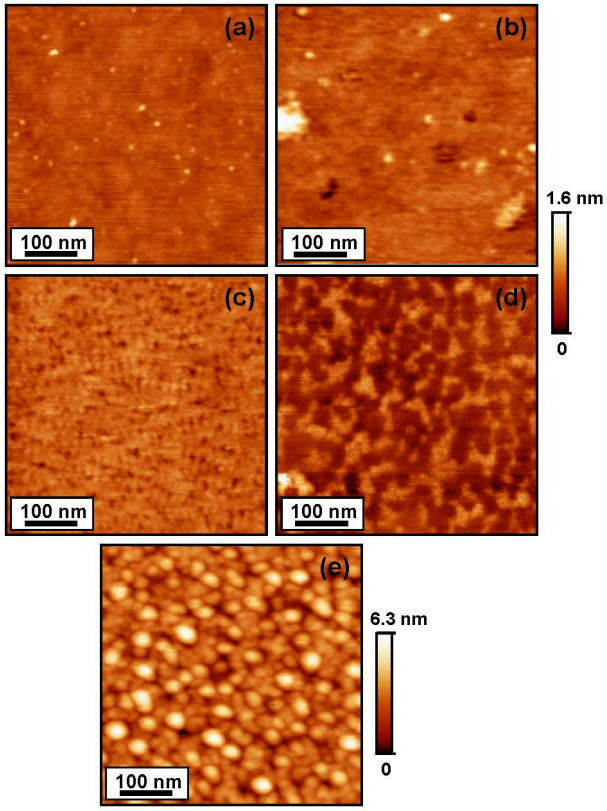

Figure 4.8: (a) As-received m-sapphire substrate (b) m-sapphire substrate after 30 min nitridation at the growth temperature and treatment in molten KOH for 5 min, in order to remove the AlN. (c) m-sapphire substrate after the growth of 3 nm of AlN starting by deposition of 2 ML of Al (without nitridation), followed by ex-situ treatment in molten KOH for 5 min. (d) m-sapphire substrate after the growth of 3 nm of AlN starting by 30 min nitridation, followed by ex-situ treatment in molten KOH for 5 min. (e) Image of the surface of a 3-nm-thick AlN deposited on m-sapphire –no difference in the surface morphology of nitridated and non-nitridated samples was observed.

4.3 Semipolar (11-22) GaN

The growth kinetics of semipolar (11-22) GaN by PAMBE was first described in the PhD work of Dr. Lise Lahourcade [Lah08, Lah09b], and I present an introductory summary in section 4.3.1. During my PhD, I have studied the effect of doping on the growth kinetics and optical and electrical properties of (11-22) GaN layers. This work is described in sections 4.3.2 and 4.3.3.

4.3.1 PAMBE growth kinetics of GaN(11-22)

In the case of GaN layers grown on *m*-sapphire, the RHEED pattern reveals that N-rich conditions (III/ V = 0.92) and stoichiometric (III/V=1) conditions lead to three-dimensional growth, shown in figure 4.9(a) and (b). Under a III/V ratio corresponding to the optimum Ga excess for GaN (0001) growth at the applied substrate temperature (III/V ~ 1.54), the RHEED becomes completely dark after few minutes, indicating gallium accumulation on the surface. In contrast, the growth under III/V ratio corresponding to one monolayer of gallium wetting the GaN (0001) surface (III/V = 1.24) leads to a stable streaky RHEED pattern (Figure 4.9(c)). However, even under the most adequate conditions for two-dimensional growth (III/V=1.24), GaN directly deposited on *m*-sapphire settles into at least two crystalline orientations, as indicated by the superimposition of two RHEED patterns with different periods (continuous and dashed lines figure 4.9(c)).

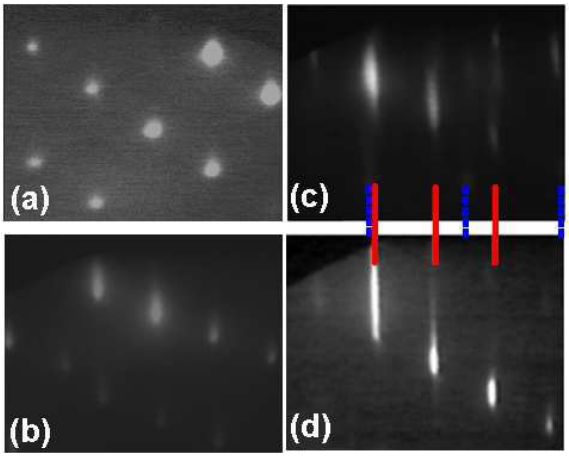

Figure 4.9: RHEED patterns of GaN layers grown directly on m-sapphire with a III/V ratio of (a) 0.92, (b) 1 and (c) 1.24, and (d) on top of AlN(11-22) with a III/V ≈ 1.24.

Lahourcade *et al.* have shown that, it is possible to isolate the (11-22) orientation by using an AlN (11-22) buffer layer [Lah08]. The RHEED pattern of a GaN layer grown with a III/V ratio of 1.24 after deposition of a 100-nm-thick AlN(11-22) buffer layer is presented in figure 4.9(d), showing only one periodic streaky pattern (continuous line). Moreover, the reciprocal space map of these samples, measured by XRD, only displays the reflections arising from the *m*-sapphire (33-00), AlN (11-22) buffer layer and the GaN (11-22) top layer [Lah07].

To understand the growth kinetics and reproduce the growth conditions, we have studied the Ga adsorption on GaN(11-22) by exposing the surface to different Ga-flux at fixed temperature, and analyzing the RHEED transient due to Ga-desorption after closing the Ga shutter. Figure 4.10 compares the Ga coverage evolution on GaN(11-22) surface when varying the Ga flux with the situation on GaN (0001).

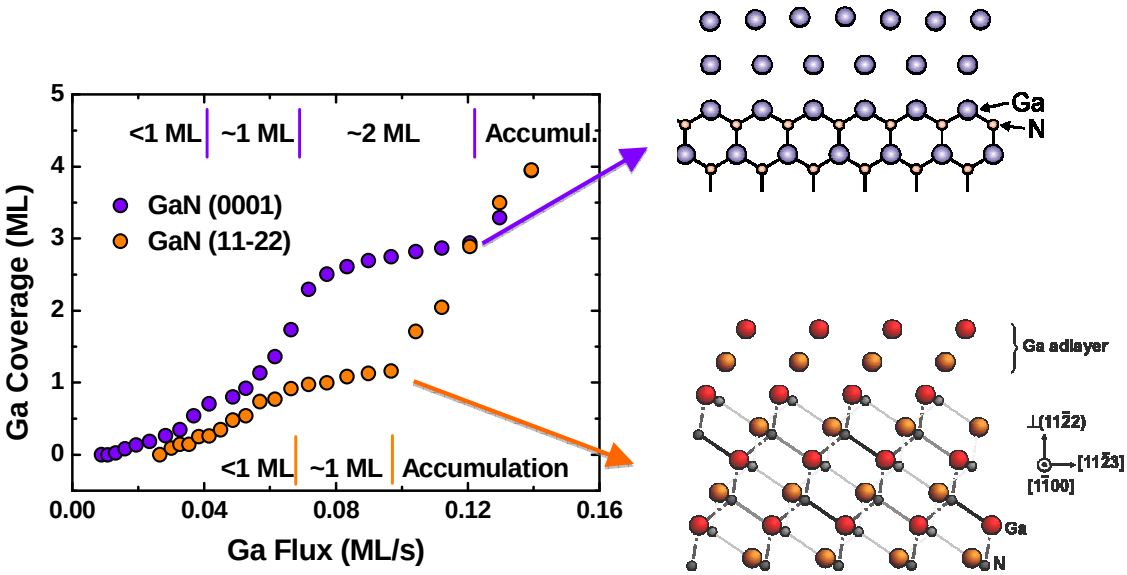

Figure 4.10: Ga coverage of the GaN(11-22) surface compared to that of the GaN(0001) surface. The maximum Ga coverage that we can stabilize on the GaN(11-22) surface is one monolayer [Lah08].

As described in chapter 3, in the GaN(0001) case, we differentiate four regimes, corresponding to coverages of <1, ~1, and 2.5 ML and Ga accumulation. In contrast, in the (11-22) surface, three regimes are identified, corresponding to coverage of <1, ~1.05 ML and Ga accumulation. The Ga flux leading to accumulation on GaN(11-22) is much lower than the one for GaN(0001).

4.3.2 p-type doping of GaN(11-22)

The effects of Mg on the PAMBE growth kinetics of polar GaN(0001) are well documented. It is known that Mg tends to segregate on the surface of GaN, inhibiting the formation of the self-regulated Ga bilayer which acts a surfactant for the growth of undoped and Si-doped two-dimensional GaN [Mon04a, Nor05]. The growth window is hence significantly reduced. On the other hand, the high vapor pressure of Mg at standard PAMBE growth temperatures results in a reduced Mg incorporation efficiency [Guh97, Hau02, Pta01]. Moreover, large Mg doses (>1.2±0.4 ML) lead to an inversion of GaN(0001) to GaN(000-1) [Ram99], and ultimately to the formation of 3C-GaN(111) [Mon04b]. In this section, I present the effect of Mg doping on the growth kinetics and optical and structural properties of GaN (11-22) [Das10].

In order to study the growth kinetics of Mg-doped GaN, we first analyzed Ga wetting of the GaN (11-22) surface during the growth of Mg-doped layers and compared with that of non intentionally doped (n.i.d) layers. Prior to the analysis, a 200-nm-thick AlN(11-22) buffer layer was deposited on *m*-sapphire, followed by a 100-nm-thick n.i.d. GaN(11-22) layer grown with a Ga excess of 1 ML. The Ga coverage was determined by analyzing the evolution of the RHEED intensity transient when stopping the growth after deposition of 3 nm of GaN. Measurements were performed successively for n.i.d. and Mg-doped GaN. In the case of doped GaN, a thin n.i.d. GaN layer of approximately 3 nm was deposited in between the different Ga fluxes, in order to have the same initial conditions for each measurement. The substrate temperature was kept at 686°C for the whole experiment, and the Mg flux corresponded to an atomic incorporation of ~3×10^{19} cm^{-3}.

The calculated Ga coverage on n.i.d. and Mg-doped GaN(11-22) as a function of the impinging Ga flux is presented in figure 4.11. In the case of n.i.d GaN, a self-regulated adlayer is formed for Ga fluxes between 0.072 ML/s and 0.101 ML/s. In contrast, the formation of a Ga adlayer is inhibited for Mg-doped GaN, and Ga accumulation starts at a weaker Ga impinging flux (0.07 ML/s). This can be compared to measurements performed on GaN (0001), showing that the Ga bilayer cannot be stabilized in the case of Mg-doped GaN [Mon04a]. This perturbation of the Ga

kinetics by Mg is attributed to a modification of the energetic balance of the GaN surface by the presence of segregating Mg atoms [Nor05].

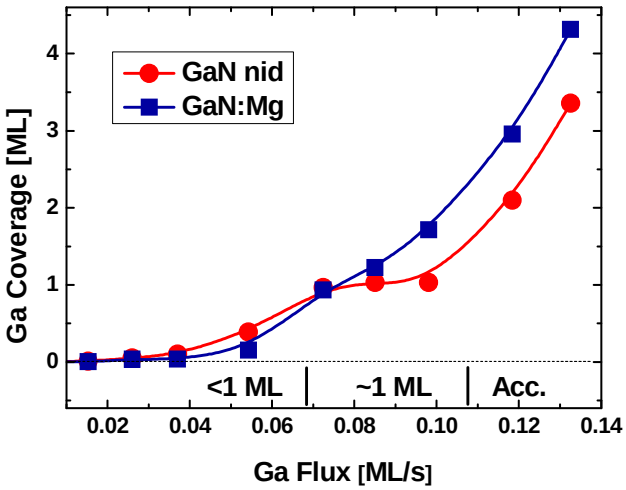

Figure 4.11: Variation of the Ga coverage on GaN(11-22) as a function of the Ga flux. The Mg flux corresponds to an incorporation of ~3×10^{19} cm^{-3}.

Mg-doped GaN(11-22) layers with a thickness of ~ 800 nm have been grown with a Ga flux at the Ga accumulation limit. Surface morphology analysis by AFM shows an increase of the surface roughness when comparing undoped layers (RMS < 2 nm in 5×5 µm^2) to Mg doped layers (RMS ~ 3-3.5 nm), as illustrated in figure 4.12.

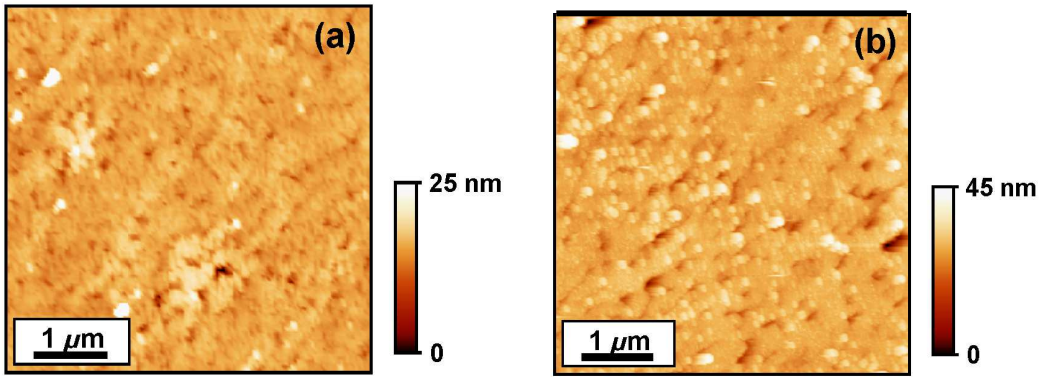

Figure 4.12: Typical AFM images of 800 nm thick (a) undoped and (b) Mg-doped (11-22)-oriented GaN layers.

The Mg incorporation is uniform along the GaN layer for atomic concentrations up to 1.6×10^{20} cm^{-3}, as verified by the SIMS depth analysis (Figure 4.13). Moreover, transmission electron microscopy does not point out any pyramidal

defects or polarity inversion at the investigated Mg concentration regime [Lah09]. Indeed, the extended defects observed in these layers correspond mainly to the usual basal stacking faults [Pot00] with no detectable Mg segregation. This result is in contrast to c-GaN, where basal and prismatic Mg-rich precipitates have been reported at comparable doping concentrations [Ven03, Lil99]. *P*-type conductivity was measured in samples with [Mg] $\geq 7\times10^{18}$ cm^{-3} (see Table 4.1).

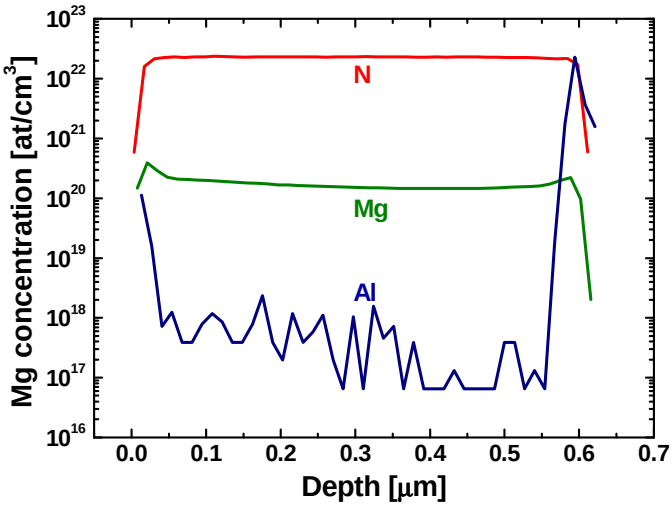

Figure 4.13: Typical SIMS profile of a Mg-doped (11-22)-oriented GaN sample.

Sample	T_{Mg} [°C]	T_S [°C]	P [cm^{-3}]	μ [cm^2/Vs]	[Mg] [cm^{-3}]
E1	350	705	1.1×10^{18}	1.3	3.4×10^{19}
E2	300	705	1.1×10^{18}	2.4	8.5×10^{18}
E3	350	685	1.1×10^{18}	--	1.6×10^{20}
E4	350	665	1.1×10^{18}	0.8	1.0×10^{20}

Table 4.1: Growth parameters and electrical properties of Mg-doped GaN(11-22) samples: Mg cell temperature, T_{Mg}; substrate temperature, T_S; room-temperature Hall carrier concentration, p; mobility, μ; and SIMS Mg concentration, [Mg].

Figure 4.14 compares the luminescence spectra of n.i.d. GaN(11-22), Mg-doped GaN(11-22) and Mg-doped GaN(0001), recorded at low temperature (T = 7K). PL of the Mg-doped samples is dominated by the Mg-related donor-acceptor pair (DAP) line around 3.27 eV. The I_1 line at 3.47 eV is generally assigned to neutral

acceptor bound excitons (A^0X) because of its predominance in the band-edge PL spectrum of *p*-type GaN [Ler99].

The emission related to excitons bound to stacking faults (SF^0X) is significantly attenuated in comparison to the band-edge emission. The nature of these transitions has been confirmed from time-resolved and temperature-dependent PL measurements. The broad blue band located around 2.8 eV which characterizes the PL spectra of heavily Mg-doped GaN (0001) ([Mg] ≥ 1×10^{19} cm^{-3}) grown by MOVPE [Ler99, Qu03] has not been observed in any of the samples under study.

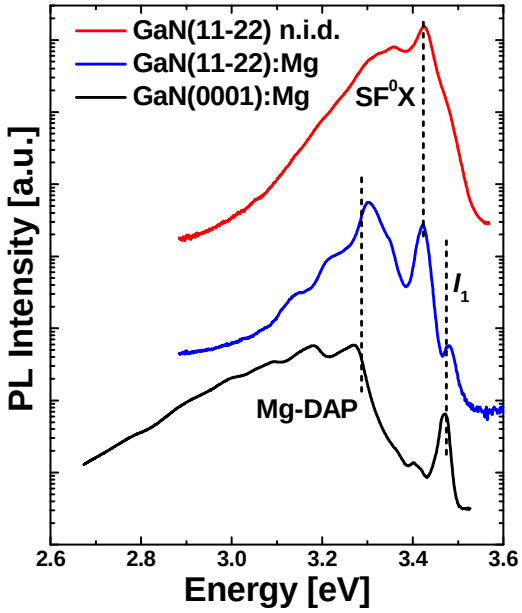

Figure 4.14: Comparison of the low temperature (T = 7 K) PL spectra of undoped GaN(11-22), Mg-doped GaN(11-22) and Mg-doped GaN(0001).

4.3.3 n-type doping of GaN(11-22)

Here also, to study the growth kinetics of Si-doped GaN, we first analyzed Ga wetting of the GaN (11-22) surface during the growth and calculated the Ga coverage. During the RHEED desorption analysis, the substrate temperature was kept at 686°C and the Si-cell temperature was 1150°C, corresponding to a dopant atomic incorporation of about 3×10^{19} cm^{-3}. Figure 4.15 presents the calculated Ga coverage on Si-doped GaN (11-22) surface and comparing with Ga coverage on n.i.d. and Mg-doped GaN(11-22) surfaces (discussed in section 4.3.2).

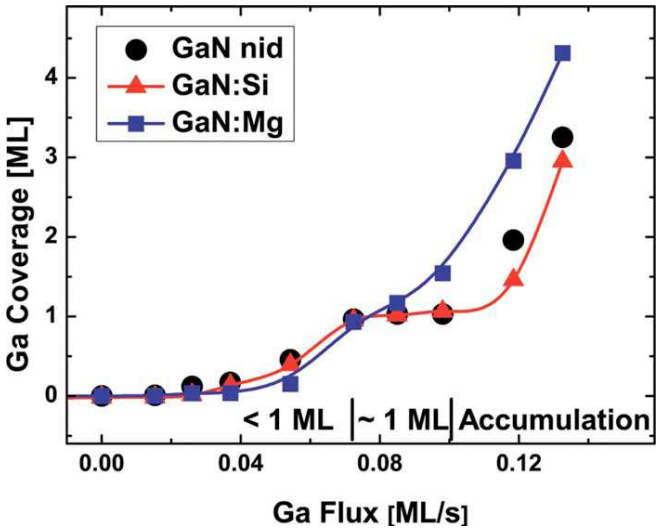

Figure 4.15: Comparison of the Ga coverage depending on Ga impinging flux for undoped, Si-doped and Mg-doped GaN(11-22) surfaces.

In the case of Si-doped GaN a stable regime is observed same like in n.i.d GaN. In both case, it occurs for nearly the same range of Ga fluxes, $0.072 \leq \Phi Ga \leq 0.107$ ML/s. In Si-doped GaN (11-22), the surface remains stable for Ga fluxes below the Ga accumulation threshold ($\Phi \approx 0.101$ ML/s). In Mg-doped layers, the same Ga impinging flux leads to darker RHEED images whose pattern can barely be distinguished, which is an evidence of Ga accumulation.

Applying the optimum growth conditions, we have synthesized ~ 800-nm-thick Si-doped layers containing up to [Si] ~ 6×10^{19} cm^{-3} with a rather flat surface morphology (RMS = 2.9 nm in a surface of 5×5 μm^2), similar to typical undoped GaN (11-22) surfaces.

4.4 Semipolar (11-22) AlGaN

In order to determine the appropriate growth condition for the synthesis of 2D AlGaN(11-22) layers, I have grown simultaneously a series of polar and semipolar $Al_xGa_{1-x}N$ (x = 0.2, 0.3, 0.4) films at the growth temperature of GaN (T_S ~ 720°C) and under Ga excess conditions. During the growth of AlGaN, the RHEED pattern from the semipolar AlGaN was darker compared to polar and the optical microscopic images of the semipolar AlGaN showed droplets on the surface. From this, we can conclude that in the case of semipolar layers, simultaneous growth with polar

structures results in accumulation of Ga droplets at the growth front. Hence, it is necessary to reduce the III/N ratio in comparison to polar AlGaN, although maintaining III/N > 1. With this condition, i.e. under moderate Ga excess, I have synthesized a series of 2D semipolar (11-22) $Al_xGa_{1-x}N$ (x = 0.2, 0.3, 0.4) layers. Note that x = 0.3 is the Al mole fraction corresponding to the specifications of the AlGaN back-contact layer of the chemical sensors targeted by the DOTSENSE project (see figure 1.1 in chapter 1).

Low-temperature (T = 10 K) PL measurements of 300-nm-thick semipolar (11-22) AlGaN layers deposited on 150 nm of AlN(11-22) on *m*-sapphire are presented in figure 4.16. They present narrow band-edge emission without significant radiative contribution from structural or punctual defects.

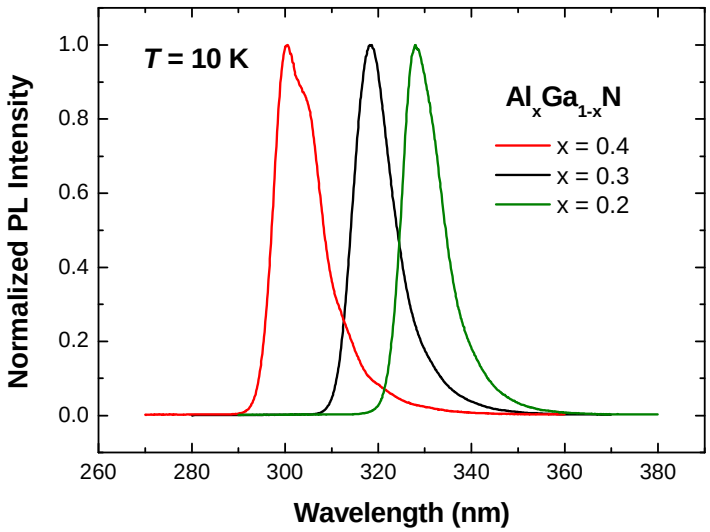

Figure 4.16: Low-temperature (T = 10 K) PL measurements from 300nm-thick semipolar (11-22)-oriented $Al_xGa_{1-x}N$ layers.

The AFM image in figure 4.17 illustrates a 700-nm-thick $Al_{0.3}Ga_{0.7}N$(11-22) layer, showing an RMS surface roughness about 3.5 nm in an image of 2×2 μm^2, comparable to that of semipolar AlN layers although slightly higher than in the case of semipolar GaN, as described above.

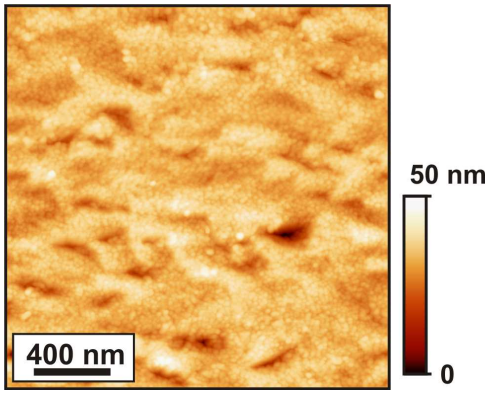

Figure 4.17: AFM image of a 700nm-thick semipolar (11-22) $Al_{0.3}Ga_{0.7}N$ layer.

4.5 Semipolar (11-22) InGaN

In this chapter, I summarize my investigation of the In kinetics during the PAMBE growth of semipolar (11-22) InGaN layers [Das10b]. Indium desorption studies confirm that it is possible to stabilize two monolayers of In on the (11-22) GaN surface, and the limits of this growth window in terms of substrate temperature and In flux lie at the same values for both polar and semipolar material. However, an inhibition of In incorporation is observed in comparison to polar (0001) InGaN.

4.5.1 Temperature calibration

The In mole fraction in the InGaN nanostructures depends critically on the growth temperature [Che01, Lim00, Mon03b]. It is therefore important to establish the reference parameters that guarantee a reasonable reproducibility of the substrate temperature. For the growth of GaN, substrate temperatures in the 700°C to 750°C range are calibrated by the Ga desorption time (see figure 16 in [Kan08]). For incorporation of In, the deposition temperature is reduced below 650°C, so that the Ga desorption rate is negligible. Therefore, I have analyzed the effect of In desorption on the RHEED intensity, to use it as a temperature reference.

Before moving to find the growth temperatures for semipolar InGaN 2D layers, I first considered the case of polar InGaN and analyzed its growth temperature. For that, at a fixed substrate temperature, e.g. T_S = 670°C, we expose the GaN (0001) surface to In during a certain time –long enough to attain a steady-state situation.

When we close the In shutter, we observe a transient variation of the RHEED intensity with a characteristic shape, as described in figure 4.18.

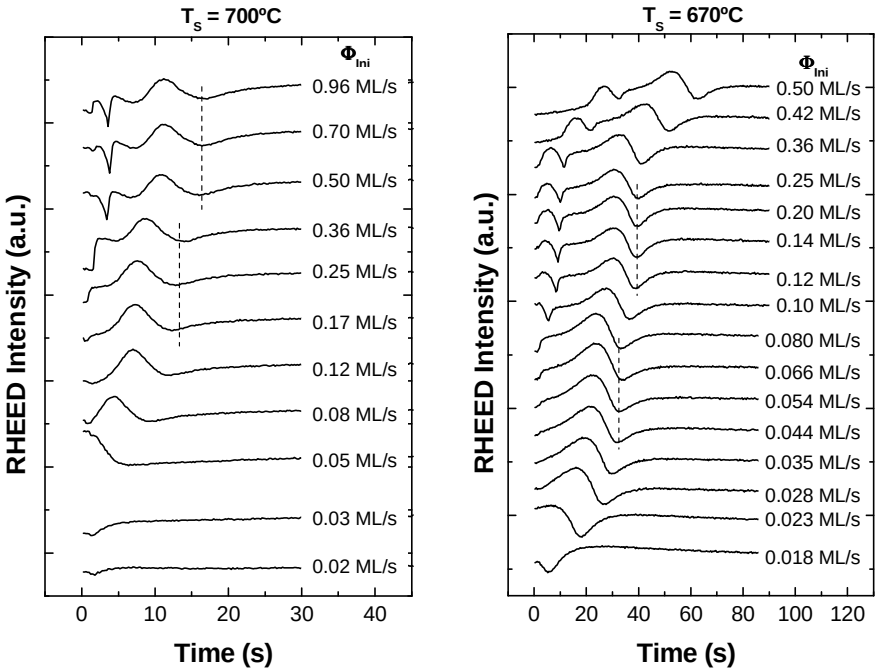

Figure 4.18: Evolution of the RHEED intensity during In desorption from GaN after 1 min exposure to the In flux, measured at substrate temperature T_S = 700°C and T_S = 670°C. The In shutter is closed at t = 0 s. The right column indicates the In flux during In exposure. Dashed lines are eye guides to highlight the stability regions.

In the diagrams in figure 4.18, we can observe the two stability regimes where small changes in the In flux have no effect on the RHEED desorption transient (see, for instance, In fluxes between 0.12 ML/S and 0.25 ML/s in the case of T_S = 670°C). From the length of the desorption time in this stability window, we can determine precisely the substrate temperature, independently of the impinging In flux. To give an idea of the precision of the method, figure 4.19(a) presents the time of the first inflexion point of the In desorption transient (see figure 4.19(b)) as a function of the substrate temperature.

For the determination of the substrate temperature for growth of semipolar InGaN, we included in our sample holder a piece of polar GaN(0001). The length of the RHEED intensity transient during In desorption from this polar GaN was used as a reference.

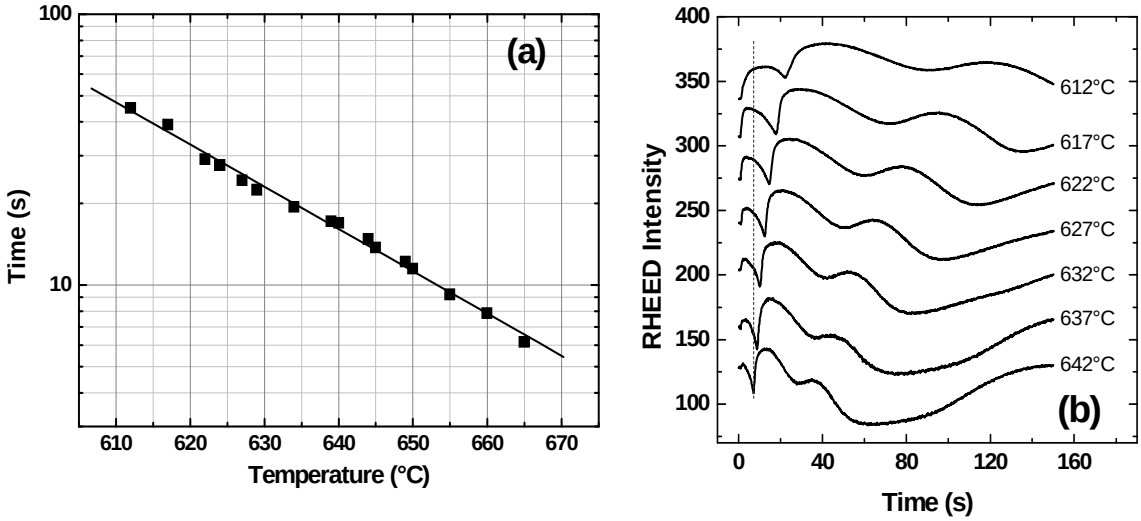

Figure 4.19: (a) Time of the first inflexion point of the In desorption transient as a function of the substrate temperature. The In shutter is closed at t = 0 s. (b) Evolution of the RHEED intensity during the In desorption measured at different substrate temperatures.

4.5.2 In kinetics on semipolar GaN

Keeping in mind that 2D InGaN is synthesized under In-rich conditions, it is important to analyze the wetting of the GaN(11-22) surface with In, to understand the behavior of the In excess during growth. These experiments were performed on a semipolar 125-nm-thick GaN(11-22) layer deposited on a 125-nm-thick AlN(11-22) buffer layer on *m*-sapphire. For comparison purposes, the same experiment was performed on a 100-nm-thick GaN(0001) layer grown on a commercial 4-µm-thick GaN-on-sapphire template. The stability and thickness of the In wetting layer on GaN was evaluated by exposing GaN to the In flux for a certain time, t_{exp}, so that an In film is deposited on the surface. After shuttering the In cell, we record the transient in the RHEED specular beam intensity during In desorption. The duration of the desorption transient is related to the thickness of the original In film. The variation of the RHEED specular intensity during the desorption of In from polar GaN(0001) and semipolar GaN(11-22) was recorded as a function of the impinging In flux, as shown in figure 4.20.

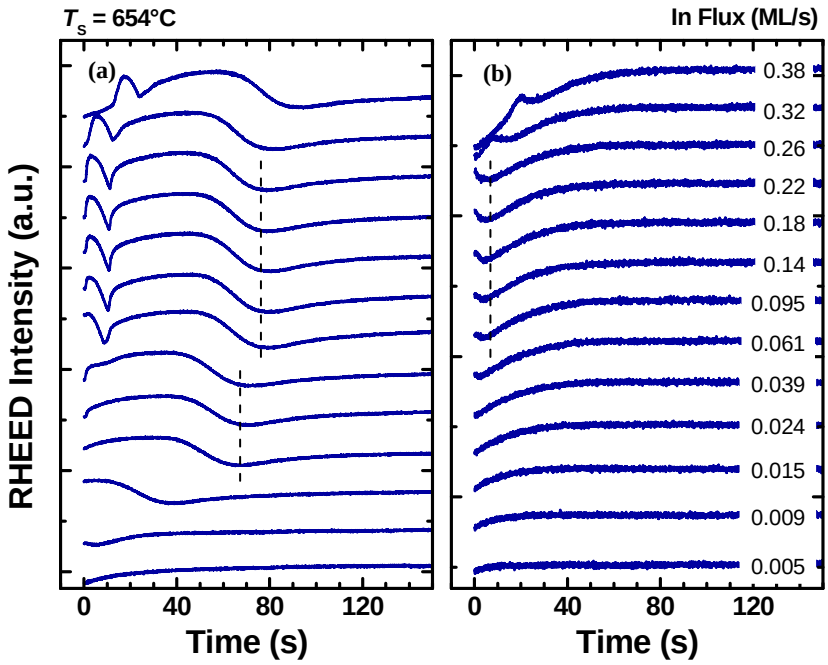

Figure 4.20: Evolution of the RHEED intensity during In desorption from (a) polar and (b) semipolar GaN after 1 min exposure to the In flux, measured at a substrate temperature of 654°C. The In shutter is closed at t = 0 s. Dashed lines indicate the stability windows[Das10b].

In order to guarantee that the desorption process starts from dynamically-stable conditions, the sample was exposed to In for t_{exp} = 1 min. For certain ranges of In fluxes, we can delimit stable regimes where the desorption time (i.e. the In coverage) remains constant (see dashed lines in figure 4.20). At high In fluxes (>0.32 ML/s), the duration of the transient increases rapidly, which is an indication of the accumulation of In forming droplets on the surface.

From the measurements of the desorption transient as a function of the impinging In flux, we can calculate the In coverage on GaN surface [Mon03a]. The variation with time of the In coverage on the sample, $c(t)$, is the difference between the impinging In flux, Φ_{Ini} and the desorption flux, $\Phi_{Ind}(t)$:

$$\partial c(t)/\partial t = \Phi_{Ini} - \Phi_{Ind}(t) \qquad (4.1)$$

The impinging In flux is determined by the temperature of the In cell, *i.e.* it is time independent. On the contrary, the In desorption flux depends on both the substrate temperature and the In coverage, *i.e.* time dependent. In the case of a self-

regulated In film ($c(t)$ = *constant*), the desorption flux is equal to the impinging flux during In exposition:

$$\Phi_{Ind}(t_E \geq t_{S\text{-}R}) = \Phi_{Ini} \tag{4.2}$$

where t_E is the exposure time and t_{S-R} the time necessary to reach the self-regulated regime.

Eq. 4.1 can be expressed as the following equation during In desorption:

$$dc(t) = -\Phi_{Ind}(t)\, dt \tag{4.3}$$

And if the GaN surface is exposed to In flux for a time long enough for the self-regulated In film to be created, *i.e.* $t_E \geq t_{S-R}$, at the moment of shuttering the In cell, we can write:

$$dc(t = 0) = -\Phi_{Ini}\, dt \tag{4.4}$$

For a certain substrate temperature, T_S, and an impinging In flux Φ^j_{Ini}, the In coverage will reach a dynamically stable value, c_j. If we assume that we were in a situation of dynamical equilibrium just before closing the In shutter, *i.e.* $\Phi_{Ind}(t=0) = \Phi_{Ini,}$ and that the In desorption flux, $\Phi_{Ind}(t)$ is only a function of the remaining In coverage, we can approximate Eq.4.4 by

$$c_j = c_{j-1} + \Phi^j_{Ini}(t_{Dj} - t_{Dj-1}) \tag{4.5}$$

where t_{Dj} is the desorption time for an impinging In flux Φ^j_{Ini}. Thus, the total coverage can be obtained from

$$c_j = c_0 + \Sigma\, \Phi^k_{Ini}(t_{Dk} - t_{Dk-1}) \tag{4.6}$$

where c_0 is the In coverage corresponding to the lower flux. In general, we start the measurement with a sufficiently low In impinging flux so that we can assume $c_0 = 0$.

Using Eq. 4.6, I have deduced the In coverage as a function of the In flux for different substrate temperatures, T_S. The results for GaN(0001) and GaN(11-22) at $T_S = 654^oC$ are illustrated in figure 4.21.

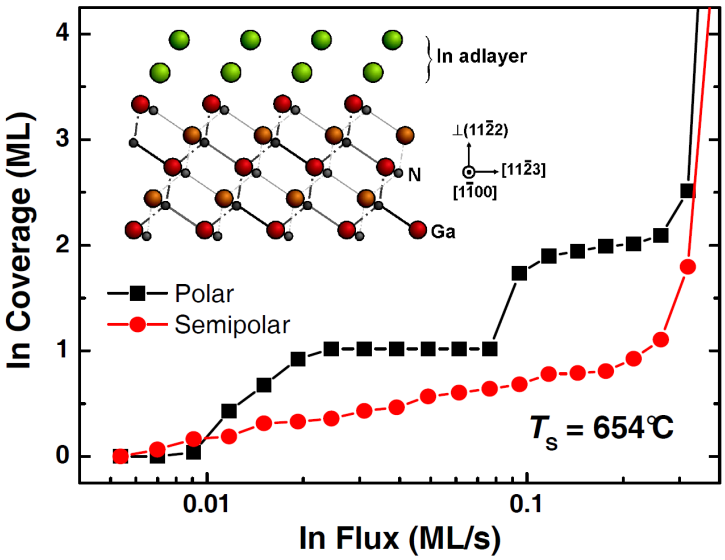

Figure 4.21: In coverage as a function of the impinging In flux, measured on a polar (0001) and semipolar (11-22) GaN layer at 654°C. In the inset, schematic description of the In adlayer on semipolar GaN(11-22)[Das10b].

In the case of GaN(0001), we observe two stable regimes, corresponding to an In coverage of c = 1 ML and $c \sim 2$ ML, in agreement with previous experimental results [Mon03a, Cho08] and *ab initio* calculations [Nor99, Neu03]. In contrast, for the case of GaN(11-22), the In coverage increases gradually with the impinging In flux, reaching a maximum stable coverage of 1 ML before accumulation. It is important to remind that in all these experiments, the In coverage represents an atomic density corresponding to a number of (0001)-oriented monolayers, i.e. 9.2×10^{14} atoms/cm^2 for relaxed InN. On the (11-22) plane, this surface atomic density corresponds to the distribution of the atoms in two layers, as illustrated in the inset of figure 4.21. These results are in excellent agreement with first-principles calculations [Nor09].

4.5.3 Growth details and properties of semipolar InGaN layers

An important result of the above-described measurements is that the range of In fluxes corresponding to the stabilization of 1 ML of In on (11-22)-oriented GaN (0.09 ML/s to 2.3 ML/s for T_S = 654°C in figure 4.21) fits well with the window of 2 ML of In on (0001)-oriented GaN. As a result, InGaN(11-22) and InGaN(0001) are

expected to have compatible growth conditions and simultaneous growth of both orientations should be possible by PAMBE. With this information, semipolar InGaN(11-22) layers were grown on top of a 280-nm-thick GaN(11-22) layer deposited on a 140-nm-thick AlN(11-22) buffer layer on *m*-sapphire. Simultaneously, InGaN(0001) layers were grown on top of 4-µm-thick commercial GaN-on-sapphire templates. The N-limited growth rate was fixed to 0.28 ML/s, i.e. ~250 nm/h. To ensure good reproducibility, the substrate temperature was measured by comparing the duration of the In desorption transient from GaN(0001) for an impinging In flux within the 2 ML stability regime. The Ga flux was fixed to 0.22 ML/s and the substrate temperature was varied from T_S = 616°C to T_S = 685°C. The growth time of the InGaN layer was one hour.

The surface morphology of the growing layers was monitored *in situ* by RHEED and analyzed *ex situ* by AFM, with the results in figure 4.22. Semipolar InGaN(11-22) layers present three-dimensional features with preferential facets whatever the III/V ratio. This faceted growth is attributed to a modification of the surface energy balance in presence of In.

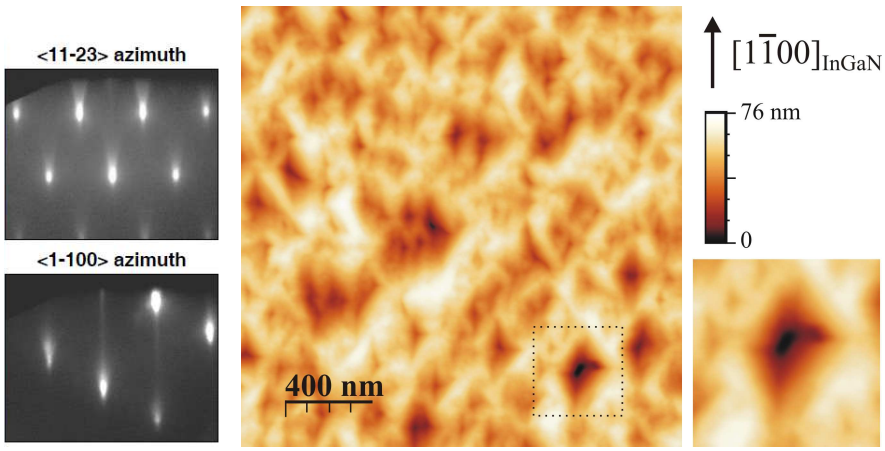

Figure 4.22: AFM image of the surface of ~140 nm thick (11-22) semipolar InGaN showing rhombic and triangular-shaped pits aligned the [1-100] crystallographic direction. The inset on the right is a magnified part of the image showing a pit with the morphology of rhombic inverted pyramid. On the left side, RHEED pattern along the <11-23> and <1-100> azimuths.

SEM images of the surface of the sample are illustrated in figure 4.23, both the AFM and SEM images showing that the surface facets are arranged into pits with a density of approximately 3×10^9 cm^{-2}. The pits had the morphology of inverted rhombic or triangular pyramids with an average diameter of ~200 nm at the surface.

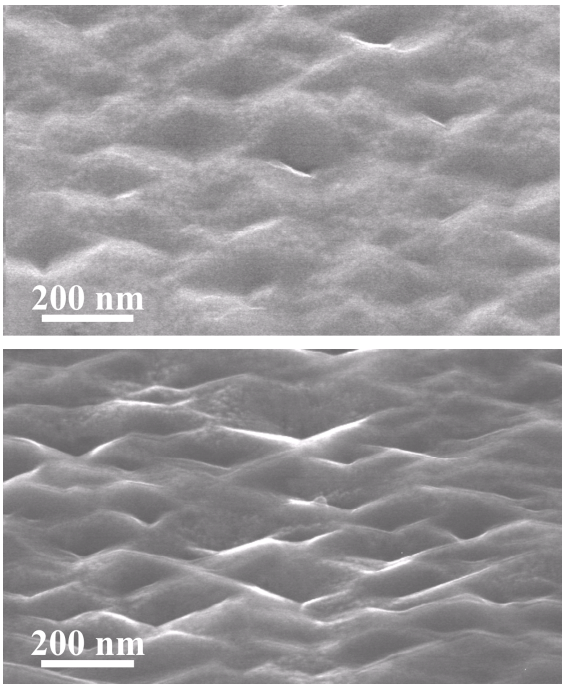

Figure 4.23: SEM images of the surface of ~140 nm thick (1122) semipolar InGaN showing facetted morphology. The facets are arranged in rhombic and triangular- shaped pits that are crystallographically aligned. (Images were recorded at 30 kV using a Hitachi 5000 microscope).

Cross sectional TEM observations were taken by the group of Ph. Komninou at the Aristotle University of Thessaloniki (Greece) in order to obtain a better insight on the 3D morphology of the pits and the related defects [Lot12]. The bright-field (BF) CTEM images from the sample is shown in figure 4.24. The main structural features observed in the TEM images were the TDs that mainly lie on the inclined basal planes and the V-shaped pits on the surface.

In order to elucidate the 3D shape of the facets, crystallographic models were constructed and were checked against the experimental observations (more details about this in [Lot12]). On one side of the rhombic pits the crystallographically equivalent pairs of facets were identified as either {1-101} or {2-201} pyramidal planes. When the pits were trigonal pyramids, these planes were replaced by the *a*-plane (11-20). On the second side of the pits the pair of equivalent facets were of the {1-10*l*} type with $l = 2$ or 3.

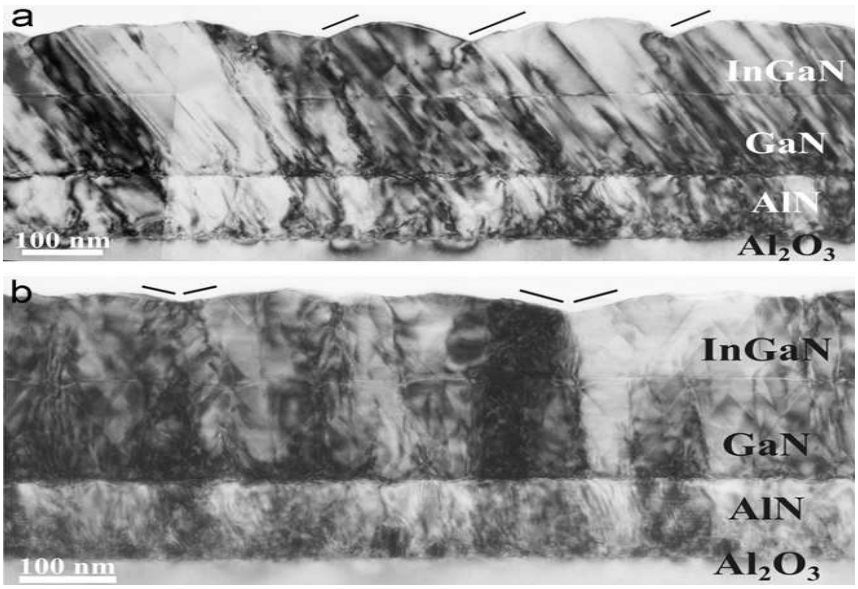

Figure 4.24: (a) Cross-sectional BF CTEM image taken along the [1-100] zone axis. Solid lines indicate (11-20) surface facets viewed edge-on. (b) Cross-sectional BF CTEM image along the [-1-123] zone axis. Solid lines indicate the projections of crystallographically equivalent facets of surface pits.

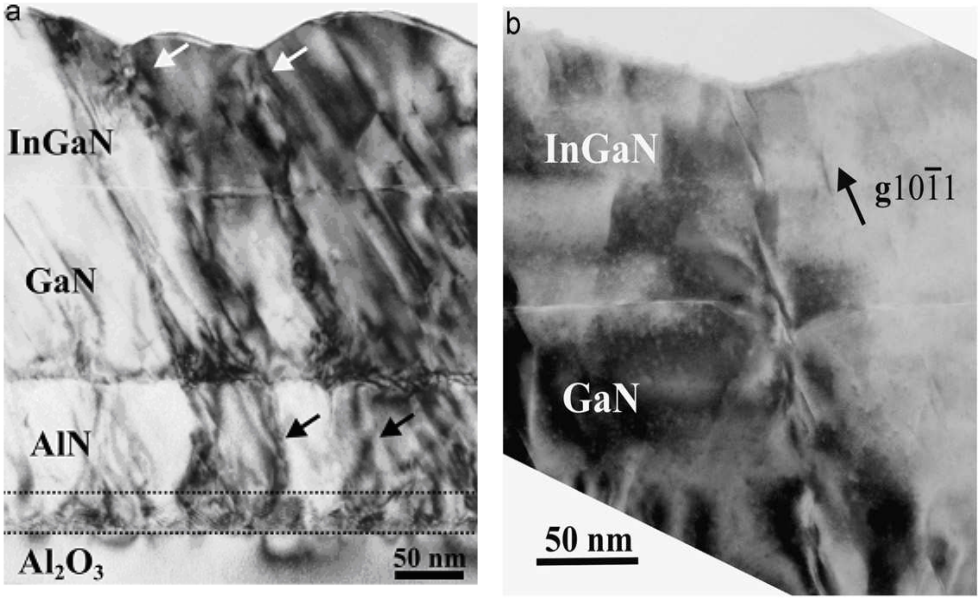

Figure 4.25: (a) Enlarged part of Fig. 4.26 (a), where the nanocrystalline interfacial zone is indicated by the dotted lines, and the arrows show TDs generated from this zone, which propagate upwards towards V-defects. (b)Two beam BF CTEM image taken off the [-1-123] zone axis. A TD is shown to end at the apex of a surface V-defect after crossing the InGaN/GaN interface through an interfacial V-defect.

The cross-sectional CTEM observations showed that the V-defects are connected to threading dislocations (TDs) that either emanate from the rough GaN/AlN interface or from a nanocrystalline interfacial zone at the AlN/sapphire

interface. This is shown in detail in figure 4.25(a) which is a zoomed view of figure 4.24(a). Figure 4.25(b) is a cross sectional CTEM image along [-1-123] showing a TD ending at the apex of a V-defect. These TD that appear systematically associated to the V-shaped pits were identified as mixed-type *a+c* dislocations by Lotsari et al. [Lot12]. In the image, it can be seen that the TD propagates from GaN to the InGaN epilayer through another V-defect at the InGaN/GaN interface. Figure 4.26 illustrates detailed images of the region depicted in figure 4.25(b). When viewed along [-1-123], the line directions of TDs that terminate at V-defects were often found to follow a zig-zag trend forming ~65^{o} angles with the trace of the (11-22) plane as shown in figure 4.26. The zigzag configuration must be attributed to the interaction of the TDs with the multiple prismatic SFs on the {1-210} planes. The interfacial V-defect depicted in the HRTEM image (Figure 4.26) is much more geometric than the surface one, with crystallographically equivalent sharp facets that subtend 26^{o} angles with (11-22), consistent with the (10-11) and (01-11) planes.

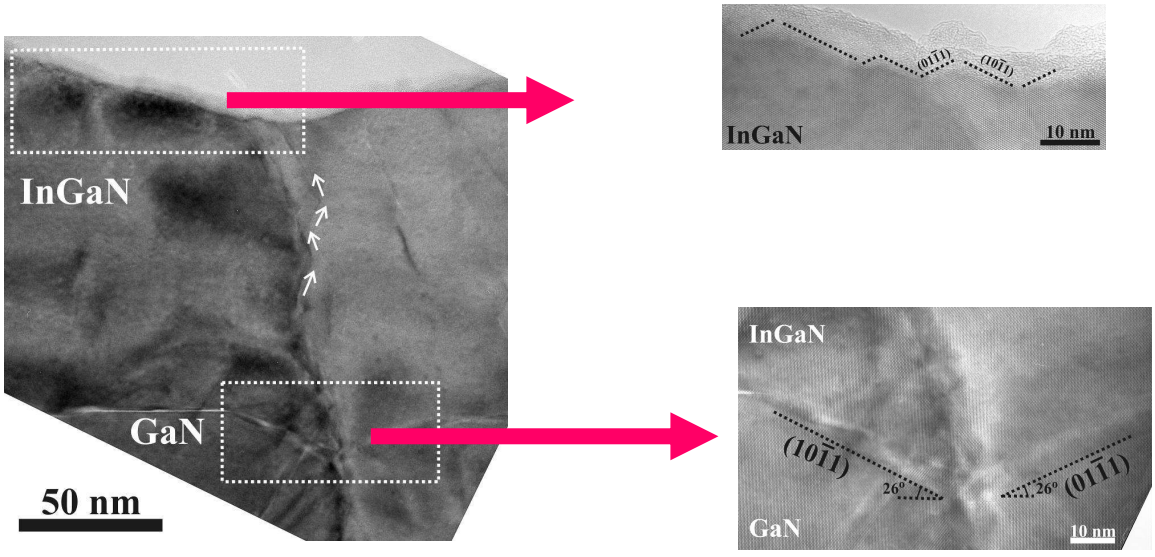

Figure 4.26: Cross sectional HRTEM image along the [-1-123] zon eaxis, showing the area of Fig. 4.25(b) with V-defects at the surface and the InGaN/GaN interface. The line direction of the TD follows a zig-zag mode indicated by white arrows. On the right side bottom one, HRTEM image of the V-defect at the InGaN/GaN interface. Both facets subtend 26^{o}angles with the (11-22) plane, consistent with {10-11} planes.

The alloy composition of the InGaN films was determined by Rutherford Backscattering Spectrometry (RBS) measurements performed by the group of K

Lorenz at the Instituto Tecnológico e Nuclear in Sacavem (Portugal) using a collimated 2 MeV $^4He^+$ ion beam. The detection angle was 140° and the detector resolution was 15 keV. To avoid channeling effects and increase the depth resolution, the samples were tilted 20° off the sample normal. RBS spectra simulations and fitting were performed using the NDF code [Bar97]. Figure 4.27 compares the RBS spectra from the polar and the semipolar InGaN samples grown simultaneously at T_S = 659°C, showing a remarkable difference in In incorporation. In the inset of figure 4.27, we summarize the In mole fraction as a function of the substrate temperature for polar and semipolar samples extracted from simulations of the RBS profiles. In the case of polar samples, the In content at low temperatures remains around 0.20, which indicates that the In incorporation is limited by the Ga flux. When increasing the substrate temperature beyond 670°C, the In mole fraction decreases due to In segregation, in agreement with previous reports. In contrast, in the case of semipolar samples, the In mole fraction remains significantly lower –about 5 times lower for T_S = 649°C, where polar samples have well entered the Ga-limited incorporation regime.

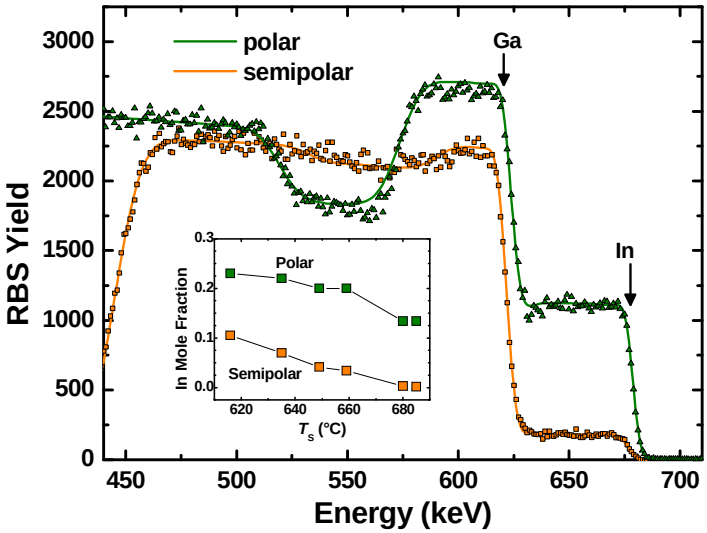

Figure 4.27: Measured and simulated (solid line) RBS spectra of polar and semipolar InGaN layers grown simultaneously at a substrate temperature of 659°C [Das10b].

These results are in good agreement with the optical properties of layers. The low temperature PL spectra from polar and semipolar InGaN layers grown at various substrate temperatures are presented in figure 4.28. The PL from polar InGaN red

shifts for decreasing growth temperature and finally stabilizes around 2.1-2.4 eV, consistent with the measured In mole fraction. Luminescence from semipolar InGaN presents also a considerable red shift for decreasing growth temperature, but the emission is systematically blue shifted in comparison to the respective polar samples grown simultaneously, which is consistent with the difference in In incorporation detected by RBS. This experimental evidence of the inhibition of In incorporation in the (11-22) face by PAMBE is in contradiction with theoretical calculations [Nor09]. Moreover, experimental results by MOVPE showed similar or higher In incorporation in the (11-22) plane compared to the (0001) plane [Kap07, Hir07].

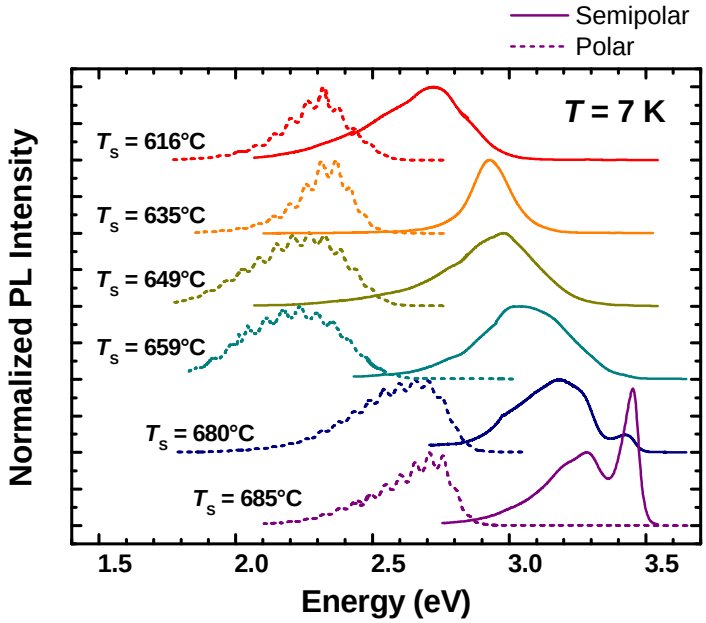

Figure 4.28: Low-temperature (T = 7 K) PL spectra from polar (dashed lines) and semipolar (solid lines) InGaN layers grown at different substrate temperature. The spectra are normalized by the intensity of the InGaN line and vertically shifted for clarity [Das10b].

RBS and PL measurements indicate lower In incorporation in semipolar samples. Low temperature PL measurements showed that, figure 4.28, for incorporating more indium in semipolar layers, it is important to reduce the substrate temperature below 500°C - the growth temperature of InN, where In desorption is negligible- (the next section dealing with the growth of InN).

4.6 Semipolar (11-22) InN

The growth of InN is the most difficult among the III–nitrides because the equilibrium vapor pressure of nitrogen over the InN is several orders higher than AlN and GaN [Amb96]. The low InN dissociation temperature as well as high equilibrium nitrogen vapor pressure over the InN necessitates the use of a low growth temperature for the preparation of InN. In PAMBE growth, optimum growth temperature and indium-to-nitrogen (In/N) flux ratio are the two important parameters that determine the quality of the InN layers.

Before starting to analyze the growth conditions of semipolar (11-22) InN, I first tried to identify reproducible growth parameters of 2D polar (0001) InN. For that, I considered 10-µm-thick GaN (0001)-on-sapphire as a template and the N flux was corresponding to a growth rate of 0.3 ML/s. Prior to calibration of InN growth, I had deposited 10 nm GaN buffer layer at the growth temperature of GaN (T_S ~ 720°C). Then, nitridation was carried out to consume excess gallium, after that the samples were cooled down to T_S = 440-460°C. At this low growth temperature range the desorption rate of In is lower that the decomposition rate of InN. For determining stoichiometric growth condition, I expose the sample surface to In during a certain time (the time of In exposure, t_{In} = 30 s, and during In exposure the RHEED intensity decreases) and after the shuttering the In cell the surface is exposed with nitrogen to consume the deposited In (time of N exposure required to consume the In, t_N).

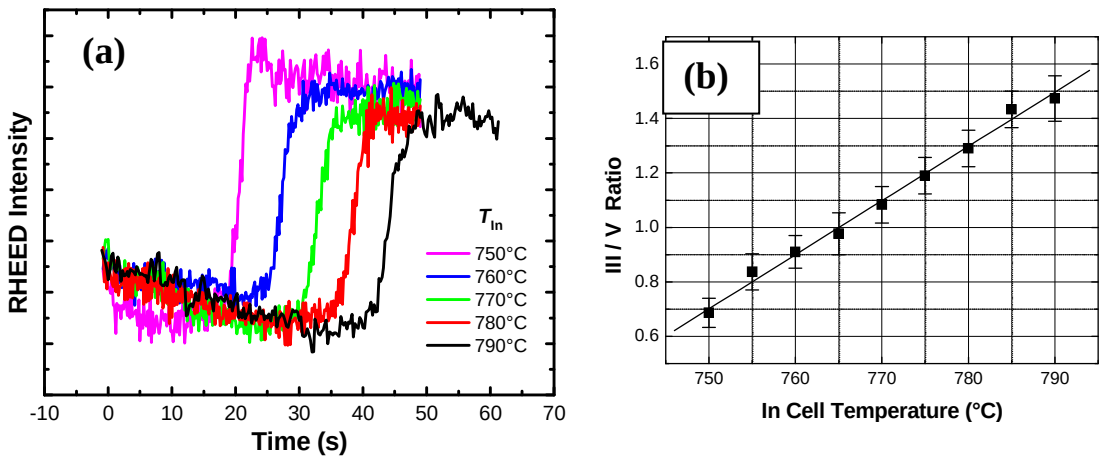

Figure 4.29: (a) Evolution in RHEED intensity during N exposure, time of In exposure was 30s. (b) Calculated In/N ratio as a function of the indium cell temperature.

We can easily identify the changes in the surface during In or N exposure and calculate t_N from the RHEED intensity transient. I repeated this experiment with different In cell temperature (T_{In} = 750-790°C) and systematic changes in RHEED during N exposure is shown in figure 4.29(a). Here, t_N varies between 20 s to 50 s and at a particular cell temperature (in the graph, between 760°C and 770°C) I measure t_N = t_{In}, that is the stoichiometric temperature. From the exposure time, t_N and t_{In}, we can determine precisely the In/N flux ratio, as shown in figure 4.29(b).

I have grown a series of InN layers on GaN (0001) surface. Prior to InN growth, I had deposited 10 nm GaN buffer layer at the growth temperature of GaN (T_S ~ 720°C). InN growth was carried out at a substrate temperature of 450°C, with an In/N ratio of 1.2. This high III/V ratio is required to achieve 2D growth. Since the desorption rate of In is lower that the decomposition rate of InN, it is not possible to stabilize an autoregulated layer of In on the InN surface, as we demonstrated on GaN. Therefore, periodic growth interruptions under N were performed to consume the In excess and prevent the accumulation of In droplets on the surface. At the beginning of the InN growth (~1 ML) the RHEED shows double lines, due to the lattice mismatch between GaN and InN, that giving a clear indication of the immediate InN relaxation when starting the growth. The surface morphology of the InN (1µm thick) was examined by AFM (Figure 4.30(a)). Flat surface morphology with atomic terraces is decorated with a high density of pits.

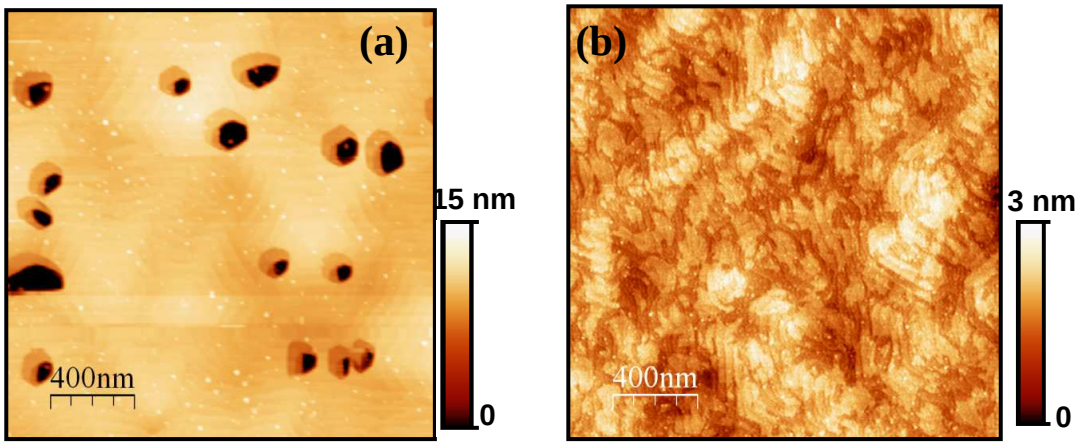

Figure 4.30: (a) AFM images from the 1µm thick InN (0001) layer showing the pits on the surface. (b) Surface morphology of the 1µm thick InN (0001) film grown on GaN(0001) template with InN/InGaN SLs buffer layer.

In the second attempt, for reducing the pit density I had deposited a 10-period $InN/In_{0.7}Ga_{0.3}N$ stack before the growth of 1µm thick InN layer. The AFM image from the sample is shown in figure 4.30(b). The crystalline quality of the InN was investigated by TEM performed by the group of P. Ruterana at ENSICAEN-CNRS, with the result presented in figure 4.31. It shows that the SL buffer layer helps to reduce the density of threading dislocations, which are mostly of edge and mixed type. The fluctuations in strain induced by the alternation of materials in the SL probably force many dislocations to bend, forming segments of misfit dislocations at the $InN/In_{0.7}Ga_{0.3}N$ interfaces. Moreover, they may react and annihilate when bending towards or back the growth direction.

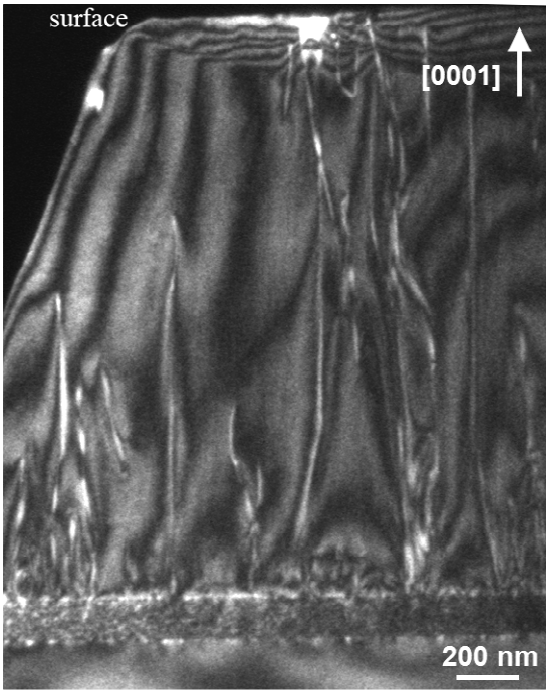

Figure 4.31: Dark field (g=0002) TEM micrograph of the 1-µm-thick polar InN layer grown with a MQW buffer layer.

Using the growth parameters (substrate temperature and III/V ratio) optimized for the (0001) orientation, I have grown a series of semipolar InN layers on GaN (11-22) templates. A polar reference sample is also systematically grown along with the semipolar. The AFM image from a semipolar InN sample is shown in figure 4.32.

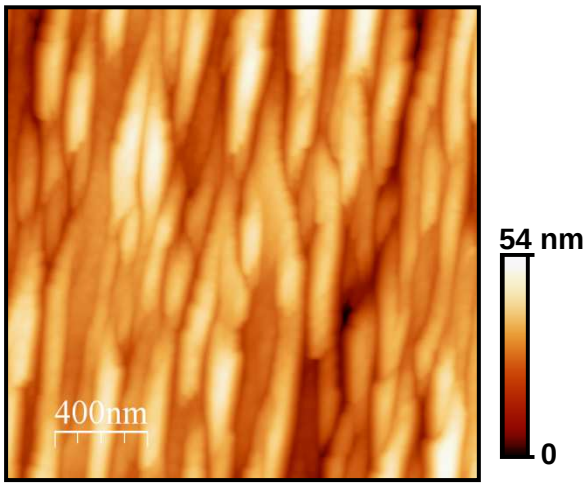

Figure 4.32: AFM images from a 1 μm thick InN (11-22) layers grown on GaN (11-22) template. The rms surface roughness is ~ 9 nm.

Figure 4.33 shows an overall structure of a semipolar InN sample along [1-100]. It can be seen that the film contains high densities of threading dislocations (TDs) and stacking faults (SFs) on the inclined basal planes. The dislocation density is in the 10^{11} cm^{-2} range. Furthermore, the InN/GaN interface exhibits holes. From the zone axis image it is observed that InN exhibits a somewhat smaller defect density compared to GaN, which shows that the InN/GaN interface could act as a potential defect stopper. However, one needs to be very cautious in interpreting this apparent defect reduction since in fact the top InN is more thinned down due to the ion milling leading to an artificial apparent reduction of TD density.

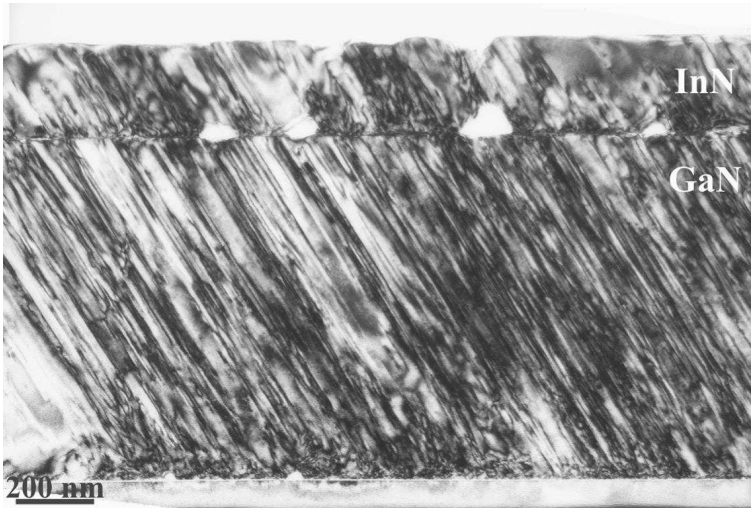

Figure 4.33: CTEM image along the [1-100] zone axis, showing an overall view of the heterostructure. Holes are visible at the InN/GaN interface (TEM images by Prof. Ph. Komninou, Aristotle University of Thessaloniki, Greece).

Two-beam imaging with the g 11-20 reflection close to the [1-100] zone axis did not show significant reduction of TDs in InGaN. However, this lack of observation of TD reduction with the g 11-20 reflection could also be attributed in part to the fact that under this imaging condition the SFs are partially inclined, and thus they are projected as bands which causes an increase of apparent TD density. On the other hand, a rather more noticeable TD reduction was observed in two-beam condition using the g 0002 reflection (Figure 4.34). This could signify that the InGaN/GaN interface is more effective in stopping TDs with a Burgers vector component along the c-axis. This includes also the 1/6<20-23> partial dislocations that delimit the I_1 basal stacking faults. Going to a larger magnification, it can be seen in figure 4.35 that in many circumstances the GaN TDs bended, probably on {11-20} prismatic planes, when crossing the InN/GaN interface and then re-acquired their orientation along the basal plane inside the InN material.

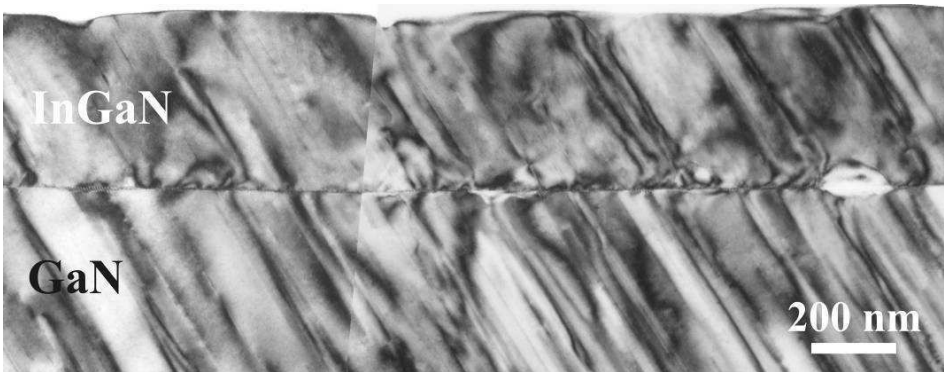

Figure 4.34: CTEM image close to the [1-100] zone axis under 2-beam conditions, using g 0002. TDs with c Burgers vector components are visible. The TD density appears to be reduced to some extent after crossing the InN/GaN interface (TEM images by Prof. Ph. Komninou, Aristotle University of Thessaloniki, Greece).

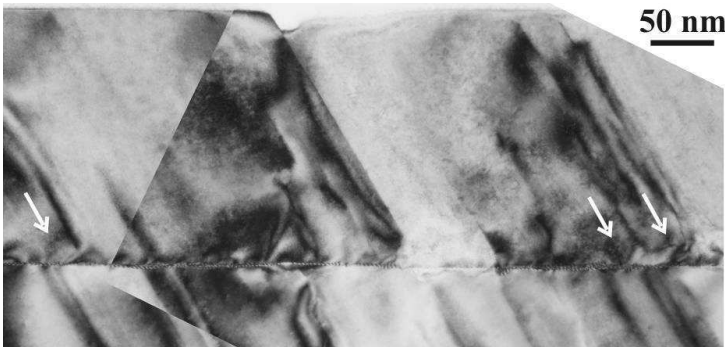

Figure 4.35: Larger magnification CTEM image taken close to the [1-100] zone axis under 2-beam conditions, using g 0002. Some TDs (arrowed) are seen to bend upon crossing the interface. (TEM images by Prof. Ph. Komninou, Aristotle University of Thessaloniki, Greece).

Overall it can be concluded that the InN/GaN interface appears to stop some of the TDs but its influence is not crucial under the given growth conditions. HRTEM showed an abrupt InN/GaN interface with a regular periodicity of misfit dislocations. Figure 4.36 includes a 2D map of the misft strain along [0001] obtained from the InN/GaN interface using geometrical phase analysis (GPA), as well as the corresponding Bragg filtered HRTEM image. The mismatch in the c-lattice constant was ~10% using as GaN as reference, as expected for relaxed InN. The arrows in the Bragg image indicate position of extra half planes introduced. The average spacing of misfit dislocations was ~11 GaN (0002) planes (or ~2.85 nm).

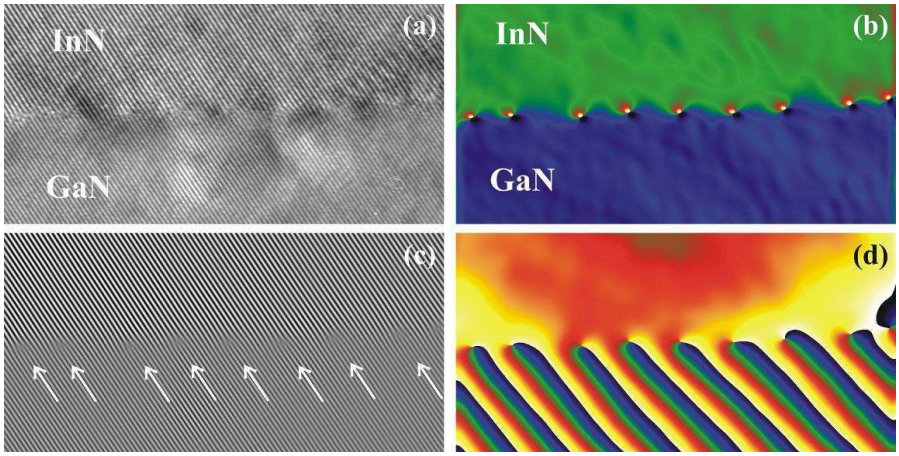

Figure 4.36: (a) Cross sectional HRTEM image of the InN/GaN interfacial region. (b) Corresponding map of the misfit along [0001], showing the strain component of misfit dislocations. (c) Bragg filtered image of (0002) lattice fringes corresponding to (a). The positions of (0002) extra half planes are indicated by arrows. (d) Corresponding GPA phase map showing phase variations due to the positions of the misfit dislocations.

From the HRTEM analysis it was found that the InN/GaN interface sometimes exhibits roughening manifested by moiré fringes. On such holes, misoriented nanocrystalls could be nucleated, as shown in figure 4.37(a), and these act as defect sources. The presence of roughness and v-shaped formations at the interface (Figure 4.37(b)) could be attributed to the pre-existing defects in the GaN template as well as possibly to the MBE GaN interlayer. In v-defects it was found that one of the facets is aligned with the (0002) basal planes and the other projected facet is almost perpendicular to them.

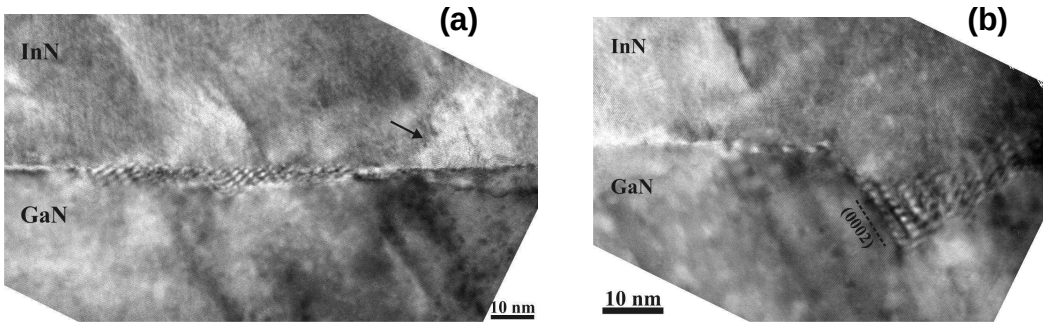

Figure 4.37: (a) HRTEM image along [1-100] from the InN/GaN interfacial region, showing an area which exhibits moiré fringes due to the interfacial roughness. The black arrow indicates an area with misoriented InN nanocrystals nucleated on a defected interfacial region.(b) HRTEM image from the InN/GaN interface where a v-shaped pit is formed.One facet is aligned with the basal planes while the other appears to be perpendicular to them. (TEM images by Prof. Ph. Komninou, Aristotle University of Thessaloniki, Greece).

The low-temperature (T = 7 K) PL spectra from semipolar and polar InN layers, grown simultaneously, is shown in figure 4.38.

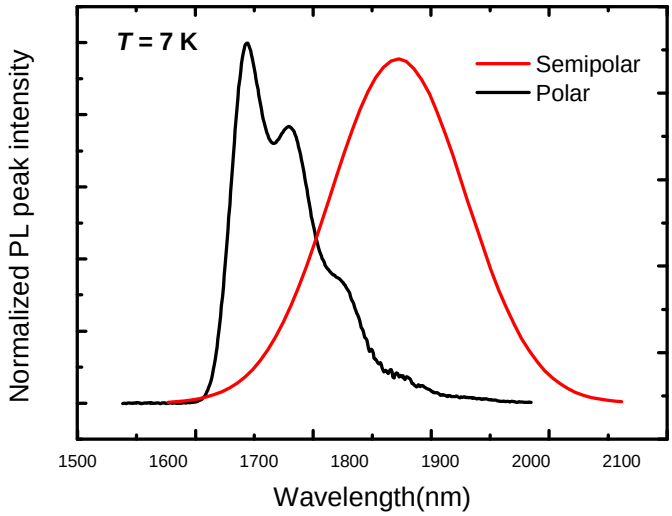

Figure 4.38: Normalized low-temperature (T = 7 K) PL spectra from polar and semipolar InN layers.

Figure 4.39(a) compares the thermal evolution of the PL intensity in the case of polar and semipolar InN layers grown simultaneously. It is observed from the graph that the PL intensity of polar layer drops fast compared to semipolar, *i.e.* the improved thermal stability of semipolar InN layer over polar InN.

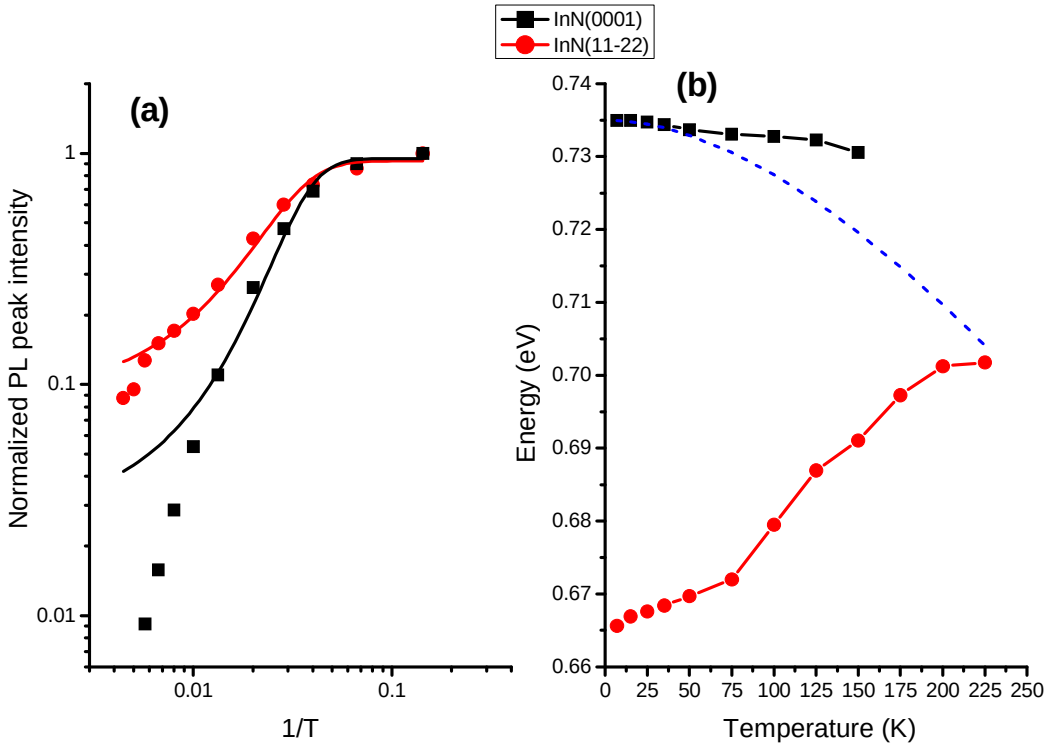

Figure 4.39: (a) Temperature evolution of the PL intensity of polar and semipolar InN layers. Solid lines correspond to fits to equation (4.9). (b) Temperature dependence of the PL peak position for polar and semipolar InN layers. The dotted line represents the evolution expected applying Varshni's equation to InN.

To interpret the variation of the PL intensity with temperature, we must keep in mind that the recombination efficiency (*RE*) can be written as:

$$RE = \frac{R_R}{R_R + R_{NR}} = \frac{1}{1 + \frac{R_{NR}}{R_R}} \tag{4.7}$$

Here, R_R and R_{NR} denote radiative and non-radiative recombination rates, respectively. Making use of simple rate equations [Ler99] under (optical) injection

$$\frac{\partial n}{\partial t} = G - \frac{n}{\tau_R} - \frac{n}{\tau_{NR}} \tag{4.8}$$

where n is the minority carrier or exciton density concerned, G the generation rate, and τ_R and τ_{NR} the radiative and non-radiative lifetimes respectively. Considering that nonradiative recombination centers are thermally activated, i.e. $\tau_{NR} = \tau_0 e^{E_a/kT}$, and that the steady-state population of minority carriers governs the PL intensity (i. e. $I_{PL} \propto n/\tau_R$) we arrive to the expression:

$$RE = \frac{1}{1 + ae^{-E_a / kT}} \tag{4.9}$$

where $a = \tau_R / \tau_0$. Thus, the recombination efficiency at low temperature should be close to unity ($RE(0)$~1), whereas at high temperature it is expected to be lower ($RE(T)$<1).

From the fit of figure 4.39(a) to equation (4.9), we can calculate activation energies (E_a) and the prefactors associated to the nonradiative-to-radiative recombination ratio (a). The obtained values for semipolar and polar InN layers are E_a = 9±1 meV, a = 10±2 and E_a = 10±1 meV, a = 37±10 respectively. Thus, the activation energies are similar, but the nonradiative recombination paths are less efficient in the semipolar material, with a lower value of a.

Figure 4.39(b) presents the evolution of the PL peak energy as a function of temperature in the cases of polar and semipolar layers. The evolution of the PL peak energy of the polar sample does not follow Varshni's equation for InN (Eq. 2.3 in chapter 2 with α = 0.414 meV/K and β = 454 K, dashed curve in figure 4.39(b)), which can be attributed to potential fluctuation associated to structural defects, and to many-body effects due to the high residual doping ($n \sim 10^{19}$ cm^{-3}). The deviation from Varshni's equation is particularly dramatic in the semipolar layer, with a higher density of defects, particularly stacking faults.

4.7 Conclusions

In conclusion, semipolar (11-22) oriented AlN, GaN, InN, AlGaN and InGaN 2D layers have been synthesized by PAMBE. AlN deposited on *m*-sapphire arranges into two main crystalline orientation domains, AlN(11-22) and AlN(10-10): The ratio of (10-10)-oriented domains decreases with the III/V ratio and with the layer thickness. I have demonstrated that the nucleation of AlN(10-10) appears associated to v-defects at the sapphire substrate, which seem to be related to a reaction with AlN, which is enhanced by starting the growth with N exposure.

Regarding semipolar GaN growth, the comparison of Ga desorption during the growth of undoped, Si-doped and Mg-doped GaN(11-22) layers revealed that Si

doping does not change the growth kinetics. Whereas during Mg doping, Mg tends to segregate on the GaN surface, leading to an inhibition of the self-regulated Ga film which is used as a surfactant for the growth of undoped and Si-doped semipolar GaN. Uniform Mg incorporation up to [Mg] = $1.0x10^{20}$ cm^{-3} is obtained, and *p*-type conductivity was found for [Mg] $\geq$ $7x10^{18}$ cm^{-3}. From the estimation of Mg concentration and its dependence on the substrate temperature and the impinging Ga flux, we found that its incorporation is enhanced in GaN(11-22) compared to GaN(0001). TEM shows no evidence of the pyramidal defects or polarity inversion domains that can be found Mg-doped GaN(0001), in agreement with the interpretation of the photoluminescence spectra.

I have synthesized semipolar (11-22) AlGaN layers to find their optimum growth conditions and to compare the properties with polar layers. The studies showed that simultaneous growth of the polar and semipolar AlGaN layers is not practicable, since it results in accumulation of Ga droplets at the semipolar growth front. It is hence necessary to reduce the III/N ratio in comparison to polar AlGaN, although maintaining III/N > 1. Under these growth conditions, I have demonstrated semipolar 700-nm-thick AlGaN samples displaying narrow band-edge PL emission and with a surface roughness about 3.5 nm.

I have also studied the In kinetics during the PAMBE growth of InGaN (11-22) layers. Similarly to (0001)-oriented InGaN, optimum growth conditions for this semipolar crystallographic orientation correspond to the stabilization of 2 ML of In on the growing InGaN surface, in excellent agreement with first-principles calculations. The limits of the growth window in terms of substrate temperature and In flux lie at same values for polar and semipolar materials. However, the In incorporation is different for polar and semipolar layers grown simultaneously. In polar samples, the In incorporation is limited by the Ga supply at low temperature, and decreases for growth temperatures higher than a certain threshold due to In segregation. In semipolar samples, RBS and PL measurements indicate lower In incorporation, even for substrate temperatures 40 °C below the segregation threshold for polar InGaN. Semipolar InGaN layers present a characteristic surface morphology with a high density of faceted pits, which are associated to mixed-type *a*+*c* threading dislocations.

I have analyzed the growth parameters and properties of semipolar InN layers. Two-dimensional layers are obtained by growth under In excess with periodic growth interruptions to consume with nitrogen the In excess. These growth conditions are compatible with the synthesis of two-dimensional polar InN layers. Optical studies shows better thermal stability of the luminescence of semipolar layers compared to polar InN.

Bibliography

[Amb96] O. Ambacher, M. S. Brandt, R. Dimitrov, T. Metzger, M. Stutzmann, R. A. Fischer, A. Miehr, A. Bergmajer, and G. Dollinger, *Thermal stability and desorption of Group III nitrides prepared by metal organic chemical vapor deposition*. Journal of Vacuum Science Technology B 14, 3532 (1996).

[Bar97] N. P. Barradas, C. Jeynes, and R. P. Webb, *Simulated annealing analysis of Rutherford backscattering data.* Applied Physics Letters 71, 291 (1997).

[Che01] H. Chen, R.M. Feenstra, J.E. Northrup, J. Neugebauer, and D.W. Greve, *Indium incorporation and surface segregation during InGaN growth by molecular beam epitaxy: experiment and theory*. MRS Internet Journal of Nitride Semiconductor Research 6, U1-U12 (2001).

[Cho08] S. Choi, T.-H. Kim, S. Wolter, A. Brown, H. O. Everitt, M. Losurdo, and G. Bruno, *Indium adlayer kinetics on the gallium nitride (0001) surface: Monitoring indium segregation and precursor-mediated adsorption.* Physical Review B 77, 115435 (2008).

[Das10] A. Das, L. Lahourcade, J. Pernot, S. Valdueza-Felip, P. Ruterana, A. Laufer, M. Eickhoff, and E. Monroy, *P-type doping of semipolar GaN(1122) by plasma-assisted molecular-beam epitaxy*. Phys. Stat. Sol. (c) 7, pp. 1913-1915 (2010)

[Das10b] A. Das, S. Magalhaes, Y. Kotsar, P. K. Kandaswamy, B. Gayral, K. Lorenz, E. J. C. Alves, P. Ruterana, and E. Monroy, *Indium kinetics during the plasma-assisted molecular-beam epitaxy of semipolar (11-22) InGaN layers*. Applied Physics Letters 96, 181907 (2010)

[Guh97] S. Guha, N. A. Bojarczuk, and F. Cardone, *Mg in GaN: Incorporation of a volatile species at high temperatures during molecular beam epitaxy.* Applied Physics Letters 71, 1685 (1997).

[Hau02] E. Haus, I. P. Smorchkova, B. Heying, P. Fini, C. Poblenz, T. Mates, U. K. Mishra, and J. S. Speck, *The role of growth conditions on the p-doping of GaN by plasma-assisted molecular beam epitaxy.* Journal of Crystal Growth 246, 55 (2002).

[Hir07] A. Hirai, Z. Jia, M. C. Schmidt, R. M. Farrell, S. P. DenBaars, S. Nakamura, J. S. Speck and K. Fujito, *Formation and reduction of pyramidal hillocks on m-plane {1-100} GaN.* Applied Physics Letters 91, 191906 (2007).

[Kan08] P. K. Kandaswamy, F. Guillot, E. Bellet-Amalric, E. Monroy, L. Nevou, M. Tchernycheva, A. Michon, F. H. Julien, E. Baumann, F. R. Giorgetta, D. Hofstetter, T. Remmele, M. Albrecht, S. Bilner, and Le Si Dang, *GaN/AlN short-period superlattices for intersubband optoelectronics: A systematic study of their epitaxial growth, design and performance*. Journal of Applied Physics 104, 093501 (2008).

[Kap07] M. J. Kappers, J. L. Hollander, C. McAleese, C. F. Johnston, R. F. Broom, J. S. Barnard, M.E. Vickers, and C. J. Humphreys, *Growth and characterisation of semi-polar (11-22) InGaN/GaN MQW structures.* Journal of Crystal Growth 300, 155 (2007).

[Lah07] L. Lahourcade, E. Bellet-Amalric, E. Monroy, M. Abouzaid and P. Ruterana, *Plasma-assisted molecular-beam epitaxy of AlN(112) on m sapphire.* Applied Physics Letters 90, 131909 (2007).

[Lah08] L. Lahourcade, J. Renard, B. Gayral, E. Monroy, M. Chauvat, and P. Ruterana, *Ga kinetics in plasma-assisted molecular-beam epitaxy of GaN(11-22): Effect on the structural and optical properties*. Journal of Applied Physics 103, 093514 (2008).

[Lah09] L. Lahourcade, J. Pernot, A. Wirthmüller, M. P. Chauvat, P. Ruterana, A. Laufer, M. Eickhoff, and E. Monroy, *Mg doping and its effect on the semipolar GaN(11-22) growth kinetics.* Applied Physics Letters 95, 171908 (2009).

[Lah09b] L. Lahourcade, *Plasma-assisted molecular beam epitaxy of (11-22)-oriented III-nitrides.* PhD Thesis. CEA-Grenoble / École Nationale Supérieure de Physique de Grenoble. Grenoble, 2009.

[Ler99] M. Leroux, N. Grandjean, B. Beaumont, G. Nafat, F. Semond, J. Massies, and P. Gibart, *Temperature quenching of photoluminescence intensities in undoped and doped GaN*. Journal of Applied Physics 86, 3721 (1999).

[Lil99] Z. Liliental-Weber, M. Benamara, W. Swider, J. Washburn, I. Grzegory, S. Porowski, D. J. H. Lambert, C. J. Eiting, and R. D. Dupuis, *Mg-doped GaN: Similar defects in bulk crystals and layers grown on Al2O3 by metal–organic chemical-vapor deposition.* Applied Physics Letters 75, 4159 (1999).

[Lim00] A. P. Lima, C. R. Miskys, U. Karrer, O. Ambacher, A. Wenzel, B. Rauschenbach, and M. Stutzmann, *Growth of quaternary AlInGaN/GaN heterostructures by plasma-induced molecular beam epitaxy.* Journal of Crystal Growth 220, 341 (2000)

[Lot12] A. Lotsari, A. Das, Th. Kehagias, Y. Kotsar, E. Monroy, Th. Karakostas, P. Gladkov, Ph. Komninou, and G.P. Dimitrakopulos, *Morphology and origin of V-defects in semipolar (11-22) InGaN*. Journal of Crystal Growth 339, 1 (2012)

[Min02] M. S. Minsky, S. Watanabe, and N. Yamada, *Radiative and nonradiative lifetimes in GaInN/GaN multiquantum wells.* Journal of Applied Physics 91, 5176 (2002).

[Mon03a] E. Monroy, B. Daudin, E. Bellet-Amalric, N. Gogneau, D. Jalabert, F. Enjalbert, J. Brault, J. Barjon, and Le Si Dang, *Surfactant effect of In for AlGaN growth by plasma-assisted molecular beam epitaxy.* Journal of Applied Physics 93, 1550 (2003)

[Mon03b] E. Monroy, N. Gogneau, D. Jalabert, E. Bellet-Amalric, Y. Hori, F. Enjalbert, Le Si Dang, and B. Daudin, *In incorporation during the growth of quaternary III-nitride compounds by plasma-assisted molecular beam epitaxy.* Applied Physics Letters 82, 2242 (2003).

[Mon04a] E. Monroy, T. Andreev, P. Holliger, E. Bellet-Amalric, T. Shibata, M. Tanaka, and B. Daudin, *Modification of GaN(0001) growth kinetics by Mg-doping*. Applied Physics Letter 84, 2554 (2004).

[Mon04b] E. Monroy, M. Hermann, E. Sarigiannidou, T. Andreev, P. Holliger, S. Monnoye, H. Mank, B. Daudin, and M. Eickhoff, *Polytype transition of N-face GaN:Mg from wurtzite to zinc-blende*. Journal of Applied Physics 96, 3709 (2004).

[Neu03] J. Neugebauer, T. K. Zywietz, M. Scheffler, J. E. Northrup, H. Chen, and R. M. Feenstra, *Adatom Kinetics On and Below the Surface: The Existence of a New Diffusion Channel.* Physical Review Letters 90, 056101 (2003).

[Nor05] J. E. Northrup, *Effect of magnesium on the structure and growth of GaN(0001).*Applied Physics Letters 86, 122108 (2005).

[Nor09] J. E. Northrup, *GaN and InGaN(11-22) surfaces: Group-III adlayers and indium Incorporation.* Applied Physics Letters 95, 133107 (2009).

[Nor99] J. E. Northrup and J. Neugebauer, *Indium-induced changes in GaN(0001) surface morphology.* Physical Review B 60, R8473 (1999).

[Pot00] V. Potin, P. Ruterana, and G. Nouet, *HREM study of stacking faults in GaN layers grown over sapphire substrate.* Journal of Physics: Condensed Matter 12, 10301(2000).

[Pta01] A. J. Ptak, T. H. Myers, L. T. Romano, C. G. Van de Walle, and J. E. Northrup, *Magnesium incorporation in GaN grown by molecular-beam epitaxy.* Applied Physics Letters 78, 285 (2001).

[Qu03] B. Z. Qu, Q. S. Zhu, X. H. Sun, S. K. Wan, Z. G. Wang, H. Nagai, Y. Kawaguchi, K. Hiramatsu, and N. Sawaki, *Photoluminescence of Mg-doped GaN grown by metalorganic chemical vapor deposition* . Journal of Vacuum Science and Technology A 21, 838 (2003).

[Ram99] V. Ramachandran, R. M. Feenstra, W. L. Sarney, L. Salamanca-Riba, J. E. Northrup, L. T. Romano, and D. W. Greve, *Inversion of wurtzite GaN(0001) by exposure to magnesium.* Applied Physics Letters 75, 808 (1999).

[Ven03] P. Vennéguès, M. Leroux, S. Dalmasso, M. Benaissa, P. De Mierry, P. Lorenzini, B. Damilano, B. Beaumont, J. Massies, and P. Gibart, *Atomic structure of pyramidal defects in Mg-doped GaN.* Physical Review B 68, 235214 (2003).

Chapter 5

Polar and semipolar (In)GaN QDs

This chapter focuses on the study of (In)GaN QDs, which is needed for the fabrication of the opto-chemical transducers. The first sections deal with the growth and characterization of polar and semipolar GaN/AlN QDs. Then I present my contribution to the domain of InGaN/GaN QDs, starting with the description of the synthesis and optical performance of the polar InGaN QDs in comparison with polar InGaN/GaN QWs. After that, I will describe the growth and properties semipolar InGaN QDs.

5.1 III-Nitride quantum dots

Semiconductor QDs are nanostructures where the 3D confinement of carriers results in a discrete energetic spectrum. The recent explosion of interest in QDs stems from their unique physical properties, which have led to devices such as low-threshold lasers [Ara82, Str06] and improved-performance intraband detectors [Hof10], in addition to other exciting physical phenomena like the generation of single and entangled photons [Ste06] or coherent manipulation of a quantum bit for quantum information processing [Li03]. QDs are interesting active objects for light-emitting devices, since they present enhanced stability against thermal perturbations due to the fact that the electronic states are spatially localized and the energy is fully quantized. In addition, the electronic density of states near the band gap is higher than in 3D and 2D systems, leading to a higher probability for optical transitions. Furthermore, the electron localization may dramatically reduce the scattering of electrons by bulk defects. So these nanostructures can play an important role in improving the performance of the device when incorporated in the active region. The HRTEM images in figure 5.1 illustrate the structural difference between GaN/AlN QW and QD superlattices.

I have already discussed (see section 1.3 in chapter 1) that for the realization of nano-optical chemical sensor, we need to use (In)GaN quantum dots as opto-chemical transducers for the detection of the pH-value in fluids and/or of hydrogen and hydrocarbon species in the gas phase. That is, to attain this goal, it is necessary to

investigate first the growth characteristics of III-N QDs, which will be the focus of this chapter.

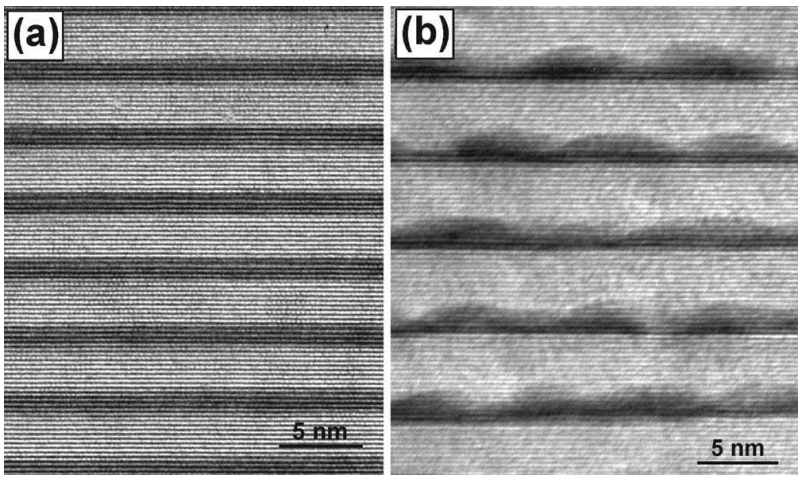

Figure 5.1: HRTEM images of GaN/AlN (a) QWs and (b) QD superlattices.

5.2 Polar GaN/AlN quantum dots

Dr. Prem Kumar Kandaswamy synthesized these QD samples as a part of his Ph.D. work. I summarize his studies in this section along with my contribution to the optical (PL) and structural (AFM) characterization of the samples, in collaboration with Dr. Gačević [Gač11].

The synthesis of GaN/AlN QDs can be performed by two methods: either by GaN deposition under N-rich conditions [Gui06] or by GaN deposition under Ga-rich conditions followed by a growth interruption [Gog03]. In both cases, GaN QDs are hexagonal truncated pyramids with {1-103} facets, and no Ga-Al interdiffusion has been observed. The application of N-rich growth implies a reduction of the mobility of the adsorbed species during growth that results, in general, in a high density (10^{11}-10^{12} cm^{-2}) of small QDs (1-2 nm high). On the contrary, Ga-rich conditions enhance the adatom mobility, leading to lower QD density (10^{10}-10^{11} cm^{-2}) and bigger QDs (2-5 nm high). The difference between these growth techniques is illustrated by the AFM images in figure 5.2.

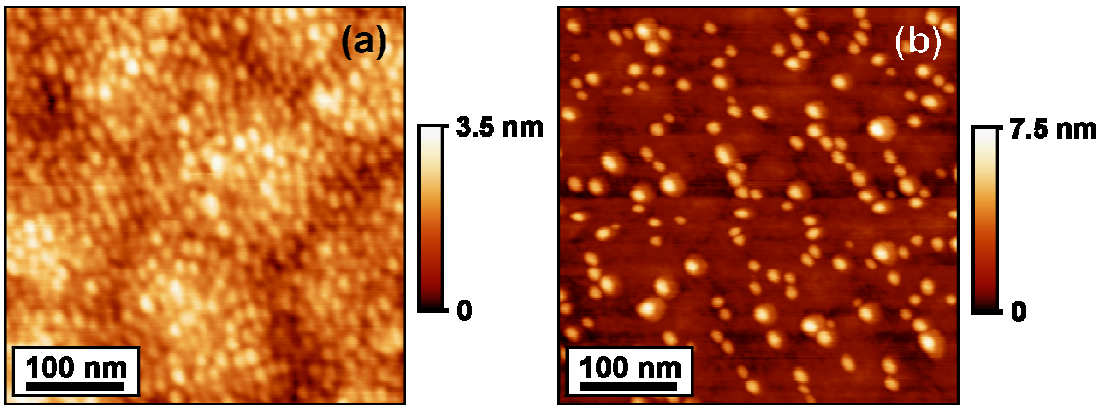

Figure 5.2: Typical AFM images of GaN QDs grown under (a) N-rich conditions and (b) Ga-rich conditions.

The photoluminescence linewidth of a QD stack depends not only on the lateral homogeneity of the QDs but also on the parameter fluctuations along the vertically stacked layers. Two relevant parameters that might cause vertical inhomogeneities are the strain-induced vertical alignment of the QDs, and the strain relaxation along the structure by introduction of misfit dislocations. Vertical alignment of the QDs is attributed to the local strain induced in the AlN matrix by the presence of dots [Sar05], in agreement with the model by Tersoff et al. [Ter96]. Studies of vertically-correlated GaN/AlN QD stacks reveal an evolution of the island dimension with increasing number of periods (decrease of the height, increase of the diameter, reduction of the density), which results in a red shift and narrowing of the photoluminescence [Gog04]. However, in the precise case of the application to opto-chemical sensors, the structures will consist in only 3-5 QD stacks. Therefore, the vertical correlation trend has no time to get fully established and it would contribute to increase the size dispersion.

In order to access the vertical arrangement of the QD layers in the cases of N-rich and Ga-rich growth, samples were analyzed by HRTEM. Figure 5.3 presents typical micrographs of N-rich GaN QDs, where no vertical correlation of the QDs is observed. This is due to the small size and high density of QDs, so that the strain in the AlN is relatively homogeneous. In contrast, in the case of growth under Ga-rich conditions (Figure 5.4), the vertical correlation of the QDs is favored by their larger size and lower density.

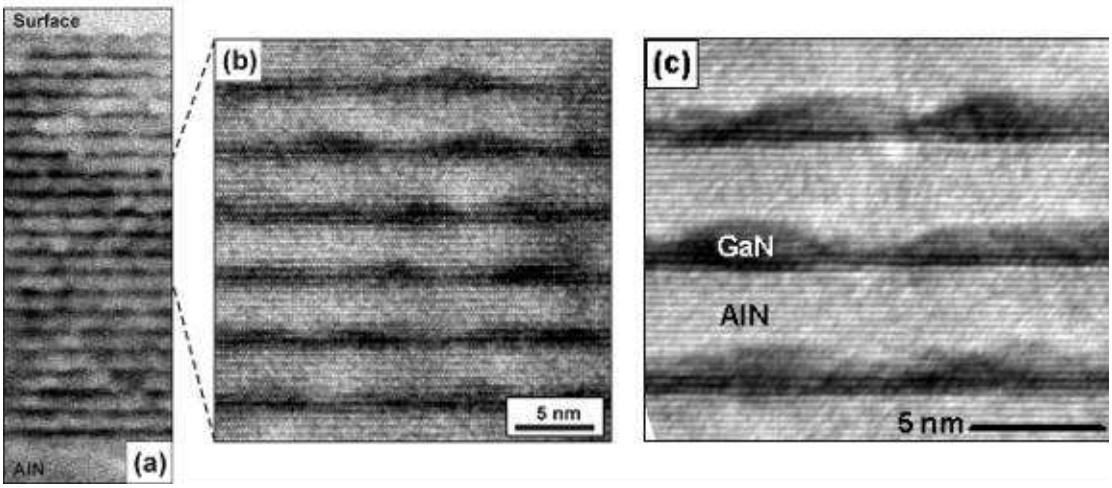

Figure 5.3: (a) Conventional bright-field TEM image of a N-rich grown GaN/AlN QD stack. No vertical alignment of the QDs can be observed (b) and (c) HRTEM image following the [2-1-10] axis and the [1-100] axis, respectively (HRTEM images by Dr. E. Sarigiannidou, CEA/INAC/SP2M, France).

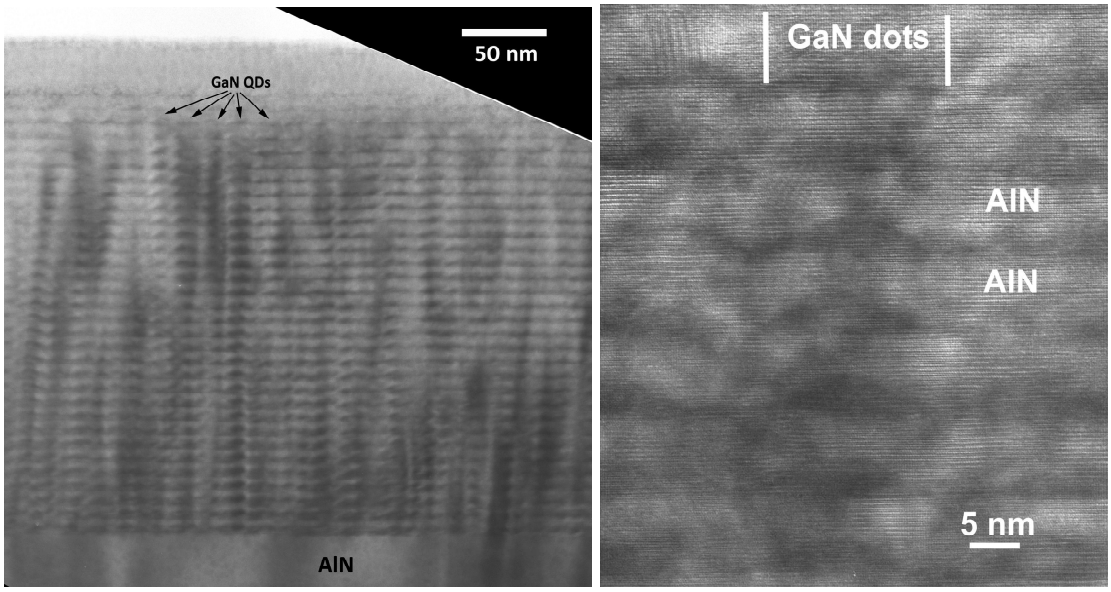

Figure 5.4: (a) Conventional bright-field TEM image of a Ga-rich grown GaN/AlN QD stack, where we observe vertical alignment of the QDs. (b) HRTEM image following the [2-1-10] axis (HRTEM images by Prof. Ph. Komninou, Aristotle University of Thessaloniki, Greece).

Typical low-temperature (T = 7 K) PL spectra from GaN/AlN QDs samples are presented in figure 5.5(a). The samples consist of 40-period SLs with 7 nm thick AlN barriers and GaN QDs whose height varies from 1 nm to 3 nm, which corresponds to emission peak energy varying from 310 nm to 450 nm. The quantum confinement blue shifts the PL of the smaller QDs, whereas the larger QDs, due to the QCSE,

show luminescence well below the GaN band gap. If we compare this QDs emission with emission of GaN/AlN QW 40-period structures, with a barrier thickness of 7 nm and a QW thickness varying between 1.25 nm and 3 nm, we can see that the QD emission is broader due to the dispersion of the QD dimensions. In the case of the GaN/AlN QWs, the spectral structure of the emission is due to monolayer thickness fluctuations in the QWs, as described elsewhere [Tch06]. In the QD structures, the broader linewidth makes it possible to observe the superimposition of a Fabry-Perot interference pattern related to the total nitride thickness.

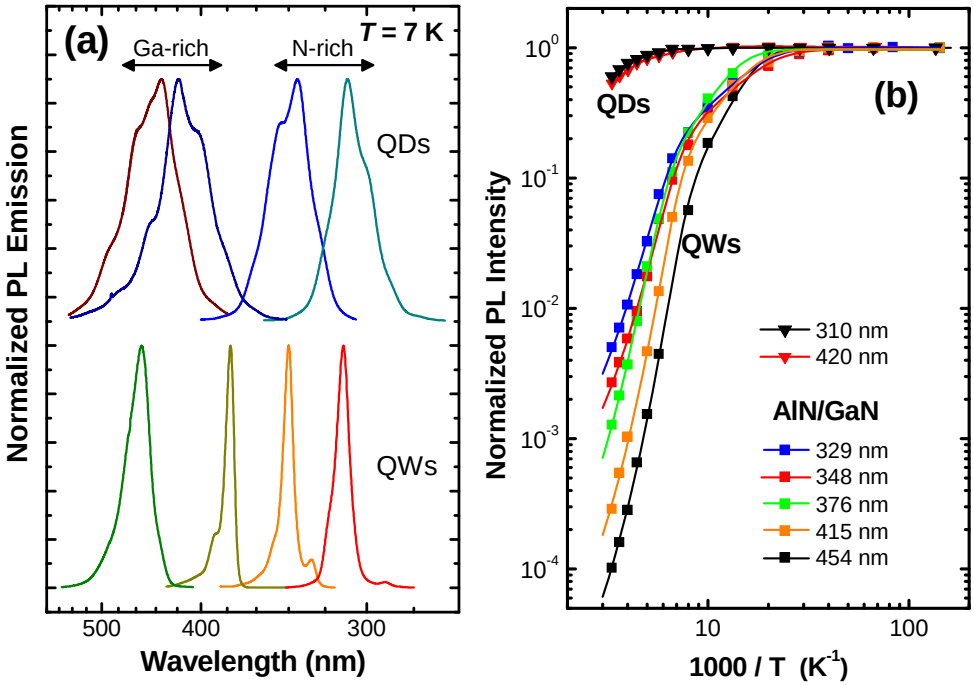

Figure 5.5:(a) Normalized PL spectra of GaN/AlN QDs compared with GaN/AlN QWs emitting at same wavelength range.(b)Temperature evolution of the integrated PL emission of GaN/AlN QW and QD samples emitting at different wavelengths.

A signature of 3D carrier confinement in QD structures is the thermal stability of the PL. The evolution of the integrated PL intensity as a function of temperature, normalized by the integrated PL intensity at low temperature (T = 7 K), is presented in figure 5.5(b) for GaN/AlN QWs and QDs. Keeping in mind that the emission intensity remains stable below 25 K for all the samples, the values presented in this figure should correspond directly to the internal quantum efficiency (IQE)[1], defined as

[1] Note that this correspondence is only valid if the nonradiative recombination is negligible at low temperature, which in the case of figure 5.5 is supported by the fact that the luminescence intensity remains constant between 7 K and 35 K.

IQE = $R_R/(R_R + R_{NR})$, with R_R and R_{NR} being the radiative and nonradiative recombination rates, respectively. These results confirm the improved thermal stability of QDs over QWs, as a result of the 3D carrier confinement, in agreement with previous reports [Ade00, Dam99, Gui06, Sén07].

Making use of simple rate equations [Ler99] under (optical) injection

$$\frac{\partial n}{\partial t} = G - \frac{n}{\tau_R} - \frac{n}{\tau_{NR}} \tag{5.1}$$

where n is the minority carrier or exciton density concerned, G the generation rate, and τ_R and τ_{NR} the radiative and non-radiative lifetimes respectively. Considering that nonradiative recombination centers are thermally activated, i.e. $\tau_{NR} = \tau_0 e^{E_a/kT}$, and that the steady-state population of minority carriers governs the PL intensity (i. e. $I_{PL} \propto n/\tau_R$) we arrive to the expression:

$$\text{IQE} \approx \frac{I(T)}{I(T=0)} = \frac{R_R}{R_R + R_{NR}} = \frac{1}{1 + ae^{-E_a/kT}} \tag{5.2}$$

where $a = \tau_R/\tau_0$.

The presence of carrier localization in potential fluctuations complicates the rate equation (5.1) by introducing an additional thermal dependence [Min02]. In this case, the radiative efficiency can be approximated by

$$\frac{I(T)}{I(T=0)} = \frac{1}{\left(1 + ae^{-E_a/kT}\right)\left(1 + be^{-E_{loc}/kT}\right)} \tag{5.3}$$

with E_{loc} being the average localization energy.

Experimental measurements of the PL intensity as a function of temperature (Figure 5.5) can be well fitted to eq. (5.3). The obtained activation energies (E_a) and localization energies (E_{loc}) are listed in Table 5.1. It is important to note that the value of E_a does not correspond to the band offset –although it is influenced by it. E_a represents the energetic barrier that the carriers must surmount in order to reach the nonradiative recombination centers. In the case of QDs, the confinement in the dot increases this potential barrier. Higher temperatures are hence required for carriers to escape, probably via the wetting layer. On the other hand, QDs samples are well fitted assuming $E_{loc} = 0$.

Table 5.1: Values of IQE = $I_{PL}(RT) / I_{PL}(T = 4\ K)$, activation energy of nonradiative processes E_a, and localization energy E_{loc} extracted from the analysis of the PL emission of GaN/AlN QWs and QDs.

Structure	GaN/AlN QWs	GaN/AlN QDs
Number of samples measured	5	3
Emission range (nm)	325 - 460	310 - 420
E_a (meV)	15±3	80±5
E_{loc} (meV)	110±15	--
IQE	0.0001 - 0.02*	0.3 - 0.8

* Decreasing for increasing PL peak wavelength.

The thermal evolution of the PL is characterized not only by the intensity decline due to the activation of nonradiative recombination processes, but also by a spectral shift, which can provide information about the carrier localization in potential fluctuations. Figure 5.6 presents the evolution of the PL peak energy as a function of temperature in the cases of (a) GaN/AlN QWs and (b) GaN/AlN QDs. The evolution of the PL peak energy from the GaN/AlN QDs fits well the evolution of the GaN bandgap calculated using Varshni's equation (Eq. 2.3 in chapter 2), with $\alpha = 0.59$ meV/K and $\beta = 600$ K (dashed curves in figure 5.6), which indicates that potential fluctuations inside the QDs are negligible. This is in contrast with the intra-dot localization reported in the case of nonpolar QDs [Rol07], which can be attributed to the presence of structural defects.

In the QW samples, the evolution of the emission peak energy as a function of temperature describes an S shape (see QW sample emitting at 2.7eV). This S-shaped variation is associated with potential fluctuations which can be related to variations in the QW thickness or/and to the presence of structural defects. This S-shape is consistent with the requirement of two activation energies to get a good fit of the thermal evolution of the PL intensity in QWs, as shown in Table 5.1.

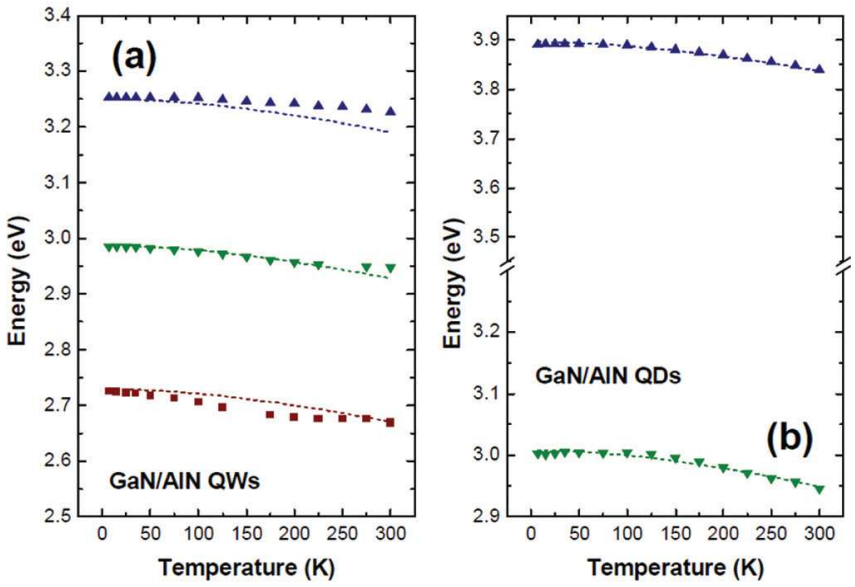

Figure 5.6: Temperature dependence of the PL peak position for (a) GaN/AlN QWs and (b) GaN/AlN QDs. Note that both figures have the same vertical span. The dashed lines represent the evolution of the emission with temperature following Varshni's equation.

The vertical homogeneity can be assessed by cathodoluminescence (CL) spectroscopy, the penetration of the electron beam being a function of the acceleration voltage. Figure 5.7 presents the normalized CL spectra of a QD sample (PL peak energy at 3.95eV) measured at room temperature with different acceleration voltages. The CL peak energy remains stable when increasing the voltage from 2 kV to 15 kV, which indicates a good vertical reproducibility of the QD layers. The low energy shoulder that appears at 15 kV corresponds to the luminescence from defects in the AlN buffer layer.

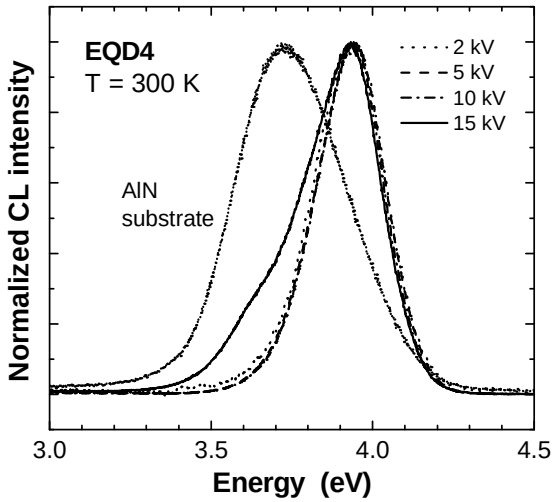

Figure 5.7: Evolution of the normalized CL spectra from a 20-period QD stack measured at room temperature with different accelerating voltages. The CL spectrum of the AlN template used as a substrate is included for comparison.

5.3 GaN/AlN QDs with reduced internal electric fields

Polar GaN/AlN QDs are, in general, defect-free structures. However, GaN/AlN heterostructures grown along the polar <0001> axis present an internal electric field of several MV/cm due to the polarization discontinuity along this axis. A strong reduction of the internal electric field has been demonstrated in nonpolar GaN/AlN QDs grown on a-plane [Fou05] and *m*-plane [Ams07]. However, the integration of such nanostructures in complete devices is challenging due to the difficulties to achieve nonpolar 2D layers with flat morphology [Fou05, Ams07] and the strong dependence of the QD morphology on the AlN underlayer [Ams07]. So for reducing QCSE in GaN/AlN QDs, we considered growth of QDs in semipolar (11-22) plane.

To study the structural properties and optical performance of semipolar GaN QDs, we have fabricated a series of samples consisting of 20 periods of GaN QDs embedded in 10-nm-thick AlN barriers. An additional QD plane was deposited on the surface to enable AFM characterization. The QDs were synthesized by deposition of a 2D GaN layer under Ga-rich conditions, followed by a 90 s growth interruption in vacuum, during which the reflections corresponding to the QD facets become visible in the RHEED pattern. The nominal amount of GaN in each QD layer varied from 3 ML to 10 ML. These samples were synthesized and characterized in collaboration with Dr. Lise Lahourcade.

The AFM micrograph in figure 5.8(a) illustrates the typical surface of a ~200-nm-thick 2D AlN(11-22) layer, whereas figure 5.8(b) shows the surface of the sample with nominally 5 ML thick GaN QD layers. The island density is around 5×10^{10} cm^{-2}, with an average island height of 2.5±0.4 nm. It is however important to remind the difficulty to quantify precisely the dimension of surface corrugations from AFM characterization, since the measured topography is a convolution of the real surface and the tip shape. Moreover, it is not possible to determine if a continuous 2D GaN wetting layer persists between the islands.

Figure 5.9 shows overall cross-sectional TEM and Z-contrast scanning-TEM images of the QD heterostructure of the 10 ML sample. It is seen that the QD

superlattices were distorted by the large density of extended defects (TDs and stacking faults) contained in the MBE-grown template. The defects introduced roughening and depressions at the GaN/AlN interface, causing many QDs to grow partially on inclined crystallographic planes. However, the great majority of QDs sat on the (11-22) plane, and the QDs were epitaxial with the (11-22) matrix.

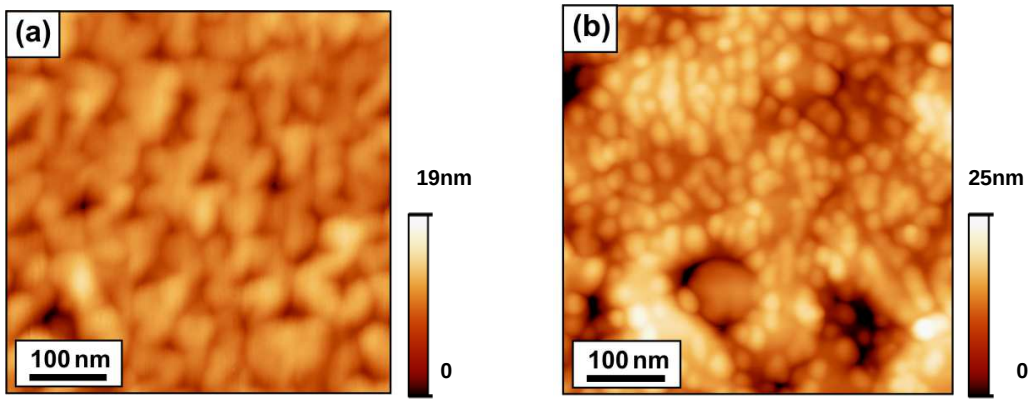

Figure 5.8: (a) AFM micrograph of a typical ~200-nm-thick AlN(11-22) layer. (b) AFM image of GaN (11-22) QDs synthesized by deposition of 5 ML of GaN under slightly Ga-rich conditions on AlN(11-22) and subsequent annealing for 90 s in vacuum.

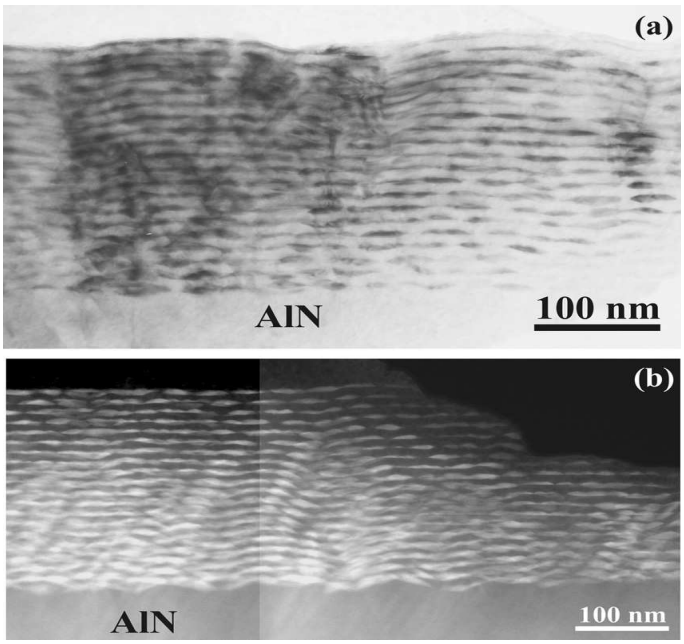

Figure 5.9:(a) Bright-field CTEM image along the [-1-123] zone axis and (b)Z-contrast STEM image along [1-100] of the overall GaN QD heterostructure of the 10 ML sample grown on semipolar (11-22) AlN template. The heterostructure is perturbed by TDs, and depressions are observed at the GaN/AlN interface (After [Dim10] TEM images by Ph. Komninou, Aristotle University of Thessaloniki, Greece).

Figure 5.10 presents cross-section HRTEM images of the QD stacks with nominally (a) 5 ML and (b) 10 ML of GaN in the QD layers. The GaN islands present a good epitaxial relationship with the AlN matrix, keeping the same (11-22) crystallographic orientation. By comparing figures 5.10(a) and (b) we observe a significant enhancement of the QD height and diameter when increasing the amount of GaN in the QD layers. Another important feature is the presence of a wetting layer, clearly resolved in the sample with 5 ML of GaN. In the sample with 10 ML of GaN, the wetting layer is not distinguished due to the higher QD density.

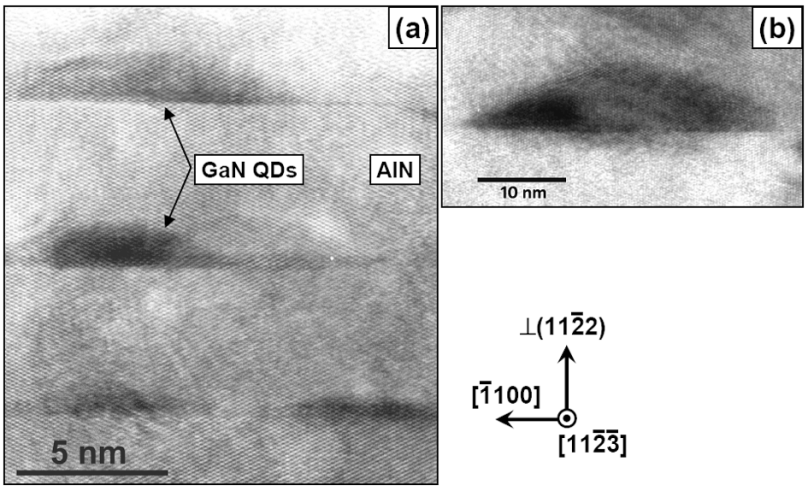

Figure 5.10: High-resolution TEM images of (11-22)-oriented GaN/AlN QDs synthesized by deposition of (a) 5 ML and (b) 10 ML of GaN under slightly Ga-rich conditions on AlN(11-22) and subsequent annealing for 90 s in vacuum, viewed along <11-2-3>$_{layer}$ axis (After [Dim10] TEM images by Ph. Komninou, Aristotle University of Thessaloniki, Greece).

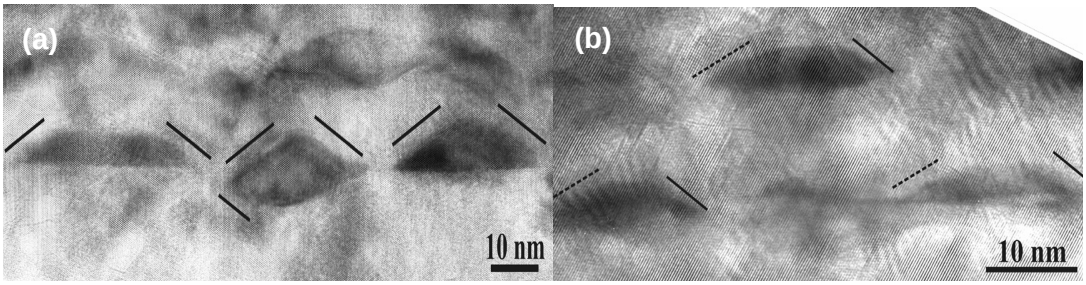

Figure 5.11: Cross sectional HRTEM image of (11-22) GaN QDs in the 10 ML sample. (a) Observed along [-1-123], the facets indicated by solid lines are of {10-11} type. (b) Observed along [1-100], the (11-20) side facets are indicated by solid lines. The dashed lines indicate facets of average orientation (11-25) or (11-26). (After [Dim10] TEM images by Ph. Komninou, Aristotle University of Thessaloniki, Greece).

Regarding the side facets of the QDs, figure 5.11(a) illustrates a cross-sectional HRTEM image along the [-1-123] zone axis. It is seen that the side facets of the QDs are aligned with the {10-11} edge-on planes that form angles of 26° with the (11-22) plane. Another possible plane orientation for these side facets is the {10-12} which is inclined in this projection and forms an angle of 27.4° with the (11-22). The QDs were either pyramidal-shaped or truncated at their top. From figure 5.11(b) we can note that the QDs exhibit a sharper facet, indicated by solid lines on the right-hand side, whereas they are more lenticular-shaped on the left-hand side (dashed lines).

Figure 5.12 illustrates the resulting delimiting geometrical shapes of the (11-22) QDs, based on the assigned crystallographic planes. When two crystallographically equivalent facets, {10-11} or {10-12}, coexist, the QD shape exhibits mirror symmetry consistent with the (1-100) glide-mirror plane of wurtzite that is perpendicular to the (11-22) plane. Alternatively, one {10-11} and one {10-12} facet may coexist in the same QD, leading to two variants of the QD shape due to the suppression of the mirror symmetry. The proposed delimiting morphologies are consistent with the plan-view observation of rectangular or trapezoidal shapes.

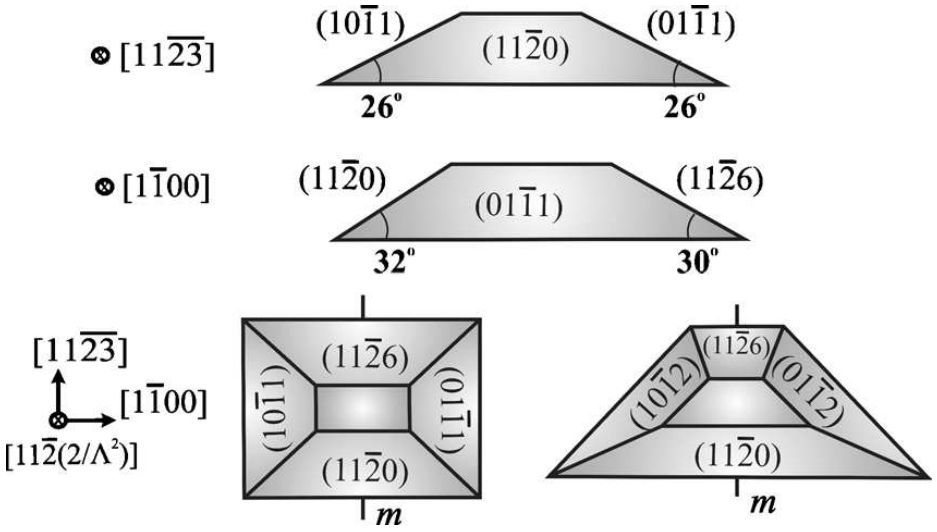

Figure 5.12: Schematic illustration, along three perpendicular projection directions, of the two delimiting QD morphologies of the (11-22)-nucleated QDs.The orientation of the (1-100) glide mirror plane is indicated (After [Dim10] TEM images by Ph. Komninou, Aristotle University of Thessaloniki, Greece).

Figure 5.13(a) presents the low temperature (T = 7 K) PL spectra from QD stacks with nominally 3 ML, 5 ML, 8 ML and 10 ML in the GaN QD layers. The PL peak energy blue shifts when reducing the amount of GaN in the QDs as a result of the improved quantum confinement. The full width at half maximum (FWHM) is in the range of 265 meV to 105 meV, which is comparable to the values obtained from c-oriented GaN/AlN QDs. However, in contrast with results in polar GaN/AlN QDs, the PL energy peak remains systematically above the GaN band gap, attesting the reduction of the QCSE.

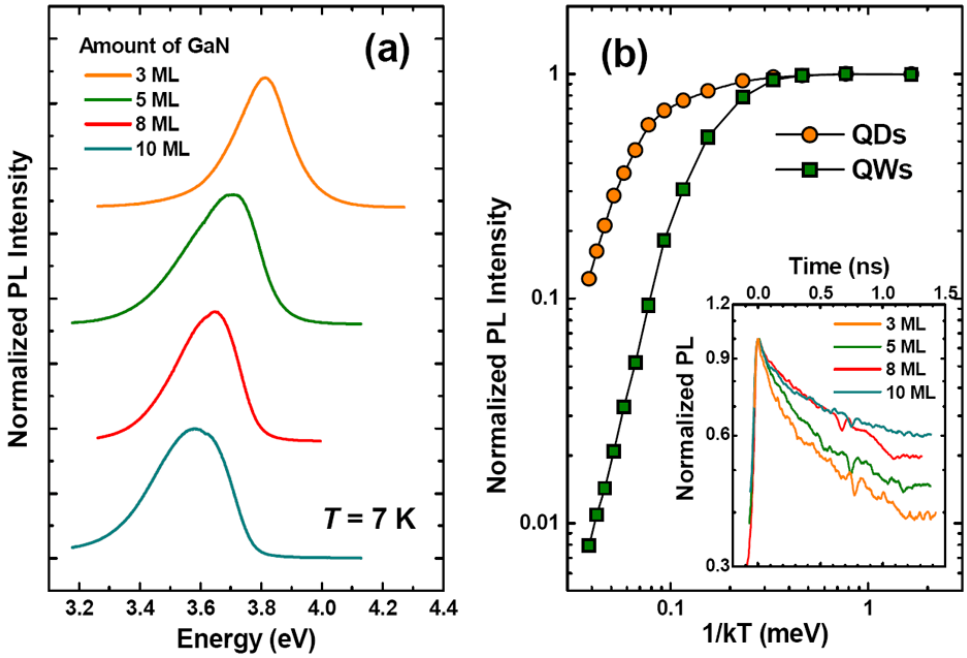

Figure 5.13: (a) Low temperature (T = 7 K) PL spectra from GaN/AlN QD stacks with the amount of GaN deposited in the QD layers varying from 3 ML to 10 ML. (b) Evolution of the PL intensity with the temperature in semipolar GaN/AlN multi-QD and multi-QW structures, both emitting around 3.65 eV. In the inset, time-resolved PL measurements of semipolar GaN/AlN QD stacks at T = 7 K (After [Lah09]).

The attenuation of the internal electric field in the semipolar QDs is further confirmed by time-resolved PL measurements. In this experiment, the excitation source was a pulsed frequency-tripled Ti:sapphire laser (λ = 270 nm) with a repetition rate of 76 MHz (pulse width of ~200 fs), focused onto a 100 µm diameter spot. The PL signal was analyzed by a streak camera using a 2.2 ns window, giving a system response of about 10 ps. The inset of figure 5.13(b) illustrates the time-resolved PL results obtained for semipolar GaN/AlN QD structures, showing decay times in the

350-500 ps range, one order of magnitude shorter than results on polar QDs with similar height [Sim03].

The thermal evolution of the PL intensity of semipolar GaN/AlN QDs is presented in figure 5.13(b). For comparison with semipolar multi-QW structures, we have chosen QD and QW samples whose luminescence peak positions occur at the same energy (~3.65 eV). For instance, in figure 5.13(b), the sample with nominally 5 ML of GaN in the QDs is compared to a GaN/AlN (1.7 nm / 5 nm) multi-QW structure. The PL intensity of the QD (QW) sample drops by a factor of ~10 (~100) between T = 7 K and room temperature. The improved thermal stability in the QDs is an indication of the 3D carrier confinement, which increases the recombination efficiency and makes them relatively insensitive to defects in the surrounding matrix. Experimental measurements of the PL intensity as a function of temperature (Figure 5.13(b)) can be well fitted to eq. (5.3). The obtained activation energies (E_a) and localization energies (E_{loc}) are listed in Table 5.2.

Table 5.2: Values of IQE = $I_{PL}(RT) / I_{PL}(T = 4\ K)$, activation energy of nonradiative processes E_a, and localization energy E_{loc} extracted from the analysis of the PL emission of GaN/AlN (11-22) QWs and QDs.

Structure	GaN/AlN QWs	GaN/AlN QDs
Number of samples measured	2	4
Emission range (nm)	326-342	325 – 355
E_a (meV)	2±1	77-136
E_{loc} (meV)	--	11-24
IQE	0.01-0.007	0.09-0.02

5.4 Polar InGaN/GaN QDs

To investigate the structural and optical performance of InGaN QDs, I have synthesized a series of a series of InGaN/GaN 20-period QD superlattices on 10-µm-thick GaN-on-sapphire templates. For the generation of InGaN QDs, the Ga flux was fixed at 30% of the stoichiometric value and the In flux was tuned close to the stoichiometry. Therefore, the Stranski-Krastanov transition is forced by the lattice mismatch, in spite of the slightly metal-rich atmosphere and the well-known surfactant effect of In, which promotes 2D growth [Neu03]. For the growth of the

5 nm spacer, the In shutter was closed and the Ga flux was fixed at the stoichiometric value. We used different Ga cells for the QD and for the barrier, to be able to synthesize the superlattice without growth interruptions. In order to use as a reference for characterization, we have fabricated also a series of InGaN/GaN QW 20-period SLs deposited on 4-µm-thick GaN-on-sapphire templates. In the case of the QWs, the Ga flux was fixed at 30% of the stoichiometric value and the In flux was tuned to have two monolayers of In excess at the growth front [Mon03]. For the growth of the 3 nm thick GaN barriers, a second Ga cell was used at the stoichometric temperature, and the In shutter was kept open to guarantee 2D growth. All structures were synthesized without growth interruptions.

Prior to the growth of each sample, we have calibrated the growth temperature by measurement of the In desorption time, as described in section 4.6.1 of chapter 4. Several samples were grown at various substrate temperatures. Figure 5.14(a) and (b) compare AFM images of InGaN/GaN QDs and the 2D surface of InGaN/GaN QWs. The AFM image of the QD samples showing a high density of small QDs. It is important to keep in mind that the QDs embedded in GaN should be different than those on the surface, due to GaN/InGaN interdiffusion. AFM images should therefore be taken as a reference, but they do not provide direct information on the morphology embedded QDs. In the case of QWs, the surface presents the typical GaN morphology with hillocks and atomic terraces.

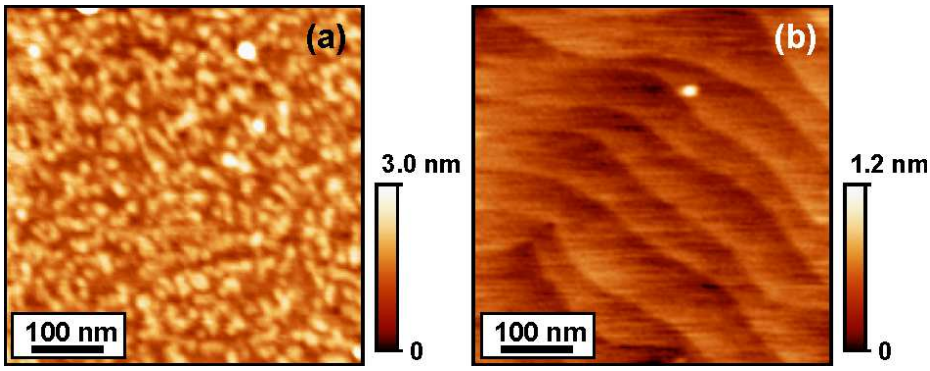

Figure 5.14: AFM image of (a) InGaN/GaN QDs as compared to (b) InGaN/GaN QWs.

HRTEM and scanning transmitting electron microscopy (STEM) imaging were implemented in order to investigate the structural properties of these samples. Figure 5.15 presents the overall cross-sectional STEM image from the InGaN/GaN

QW heterostructure. The 20 periods of the InGaN/GaN QWs are clearly visible (Figure 5.15, left). In the magnified image on the right, atomically sharp GaN/InGaN interfaces along the growth axis are observed, whereas the InGaN/GaN interfaces present interdiffusion with an average value of 0.7±0.1 nm. Let us remind the reader that certain degree of interdiffusion is commonly observed in this kind of structures grown by molecular-beam epitaxy [Wal02, Dus03].

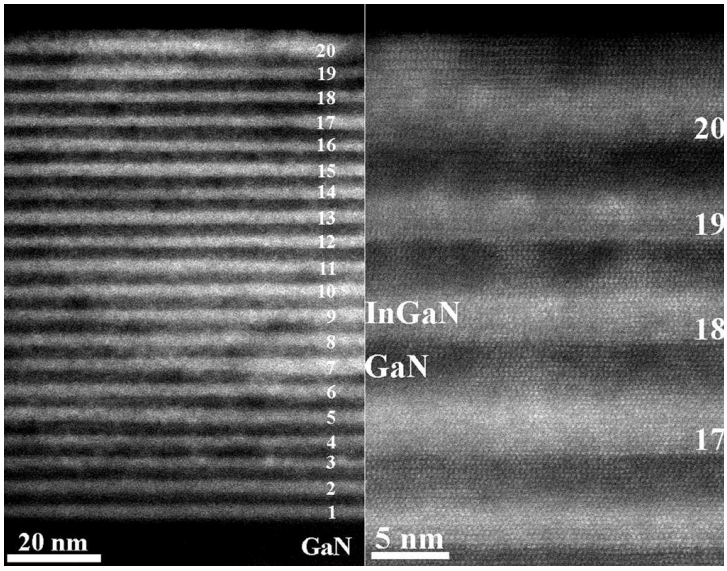

Figure 5.15: Cross-sectional STEM images of InGaN/GaN QWs. Left: Overall view of the 20-period superlattice, in which the InGaN QWs present with brighter contrast because they comprise the heavier element. Right: A magnified part of the image on the left showing the atomically flat GaN/InGaN interfaces and the interdiffusion at the InGaN/GaN interfaces along the growth axis (TEM images by Ph. Komninou, Aristotle University of Thessaloniki, Greece).

Figure 5.16 shows HRTEM observations of InGaN/GaN QDs, taken along the $[11\text{-}20]_{GaN}$ zone axis. Truncated pyramidal-shaped QDs of wurtzite structure are identified. Although the shape of the surface QDs is well defined, the embedded QDs are less clear due to thickness effects from projected material overlap and scattered contrast from beam-induced partial indium clustering. In general, the projected diameter of the QDs ranges from 17 to 25 nm, and their height is measured as ~2.2±0.2 nm. The wetting layers are also visible and no stacking faults were found in the structures.

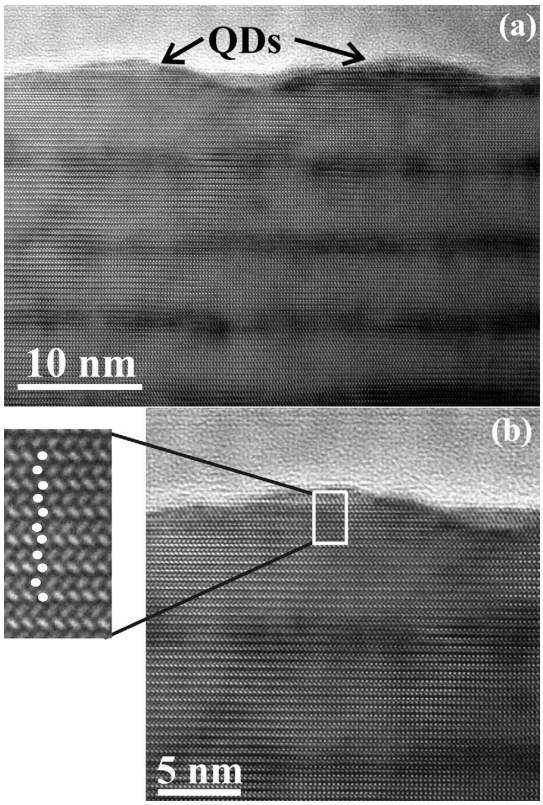

Figure 5.16: HRTEM images of InGaN QDs viewed along the [11-20] zone axis.(a) Surface and embedded QDs are detected along with the wetting layers.(b) A magnified view of a surface QD depicting its wurtzite structure in atomic scale (TEM images by Ph. Komninou, Aristotle University of Thessaloniki, Greece).

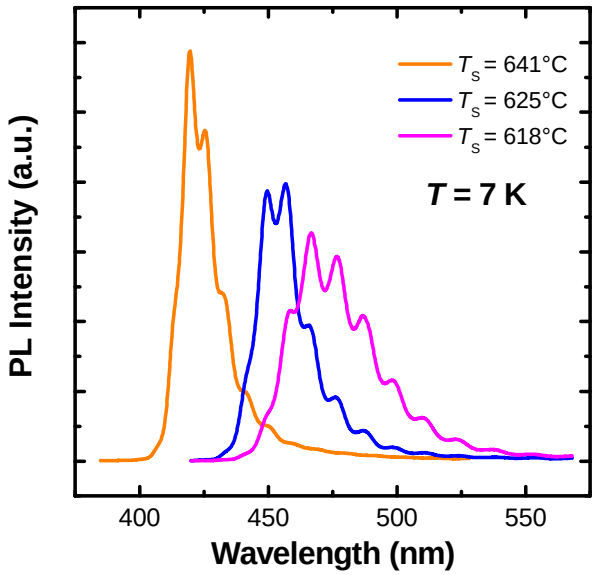

Figure 5.17: Low temperature PL spectra from InGaN/GaN QWs grown at different substrate temperature.

The low-temperature (T = 7 K) PL spectra of the InGaN/GaN QW samples grown under different substrate temperatures, between 610°C and 640°C, are presented in figure 5.17. The spectrum shows a red shift in the emission with decreasing growth temperature, as a result of the enhanced In incorporation in the QWs.

Figure 5.18 presents low temperature (T = 7 K) PL spectra obtained from InGaN/GaN QD superlattices grown at different substrate temperature. In InGaN QD samples, the variation of the PL peak energy with the substrate temperature does not follow a monotonous trend (see Table 5.3). This is due to the fact that the substrate temperature modifies not only the In content in the QDs but also their morphology (height, diameter, density).

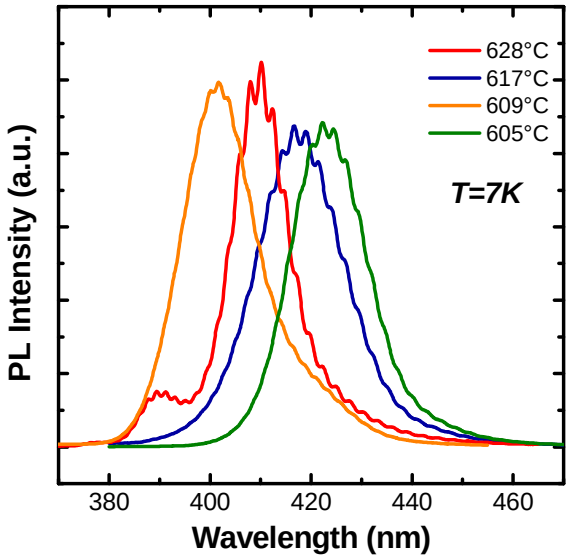

Figure 5.18: Low temperature PL spectra of the InGaN/GaN QDs samples grown at different substrate temperature.

Sample	Growth temperature	PL peak wavelength
E1932	628°C	411 nm
E1930	617°C	420 nm
E1933	609°C	398 nm
E1934	605°C	423 nm

Table 5.3: InGaN/GaN QDs samples grown at different substrate temperature.

Figure 5.19 Presents the low temperature (T = 7 K) PL spectra from a second series of QDs samples with 20 periods of nominally 3 ML, 4 ML, 5 ML and 6 ML of InGaN QDs embedded in 5 nm thick GaN barriers. Here, the linewidth is broader than

in the previous series, indicating larger dispersion of the QD parameters. And also the PL peak energy red shifts systematically for increasing amount of InGaN in the QDs (keep in mind that these samples were grown at the same temperature, T_S = 610°C).

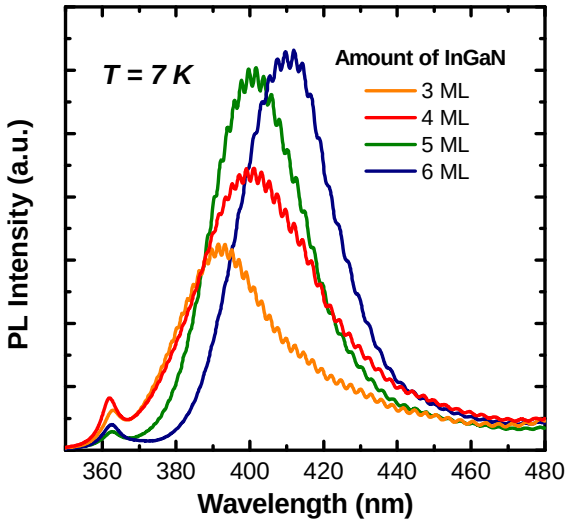

Figure 5.19: Low temperature PL spectra from 20 periods of InGaN/GaN QD stacks with the amount of InGaN deposited in the QD layers varying from 3 ML to 6 ML.

Figure 5.20 compares the thermal evolution of the PL intensity for the case of InGaN/GaN QWs and QDs. From the figure, we observe that in the case of QDs, the PL intensity remains constant up to almost 100 K, whereas in QWs the PL starts to decay at about 30 K. This is a confirmation of the QD 3D carrier confinement, which separates the carriers from nonradiative recombination centers. The experimental measurements in figure 5.20 can be well fitted to eq. (5.3). The obtained values of activation energies (E_a) and localization energies (E_{loc}) are listed in Table 5.4. Similarly to the GaN/AlN case, QDs samples are well fitted assuming E_{loc} = 0.

Table 5.4: Values of IQE = $I_{PL}(RT) / I_{PL}(T = 4\ K)$, activation energy of nonradiative processes E_a, and localization energy E_{loc} extracted from the analysis of the PL emission of InGaN/GaN QWs and QDs.

Structure	InGaN/GaN QWs	InGaN/GaN QDs
Number of samples measured	6	8
Emission range (nm)	430 – 530	390 – 410
E_a (meV)	11±4	50±2
E_{loc} (meV)	30 - 80*	--
IQE	0.0004 - 0.01	0.1 - 0.6

* Increasing for increasing PL peak wavelength.

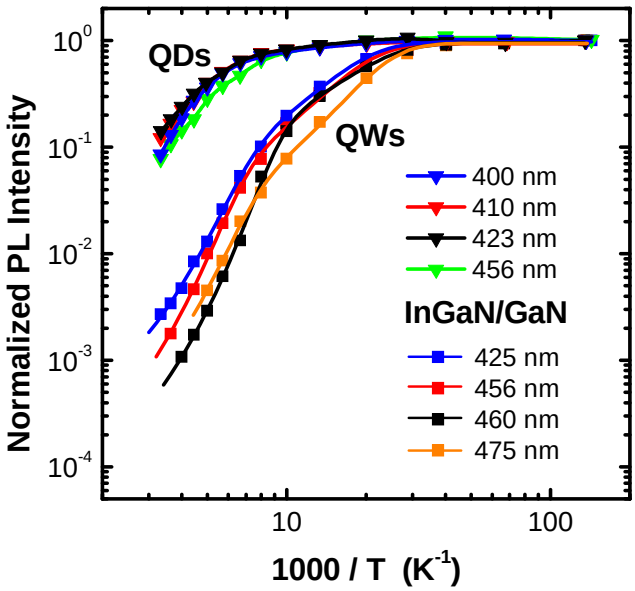

Figure 5.20: Temperature evolution of the integrated PL emission of InGaN/GaN QW and QD samples emitting at different wavelengths.

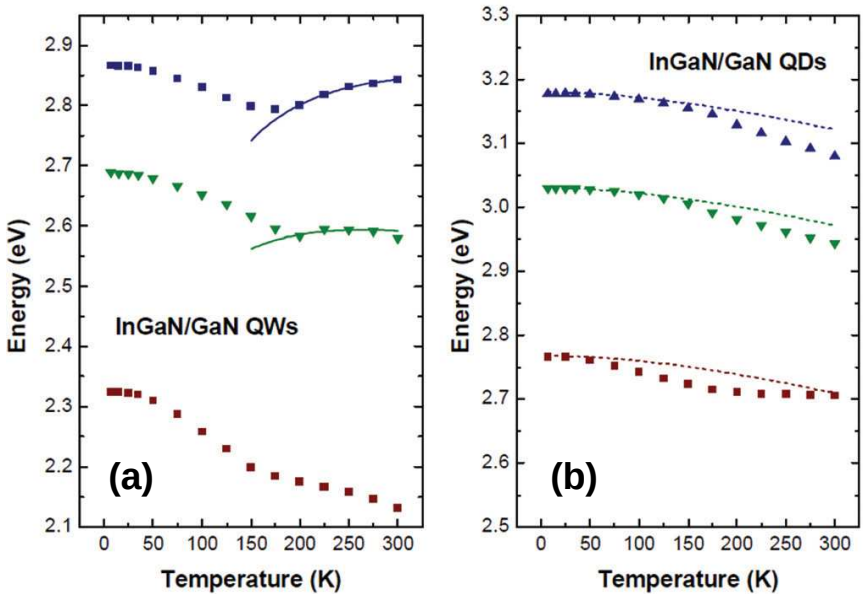

Figure 5.21: The temperature dependence of the PL peak position for (a) InGaN/GaN QWs and (b)InGaNGaN QDs. Note that all of the figures have the same vertical span. The solid lines in (a) are fits to Eliseev's correction [Eli97] to model InGaN alloy fluctuations. The dashed lines in (b) represent the evolution of the emission with temperature following Varshni's equation.

Figure 5.21 presents the evolution of the PL peak energy as a function of temperature in the cases of (a) InGaN/GaN QWs and (b) InGaN/GaN QDs. In the case of InGaN/GaN QDs emitting in the 3.0-2.85 eV spectral range, Lefebvre et al. reported carrier localization by potential fluctuations with a spatial extension much

smaller than the QD Size [Lef01]. In our case, a deviation from Varshni's equation associated to InGaN/GaN intra-dot localization is resolved, being particularly important in the QD sample emitting lower energy, which points to a more uniform In distribution in the QDs with a lower In content (3.2–3.0 eV spectral range).

In the QW samples, the evolution of the emission peak energy as a function of temperature describes an S shape. This S-shaped variation is associated with potential fluctuations in the QWs: the blue shift at intermediate temperatures is explained by the filling of potential valleys with different depths upon excitation [Eli97, Lef01, Cho97]. The remarkable enhancement of the S-shape in InGaN QWs points to alloy inhomogeneities. For quantification of the potential fluctuations, Eliseev et al. [Eli97] proposed a band-tail model assuming a Gaussian-like distribution of the density of states, which results in a correction to Varshni's equation by $-\sigma^2/kT$, where σ is dispersion of the Gaussian band-tail density of states. From the analysis of InGaN/GaN QWs, values of σ = 40±15 meV are obtained, which are comparable to typical measurements in InGaN light emitting diodes [Eli97]. In the case of InGaN QDs, it was not possible to extract a reliable value of σ.

5.5 InGaN/GaN QDs with reduced internal electric field

In order to study the optical and structural performance of semipolar InGaN QDs, I have synthesized a series of self-assembled semipolar InGaN/GaN 10-period QD superlattices. These semipolar samples were grown using 1 μm thick (11-22) GaN template deposited by MOVPE on *m*-plane sapphire provided by Dr. Ph. De Mierry and Dr. G. Nataf (CRHEA-CNRS, Valbonne France) [Mie09]. Identical samples were simultaneously deposited on commercial 4 μm thick polar (0001) GaN substrates, to allow for comparison. Prior to the growth of each sample, I have calibrated the growth temperature by measurement of the In desorption time from polar GaN on the same sample holder. During the growth of the QDs, the Ga flux was fixed at 30% the stoichiometric value and the In flux was tuned to have a slight In excess. A growth interruption for 10 s in vacuum after the InGaN deposition favors InGaN islanding. For the growth of the 5 nm thick GaN barriers, the Ga flux was fixed at the stoichiometric value, using a second Ga cell. Several samples were grown at various

substrate temperatures ranging from 650^{o}C to 510^{o}C, where In desorption is active. The In incorporation rate is very sensitive to the substrate temperature, so that we expect a variation of the In mole fraction in the QDs.

Figure 5.22 is a bright field (BF) cross-section TEM micrograph, from a semipolar sample grown at 560^{o}C, along the [1-100] zone axis. It shows the InGaN/GaN superlattice on top of the (11-22) MOVPE GaN template, and the defect structure dominated by TDs lying on the (0002) basal plane with a measured density of 3×10^{10} cm^{-2}.

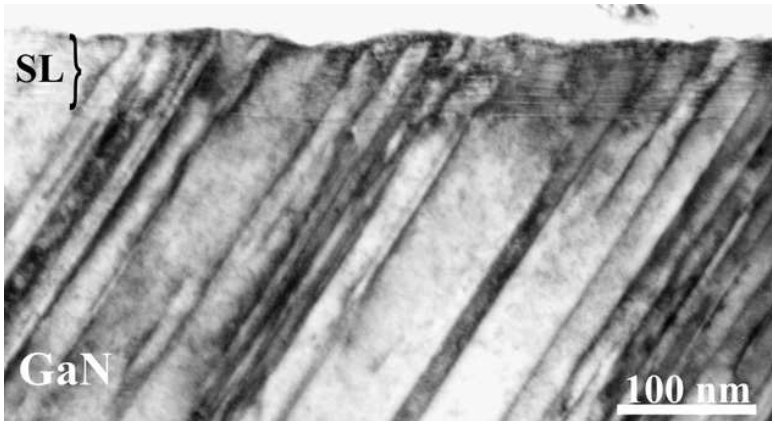

Figure 5.22: BF CTEM image along the [1-100] zone axis showing the InGaN/GaN superlattice on top of the MOVPE GaN template. The inclined TDs lie on the basal plane (TEM images by Ph. Komninou, Aristotle University of Thessaloniki, Greece).

InGaN QDs were found to nucleate preferentially at sites where the nucleating plane deviated from the exact (11-22) orientation. These local deviations are attributed to the facetted surface roughness associated with the growth of (11-22) oriented GaN, and to the effect of the local strain field of the TDs. The HRTEM image of figure 5.23(a) illustrates QDs viewed along the [11-2-3] direction, and figure 5.23(b) shows QDs viewed along the [1-100] direction. The latter image shows wetting layers and QDs nucleated on inclined planes in the vicinity of TDs. The QDs were elongated along their base with an average width of ~15 nm and their height was ~2 nm. The GaN barriers had a height of 5 nm. QDs that nucleated on the (11-22) plane or on depressions of the GaN barriers exhibited a lenticular morphology. On the contrary, QDs nucleated on inclined planes were more facetted and generally larger in height. Figure 5.23(c) is an enlarged HRTEM image of a facetted inclined QD. The preferential nucleation on inclined planes and surface depressions is similar to what

has been observed for the case of (11-22) GaN QDs in an AlN (11-22) matrix [Dim10]. Inclined planes such as {10-11} can be favorable sites of indium adsorption [Nor99].

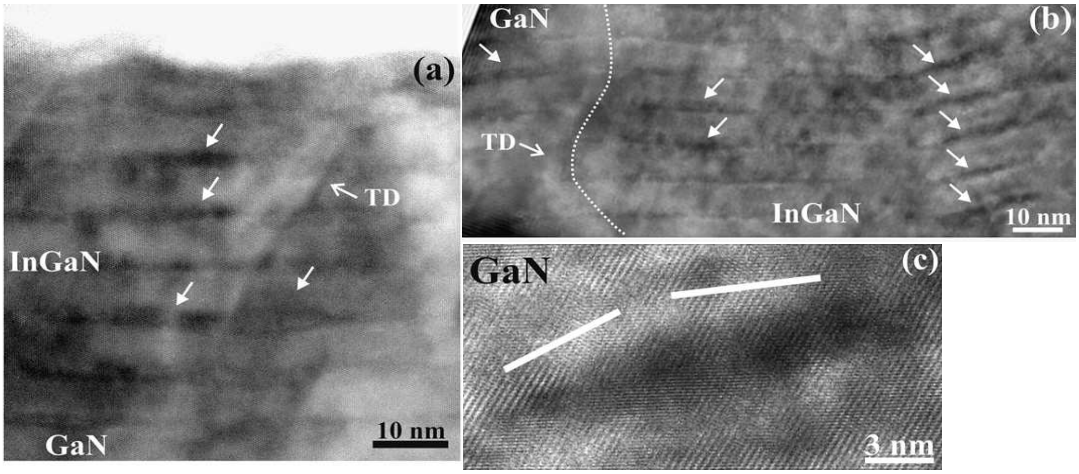

Figure 5.23: (a) HRTEM image along the [11-2-3] zone axis showing QDs nucleated on (11-22) and at depressions of the GaN barriers. Arrows indicate some of the larger QDs as well as an ascending TD. (b) HRTEM image along the [1-100] zone axis, where by arrows indicate QDs nucleated on (11-22) as well as on inclined planes due to the distortion caused by TDs. The dashed line follows an ascending TD. (c) Enlargement of an inclined QD showing a more faceted shape in contrast to the (11-22)-grown QDs. The average orientations of QD facets are indicated by white lines (TEM images by Ph. Komninou, Aristotle University of Thessaloniki, Greece).

Other than the clearly resolved QD formations, the (11-22) InGaN layers exhibited corrugated morphology (Figure 5.24(a)). Such layers were strained and comprised indium fluctuations leading to self-assembled narrow QDs of diameter ~2 nm as shown in figure 5.24(b) [Uso07]. Although the influence of the electron beam cannot be excluded as a cause of indium clustering during TEM observation [Hum07], precautions were taken in order to minimize beam exposure as much as possible. Strain relaxation constitutes another possible mechanism causing the indium fluctuations since the Stranski–Krastanow transition is induced by the lattice mismatch. Enhanced clustering is observed at the points of intersection of the layers with the TDs (Figure 5.24(a)) in agreement with recent molecular dynamics simulations [Lei10].

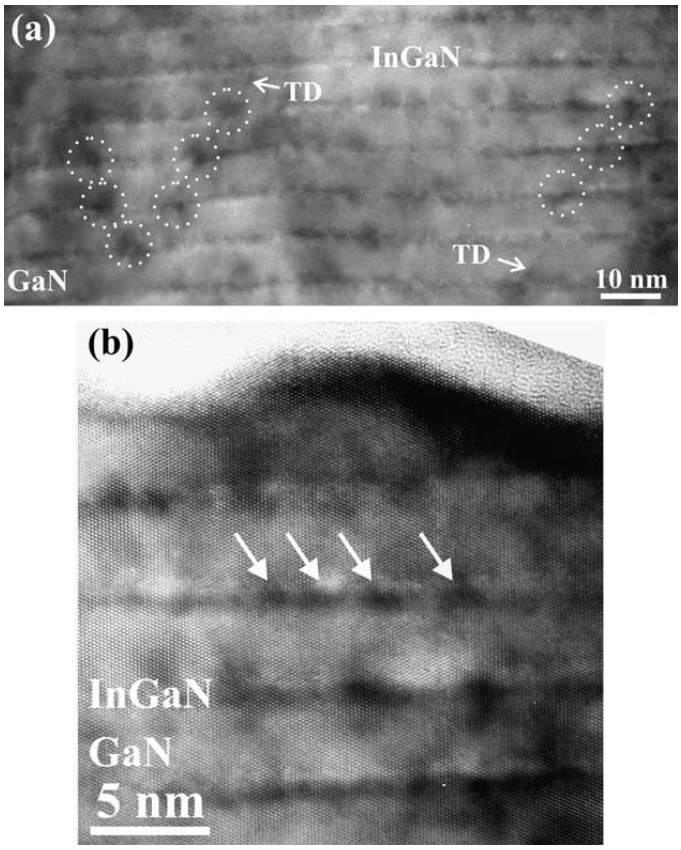

Figure 5.24: (a) HRTEM image along the [-1-123] zone axis, showing InGaN layers with corrugated morphology. TDs indicated by arrows are observed to induce clustering at the points of their intersection with the layers (dotted circles). (b) Magnified HRTEM image along [-1-123] showing that the layers break apart into small QDs (arrows). (TEM images by Ph. Komninou, Aristotle University of Thessaloniki, Greece).

The existence of strain in the layers is consistent with the observation of upward oriented TD semi-loops as in figure 5.24(a). Such semi-loops could be introduced by the Matthews–Blakeslee mechanism [Mat74], since a critical resolved shear stress is present on the basal plane in the case of semipolar growth, in contrast to the polar case. TD introduction would be promoted when the overall elastic strain in the InGaN/GaN superlattice exceeds a critical value. Another possible mechanism is the upward climb of threading arms connected to misfit dislocation segments. Misfit dislocation formation may be promoted by the roughening of the growth front [Mei07].

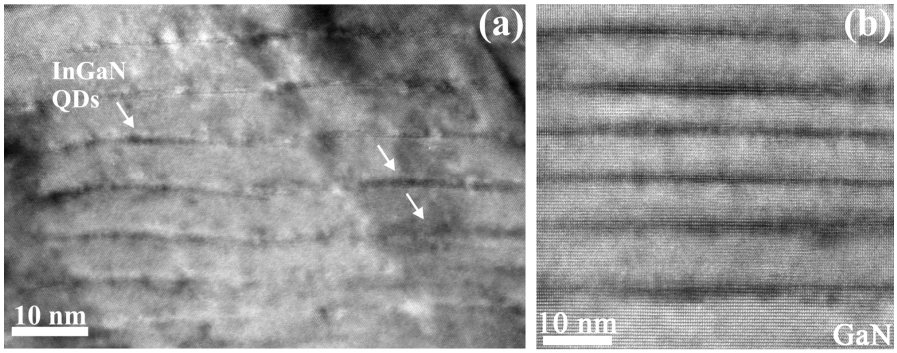

Figure 5.25: Cross-sectional HRTEM images of self-assembled InGaN/GaN QD superlattices, grown at T_S = 510°C: (a) semipolar sample, viewed along the [1-100] zone axis. (b) polar sample, viewed along [11-20]. (TEM images by Ph. Komninou, Aristotle University of Thessaloniki, Greece)

Figures 5.25 comparing HRTEM images from semipolar and polar QDs samples respectively grown simultaneously at 510^{o}C. In the semipolar case, QDs, indicated by arrows in figure 5.25(a), were of height ~2 nm and are elongated at their base having average width of ~15 nm. Under the same growth conditions, polar QDs were also well-defined and with elongated lenticular shape. Their height was similar to the semipolar case, but their projected width was approximately double.

The low-temperature PL spectra from polar and semipolar InGaN/GaN QD superlattices grown at various substrate temperatures are illustrated in figure 5.26. The emission from semipolar InGaN QDs is systematically blue shifted in comparison to the respective polar samples grown simultaneously (see figure 5.27). Not withstanding the variation in the internal electric field between the two samples, the observed shift in the PL spectrum can be attributed to the different In incorporation in the two crystallographic orientations. From the figure 5.27, we can see that the variation of the PL peak energy with the substrate temperature does not follow a monotonous trend. This might be due to the fact that the substrate temperature modifies not only the In content in the QDs but also their morphology.

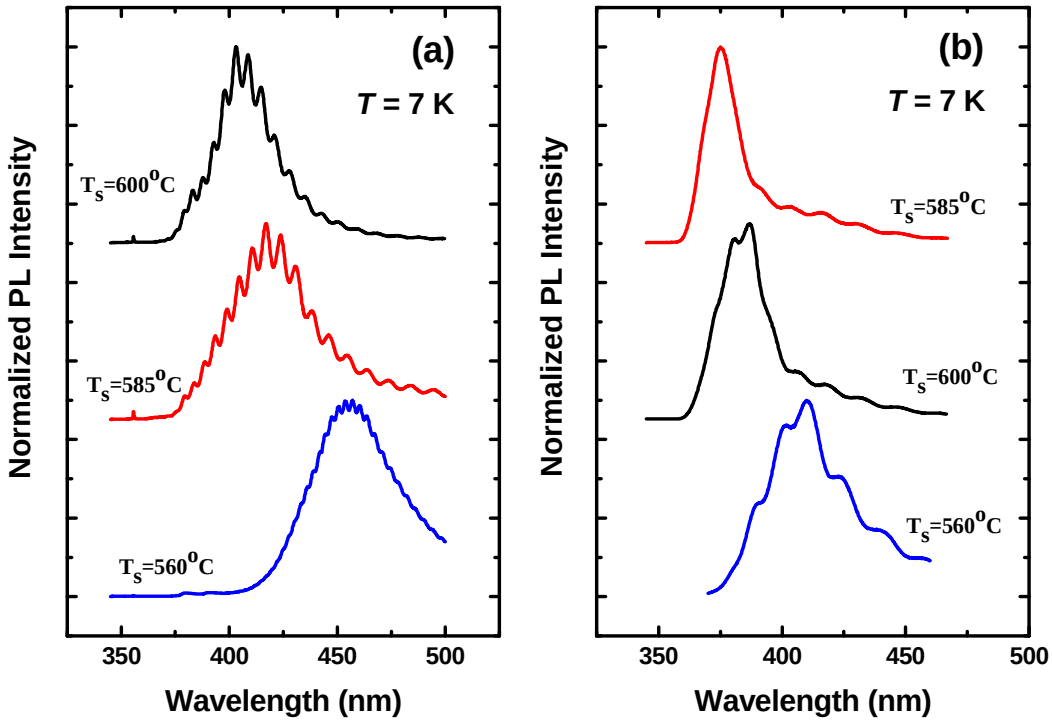

Figure 5.26: Low temperature (T = 7 K) PL spectra from (a) polar and (b) semi polar InGaN/GaN QDs grown at different substrate temperature. The spectra are vertically shifted for clarity.

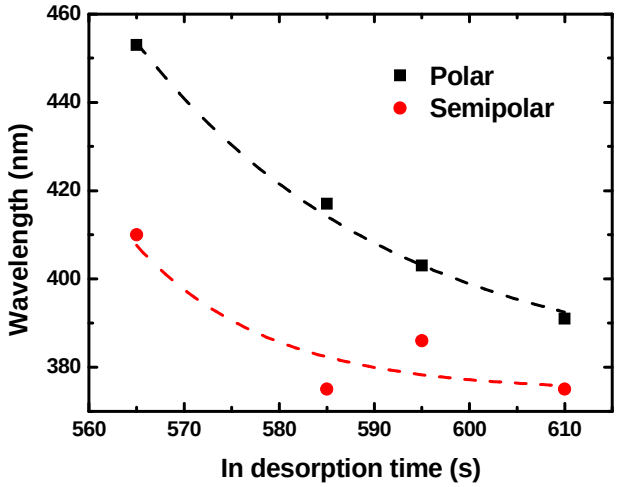

Figure 5.27: PL emission wavelength vs growth temperature for polar and semipolar InGaN/GaN QDs series.

In summary, the PL characterization of the QDs is consistent with a significantly lower In incorporation in the semipolar QDs, compared with polar structures. The longer emission wavelength from this semipolar QDs series was 410 nm. For further red shifting the emission, we need to incorporate more indium in

semipolar QDs, that is, we must consider the growth of QDs at lower substrate temperature (below 510^{o}C).

5.6 Growth of semipolar InGaN QDs at low- T_S

With the purpose of extending the emission wavelength from 410 nm to longer wavelengths, I have synthesis another series of semipolar QDs at significantly lower substrate temperature (T_S = 460-440^{o}C), where In desorption is negligible. In this temperature range, I had previously demonstrated that the synthesis of semipolar InN was possible (see section 4.6 in the previous chapter). Here also for comparison, similar samples were grown along the polar orientation under the same condition. As in this case In does not desorb from the growing surface, the In and Ga fluxes must be adjusted to the targeted mole fraction in the QDs.

Figure 5.28, shows the TEM image from the low temperature grown semipolar sample. In the low-T_S case, the QD layers exhibited a more continuous corrugated form compared to high-T_S growth. The heterostructures were evidently distorted by the high density of TDs contained in the (11-22) MOVPE template, which mostly lied on the (0002) basal planes inclined relative to the growth direction. The inclined TDs were found to change their orientation upon encountering the superlattice, and to bend almost straight upwards. This effect was most probably induced during growth and must be attributed to the influence of the elastic strain in the InGaN layers. As a result of the interaction with the TD strain fields, the growth front was distorted and depressions were introduced in the QD layers as seen in figure 5.28 and figure 5.29(a). The QDs that were nucleated in such depressions were larger on average than the rest. This could be justified if we take into account that planes such as {10-11} could act as preferable sites of indium adsorption [Nor99]. Same like in high-T_S case, the QDs had an average height of 2 nm and width of 15 nm, and exhibited rather similar lenticular morphology.

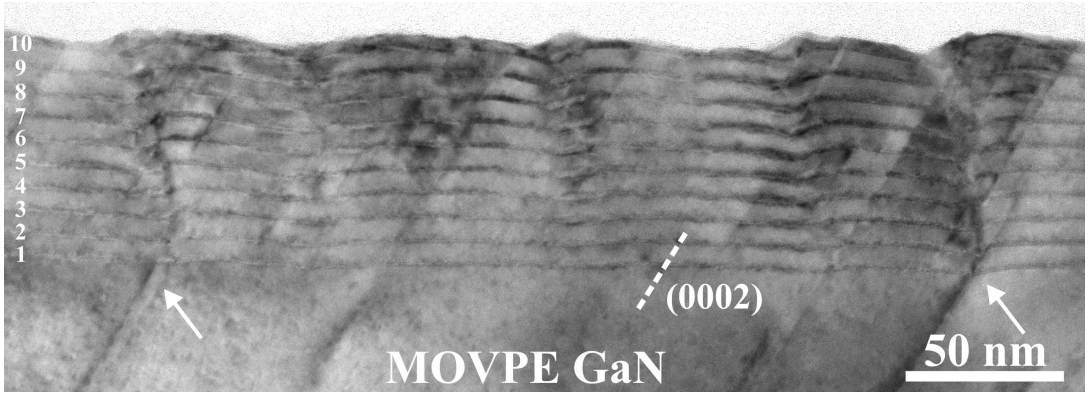

Figure 5.28: TEM image along [1-100] of the low-T semipolar (11-22) sample. Arrows indicate TDs initially inclined on the basal plane that change their orientation inside the InGaN QD superlattice. The orientation of the basal plane is indicated by a dotted line (TEM images by Ph. Komninou, Aristotle University of Thessaloniki, Greece).

Figures 5.29(a) and (b) depict HRTEM images of semipolar samples grown at low T_S. The average height of the InGaN layers is about the same as in the high-T_S case and the QDs are not easily discriminated (see figure 5.29(b)).

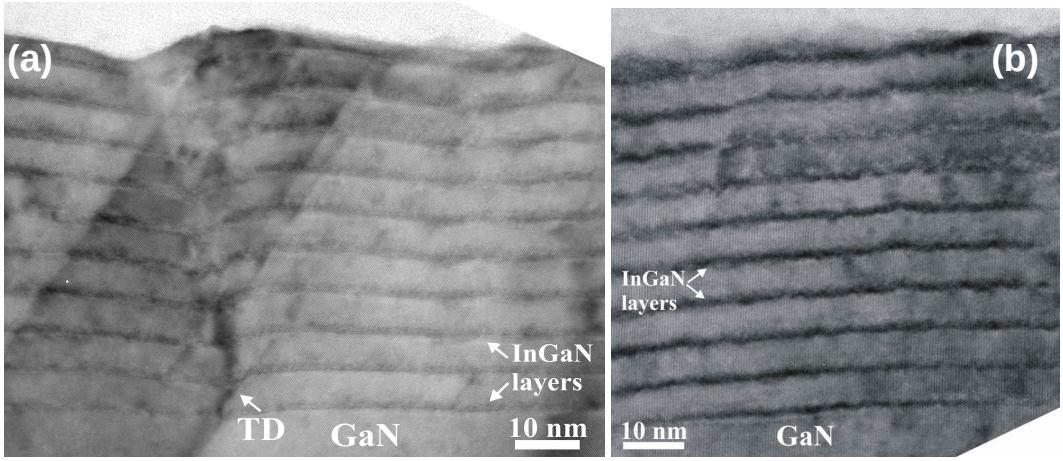

Figure 5.29: (a) HRTEM image along [1-100]$_{GaN}$ showing a TD that disturbs growth along the (11-22) orientation and resulting in formation of inclined QDs along orientations different from the (11-22).(b)HRTEM image along [-1-123]$_{GaN}$ showing continuous InGaN layers. The QDs are not easily discriminated and the layers have a corrugated form (TEM images by Ph. Komninou, Aristotle University of Thessaloniki, Greece).

Regarding the low-T_S polar sample, the superlattice structure is heavily distorted by multiple basal plane stacking faults (BSFs) and associated partial dislocations, shown in figure 5.30. Overlapping of these BSFs results in local transformations of the wurtzite …ABAB… stacking sequence to the sphalerite …ABCABC… one and thus formation of cubic 'pockets'. The introduction of the BSFs should be attributed to the low growth temperature, which causes low adatom

mobility for GaN growth. As shown in figure 5.30(b), clearly resolved QDs could not be distinguished, due to the structural distortion.

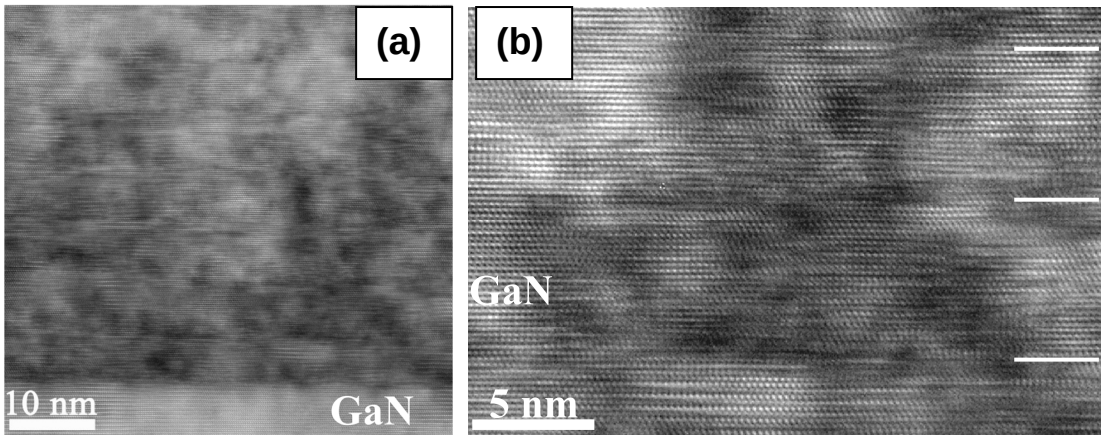

Figure 5.30: (a) HRTEM image of the low-T polar sample along [11-20] zone axis. (b) A magnified view showing the three InGaN layers with positions denoted by white lines. The structure is distorted by a high BSF density and the QDs cannot be clearly distinguished (TEM images by Ph. Komninou, Aristotle University of Thessaloniki, Greece).

The optical performance of the InGaN QDs was investigated by PL measurements. Low temperature (T = 7 K) PL spectra from semipolar and polar QDs grown at various T_S are shown in figure 5.31. For ease of understanding, I included the PL spectra from the QDs samples grown at high temperature (T_S = 650-510^{o}C) along with the PL spectra of low- T_S grown samples. In general, for high-T_S growth, we observe a red shift of the emission wavelength when decreasing T_S. In the case of low-T_S growth, same like in high T_S growth luminescence from semipolar InGaN QDs is systematically blue-shifted in comparison to the respective polar samples grown simultaneously. Here the spectral shift of the emission from semipolar QDs is consistent with the Ga/In flux ratio. In contrast, in this T_S range, the only emission from polar QDs is a broad band located around 630 nm wavelength, which correspond to the spectral location of the yellow band in cubic GaN [Wu97], which is justified in view of the crystalline structure described in figure 5.30.

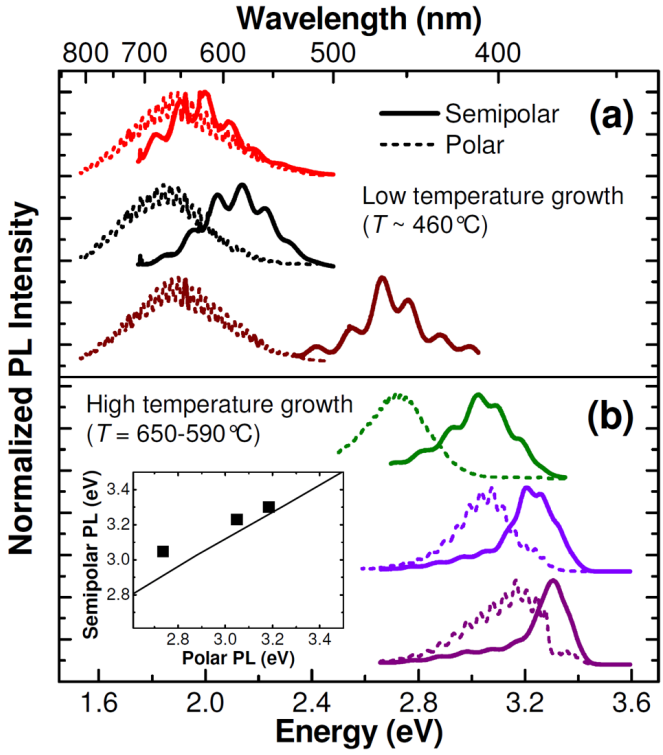

Figure 5.31: Low temperature (T = 7 K) PL spectra from semipolar and polar QDs grown (a) at low T_S and (b) at high T_S. In both figures, the spectra have been normalized and vertically shifted for clarity. The oscillations superimposed to the spectra are due to Fabry-Perot interference associated to the nitride epilayer thickness (~ 1 µm for semipolar samples and ~ 10 µm for polar samples).

Figure 5.32(a) compares the evolution of the integrated PL intensity in polar InGaN QWs and in polar and semipolar InGaN QDs, all emitting around 410 nm. The improved thermal stability of polar QDs over QWs as a result of the 3D carrier confinement has been reported [Dam99, Sén07, Gač11]. Similar to polar QDs, the emission from semipolar QDs remains stable up to ~ 100 K, which points to a comparable confinement. However, the faster drop of efficiency for higher temperatures indicates an enhancement of nonradiative recombination. The thermal stability of the PL from semipolar QDs improves for emission at longer wavelengths (Figure 5.32(b)).

By fitting the data in figure 5.32 to the equation (5.3) assuming a single activation energy, I obtained the results summarized in Table 5.5. The values of $E_A = 95 \pm 15$ eV are significantly higher than the $E_A = 11 \pm 4$ eV measured in polar InGaN/GaN QWs (see table 5.4), which is a confirmation of 3D confinement. For high-T_S growth, the values of *a* confirm an enhancement of nonradiative

recombination in semipolar QDs compared to their polar counterparts. However, low T_S results in an improvement of the semipolar QD efficiency.

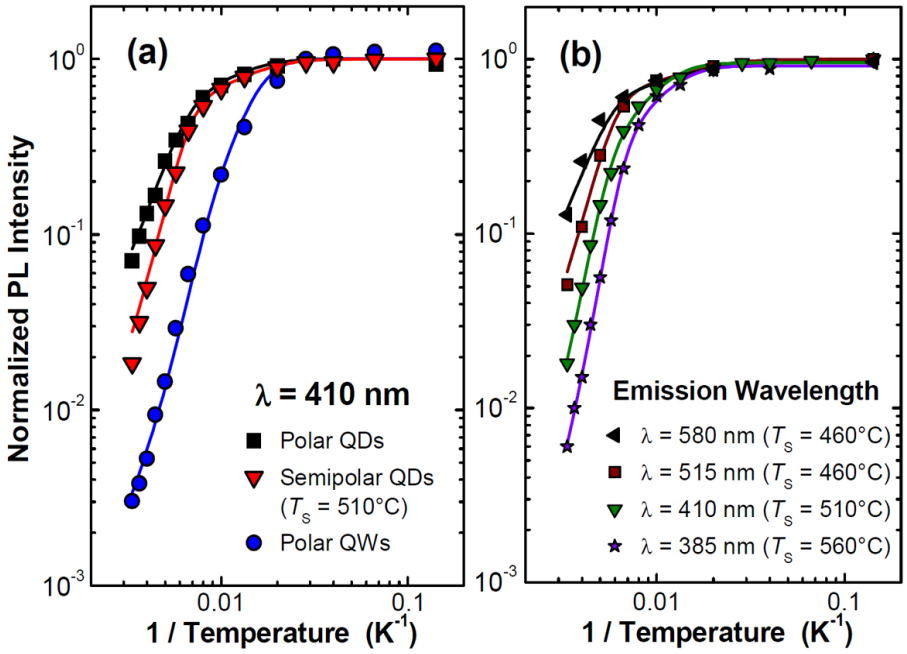

Figure 5.32: Variation of PL intensity with temperature. (a) Comparison of polar and semipolar (T_S = 510°C) InGaN/GaN QDs and polar QWs, all of them emitting at ~ 410 nm wavelength. (b) Semipolar InGaN/GaN QDs grown at different temperatures.

Sample	T_S [°C]	Orientation	Emission wavelength at T = 7 K [nm]	E_A [meV]	a
E 2251	560	Semipolar	385	105	1800
		Polar	407	96	190
E2254	510	Semipolar	410	110	780
		Polar	450	89	68
E2400	460	Semipolar	515	110	620
		Polar	--	--	--
E2402	460	Semipolar	580	74	280
		Polar	--	--	--

Table 5.5: Calculated E_A and a values of polar and semipolar InGaN/GaN QD samples grown simultaneously at various substrate temperatures.

Figure 5.33 presents the evolution of the PL peak energy with temperature for semipolar InGaN QDs, showing a clear deviation from Varshni's equation, which points out the relevance of potential fluctuations within the QDs. In polar QDs, these

intra-dot carrier localization is only observed for samples with high In content (emission wavelength >440 nm), and is attributed to alloy fluctuations within the QDs in the scale of the exciton radius (~ 2.8 nm for GaN), as verified by HRTEM. In semipolar QDs, the presence of defects provides additional sources of potential fluctuations.

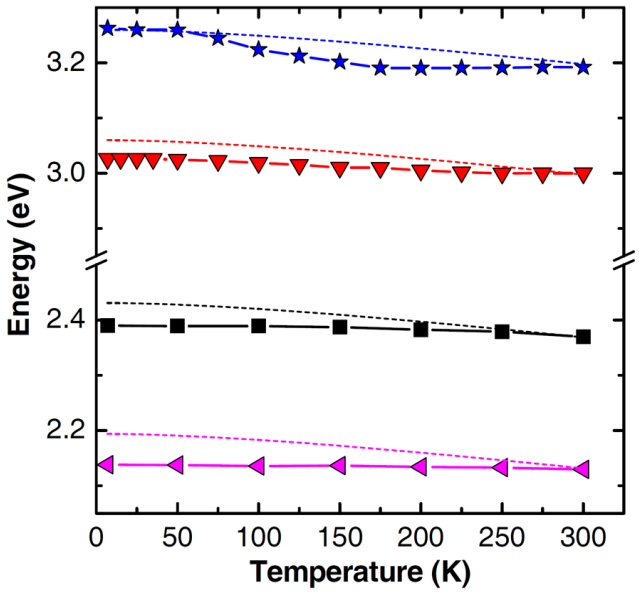

Figure 5.33: Temperature dependence of the PL peak position for the semipolar InGaN/GaN QD stacks in figure 5.32(b). Dashed lines indicate the theoretical evolution of the bandgap with temperature calculated using Varshni's equation.

5.7 Lattice strain and indium content in the InGaN QDs

Strain measurements, from the polar and semipolar QDs samples grown at high and low temperature ranges, were performed at Aristotle University of Thessaloniki, under the supervision of Dr. G.P. Dimitrakopulos [Kou12] and I will summarize the results in this section.

Figure 5.34 shows HRTEM images of the high and low-T semipolar and polar samples along with their corresponding lattice strain maps and strain profiles along the growth direction. The average lattice strain along the growth direction was determined using geometrical phase analysis (GPA) [Hÿt98].

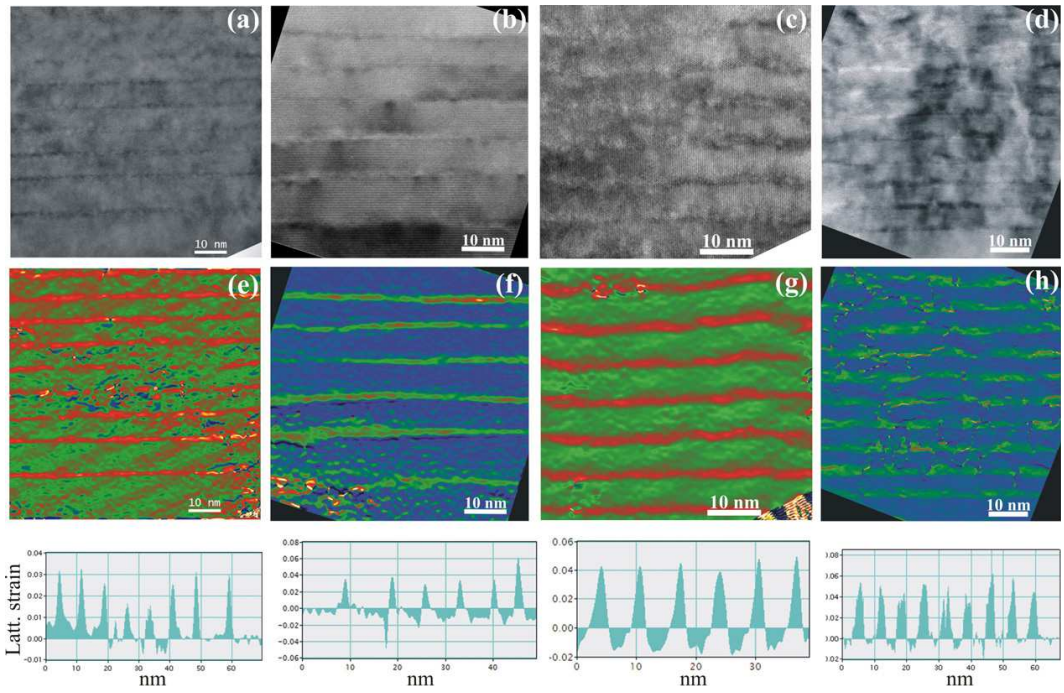

Figure 5.34: HRTEM images of (a) high-T semipolar along [11-2-3], (b) high-T polar sample along [11-20], (c) low-T semipolar sample along [11-2-3], (d) low-T polar sample along [1-100]. (e)–(h) Corresponding 2D maps of lattice strain and strain profiles along the growth direction obtained by GPA.

GPA provides a measurement of the deformation of the lattice along the growth axis, ε_{zz}^{l}, with respect to the ideal value for GaN, d_{GaN}. The value of strain along the growth direction for InGaN, ε_{zz}, is obtained using: $d_{GaN}\left(1+\varepsilon_{zz}^{l}\right)=d_{InGaN}\left(1+\varepsilon_{zz}\right)$, where d_{InGaN} is the interplanar spacing along the growth direction for relaxed InGaN. The In content can be estimated from the previous equation assuming biaxial strain. This is a reasonable assumption given the small aspect ratio of these QDs. For our calculation, the lattice and elastic constants of InGaN were linearly extrapolated from those of InN and GaN [Mor09] and the band gap bowing parameter was taken as 1.4eV [Mos10]. The results are listed in Table 5.6, together with the PL energy of the samples. Based on the estimated In concentration, the expected band gap and emission energy was calculated using the nextnano[3] one-dimensional Schrödinger-Poisson solver. The experimental PL peak energy is slightly lower than the calculations using the structurally-determined values, which can be explained by alloy fluctuations. In the case of high T_S growth, the lower In incorporation in the semipolar samples is confirmed. A similar conclusion cannot be attained for the low T_S case since the polar sample contains a very large defect

density which causes partial strain relaxation, and hence the In concentration is underestimated.

	High-T_S semipolar	**High-T_S polar**	**Low-T_S semipolar**	**Low-T_S polar**
Ga/N flux ratio	30%	30%	50%	40%
Emission energy at T = 7 K (eV)	3.02	2.76	2.21	--
ε_{zz}^{l}	3.2 ± 0.8 %	4.3 ± 0.6 %	5.5 ± 0.7 %	4.9 ± 0.4%
X	0.15 ± 0.04	0.25 ± 0.04	0.32 ± 0.04	0.29 ± 0.03
Calculated E_g (eV)	3.01 ± 0.15	2.92 ± 0.14	2.47 ± 0.13	2.82 ± 0.10
Calculated emission energy (eV)	3.17	2.83	2.66	2.68

Table 5.6: Measurements of lattice strain ε_{zz}^{l} along the growth direction, and derived indium content of $In_xGa_{1-x}N$ assuming biaxial strain. Calculated $In_xGa_{1-x}N$ bandgap (E_g) and QD emission energy obtained using the nextnano[3] software with the deduced In mole fraction, an $In_xGa_{1-x}N$ bowing parameter of 1.4 eV, a low temperature InN bandgap of 0.7 eV.

5.8 Conclusions

In summary, we have successfully fabricated SLs of GaN/AlN and InGaN/GaN QDs, both in polar (0001) and semipolar (11-22) orientations, using PAMBE. The 3D nature of the structures has been verified using AFM and TEM. PL measurements confirm the superior room-temperature emission efficiency of the QD structures as compared to the respective QWs, as a result of the 3D carrier localization.

The synthesis of polar GaN/AlN QDs was possible by two methods: either by GaN deposition under N-rich conditions or by GaN deposition under Ga-rich conditions followed by a growth interruption. In both cases, GaN QDs are hexagonal truncated pyramids with {1-103} facets and optical studies showed that potential fluctuations inside the QDs are negligible. Whereas during semipolar GaN/AlN QDs growth, two types of QDs, sitting either on the (11-22) plane or on the inclined crystallographic plane, were formed due to the large density of defects present in the growth front and is confirmed by HRTEM. The low temperature PL measurements

and time-resolved PL measurements confirmed the reduction of the internal electric field in the semipolar GaN/AlN QDs in comparison with polar structures.

The influence of the growth temperature on the optical and structural properties of the polar and semipolar InGaN QDs has been also studied, considering growth at high temperature (T_S = 650–510 °C, where In desorption is active) and at low temperature (T_S = 460–440 °C, where In desorption is negligible). Polar QDs grown at high-T_S showed better thermal stability of their luminescence than that of the semipolar QDs, due to the higher density of structural defects in the semipolar heterostructure. But Low-T_S growth conditions are not compatible with polar plane (0001) whereas they provide a favorable environment to semipolar plane (11-22) to enhance the internal quantum efficiency of InGaN nanostructures. I have synthesized semipolar InGaN (11-22) QDs emitting in the 380–700 nm spectral range and to the best of our knowledge, this is the first demonstration of semipolar (11-22) InGaN/GaN QDs.

Bibliography

[Ade00] C. Adelmann, J. Simon, G. Feuillet, N. T. Pelekanos, B. Daudin, and G. Fishman, *Self-assembled InGaN quantum dots grown by molecular-beam epitaxy* Applied Physics Letters 76, 1570 (2000).

[Ams07] B. Amstatt, J. Renard, C. Bougerol, E. Bellet-Amalric, B. Gayral, and B. Daudin, *Growth of* m-*plane GaN quantum wires and quantum dots on* m-*plane 6H-SiC.* Journal Applied Physics 102, 074913 (2007).

[Ara82] Y. Arakawa and H. Sakaki, *Multidimensional quantum well laser and temperature dependence of its threshold current.* Applied Physics Letters 40, 939 (1982).

[Cho97] Y.-H. Cho, G. H. Gainer, A. J. Fisher, J. J. Song, S. Keller, U. K. Mishra, and S. P. DenBaars, *"S-shaped" temperature-dependent emission shift and carrier dynamics in InGaN/GaN multiple quantum wells.* Applied Physics Letters 73, 1370 (1997).

[Dam99] B. Damilano, N. Grandjean, S. Dalmasso, and J. Massies, *Room-temperature blue-green emission from InGaN/GaN quantum dots made by strain-induced islanding growth.* Applied Physics Letters 75, 3751 (1999).

[Dim10] G.P. Dimitrakopulos, E. Kalesaki, J. Kioseoglou, Th. Kehagias, A. Lotsari, L. Lahourcade, E. Monroy, I. Hausler, H. Kirmse, W. Neumann, G. Jurczak, T.D. Young, P. Dłuzewski, Ph. Komninou and Th. Karakostas, *Morphology and strain of self-assembled semipolar GaN quantum dots in (11-22) AlN.* Journal of Applied Physics 108, 104304 (2010).

[Dus03] A. Dussaigne, B. Damilano, N. Grandjean, and J. Massies, *In surface segregation in InGaN/GaN quantum wells.* Journal of Crystal Growth 251, 471 (2003).

[Eli97] P. G. Eliseev, P. Perlin, J. Lee, and M. Osinski, *"Blue" temperature-induced shift and band-tail emission in InGaN-based light sources.* Applied Physics Letters 71, 569 (1997).

[Fou05] S. Founta, F. Rol, E. Bellet-Amalric, J. Bleuse, B. Daudin, B. Gayral, H. Mariette, and C. Moisson, *Optical properties of GaN quantum dots grown on nonpolar (11-20) SiC by molecular-beam epitaxy.* Applied Physics Letters 86, 171901 (2005).

[Gač11] Ž. Gačević, A. Das, J. Teubert, Y. Kotsar, P. K. Kandaswamy, Th. Kehagias, T. Koukoula, Ph. Komninou, and E. Monroy, *Internal quantum efficiency of III-nitride quantum dot superlattices grown by plasma-assisted molecular-beam epitaxy.* Journal of Applied Physics 109, 103501 (2011).

[Gog03] N. Gogneau, D. Jalabert, E. Monroy, T. Shibata, M. Tanaka, and B. Daudin, *Structure of GaN quantum dots grown under "modified Stranski–Krastanow" conditions on AlN.* Journal of Applied Physics 94, 2254 (2003)

[Gog04] N. Gogneau, F. Fossard, E. Monroy, S. Monnoye, H. Mank, and B. Daudin, *Effect of stacking on the structural and optical properties of self-assembled GaN/AlN quantum dots,* Applied Physics Letters 84, 4224 (2004)

[Gui06] F. Guillot, E. Bellet-Amalric, E. Monroy, M. Tchernycheva, L. Nevou, L. Doyennette, F. H. Julien, Le Si Dang, T. Remmele, M. Albrecht, T. Shibata and M. Tanaka, *Si-doped GaN/AlN quantum dot superlattices for optoelectronics at telecommunication wavelengths.* Journal of Applied Physics 100, 044326 (2006)

[Hof10] D. Hofstetter, J. Di Francesco, P. K. Kandaswamy, A. Das, S. Valdueza-Felip, and E. Monroy, *Performance Improvement of AlN–GaN-Based Intersubband Detectors by Using Quantum Dots*, IEEE Photon. Technol. Lett. 15, 1087 (2010)

[Hum07] C.J. Humphreys, *Does In form In-rich clusters in InGaN quantum wells?* Philosophical Magazine 87, 1971 (2007).

[Hÿt98] M. J. Hÿtch, E. Snoeck, and R. Kilaas, *Quantitative measurement of displacement and strain fields from HREM micrographs.* Ultramicroscopy 74, 131 (1998).

[Kou12] T. Koukoula, A. Lotsari, Th. Kehagias, G.P. Dimitrakopulos, I. Häusler, A. Das, E. Monroy, Th. Karakostas and Ph. Komninou, *Structure and strain state of polar and semipolar InGaN quantum dots.* Applied Surface Science (2012).

[Lah09] L. Lahourcade, S. Valdueza-Felip, T. Kehagias, G. P. Dimitrakopulos, P. Komninou, and E. Monroy, *Stranski-Krastanow growth of (11-22)-oriented GaN/AlN quantum dots,* Applied Physics Letters 94, 111901 (2009)

[Lef01] P. Lefebvre, T. Taliercio, A. Morel, J. Allegre, M. Gallart, B. Gil, H. Mathieu, B. Damilano, N. Grandjean, and J. Massies, *Effects of GaAlN barriers and of dimensionality on optical recombination processes in InGaN quantum wells and quantum boxes.* Applied Physics Letters 78, 1538 (2001).

[Lei10] H. Lei, J. Chen and P. Ruterana, *Influences of the biaxial strain and* c*-screw dislocation on the clustering in InGaN alloys.* Journal of Applied Physics 108, 103503 (2010).

[Ler99] M. Leroux, N. Grandjean, B. Beaumont, G. Nataf, F. Semond, J. Massies, and P. Gibart, *Temperature quenching of photoluminescence intensities in undoped and doped GaN.* Journal of Applied Physics 86, 3721 (1999).

[Li03] X. Li, Y. Wu, D. Steel, D. Gammon, T. H. Stievater, D. S. Katzer, D. Park, C. Piermarocchi and L. J. Sham, *An All-Optical Quantum Gate in a Semiconductor Quantum Dot.* Science 301, 809 (2003).

[Mat74] J.W. Matthews and A.E. Blakeslee, *Defects in epitaxial multilayers: I. Misfit dislocations.* Journal of Crystal Growth 27, 118 (1974).

[Mei07] J. Mei, R. Liu, F.A. Ponce, H. Omiya and T. Mukai, *Basal-plane slip in InGaN/GaN heterostructures in the presence of threading dislocations.* Applied Physics Letters 90, 171922 (2007).

[Mie09] P. De Mierry, T. Guehne, M. Nemoz, S. Chenot, E. Beraudo, and G. Nataf, *Comparison between Polar (0001) and Semipolar (1122) Nitride Blue–Green Light-Emitting Diodes Grown on c- and m-Plane Sapphire Substrates.* Japanese Journal of Applied Physics 48, 031002 (2009).

[Mon03] E. Monroy, B. Daudin, E. Bellet-Amalric, N. Gogneau, D. Jalabert, F. Enjalbert, J. Brault, J. Barjon, and Le Si Dang, *Surfactant effect of In for AlGaN growth by plasma-assisted molecular beam epitaxy.* Journal of Applied Physics 93, 1550 (2003).

[Mor09] F. M .Morales, D. González, J.G. Lozano, R. García, S. Hauguth-Frank, V. Lebedeve, V. Cimalla, and O. Ambacher, *Determination of the composition of $In_xGa_{1-x}N$ from strain measurements.* Acta Materialia 57, 5681 (2009).

[Mos10] P. G. Moses and C. G. Van de Walle, *Band bowing and band alignment in InGaN alloys.* Applied Physics Letters 96, 021908 (2010).

[Neu03] J. Neugebauer, T. K. Zywietz, M. Scheffler, J. E. Northrup, H. Chen, and R. M. Feenstra, *Adatom Kinetics On and Below the Surface: The Existence of a New Diffusion Channel.* Physical Review Letters 90, 056101 (2003).

[Nor99] J.E. Northrup, L.T. Romano and J. Neugebauer, *Surface energetics, pit formation, and chemical ordering in InGaN alloys.* Applied Physics Letters 74, 2319 (1999).

[Rol07] F. Rol, S. Founta, H. Mariette, B. Daudin, Le Si Dang, J. Bleuse, D. Peyrade, J.-M. Gerard, and B. Gayral, *Probing exciton localization in nonpolar GaN/AlN quantum dots by single-dot optical spectroscopy.* Physical Review B 75, 125306 (2007).

[Sar05] E. Sarigiannidou, E. Monroy, B. Daudin, J.L. Rouvière, and A.D. Andreev, *Strain distribution in GaN/AlN quantum-dot superlattices.* Applied Physics Letters 87, 203112 (2005)

[Sén07] M. Sénès, K. L. Smith, T. M. Smeeton, S. E. Hooper, and J. Heffernan, *Strong carrier confinement in $In_xGa_{1-x}N$/GaN quantum dots grown by molecular beam epitaxy.* Physical Review B 75, 045314 (2007).

[Sim03] J. Simon, N. T. Pelekanos, C. Adelmann, E. Martinez-Guerrero, R. Andre, and B. Daudin, L. S. Dang, and H. Mariette, *Direct comparison of recombination dynamics in cubic and hexagonal GaN/AlN quantum dots.* Physical Review B 68, 035312 (2003).

[Ste06] R. M. Stevenson, R. J. Young, P. Atkinson, K. Cooper, D. A. Ritchie and A. J. Shields, *A semiconductor source of triggered entangled photon pairs.* Nature 439, 179 (2006).

[Str06] S. Strauf, K. Hennessy, M. T. Rakher, Y.-S. Choi, A. Badolato, L. C. Andreani, E. L. Hu, P. M. Petroff and D. Bouwmeester, *Self-Tuned Quantum Dot Gain in Photonic Crystal Lasers.* Physical Review Letters 96, 127404 (2006).

[Tch06] M. Tchernycheva, L. Nevou, L. Doyennette, F. H. Julien, E. Warde, F. Guillot, E. Monroy, E. Bellet-Amalric, T. Remmele and M. Albrecht, *Systematic experimental and theoretical investigation of intersubband absorption in GaN/AlN quantum wells.* Physical Review B 73, 125347 (2006).

[Ter96] J. Tersoff, C. Teichert, and M. G. Lagally, *Self-Organization in Growth of Quantum Dot Superlattices.* Physical Review Letters 76, 1675 (1996)

[Uso07] S.O. Usov, A.F. Tsatsulnikov, V.V. Lundin, A.V. Sakharov, E.E. Zavarin, D.S. Sizov, Yu G. Musikhin, N.A. Bert, E.M. Arakcheeva and N.N. Ledentsov, *Analysis of the local indium composition in ultrathin InGaN layers.* Semiconductor Science and Technology 22, 528 (2007).

[Wal02] P. Waltereit, O. Brandt, K. H. Ploog, M. A. Tagliente, and L. Tapfer, *In surface segregation during growth of (In,Ga)N/GaN multiple quantum wells by plasma-assisted molecular beam epitaxy.* Physical Review B 66, 165322 (2002).

[Wu97] J. Wu, H. Yaguchi, K. Onabe, R. Ito, and Y. Shiraki, *Photoluminescence properties of cubic GaN grown on GaAs(100) substrates by metalorganic vapor phase epitaxy*. Applied Physics Letters 71, 2067 (1997).

Chapter 6

Opto-chemical sensors based on (In)GaN QDs as optical transducers

The chapter begins by explaining different opto-chemical transducer structures, including the polar GaN/AlN QDs, semipolar GaN/AlN QDs, polar InGaN/GaN QDs and semipolar InGaN/GaN QDs transducers. Then, I describe the fabrication of QD transducer structures and its characterization, mainly the dependence of luminescence characteristics on electric fields. Details of the integrated chemical sensor based on InGaN QDs transducer is presented at the end of this chapter.

6.1 Introduction

The detection of chemical processes using semiconductor nanostructures has become a field of increasing interest during the past few years. The objective of our project (DOTSENSE) was the application of III-nitride QDs as opto-chemical transducers for the detection of hydrogen, hydrocarbons and the pH-value in gaseous and liquid environments. So in this project, we are combining the optical properties of III-nitrides (transparency, direct bandgap, efficient luminescence) with their chemical surface properties in order to develop novel kinds of opto-chemical sensor systems. The characteristics of intense room-temperature luminescence from III-nitride nanostructures can be altered by chemically-induced variations of the surface potential. The transparency of the substrate material and the involved buffer layers allow optical excitation and detection of the changes in QD luminescence from the substrate backside. These transducers are hence capable of operating in harsh environments (high pressure, explosive media), as neither electrical feedthroughs nor a deterministic current are necessary for the sensor signal read-out. Furthermore, spatially-resolved detection of variations in the surface potential is possible, since the spatial extension of excited nanostructures is determined by the diameter of the incident light beam. In this chapter I describe the growth and characterization of the transducer structures, which I performed at CEA, and I summarize the results of characterization under electrical or chemical stress performed by the groups of Prof. M. Eickhoff, at Justus Liebig University in Giessen, and Dr. A. Helwig, at EADS in Munich.

6.2 Description of the opto-chemical transducers

The transducer structure had to fulfil the following requirements for their application in the targeted chemical sensor device:

- High luminescence intensity at room temperature
- High sensitivity of the luminescence intensity to H_2 exposure (application in gas atmosphere) and to changes in the pH of the electrolyte solution (application in liquid environment)
- High electrochemical stability for application in liquids
- Luminescence excitable and detectable with commercial light emitters and detectors
- Capability for integration into the optical sensor unit (spectral separation of excitation and emission energy)

So during this project work, different transducer structures were investigated and taken into consideration for the realization of the target device structure:

- Polar GaN /AlN quantum dot superlattices (QDSLs)
- GaN/AlN QDSLs with reduced internal electric field
- Polar InGaN/GaN QDSLs
- InGaN/GaN QDSLs with reduced internal electric field

These transducers will be integrated with commercially-available light emitters and detectors to form a complete sensor system. Therefore, the excitation wavelength should be commercially available and far enough from the emission energy. Based on the availability of commercial light emitters, we decided to fix 420-450 nm as the targeted spectral range for the final devices. Note that this wavelengths can be attained both by GaN/AlN QDs (thanks to the electric field induced by the spontaneous polarization) or by InGaN/GaN QDs. On the other hand, to make it possible to excite through the transducer substrate, all the buffer and back-contact layers must be transparent to the excitation wavelength, which implies that wider band gap is desirable for the buffer and contact layers. In addition, the formation of QDs by the Stranski-Krastanow growth method requires compressive strain in the QD layer. As a result, a small lattice parameter is preferred for the buffer and contact

layers. However, the contact layer must be conductive to guarantee a homogeneous electric field in the active layer. The conductivity decreases for increasing band gap, which sets a limit to the transparency of the contact layer. In view of all these points, we considered AlGaN with an Al mole fraction in the 30-40% range as a contact layer.

6.3 Polar GaN/AlN QDs opto-chemical transducers

In a first approach, we studied the behavior of GaN/AlN QD opto-chemical transducers grown on polar surfaces. To analyze the impact of variation in the surface potential on the luminescence characteristics, GaN QD multilayers were grown on a highly Si-doped ([Si] = $5x10^{19}cm^{-3}$) AlGaN layer with an Al concentration of ~40%, which served as a backside-contact.

6.3.1 Synthesis and characterization

In a first approach to tune the QD emission to the desired wavelength range, I have grown a series of 3-period GaN/AlN QDs samples with 7 nm thick barriers and cap layer, changing the growth conditions of the QDs and the amount of GaN deposited. The QD structures were grown on 1 μm thick (0001)-oriented AlN-on-sapphire templates. Growth was initiated by the deposition of a ~550 nm thick Si-doped $Al_{0.5}Ga_{0.5}N$ layer at 680°C using In as a surfactant [Mon03], at a growth rate of 0.3 ML/s. Subsequently, the substrate temperature is increased to 720°C for the growth of the QDSL. The formation of self-assembled QDs on the surface of AlN spacer is achieved either by deposition of GaN under N-rich conditions at a growth rate of 0.25 ML/s or under Ga-rich conditions at a N-limited growth rate of 0.3 ML/s. The amount of GaN in the QD layer varies between 3-6 ML. The synthesis of each GaN QD layer is followed by a growth interruption for 2 min in vacuum. The schematic description of the samples is presented below (Figure 6.1 and Table 6.1), together with their room-temperature PL spectra (Figure 6.2). These results confirm that Ga-rich deposition of the QDs is a requirement to attain the targeted spectral range.

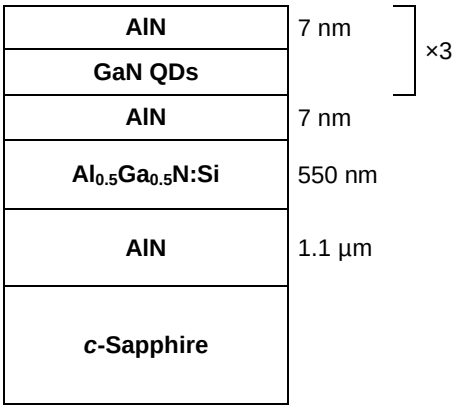

Figure 6.1: Schematic description of the first generation of GaN/AlN QD transducer structures.

Sample	Growth conditions	Amount of GaN in the QD layer	PL peak wavelength
E1760	N rich	6 ML	340 nm
E1763	Ga rich	5 ML	500 nm
E1767	Ga rich	3 ML	430 nm

Table 6.1: Description of the growth conditions and PL peak wavelength of the first generation of GaN/AlN QD transducer structures.

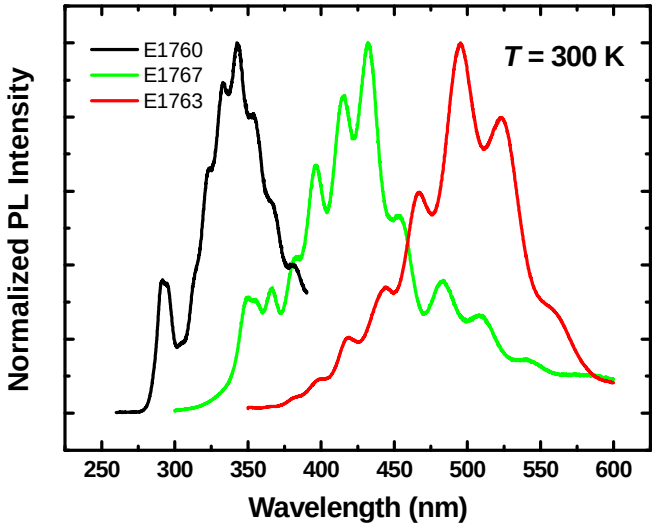

Figure 6.2: Room temperature PL emission from 3-period GaN/AlN QD sensor structures.

The structural quality of the samples is characterized using TEM and the figure 6.3 presents cross-section TEM images from the samples E1763 and E1767. Figures, showing the TDs emanate from the AlN template/AlGaN interface as well as the AlN/Al_2O_3 interface. A good percentage of these TDs annihilates as the layer

thickness increases. The AlGaN/QDSL interface appears uniform and it is not associated to new TDs.

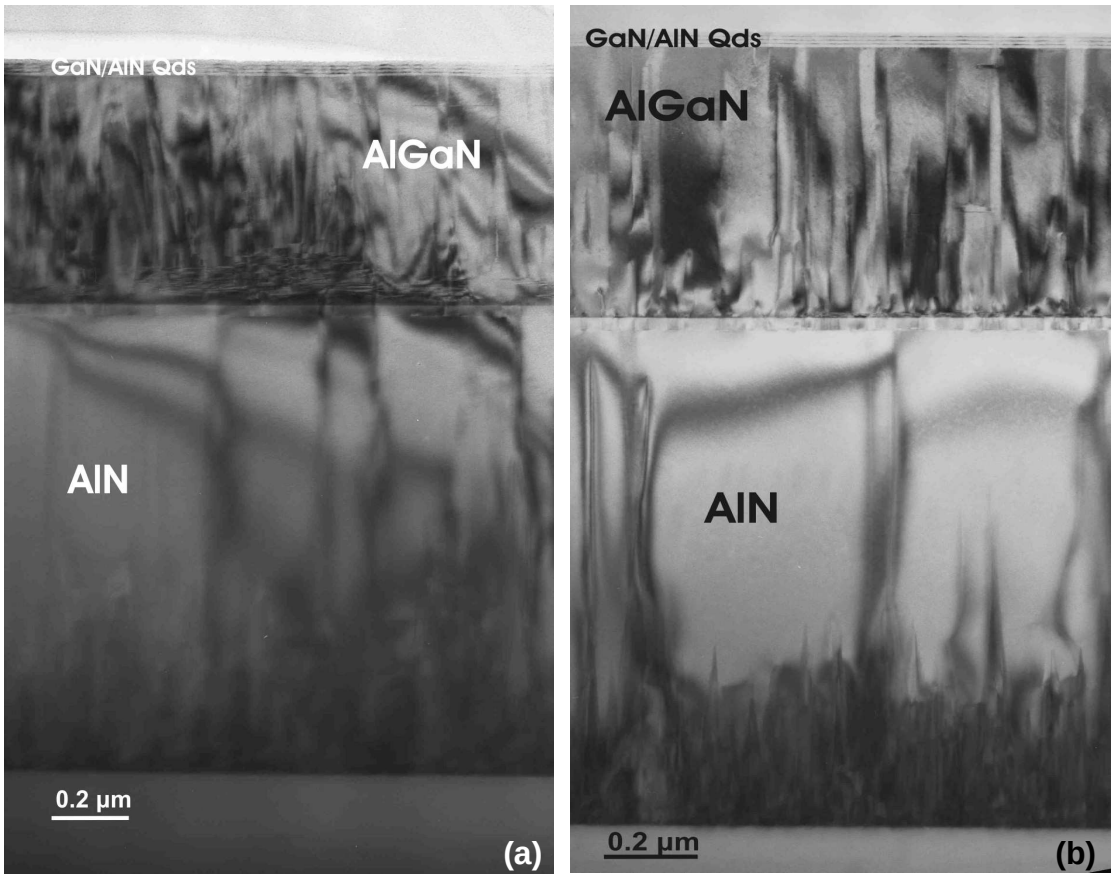

Figure 6.3: Cross-sectional TEM BF images showing the overall structure of the samples (a) from sample E1763 and (b) from sample E1767 (TEM images by Prof. Ph. Komninou, Aristotle University of Thessaloniki, Greece).

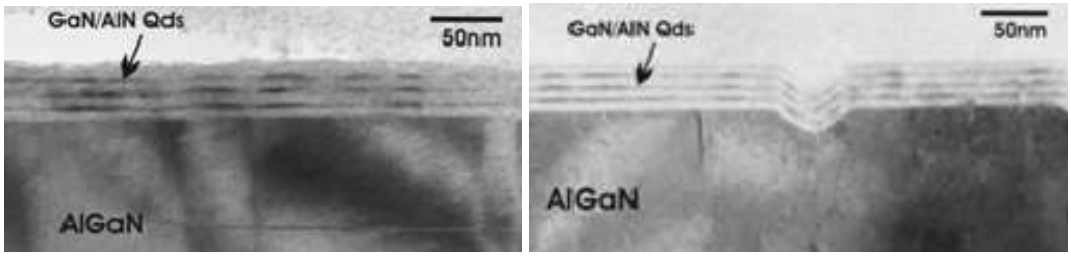

Figure 6.4: XTEM BF images, the top area of the E1763 (left) and E1767 (right) transducer structures respectively (TEM images by Prof. Ph. Komninou, Aristotle University of Thessaloniki, Greece).

Figure 6.4 present a zoomed view the top area of the E1763 and E1767 sensor structure samples, illustrating the 3 layers of GaN/AlN QDs grown on top of the AlGaN contact layer. The stacking of the GaN QDs and the wetting layer are visible

in E1763, while in E1767 due to the small nominal thickness of the GaN QDs, originated from only 3 ML of GaN, the density of the QDs that are formed is rather small compared to that of E1763.

The side-facets of the QDs of E1763 are inclined from 25^{o} up to 33^{o} relative to the basal plane, consistent with {1-103} crystallographic planes. The average size of the dots at their base is approximately 17 nm as measured from HRTEM images (see figure 6.5). The average height of the dots is 10-14 ML, while the wetting layer has thickness of approximately 2 ML.

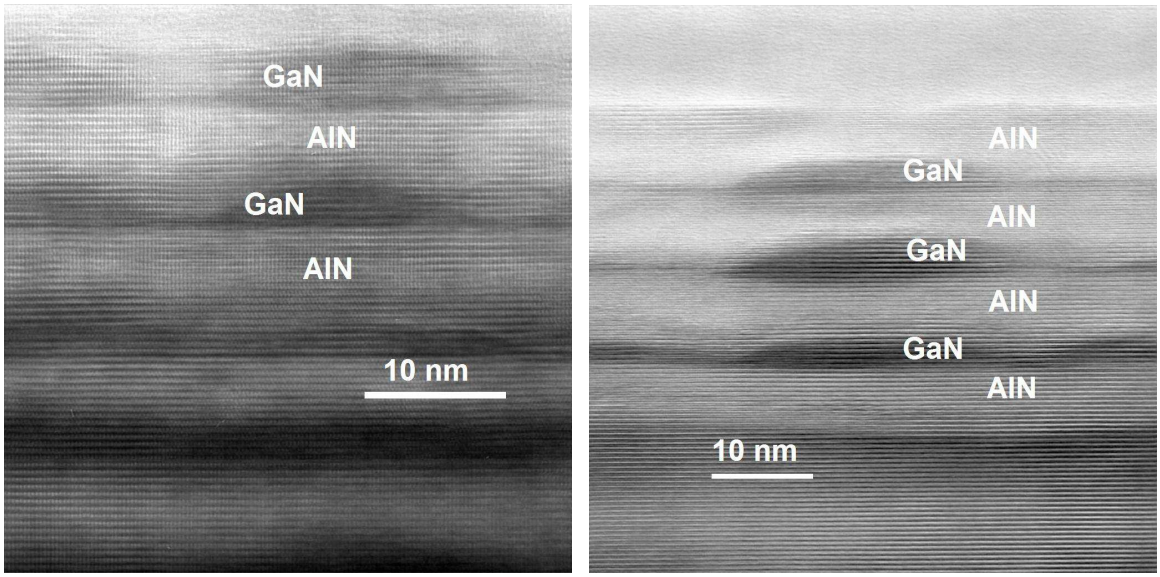

Figure 6.5: HRTEM images from the sample E1763 (HRTEM images by Prof. Ph. Komninou, Aristotle University of Thessaloniki, Greece).

For the realization of the sensor structure, a good external quantum efficiency of the transducer structure at room temperature is mandatory, which is at the origin of the choice of QDs as active structures. To confirm this decision, I have synthesized various QW-based and QD- based structures, to compare their performance. The schematic description of the samples is presented below (Table 6.2 and Figure 6.6).

Sample	GaN nanostructures	AlN barrier thickness
E1962	QW – 3 nm	3 nm
E1963	QW – 3 nm	5 nm
E1964	QD – 5 ML, Ga-rich	5 nm

Table 6.2: Description of the growth parameters of GaN/AlN QW vs. QD structures.

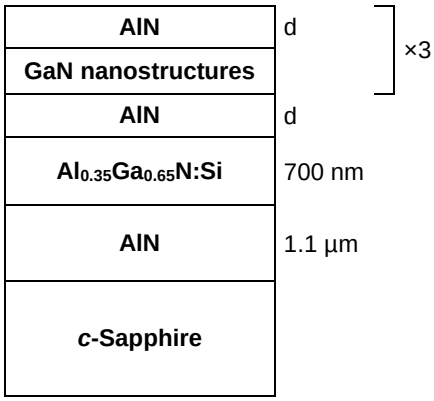

Figure 6.6: Schematic description of GaN/AlN QW vs. QD structures.

The PL spectra of these samples have been measured at low temperature and at room temperature, with the results presented in figure 6.7. The emission from the QD structure decreases by less than one order of magnitude when increasing the measurement temperature. In contrast, the emission from the QWs well resolved at T = 8 K and remains below the noise level at room temperature. This result supports the requirement of QDs as active media, in order to enhance the emission efficiency thanks to the 3D carrier confinement.

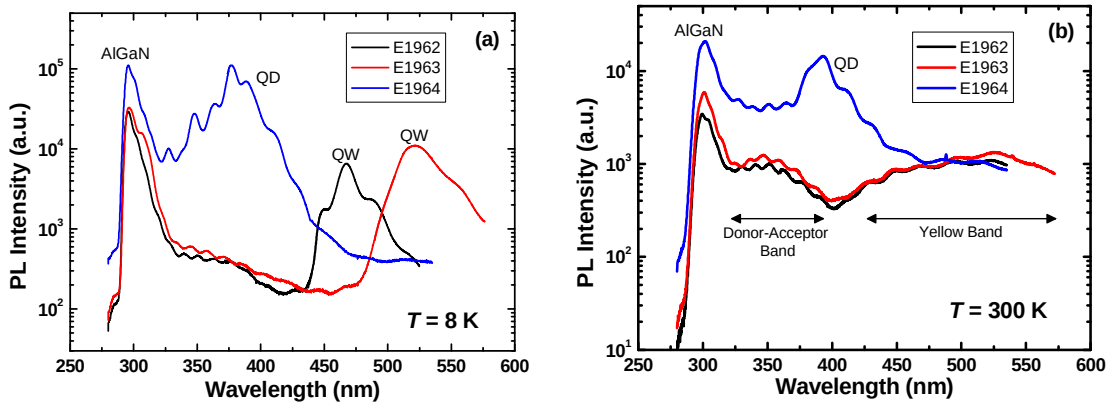

Figure 6.7: PL spectra of samples E1962-63-64 measured (a) at low temperature and (b) at room temperature.

6.3.2 Emission characteristics of GaN QDs in external electric fields

In this section, I will briefly describe the electric field dependent PL characteristics of the GaN/AlN QDSLs. This is a relevant step towards the understanding of the sensor behavior, since chemical variations in the atmosphere result in changes of the surface potential of the sensor. This work was performed by

Dr. Jorg Teubert under the direction of Prof. Martin Eickhoff, at Justus Liebig University in Giessen, Germany. The effect of bias on the emission is studied with variation of different structural parameters, such as QD size, number of QD layers, and spacer thickness, in order to understand the sensing mechanism and define a transducer structure with high sensing performance.

The schematic description of the structure to study the effect of vertical electric fields on the luminescence properties of a GaN/AlN QDSL is shown in figure 6.8. The design of the structures allows the appliance of a preferably homogeneous vertical electric field across the QDSL with a highly Si-doped AlGaN buffer layer acting as conductive back contact. After growth of the QDSL and backside polishing of the sapphire substrate, reactive ion etching in a BCl_3/Cl_2 mixture is used to gain access to the AlGaN:Si back contact layer for Ohmic contact formation. Ti/Au contact pads of 10 nm/300 nm nominal thickness are evaporated onto the AlGaN surface and subsequently annealed for 10 min at 650 °C. For formation of the Schottky top-contact and with respect to one of the target applications as a hydrogen detector, a semitransparent 10 nm thick catalytic Pt film is evaporated and patterned on the front side. As a result, a device as depicted in figure 6.8(b) is obtained, which allows application of vertical electric fields along the growth direction of the sample and across the QDSL.

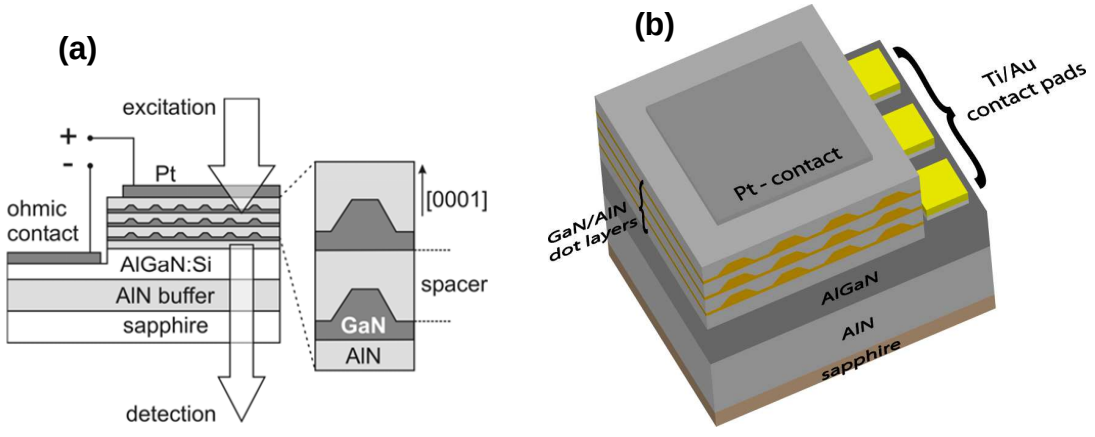

Figure 6.8(a) and (b): Schematic of processed test structure for measurements of the field-dependent luminescence characteristics and for characterization of the hydrogen sensitivity. Measurements of the PL characteristics in the PL microscope were carried out in upsidedown geometry, i.e. by excitation and detection of the PL from the sample backside.

GaN/AlN QDSLs with different AlN spacer thickness (3 nm, 5 nm, 7 nm, 10 nm) are characterized with respect to the effect of an external electric field applied between the conductive AlGaN:Si back contact and the semitransparent Pt top contact. PL spectroscopy was performed by excitation from the sample front side using the 244 nm line of a frequency-doubled Ar ion laser with an estimated power density of 100 mW/cm^2. The luminescence signal was collected from the substrate back side using a DILOR XY 800 mm triple monochromator and a single-channel photomultiplier. In figures 6.9(a) and (b) the dependence of the PL emission on the bias voltage is displayed for samples with a spacer thickness of 7 nm and 3 nm, respectively. For both samples a blue shift of the emission energy with increasing external field (negative bias) can be observed. This behavior can be explained by the external field counteracting the polarization-induced internal electric fields and therefore reducing the emission red-shift due to the polarization-induced quantum confined Stark effect. For samples with thick AlN spacers, 7 nm, this blue shift in emission energy is accompanied by an increase of the emission intensity.

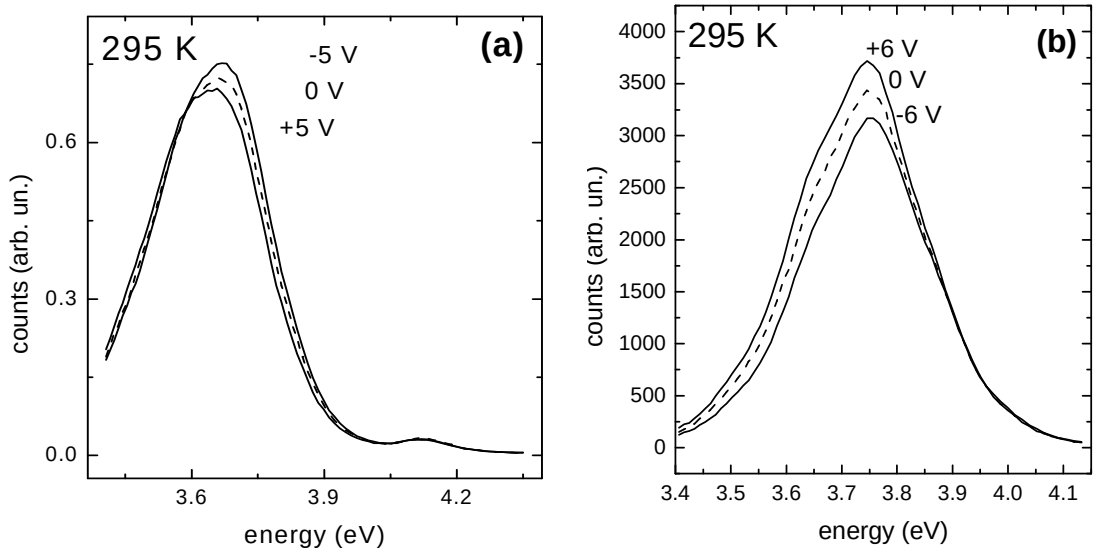

Figure 6.9: Bias dependent photoluminescence spectra of GaN/AlN QDSLs with two different AlN spacer thicknesses: (a) 7 nm and (b) 3 nm.

In contrast, QDSL samples with thin AlN spacers, 3 nm, show a decrease in the emission intensity with increasing external field. The observed decrease in emission intensity for negative bias cannot be explained in terms of the reduction of the QCSE, which, in contrary, should result in an increased radiative transition

probability. The accompanying decrease in emission intensity is explained by a field-assisted tunneling current of photogenerated carriers as a competitive process to radiative carrier recombination inside the QDs [Wei09].

A study of samples with different number of QD layers revealed the general trend that the sensitivity to variations in the external field increases with decreasing number of QD layers.

6.3.3 Hydrogen sensitivity of GaN QDs transducers

The characterization described in this section was performed by Dr. Jorg Teubert under the direction of Prof. Martin Eickhoff, at Justus Liebig University in Giessen, Germany. The electric field underneath the catalytic Pt contact can be altered by adsorption of atomic hydrogen at the Pt/AlN interface after dissociation of molecular hydrogen at the Pt surface, which leads to a decrease of the effective height of the Pt Schottky barrier [Lun75]. Following the considerations described above, this should lead to an increase of the PL intensity for the case of thin AlN spacers and to a decrease for the case of thick AlN spacers, respectively. This behavior is shown in figure 6.10, which shows the transient response of the PL emission intensity at a fixed detection wavelength upon exposure to hydrogen (10%, 100%) in nitrogen and synthetic air for two samples with a spacer thickness of (a) 7 nm, and (b) 3 nm.

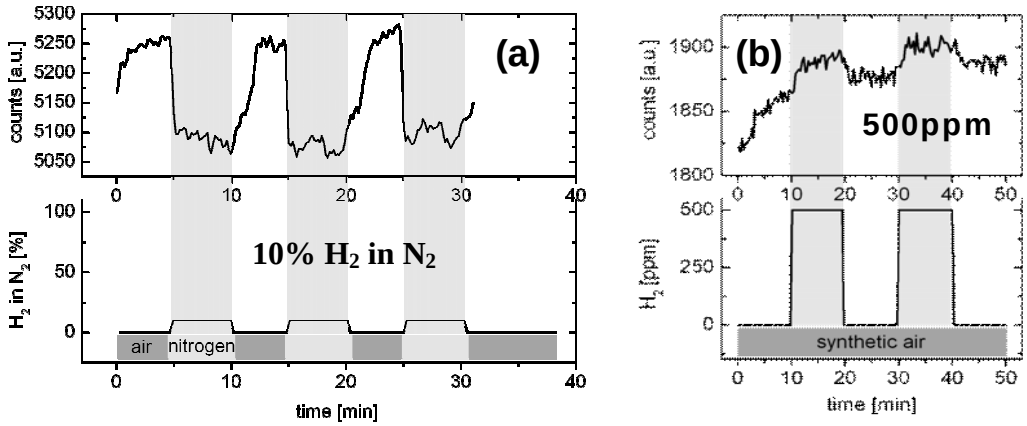

Figure 6.10: Transient hydrogen response of different GaN/AlN QDSL test structures (a) 5 QD layers with 7 nm spacers, (b) 5 QD layers with 3 nm spacers.

In accordance to earlier publications, the device is already saturated at 10% hydrogen concentration [Wei03, Eri05], i.e., even exposure to pure hydrogen atmosphere does not lead to a higher response. On the other hand, a concentration as low as 500 ppm of hydrogen in a synthetic air carrier gas could be clearly resolved (Figure 6.10(b)).

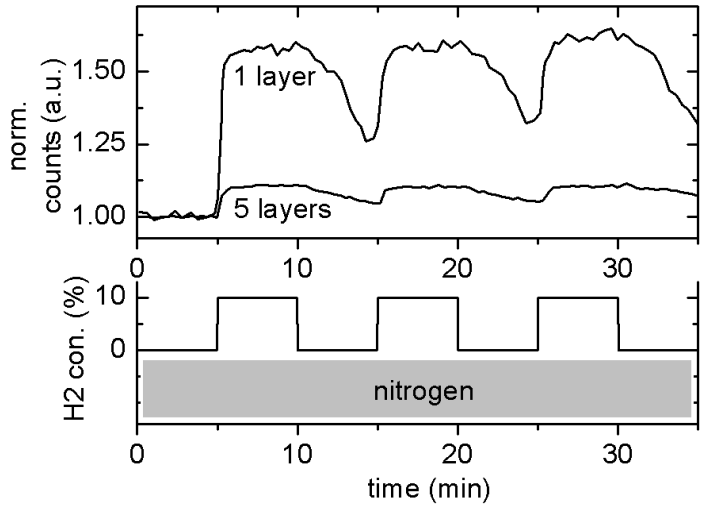

Figure 6.11: Response of the PL intensity to introduction of 10% hydrogen in a nitrogen atmosphere for samples with one and five QD layers. The PL intensity was recorded at a fixed detection wavelength near the emission maximum.

The proposed detection mechanism implies that the adsorption of dissociated hydrogen mainly affects the topmost QD layers, proposing a stronger relative response for structures with a smaller number of layers. This behavior is demonstrated in figure 6.11, where the relative response of a sample with one layer of QDs is compared to that of the QDSL sample with five layers.

6.4 Semipolar GaN QD opto-chemical transducers

I have synthesized semipolar (11-22)-oriented GaN/AlN QD transducer structures following the design in figure 6.12. The AlGaN contact layer has been replaced by an AlGaN/GaN superlattice in order to moderate the surface roughness while keeping a small-enough in-plane lattice parameter to enable QD formation on top. The PL emission from the sample at low temperature and at room temperature is illustrated in figure 6.13. In semipolar structures, the absence of electric field results in a PL emission at higher energies than the GaN bandgap.

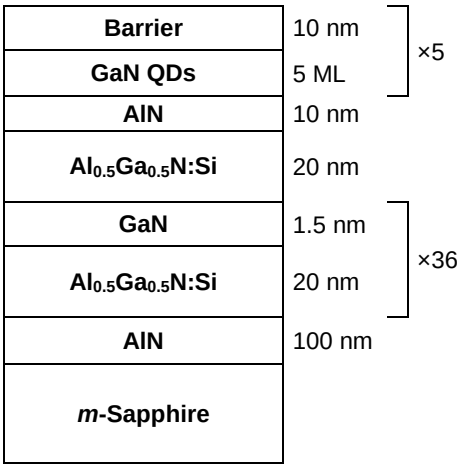

Figure 6.12: Schematic description of the first series of semipolar GaN/AlN QD transducer structures.

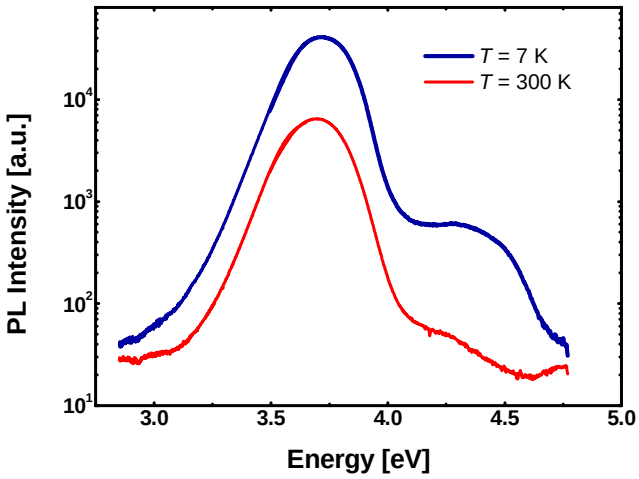

Figure 6.13: PL spectra from the semipolar GaN QD sample measured at low temperature and at room temperature.

Due to the significantly reduced internal electric fields, GaN/AlN QDSLs grown on (11-22) surfaces show enhanced luminescence efficiency, but the emission energy remains systematically higher than the GaN bandgap. A red shift of the emission to the spectral regime that can be covered by commercial LEDs cannot be achieved by controlling the QD size and requires the incorporation of indium in the QDs.

6.5 Polar InGaN QD opto-chemical transducers

6.5.1 Synthesis and characterization

In order to study the sensing performance of InGaN QDs transducer structures, I have synthesized various series of polar InGaN QDSLs. In the final transducer, the QDSL must be deposited on top of an AlGaN contact layer with an Al mole fraction of 30-40%. The presence of this contact layer will modify the strain state of the QD structures, and might affect their formation mechanism. In order to assess the effect of the Al content of the contact layer on the QDSL stack, I have grown a first series of transducers consisting of four samples with different Al mole fraction in the AlGaN contact layer (0%, 10%, 20% and 33%), as illustrated in figure 6.14.

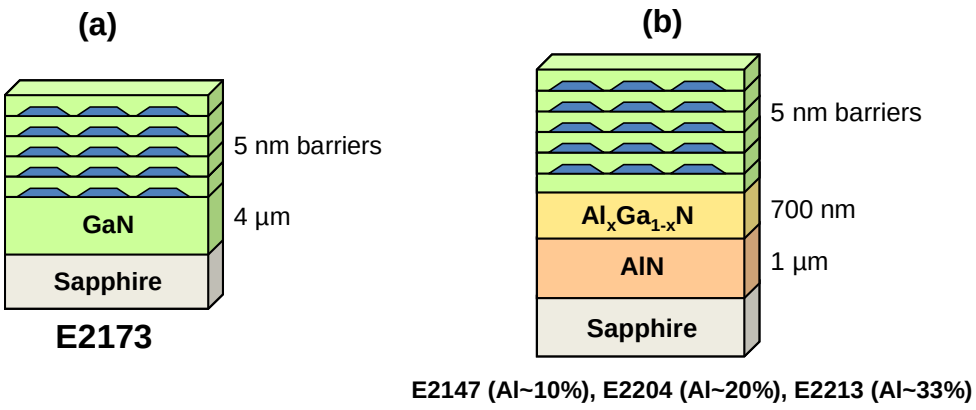

Figure 6.14: Schematic description of the InGaN/GaN QDs transducer structures with different Al mole fraction in the AlGaN contact layer.

The room temperature PL emission from these samples is presented in figure 6.15. All the samples are emitting in the 410-425 nm spectral range, with comparable intensity. The slight variation in the PL peak energy, which does not follow a monotonous trend as a function of the contact layer, is attributed to slight variations of the sample growth temperature. The TEM image in the figure 6.16(a) showing the overall structure of the sample E2173 (GaN contact layer). Low density of threading dislocations observed in GaN and the arrow in the figure indicates the starting point of the InGaN layers. Figure 6.16(b) illustrating the InGaN/GaN QDs structure more clearly. QD side facets were determined as {10-13} and the embedded QDs have an average width of 15-30 nm and height of 2.3 ± 0.2 nm.

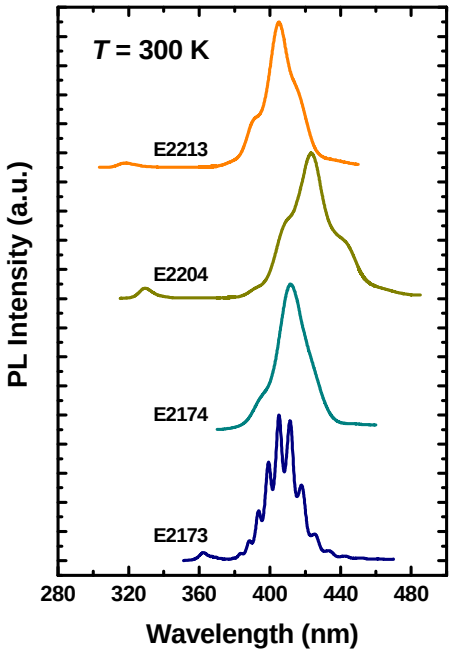

Figure 6.15: Room temperature PL emission from InGaN QD transducers with different contact layers. The spectra are vertically shifted for clarity.

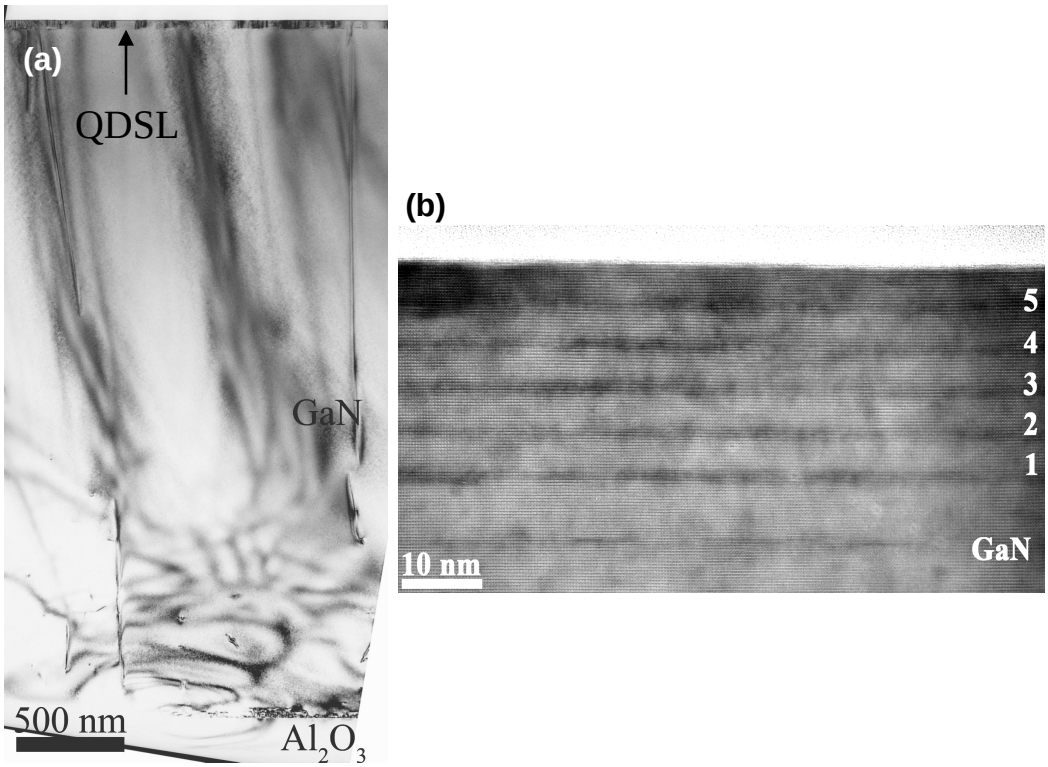

Figure 6.16: TEM images from the sample E2173; (a)Cross-sectional TEM image, taken along [11-20]$_{GaN}$ zone axis., showing the overall structure,(b) Cross-sectional HRTEM image along [11-20]$_{GaN}$ zone axis illustrating the InGaN/GaN QDSL structure. (TEM images by Prof. Ph. Komninou, Aristotle University of Thessaloniki, Greece).

Figure 6.17 shows TEM images from the sample E2213 (Al mole fraction in the contact layer = 33%). High density of threading dislocations observed in both AlN and AlGaN layers, emanating from the AlN/AlN MOVPE and AlN/AlGaN interfaces respectively (Figure 6.17(a)). The density of dislocations decreases with the layer thickness. Embedded QDs are well identified in the high-resolution images in figures 6.17(b) and (c); they present a width of 10-28 nm and height of 2 ± 0.2 nm.

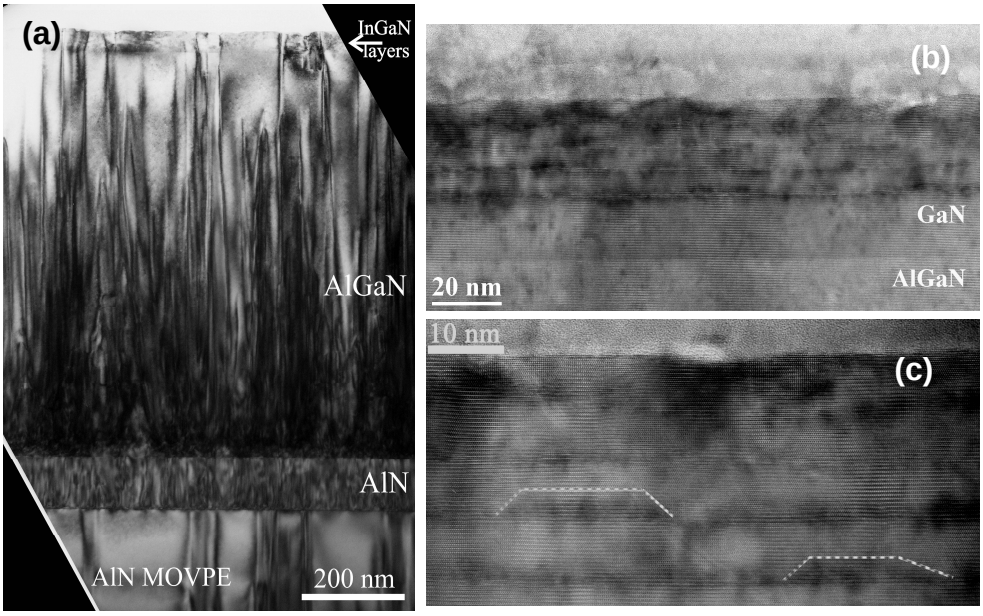

Figure 6.17: TEM images from the sample E2213; (a) Cross-section TEM image, taken along [11-20]$_{GaN}$ zone axis, showing the overall structure and cross-section HRTEM images, along [11-20]$_{GaN}$ zone axis, (b) showing the GaN/InGaN superlattice and (c) showing InGaN QDs. (TEM images by Prof. Ph. Komninou, Aristotle University of Thessaloniki, Greece).

A second series of InGaN/GaN QDs opto-chemical transducers (as described in figure 6.14(b)) have been synthesized at different substrate temperature, in order to get an insight on the reproducibility, limitations and critical steps in the fabrication process. The Al mole fraction in the contact layer was ~ 35% to keep transparency at 325 nm wavelength, and thus enable backside excitation with a HeCd laser. Figure 6.18 illustrates the room temperature PL emission of samples. The In incorporation in the QDs is strongly influenced by the substrate temperature, and hence the PL peak wavelengths red shifts from 420 nm to 450 nm and then to 530 nm when decreasing the growth temperature from 550°C to 500°C and finally to 470°C. From this experiment we conclude that precise control of the substrate temperature is required to attain the targeted wavelength. I have verified the substrate temperature for the

growth of the QDs by measuring the In desorption time after the deposition of the first GaN barrier. The substrate temperature is then corrected to obtain a certain In desorption time before the growth of the QDSL.

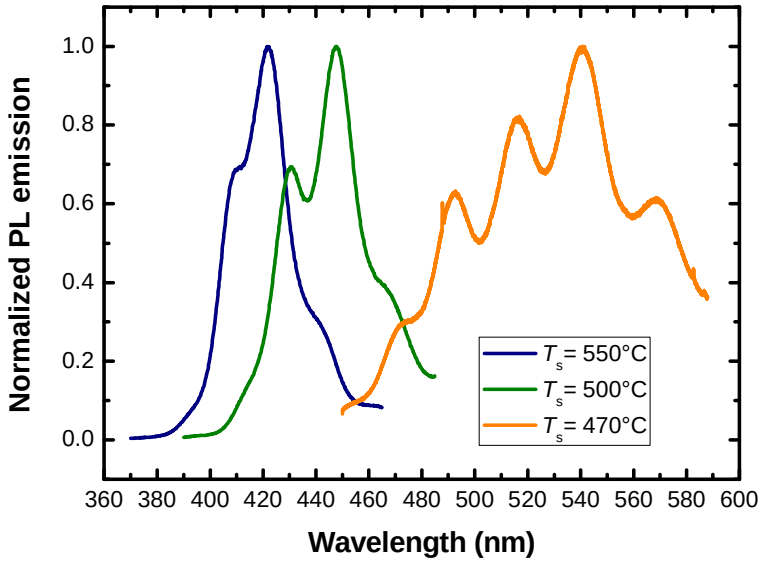

Figure 6.18: Room temperature PL emission from InGaN QD transducers where the QDs were deposited at different substrate temperatures.

6.5.2 Emission characteristics of InGaN QDs in external electric fields

These studies were carried out by our collaborators Dr. J. Teubert and Prof. Martin Eickhoff at Justus Liebig University Giessen, Germany. I will summarize some important results below.

The samples under study were process into the mesa structures described in figure 6.8. A major technological difficulty for the application of InGaN/GaN QDSLs as optochemical transducers was the presence of high leakage currents, between the conductive AlGaN buffer and the Pt top contact (or the electrolyte solution). This problem is overcome by introducing a step of anodic oxidation before the deposition of Pt. Preferential oxidation of threading dislocations is known to improve the performance of GaN Schottky contacts [Wei05].

Figure 6.19(a) shows photoluminescence spectra of an InGaN-QD transducer structure recorded at various bias voltages. The measurements reveal a superlinear increase of the PL intensity by more than one order of magnitude when changing the

bias voltage by only 600 mV which is accompanied by only a weak blue-shift of the emission energy. In the experimental setup, bias voltages are defined with respect to the electrolyte (reference electrode). Thus, considering the schematic band diagram in figure 6.19(b), the results are in qualitative agreement with a bias-induced modification of the QCSE: Positive bias voltages compensate internal electric fields in the QDs and reduce the impact of the QCSE, therefore increasing the intensity and blue shifting the emission energy.

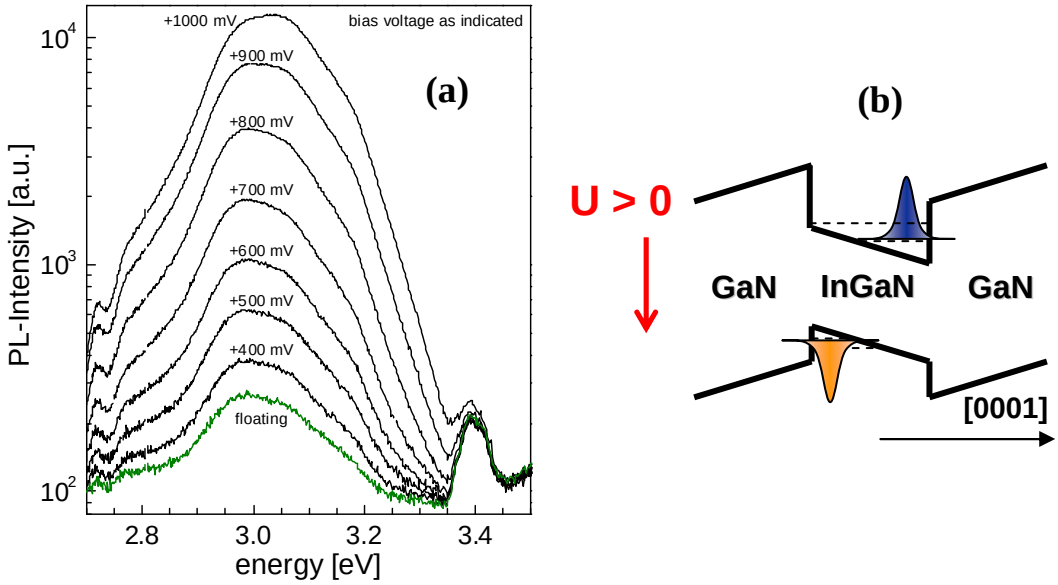

Figure 6.19: (a) PL spectra of an InGaN QD transducer structure recorded for different bias voltages. (b) Schematics of the QD-band structure with the surface to the right and the back contact to the left. Positive bias voltages lead to a band flattening as indicated by the red arrow.

However, comparing the results of the InGaN-transducer structures to those of GaN/AlN QDs (Figure 6.20) important differences arise. For GaN/AlN QDs the intensity variations were much less pronounced and accompanied by a clear shift in emission energy. In the case of InGaN-structures the comparatively weak blue-shift is accompanied by much stronger intensity variations. In order to clarify the origin of these quantitative difference, numerical simulations of the electronic band structures were carried out.

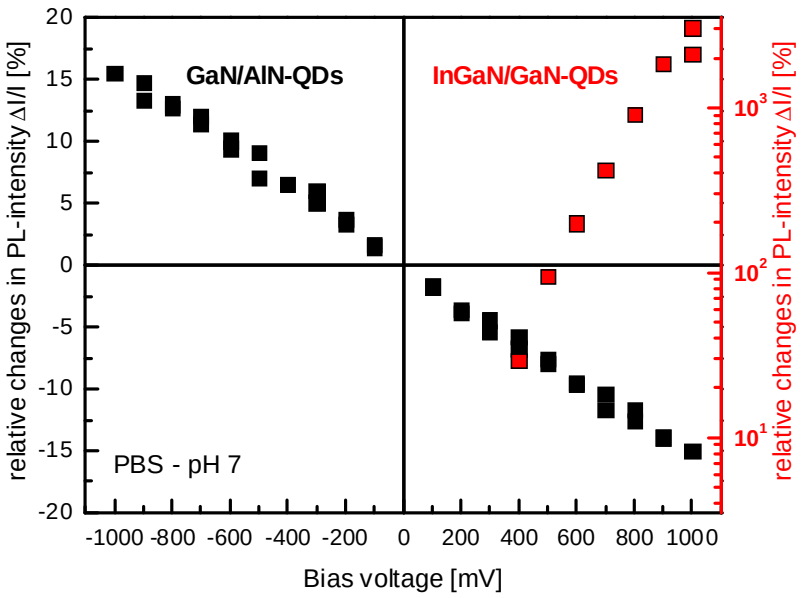

Figure 6.20: relative changes in PL intensity as a function of applied bias voltage for GaN/AlN and InGaN/GaN QDSL structure.

These band structure calculations considered the QD height and In-content, obtained from TEM analysis. The boundary conditions for solving the Poisson equation were chosen to represent an external bias of U_{bias} = 0 V.

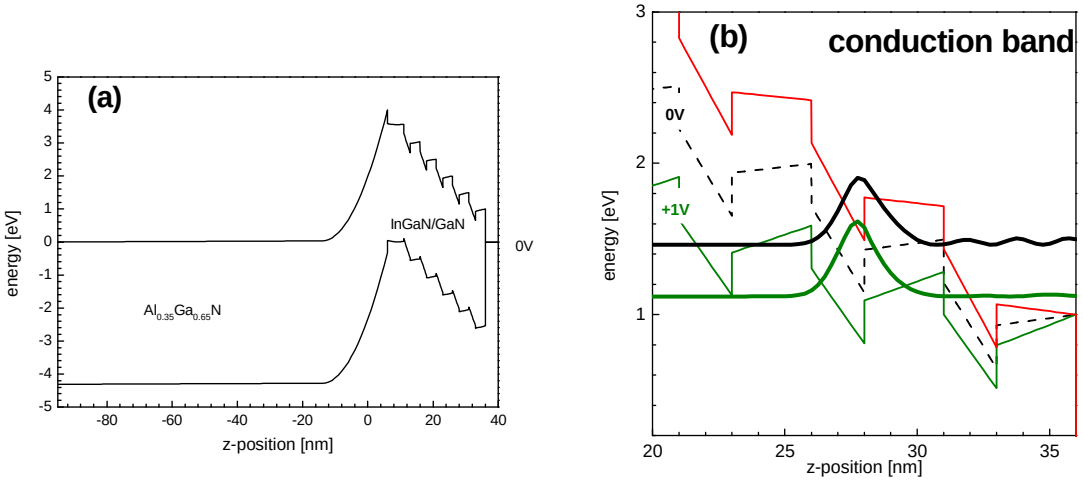

Figure 6.21: Simulations of the band structure using the nextnano3 software. (a) Band-structure of the overall simulated area including the back contact.(b) Influence of different bias voltages on the confinement potential for electrons in the conduction band. Additionally electron wave functions are shown: For U_{bias} = 0 V significant tunneling can be identified which is reduced for positive bias (+1 V). In the case of negative bias (-1 V) there are no confined states.

Figure 6.21(a) shows the overall transducer structure including the highly doped AlGaN buffer layer. Due to polarization induced charges at the interface to the

GaN matrix, strong interface band bending effects occur that also tilt the bands in the QDSL region. This effect leads to a strongly asymmetric confinement potential that favors tunneling of electrons towards the surface and holes towards the buffer layer. By application of an external bias the shape of this confinement potential can be tuned as shown in figure 6.21(b). As the bias potentials in the experimental setup are defined with respect to the reference electrode, i.e. to the electrolytic bulk, positive bias flattens the band structure in the QDSL region leading to a better confinement of carriers. As a consequence the probability for radiative recombination is enhanced leading to a higher PL-intensity. On the other hand, negative bias further weakens the confinement which results in improved tunneling and reduced PL-intensity.

6.5.3 pH-sensitivity of InGaN QDs transducers

This characterization was performed by Dr. Jorg Teubert under the direction of Prof. Martin Eickhoff, at Justus Liebig University in Giessen, Germany. The strong response of InGaN-QDSLs towards application of external electric fields is very promising for the fabrication of pH-sensitive devices, since protonation or deprotonation of the semiconductor surface in contact with a liquid environment as well as charge transfer processes modify the surface potential resulting in similar effects as external electric fields.

Figure 6.22(a) shows the transients of the PL-intensity under variation of the pH-value within pH = 7 and pH = 1 applying a fixed bias voltage of 500 mV and using Phosphate Buffer Saline (PBS) as electrolyte. A clear response can be observed with a maximum variation in intensity of 80% for ΔpH = 6. Figure 6.22(b) shows the pH-induced PL-response for various bias voltages during the pH-cycle. It is found that the strongest sensitivity is achieved between 500 mV and 700 mV. At higher bias the sensitivity is significantly reduced. Both positive bias and acidic pH add to the surface potential and lead to a flattening of the band structure in the QDSL section i.e. to a better confinement in the QDs. The weaker sensitivity at higher bias voltages may be interpreted as a saturation of the proposed confinement effect.

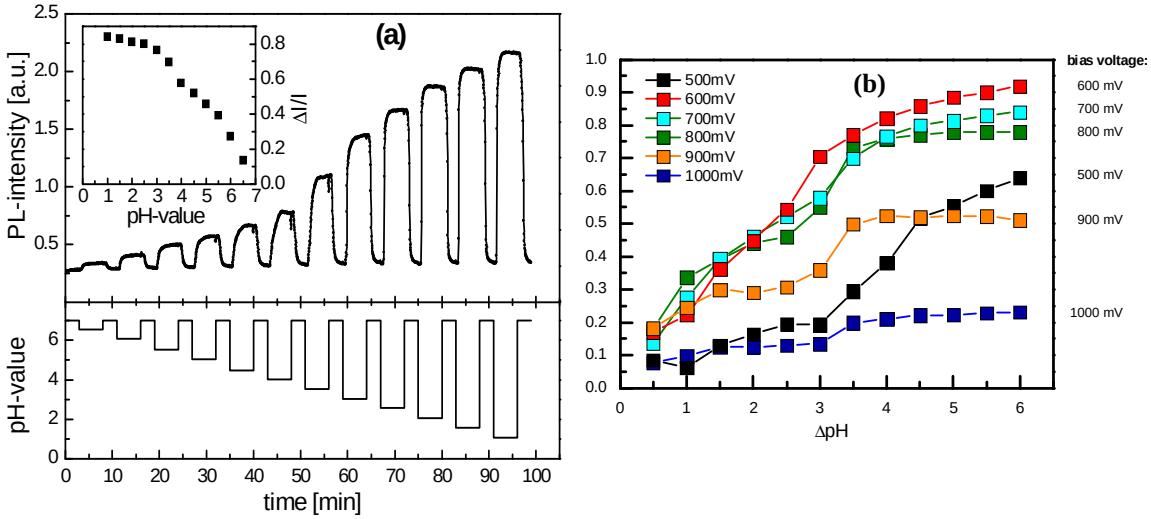

Figure 6.22:(a) Transients of the PL-intensity under variation of the pH-value within pH=7 and pH=1 applying a fixed bias voltage of 500 mV. Both acidic pH and positive bias lead to a stronger PL intensity. (b) Relative variations in PL-intensity (with respect to pH=7) for various bias voltages.

6.6 Semipolar InGaN QD opto-chemical transducers

6.6.1 Synthesis and characterization

In a first attempt to compare the chemical response of polar and semipolar InGaN QDs, I have fabricated AlGaN-free semipolar sensor structures, i.e. the InGaN/GaN QDSL is deposited on top of a 1-µm-thick GaN(11-22) layer deposited on *m*-sapphire. In these samples, the 5 periods of InGaN/GaN (5 ML / 5 nm) QDs were deposited on top of a 1.2 µm thick GaN(11-22) contact layer. I have synthesized a series of 3 samples at different substrate temperature ranging between 650°C and 500°C, with the photoluminescence results illustrated in figure 6.23, and demonstrate the feasibility of the approach to reach a spectral range (420-500 nm wavelength) that can be excited using commercial LEDs.

For the elaboration of the AlGaN:Si contact layers, I have studied and identified the growth conditions for the synthesis of 2D semipolar (11-22)-oriented $Al_xGa_{1-x}N$ (see section 4.5 in chapter 4). Although the surface roughness is significantly higher than in the case of polar AlGaN, the quality is reasonable enough for the fabrication of the transducers.

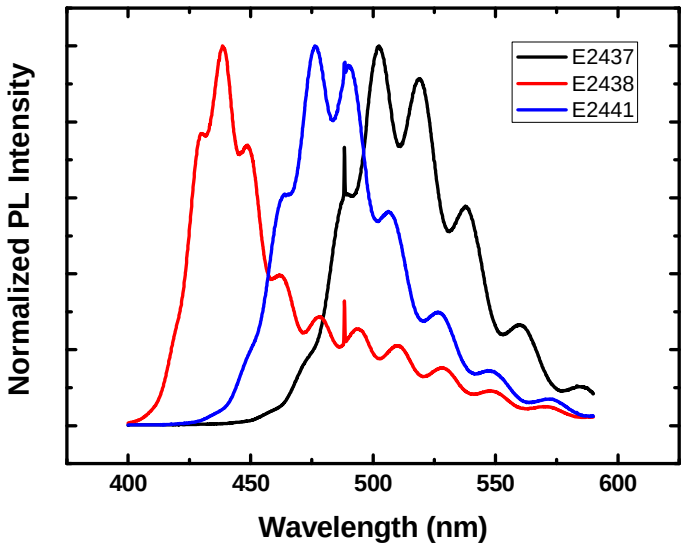

Figure 6.23: Room temperature photoluminescence spectra from AlGaN-free semipolar InGaN/GaN sensor structures grown at different substrate temperatures.

A complete semipolar opto-chemical transducer structure has been fabricated on *m*-sapphire, following the design in figure 6.24(a). Figure 6.24(b) presents the low-temperature PL emission from the active region of this structure, peaking at 450 nm wavelength. The oscillations superimposed to the emission are the result of a Bragg interference associated to the total nitride thickness. Unfortunately, the PL emission decreases markedly with temperature, so that characterization at room temperature was not possible.

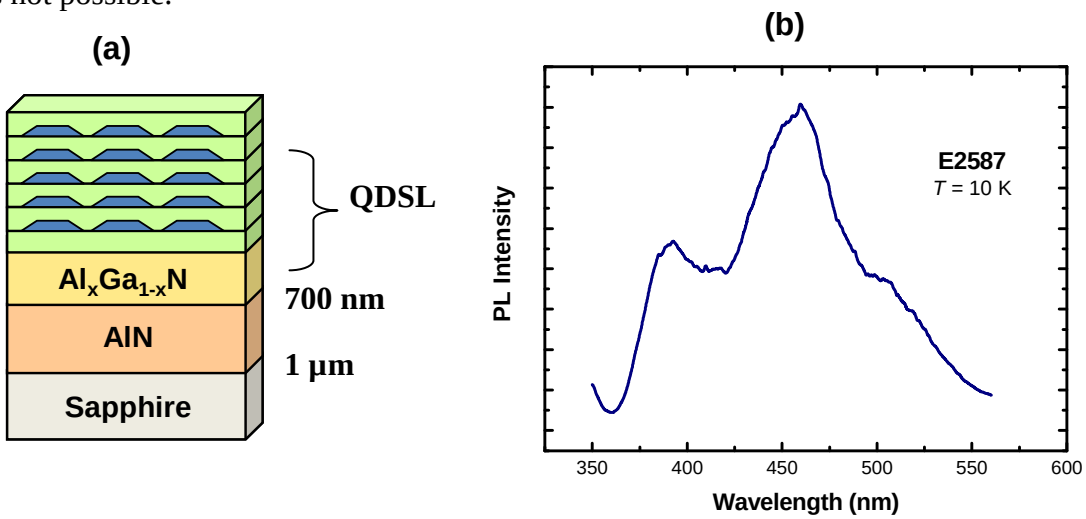

Figure 6.24:(a) Schematic description of the semipolar InGaN QD transducer structure (b) Low-temperature (T = 10 K) PL measurements from a semipolar InGaN QDs transducer.

In conclusion, although a first complete opto-chemical transducer structure has been synthesized, further work would be necessary for the optimization of the room-temperature emission.

6.6.2 Emission characteristics of semipolar InGaN QDs in external electric fields

This characterization was performed by Dr. Jorg Teubert under the direction of Prof. Martin Eickhoff, at Justus Liebig University in Giessen, Germany. For this characterization we used the AlGaN-free semipolar InGaN-QD transducers. The general conclusion of these measurements is that semi-polar InGaN QDSL structures cannot compete with their polar counterparts. This is shown in figure 6.25 which compares the electric field characteristics of the standard polar transducer structure (Figure 6.25(a)) to that of a QDSL on semipolar substrate (Figure 6.25(b)). This experiment supports the association of the sensing mechanism in polar InGaN QD transducers to the polarization-induced internal electric fields.

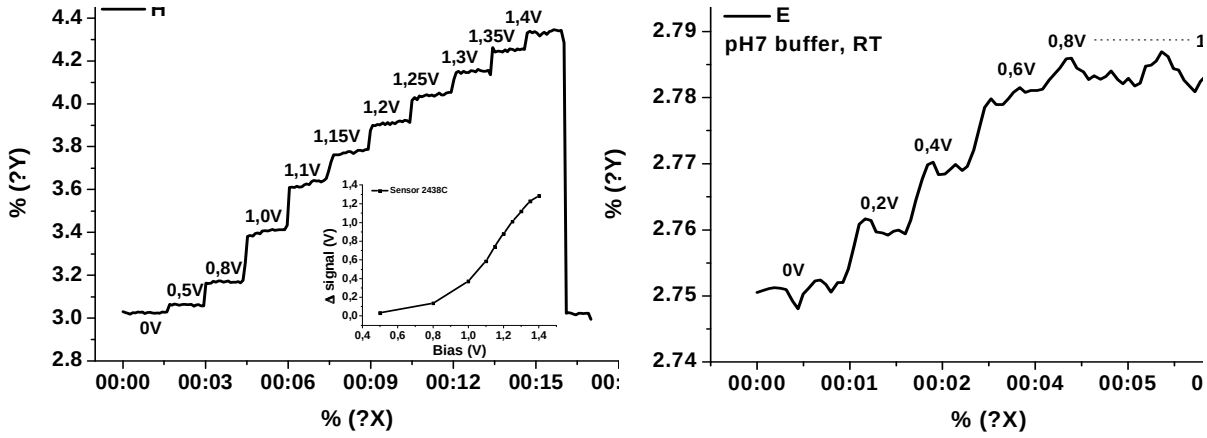

Figure 6.25: Electric field response of (a) polar QDSL structure and (b) semipolar QDSL structure. The latter exhibits a much weaker response; voltage steps are barely visible in the variation of the signal.

6.7 Chemical sensor system based on InGaN QDs

For making a complete sensor system, the transducers must be integrated with commercially-available light emitters and detectors. The design and implementation of the sensor system has been realized by Dr. Andreas Helwig and Dr. Sumit Paul (European Aeronautic Defence and Space Company, Germany), within the framework of the DOTSENSE project.

A conceptual design for fiber based sensor readout unit is shown in figure 6.26. The system consists of three major subassemblies: sensor holder with QD

transducer, illumination unit, and detection unit. The connection between illumination, detection and sensor unit is realized using a four way light fiber setup. The illumination assembly is needed to couple the excitation energy produced by the UV LED into the light fiber (Figure 6.27(a)). An optical band pass filter device filters the transmitted excitation wavelength. The detector assembly consists of a photomultiplier tube, an optical filter device and two UV lenses that focus the emitted light onto the photomultiplier detector and the end of the light fiber respectively (Figure 6.27(b)). The sensor holder unit, figure 6.27(c), contains the QD transducer and couples the head of the reflection probe to the transducer. The measurement chamber has an inner volume of a few milliliters. Different electronic devices are necessary driving excitation LEDs, powering and reading the photomultiplier tube and controlling flow of the pump and the multiposition valve of the fluidic system.

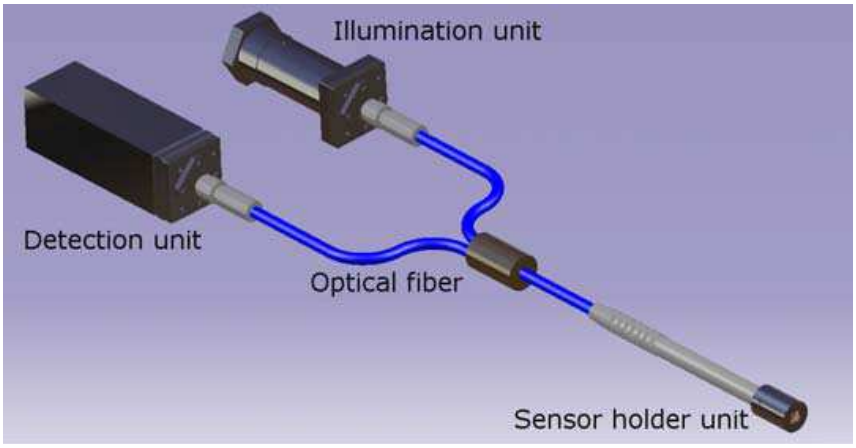

Figure 6.26: Design of fiber based sensor readout system.

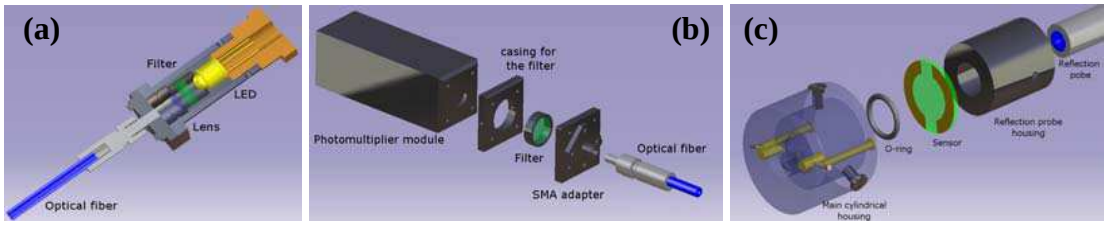

Figure 6.27:(a) Illumination assembly containing LED, (b) Detection unit containing the photomultiplier module and (c) Sensor head unit containing the QD transducer.

Figure 6.28 shows a picture of the assembled DOTSENSE sensor system. In this system, a multi-position valve selects the desired fluid (water or hydraulic fluid) from sample bottles and guides them into the measurement chamber. A micro pump routes the different fluids from the multi-position valve to the measurement chamber.

The measurement chamber contains the optical transducer and the optical fiber probe. The optical fiber probe guides the excitation light from the LEDs to the transducer and directs the luminescence signal from the transducer to the detector.

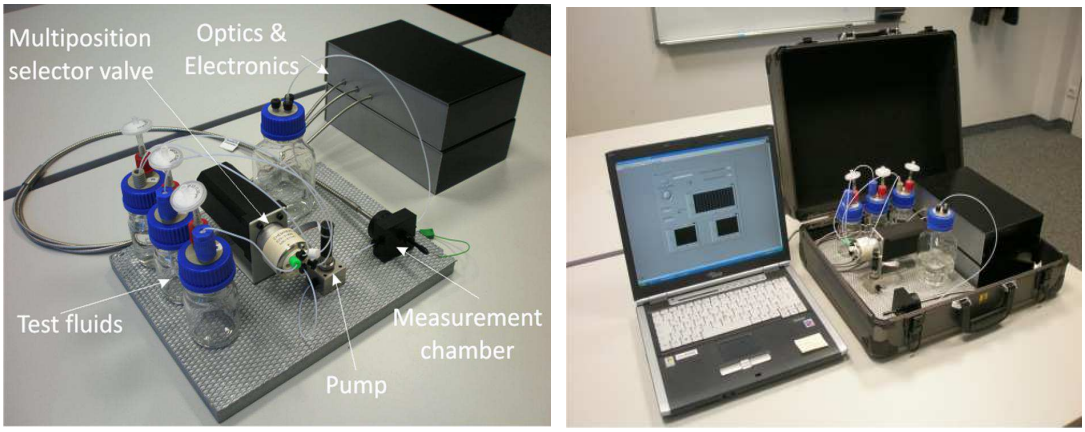

Figure 6.28: Assembled DOTSENSE Demonstrator system.

As an example, I describe here the application of the sensor system to the monitorization of the pH value of water (experiments performed by EADS). Before starting the actual pH sensing experiments the QD transducers were analyzed with regard to their intrinsic luminescence bahaviour, in order to determine the optimum bias condition. To this end, the transducers were mounted inside the DOTSENSE demonstrator system and the measurement chamber was filled with pH7 buffer solution. Results obtained with this arrangement for different QD transducers (samples E2438, E2291 and E2344) are shown in figure 6.29. These experimental data showed that all samples show a substantial increase in luminescence when the external voltage is raised from zero to 1.4 V.

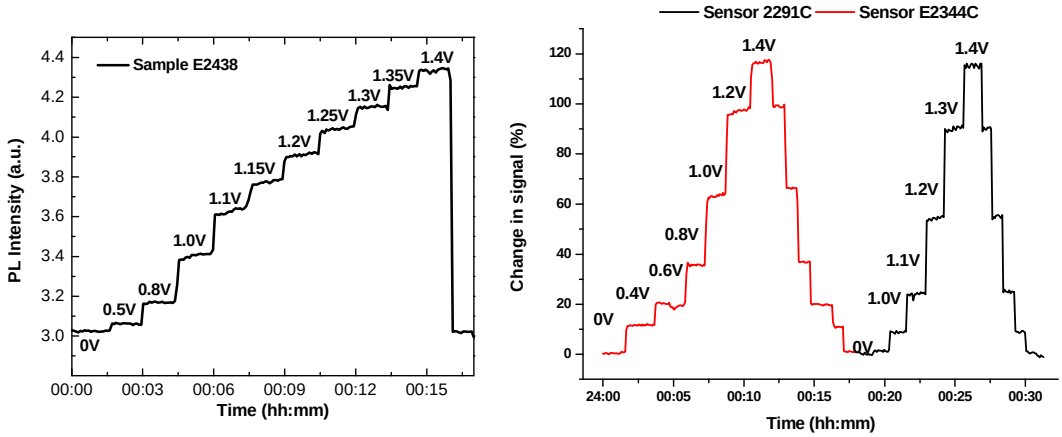

Figure 6.29: Variation of luminescence with externally applied potential of quantum dot transducers (samples E2438, E2344 and E2291).

After determination of optimum bias conditions, the QD transducers were exposed to different liquids with varying pH values while recording their luminescence signal. The results of these measurements are displayed in figure 6.30. The QD transducers react to decreasing pH with an increase in their luminescence output.

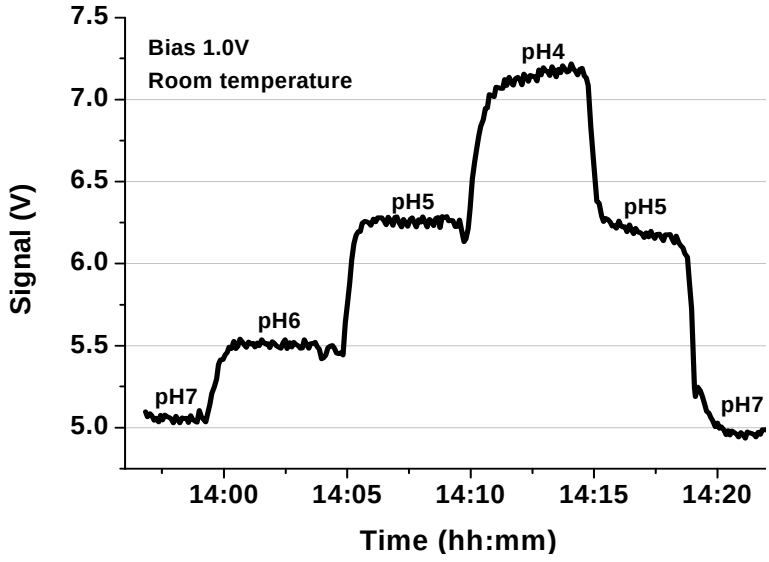

Figure 6.30: Luminescence signal of a QD transducer (sample E2291) in response to different pH values.

6.8 Conclusions

In summary, I have synthesized a number of GaN/AlN and InGaN/GaN QD optical transducers, grown in polar and semipolar orientations. In each case, the growth conditions to attain the targeted spectral range were identified. The behavior of the devices under electrical and chemical stress was studied by our collaborators: the group of Prof. M. Eickhoff, at Justus Liebig University in Giessen, and Dr. A. Helwig, at EADS in Munich.

With the feedback from sensor experiments, the specifications of the targeted opto-chemical transducer structures have been established, as described in figure 6.31(right). The Al mole fraction in the contact layer should be high enough to keep transparency at 325 nm wavelength (~35% Al). Figure 6.31(left) illustrates the room temperature PL emission of samples where the QDs have been deposited at various substrate temperatures. I have synthesized a number of InGaN/GaN opto-chemical

transducers in order to get an insight on the reproducibility, limitations and critical steps in the fabrication process.

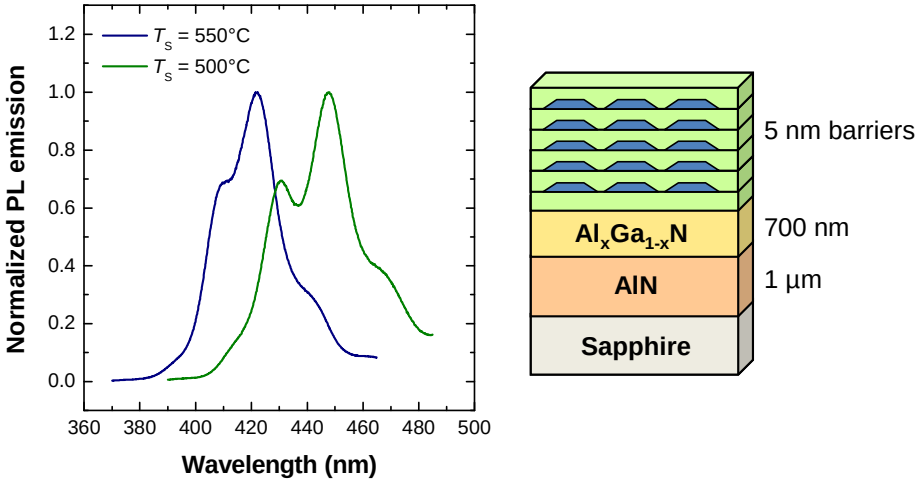

Fig. 6.31. Room temperature PL emission from InGaN QD sensor structures where the QDs were deposited at different substrate temperatures. On the right, schematic description of the model InGaN QD sensor structure.

From the various samples characterized in this study, I can extract the following conclusions:

- For the especifications (QDs emitting in the 420±10 nm range), the substrate temperature during the growth of the QD structure is critical in a range of ±20°C (precise callibration by measurement of the In desorption time for an In excess of 2 ML).
- The In cell temperature during the growth of the QDs can fluctuate ±10°C (operating value fixed by the In accumulation limit at the growth temperature).
- The Ga cell temperatures during the growth of the QDs and the barriers should be fixed within a range of ±3°C (operating value determined from RHEED oscillations during the growth of GaN).
- The growth of the AlGaN:Si contact layer is the *most critical parameter*. A slight deviation of the III/V ratio towards metal-rich would imply the inhibition of the QD formation. It is therefore recommended to finish the growth of the buffer layer under slightly N-rich conditions.

The influence of an external electric field on the PL characteristics of QDSLs was analyzed in detail by our collaborators, and polar QDSLs structures showed excellent performance compared to semipolar. Best results were obtained in the case of polar InGaN QD-structures, where a superlinear increase of the PL intensity is accompanied by only a weak blue-shift of the emission energy is observed when changing the bias voltage. The strong response of polar InGaN-QDSLs towards application of external electric fields is very promising for the fabrication of pH-sensitive devices. We have achieved an integrated sensor system based on polar InGaN QDSLs, and the system was useful for monitorization of the pH value of water.

Bibliography

[Eri05] M. Eriksson, A. Salomonsson, I. Lundström, D. Briand, and A. Elisabeth Åbom, *The influence of the insulator surface properties on the hydrogen response of field-effect gas sensors.* Journal of Applied Physics 98, 034903 (2005).

[Lun75] I. Lundström, S. Shivaraman, C. Svensson, and L. Lundkvist, *A hydrogen-sensitive MOS field−effect transistor.* Applied Physics Letters 26, 55 (1975).

[Mon03] E. Monroy, B. Daudin, E. Bellet-Amalric, N. Gogneau, D. Jalabert, F. Enjalbert, J. Brault, J. Barjon, and Le Si Dang, *Surfactant effect of In for AlGaN growth by plasma-assisted molecular beam epitaxy. Journal of Applied Physics 93, 1550 (2003)*

[Wei05] O. Weidemann, E. Monroy, E. Hahn, M. Stutzmann, and M. Eickhoff. *Influence of thermal oxidation on the electronic properties of Pt Schottky contacts on GaN grown by molecular beam epitaxy.* Appl. Phys. Lett. 86, 083507 (2005).

[Wei09] O. Weidemann, P. K. Kandaswamy, E. Monroy, G. Jegert, M. Stutzmann, and M. Eickhoff, *GaN quantum dots as optical transducers for chemical sensors.* Applied Physics Letters 94, 113108 (2009).

Chapter 7

Conclusions and perspectives

This thesis work has focused on the PAMBE growth of (In)GaN-based QD structures, deposited in both polar (0001) and semipolar (11-22) crystallographic orientations, for application as optical transducers for chemical sensors for detection of pH levels, and hydrogen or hydrocarbon concentrations in gas or liquid environments.

In the first part of this work, I have synthesized semipolar (11-22) oriented 2D layers: binary alloys (AlN, GaN and InN) and ternary alloys (AlGaN and InGaN). AlN deposited on *m*-sapphire arranges into two main crystalline orientation domains, AlN(11-22) and AlN(10-10). The ratio of (10-10)-oriented domains decreases with the III/V ratio and with the layer thickness. I have demonstrated that the nucleation of AlN(10-10) appears associated to v-defects at the sapphire substrate, which seem to be related to a reaction with AlN, which is enhanced by starting the growth with N exposure.

Regarding semipolar GaN growth, the comparison of Ga desorption during the growth of undoped, Si-doped and Mg-doped GaN(11-22) layers revealed that Si doping does not change the growth kinetics. Whereas during Mg doping, Mg tends to segregate on the GaN surface, leading to an inhibition of the self-regulated Ga film which is used as a surfactant for the growth of undoped and Si-doped semipolar GaN. Uniform Mg incorporation up to [Mg] = 1.0×10^{20} cm^{-3} is obtained, and *p*-type conductivity was found for [Mg] $\geq$ 7×10^{18} cm^{-3}. From the estimation of Mg concentration and its dependence on the substrate temperature and the impinging Ga flux, we found that its incorporation is enhanced in GaN(11-22) compared to GaN(0001). TEM shows no evidence of the pyramidal defects or polarity inversion domains that can be found in Mg-doped GaN(0001), in agreement with the interpretation of the photoluminescence spectra.

The studies of semipolar (11-22) AlGaN showed that simultaneous growth of the polar and semipolar AlGaN layers is not practicable, since it results in

accumulation of Ga droplets at the semipolar growth front. It is hence necessary to reduce the III/N ratio in comparison to polar AlGaN, although maintaining III/N > 1. Under these growth conditions, I have demonstrated semipolar 700-nm-thick AlGaN samples displaying narrow band-edge PL emission and with a surface roughness about 3.5 nm.

Indium kinetics during the PAMBE growth of InGaN(11-22) layers showed that, similarly to (0001)-oriented InGaN, optimum growth conditions for this semipolar crystallographic orientation correspond to the stabilization of 2 ML of In on the growing InGaN surface, in excellent agreement with first-principles calculations. The limits of the growth window in terms of substrate temperature and In flux lie at same values for polar and semipolar materials. However, the In incorporation is different for polar and semipolar layers grown simultaneously. In polar samples, the In incorporation is limited by the Ga supply at low temperature and decreases for growth temperatures higher than a certain threshold due to In segregation. In semipolar samples, RBS and PL measurements indicate lower In incorporation, even for substrate temperatures 40°C below the segregation threshold for polar InGaN. Semipolar InGaN layers present a characteristic surface morphology with a high density of faceted pits, which are associated to mixed-type *a+c* threading dislocations.

I have analyzed the growth parameters and properties of semipolar InN layers. Two-dimensional layers are obtained by growth under In excess with periodic growth interruptions to consume with nitrogen the In excess. These growth conditions are compatible with the synthesis of two-dimensional polar InN layers. Optical studies shows better thermal stability of the luminescence of semipolar layers compared to polar InN.

In the second part, we have successfully fabricated SLs of GaN/AlN and InGaN/GaN QDs, both in polar (0001) and semipolar (11-22) orientations. The 3D nature of the structures has been verified using AFM and TEM. PL measurements confirm the superior room-temperature emission efficiency of the QD structures as compared to the respective QWs, as a result of the 3D carrier localization.

The synthesis of polar GaN/AlN QDs was possible by two methods: either by GaN deposition under N-rich conditions or by GaN deposition under Ga-rich conditions followed by a growth interruption. In both cases, GaN QDs are hexagonal truncated pyramids with {1-103} facets and optical studies showed that potential fluctuations inside the QDs are negligible. Whereas during semipolar GaN/AlN QDs growth, two types of QDs, sitting either on the (11-22) plane or on the inclined crystallographic plane, were formed due to the large density of defects present in the growth front and is confirmed by HRTEM. The low temperature PL measurements and time-resolved PL measurements confirmed the reduction of the internal electric field in the semipolar GaN/AlN QDs in comparison with polar structures.

The influence of the growth temperature on the optical and structural properties of the polar and semipolar InGaN QDs has been also studied, considering growth at high temperature (T_S = 650–510 °C, where In desorption is active) and at low temperature (T_S = 460–440 °C, where In desorption is negligible). Polar QDs grown at high-T_S showed better thermal stability of their luminescence than that of the semipolar QDs, due to the higher density of structural defects in the semipolar heterostructure. But Low-T_S growth conditions are not compatible with polar plane (0001) whereas they provide a favorable environment to semipolar plane (11-22) to enhance the internal quantum efficiency of InGaN nanostructures. I have synthesized semipolar InGaN (11-22) QDs emitting in the 380–700 nm spectral range.

I have synthesized a number of GaN/AlN and InGaN/GaN QD optical transducers, grown in polar and semipolar orientations. In each case, the growth conditions to attain the targeted spectral range (emission at 420-450 nm with buffer transparent for wavelengths shorter than 325 nm) were identified. The influence of an external electric field on the PL characteristics of the transducers was analyzed in detail by our collaborators, and polar QD structures showed excellent performance compared to semipolar. Best results were obtained in the case of polar InGaN QD-structures, where a superlinear increase of the PL intensity is observed when changing the bias voltage.

Therefore, with the feedback from sensor experiments, the specifications of the targeted opto-chemical transducer structures have been established (5 InGaN/GaN

QD layers on $Al_{0.35}Ga_{0.65}N$:Si). Then, I have synthesized a number of InGaN/GaN opto-chemical transducers in order to get an insight on the reproducibility, limitations and critical steps in the fabrication process. Using these samples, we have achieved an integrated sensor system based on polar InGaN QDSLs, and the system was useful for monitorization of the pH value of water.

This thesis work open perspectives in three research fields, namely the development of quantum dot structures, the application of semipolar nitride-semiconductors and the implementation of new chemical sensors.

In the domain of quantum dots, the optical performance achieved at room temperature is promising for the development of new optoelectronic devices. Thus, extending the knowledge developed in GaN/AlN QDs, my host laboratory has initiated a project on UV emitters using GaN/AlN and AlGaN/AlN as active media. At longer wavelengths, it is not realistic to think of a competition for light emission with other well-established technologies. However, the application in detection, and particularly as active element in nitride-based solar cells, its possibility is under study. There, the QD structures should make it possible to shift the absorption band-edge with a reduced defect density in comparison to two-dimensional growth.

On the other hand, a relevant part of my thesis work was devoted to the understanding of growth mechanisms and properties of semipolar III nitride structures, in comparison to the well-known (0001) polar crystallographic orientation. In spite of numerous advantages offered by the growth of optoelectronic devices on semipolar III-nitride substrates, it is so far difficult for device manufacturers to fully realize the expected inherent advantages. The results from my thesis work indicate that a reduction of the extended defect density is critical to significantly improve the optical properties of the overlying quantum heterostructures. The reduction of dislocation density can be done by using free-standing substrates for growth, although the high price and reduced surface are still a problem for their introduction in the market. Therefore, semipolar III-Nitride technology is still relatively immature. Although this thesis presents some progress in semipolar (11-22) heterostructure growth, further studies are important to obtain layers having device quality.

Finally, this thesis has set a first basis for a new kind of chemical sensors based on transparent substrates and with the possibility of optical probing. In collaboration with the University of Guissen and EADS, research on this line will continue with a perspective of extending the application to the biological domain and achieving a two-dimensional sensor matrix by combination of the nitride opto-chemical transducer and a microscope-based readout.

Annex

Details of the complete sensor structures that I grew during the DOTSENSE project.

Sample	Basic Structure	Substrate
E1352	10 nm AlN + 500 nm AlGaN + 5 x (5 nm AlN / 3 ML N-rich GaN QDs) + 5 nm AlN	AlN on *c*-sapphire
E1353	10 nm AlN + 500 nm AlGaN + 5 x (7 nm AlN / 3 ML N-rich GaN QDs) + 7 nm AlN	AlN on *c*-sapphire
E1355	10 nm AlN + 500 nm AlGaN + 5 x (10 nm AlN / 3 ML N-rich GaN QDs) + 10 nm AlN	AlN on *c*-sapphire
E1356	10 nm AlN + 500 nm AlGaN + 5 x (3 nm AlN / 3 ML N-rich GaN QDs) + 3 nm AlN	AlN on *c*-sapphire
E1357	10 nm AlN + 500 nm AlGaN + 5 x (2 nm AlN / 3 ML N-rich GaN QDs) + 2 nm AlN	AlN on *c*-sapphire
E1442	10 nm AlN + 500 nm AlGaN + 3 nm AlN + 3 ML N-rich GaN QDs + 3 nm AlN	AlN on *c*-sapphire
E1444	10 nm AlN + 500 nm AlGaN + 3 x (3 nm AlN / 3 ML N-rich GaN QDs) + 3 nm AlN	AlN on *c*-sapphire
E1572	10 nm AlN + 700 nm AlGaN + 3 x (3 nm AlN / 3 ML Ga-rich GaN QDs) + 3 nm AlN	AlN on *c*-sapphire
E1574	10 nm AlN + 700 nm AlGaN + 3 x (3 nm AlN / 3 ML N-rich GaN QDs) + 10 nm AlN	AlN on *c*-sapphire
E1576	10 nm AlN + 700 nm AlGaN + 3 x (3 nm AlN / 3 ML N-rich GaN QDs) + 3 nm AlN	AlN on *c*-sapphire
E1578	10 nm AlN + 700 nm AlGaN + 3 x (3 nm AlN / 3 ML N-rich GaN QDs) + 30 nm AlN	AlN on *c*-sapphire
E1760	10 nm AlN + 700 nm AlGaN + 3 x (6 nm AlN / 6 ML N-rich GaN QDs) + 6 nm AlN	AlN on *c*-sapphire
E1763	10 nm AlN + 500 nm AlGaN + 3 x (6 nm AlN / 5 ML Ga-rich GaN QDs) + 6 nm AlN	AlN on *c*-sapphire
E1767	10 nm AlN + 500 nm AlGaN + 3 x (6 nm AlN / 3 ML Ga-rich GaN QDs) + 6 nm AlN	AlN on *c*-sapphire
E1951	100 nm AlN + 500 nm AlGaN + 5 x (5 ML Ga-rich GaN QDs / 10 nm AlN)	*m*-sapphire
E1952	100 nm AlN + 500 nm AlGaN + 5 x (5 ML Ga-rich GaN QDs / 10 nm AlN)	*m*-sapphire
E1957	10 nm AlN + 700 nm AlGaN + 5 x (7ML InGaN QDs / 5 nm GaN)	AlN on *c*-sapphire
E1959	10 nm AlN + 700 nm AlGaN + 5 x (7ML InGaN QDs / 5 nm AlN)	AlN on *c*-sapphire
E1962	10 nm AlN + 700 nm AlGaN + 5 x (3 nm GaN / 3 nm AlN)	AlN on *c*-sapphire
E1963	10 nm AlN + 700 nm AlGaN + 5 x (3 nm GaN / 5 nm AlN)	AlN on *c*-sapphire

Sample	Basic Structure	Substrate
E1964	10 nm AlN + 700 nm AlGaN + 5 x (5 ML Ga-rich GaN QDs / 5 nm AlN)	AlN on *c*-sapphire
E2000	10 nm AlN + 500 nm AlGaN + 3 x (3 ML Ga-rich GaN QDs / 5 nm AlN)	AlN on *c*-sapphire
E2001	10 nm AlN + 500 nm AlGaN + 3 x (5 ML Ga-rich GaN QDs / 5 nm AlN)	AlN on *c*-sapphire
E2020	10 nm AlN + 500 nm AlGaN + 5 x (4ML InGaN QDs / 5 nm AlN)	AlN on *c*-sapphire
E2021	10 nm AlN + 500 nm AlGaN + 5 x (4ML InGaN QDs / 5 nm AlN)	AlN on *c*-sapphire
E2073	100 nm AlN + 700 nm AlGaN + 3 x (4 ML Ga-rich GaN QDs / 5 nm AlN)	AlN on *c*-sapphire
E2075	100 nm AlN + 700 nm AlGaN + 3 x (4 ML Ga-rich GaN QDs / 5 nm AlN)	AlN on *c*-sapphire
E2076	100 nm AlN + 700 nm AlGaN + 3 x (4 ML Ga-rich GaN QDs / 5 nm AlN) + 5 nm AlN	AlN on *c*-sapphire
E2078	100 nm AlN + 700 nm AlGaN + 3 x (4 ML Ga-rich GaN QDs / 5 nm AlN) + 1nm GaN	AlN on *c*-sapphire
E2173	10 nm GaN + 5 x (5ML InGaN QDs / 5 nm GaN)	AlN on *c*-sapphire
E2174	10 nm AlN + 700 nm AlGaN + 5 x (5ML InGaN QDs / 5 nm GaN)	AlN on *c*-sapphire
E2204	10 nm AlN + 700 nm AlGaN + 5 x (5ML InGaN QDs / 5 nm GaN)	AlN on *c*-sapphire
E2213	10 nm AlN + 700 nm AlGaN + 5 x (5ML InGaN QDs / 5 nm GaN)	AlN on *c*-sapphire
E2215	10 nm AlN + 700 nm AlGaN + 3 x (4ML GaN QDs / 5 nm AlN)	AlN on *c*-sapphire
E2291	100 nm AlN + 700 nm AlGaN + 5 x (5 ML InGaN QDs / 5 nm GaN)	AlN on *c*-sapphire
E2292	100 nm AlN + 700 nm AlGaN + 5 x (5 ML InGaN QDs / 5 nm GaN)	AlN on *c*-sapphire
E2293	100 nm AlN + 700 nm AlGaN + 5 x (5 ML InGaN QDs / 5 nm GaN)	AlN on *c*-sapphire
E2329	100 nm AlN + 700 nm AlGaN + 5 x (5 ML InGaN QDs / 5 nm GaN)	AlN on *c*-sapphire
E2331	100 nm AlN + 700 nm AlGaN + 5 x (5 ML InGaN QDs / 5 nm GaN)	AlN on *c*-sapphire
E2344	100 nm AlN + 700 nm AlGaN + 5 x (5 ML InGaN QDs / 5 nm GaN)	AlN on *c*-sapphire
E2387	100 nm AlN + 700 nm AlGaN + 5 x (5 ML InGaN QDs / 5 nm GaN)	AlN on *c*-sapphire
E2390	100 nm AlN + 700 nm AlGaN + 5 x (5 ML InGaN QDs / 5 nm GaN)	AlN on *c*-sapphire
E2392	100 nm AlN + 700 nm AlGaN + 5 x (5 ML InGaN QDs / 5 nm GaN)	AlN on *c*-sapphire
E2437	200 nm GaN + 5 x (5 ML InGaN QDs / 5 nm GaN)	GaN on *m*-sapphire

Sample	Basic Structure	Substrate
E2438	100 nm AlN + 700 nm AlGaN + 5 x (5 ML InGaN QDs / 5 nm GaN)	AlN on *c*-sapphire
E2439	200 nm GaN + 5 x (5 ML InGaN QDs / 5 nm GaN)	GaN on *m*-sapphire
E2441	200 nm GaN + 5 x (5 ML InGaN QDs / 5 nm GaN)	GaN on *m*-sapphire
E2444	100 nm AlN + 700 nm AlGaN + 5 x (5 ML InGaN QDs / 5 nm GaN)	AlN on *c*-sapphire
E2502	100 nm AlN + 700 nm AlGaN + 5 x (5 ML InGaN QDs / 5 nm GaN)	AlN on *c*-sapphire
E2504	100 nm AlN + 700 nm AlGaN + 5 x (5 ML InGaN QDs / 5 nm GaN)	AlN on *c*-sapphire
E2505	100 nm AlN + 700 nm AlGaN + 5 x (5 ML InGaN QDs / 5 nm GaN)	AlN on *c*-sapphire
E2507	100 nm AlN + 700 nm AlGaN + 5 x (5 ML InGaN QDs / 5 nm GaN)	AlN on *c*-sapphire
E2514	100 nm AlN + 700 nm AlGaN + 5 x (5 ML InGaN QDs / 5 nm GaN)	AlN on *c*-sapphire
E2515	100 nm AlN + 700 nm AlGaN + 5 x (5 ML InGaN QDs / 5 nm GaN)	AlN on *c*-sapphire
E2516	100 nm AlN + 700 nm AlGaN + 5 x (5 ML InGaN QDs / 5 nm GaN)	AlN on *c*-sapphire
E2517	100 nm AlN + 700 nm AlGaN + 5 x (5 ML InGaN QDs / 5 nm GaN)	AlN on *c*-sapphire
E2518	100 nm AlN + 700 nm AlGaN + 5 x (5 ML InGaN QDs / 5 nm GaN)	AlN on *c*-sapphire
E2519	100 nm AlN + 700 nm AlGaN + 5 x (5 ML InGaN QDs / 5 nm GaN)	AlN on *c*-sapphire
E2520	100 nm AlN + 700 nm AlGaN + 5 x (5 ML InGaN QDs / 20 nm GaN) + 30 nm GaN cap	AlN on *c*-sapphire
E2521	100 nm AlN + 700 nm AlGaN + 5 x (5 ML InGaN QDs / 5 nm GaN) + 30 nm GaN cap	AlN on *c*-sapphire
E2587	100 nm AlN + 700 nm AlGaN + 5 x (5 ML InGaN QDs / 5 nm GaN) + 30 nm GaN cap	AlN on *c*-sapphire GaN on *m*-sapphire

Glossary

2D	Two Dimensional
3D	Three Dimensional
a	in-plane lattice parameter
AFM	Atomic Force Microscopy
b	Burgers vector
BF	Bright-Field
c	Lattice parameter along the [0001] axis
CBED	Convergent Beam Electron Diffraction
CCD	Charge-Coupled Device
CL	Cathodoluminescence
DAP	Donor-Acceptor Pair
GPA	Geometrical Phase Analysis
HEMT	High Electron Mobility Transistors
HRTEM	High-Resolution Transmission Electron Microscopy
HVPE	Hydride Vapor Phase Epitaxy
IQE	Internal Quantum Efficiency
LED	Light Emitting Diode
LD	Laser Diode
LPE	Liquid Phase Epitaxy
MBE	Molecular Beam Epitaxy
ML	Monolayer
MOCVD	Metal-Organic Chemical Vapor Deposition
MOS	Metal-Oxide-Semiconductor
MOVPE	Metal-Organic Vapor Phase Epitaxy
NW	Nanowires
PAMBE	Plasma-Assisted Molecular Beam Epitaxy
PL	Photoluminescence
QCSE	Quantum Confined Stark Effect
QD	Quantum Dot
QDSL	quantum Dot Superlattice

QW	Quantum Well
RBS	Rutherford Backscattering Spectroscopy
RF	Radiofrenquency
RHEED	Reflection High Energy Electron Diffraction
SF	Stacking Fault
SK	Stranski-Krastanow
SL	Superlattice
SLPT	Scanning Light-Pulse Technique
STM	Scanning Tunneling Microscopy
$\boldsymbol{T}$	Temperature
$\boldsymbol{T_S}$	Substrate temperature
TD	Threading Dislocation
TEM	Transmission Electron Microscopy
TRPL	Time-Resolved Photoluminescence
UHV	Ultra-High Vacuum
XPD	X-ray Photoelectron Diffraction
XPS	X-ray Photoemission
XRD	X-ray Diffraction

Publications and conference contributions

Publications in international journals

2012

[1] **Morphology and origin of V-pits in semipolar (11-22) InGaN**
A. Lotsari, A. Das, Th. Kehagias, Y. Kotsar, E. Monroy, Th. Karakostas, P. Gladkov, Ph. Komninou, G.P. Dimitrakopulos
J. Cryst. Growth 339, pp. 1-7 (2012)

[2] **Structural properties of semipolar InGaN/GaN quantum dot superlattices grown by plasma-assisted MBE**
A. Lotsari, G.P. Dimitrakopulos, Th. Kehagias, A. Das, E. Monroy, Ph. Komninou
Microelectronic Engineering 90, pp. 108-111 (2012)

[3] **Structure and Strain State of Polar and Semipolar InGaN Quantum Dots**
T. Koukoula, A. Lotsari, Th. Kehagias, G. P. Dimitrakopulos, I. Häusler, A. Das, E. Monroy, Th. Karakostas, and Ph. Komninou
Appl. Surf. Sci. (accepted)

2011

[4] **Improved luminescence and thermal stability of semipolar (11-22) InGaN quantum dots**
A. Das, G. P. Dimitrakopulos, Y. Kotsar, A. Lotsari, Th. Kehagias, Ph. Komninou, and E. Monroy
Appl. Phys. Lett. 98, 201911 (2011)

[5] **Growth and characterization of polar (0001) and semipolar (11-22) InGaN/GaN quantum dots**
A. Das, P. Sinha, Y. Kotsar, P. K. Kandaswamy, G. P. Dimitrakopulos, Th. Kehagias, Ph. Komninou, G. Nataf, P. De Mierry, and E. Monroy
J. Crystal Growth 323, 161 (2011)

[6] **Internal Quantum Efficiency of III-nitride Quantum Dot Superlattices Grown by Plasma-Assisted Molecular-Beam Epitaxy**
Ž. Gačević, A. Das, J. Teubert, Y. Kotsar, P. K. Kandaswamy, Th. Kehagias, T. Koukoula, Ph. Komninou, and E. Monroy
J. Appl. Phys. 109, 103501 (2011)

[7] **Strain relaxation in GaN/$Al_xGa_{1-x}N$ superlattices grown by plasma-assisted molecular-beam epitaxy**
Y. Kotsar, B. Doisneau, E. Bellet-Amalric, A. Das, E. Sarigiannidou, and E. Monroy
J. Appl. Phys. 110, 033501 (2011)

[8] **Strain relaxation in GaN/$Al_{0.1}Ga_{0.9}N$ superlattices for mid-infrared intersubband absorption**
Y. Kotsar, P. K. Kandaswamy, A. Das, E. Sarigiannidou, and E. Monroy
J. Crystal Growth 323, 64 (2011)

2010

[9] **Indium kinetics during the plasma-assisted molecular-beam epitaxy of semipolar (11-22) InGaN layers**
A. Das, S. Magalhaes, Y. Kotsar, P. K. Kandaswamy, B. Gayral, K. Lorenz, E. J. C. Alves, P. Ruterana, and E. Monroy
Appl. Phys. Lett. 96, 181907 (2010)

[10] **P-type doping of semipolar GaN(1122) by plasma-assisted molecular-beam epitaxy**
A. Das, L. Lahourcade, J. Pernot, S. Valdueza-Felip, P. Ruterana, A. Laufer, M. Eickhoff, and E. Monroy
Phys. Stat. Sol. (c) 7, pp. 1913-1915 (2010)

[11] **Performance Improvement of AlN–GaN-Based Intersubband Detectors by Using Quantum Dots**
D. Hofstetter, J. Di Francesco, P. K. Kandaswamy, A. Das, S. Valdueza-Felip, and E. Monroy
IEEE Photon. Technol. Lett. 15, pp. 1087-1089 (2010)

[12] **Effect of doping on the mid-infrared intersubband absorption in GaN/AlGaN superlattices grown on Si(111) templates**
P. K. Kandaswamy, H. Machhadani, Y. Kotsar, S. Sakr, A. Das, M. Tchernycheva, L. Rapenne, E. Sarigiannidou, F. H. Julien, and E. Monroy
Appl. Phys. Lett. 96, 141903 (2010)

[13] **Performance improvement of AlN/GaN-based intersubband detectors thanks to quantum dot active regions.**
D. Hofstetter, J. Di Francesco, E. Baumann, F. R. Giorgetta, P. K. Kandaswamy, A. Das, S. Valdueza-Felip, and E. Monroy
Proc. SPIE 7808, 78080A (2010).

Invited presentations

[1] **Polar and Semipolar III-Nitrides for long wavelength intersubband devices**
E. Monroy, P. K. Kandaswamy, H. Machhadani, A. Wirthmüller, S. Sakr, L. Lahourcade, A. Das, M. Tchernycheva, and F. H. Julien
Photonics West (SPIE), San Francisco, U.S.A. January 2010.

[2] **III-nitride nanostructures for intersubband optoelectronics**
E. Monroy, Y. Kotsar, P. Sinha, A. Das, L. Lahourcade, P. K. Kandaswamy, H. Machhadani, S. Sakr, M. Tchernycheva, and F. H. Julien
3rd Int. Symposium on the Growth of III-Nitrides (ISGN3). Montpellier, France. July 2010.

[3] **III-Nitride semiconductors for intersubband devices**
E. Monroy, Y. Kotsar, P. K . Kandaswamy, A. Das, A. Wirthmüller, H. Machhadani, S. Sakr, M. Tchernycheva, F. H. Julien, A. Vardi, and G. Bahir,
Photonics West (SPIE), San Francisco, U.S.A. January 2011

[4] **Internal Quantum Efficiency of polar and semipolar InGaN QDs**
A. Das, A. Lotsari, Y. Kotsar, G. P. Dimitrakopulos, Th. Kehagias, Ph. Komninou, and E. Monroy
Tata Institute of Fundamental Research (TIFR), India, September 2011

[5] **Strain relaxation in GaN/AlGaN superlattices grown by PAMBE for intersubband applications**
B. Doisneau, Y. Kotsar, E. Sarigiannidou, E. Bellet-Amalric, A. Das, and E. Monroy
Extended Defects in Semiconductors EDS2012. Thessaloniki, Greece. Sept. 2012

[6] **GaN quantum devices for infrared optoelectronics**
E. Monroy, Y. Kotsar, A. Das, S. Valdueza-Felip, E. Bellet-Amalric, C. Bougerol, R. Songmuang, L. Rapenne, E. Sarigiannidou, S. Sakr, M. Tchernycheva, F. H. Julien, E. Gross, A. Pesach, and G. Bahir
4th Int. Symposium on the Growth of III-Nitrides (ISGN4), St. Petersburg, Russia. July 2012

Contributions to international conferences

[1] (Oral) **Study of Indium incorporation during the MBE growth of polar and semipolar InGaN layers**
A. Das, Y. Kotsar, P. K. Kandaswamy, B. Gayral, and E. Monroy
E-MRS Spring Meeting, Strasbourg, France. May 2010

[2] (Oral) **Effect of doping on the mid-infrared intersubband absorption in III-nitride superlattices grown on Si(111) templates**
P. K. Kandaswamy, Y. Kotsar, H. Machhadani, S. Sakr, A. Das, M. Tchernycheva, F. H. Julien, and E. Monroy
E-MRS Spring Meeting, Strasbourg, France. May 2010

[3] (Poster) **Different In incorporation in polar and semipolar InGaN layers during MBE growth**
A. Das, S. Magalhães, Y. Kotsar, P. K. Kandaswamy, B. Gayral, K. Lorenz, E. Alves, and E. Monroy
3rd Int. Symposium on the Growth of III-Nitrides (ISGN3). Montpellier, France. July 2010

[4] (Oral) **Effect of doping on the interband and intersubband properties of III-nitride superlattices grown on Si(111) templates**
Y. Kotsar, P. K. Kandaswamy, H. Machhadani, S. Sakr, A. Das, M. Tchernycheva, F. H. Julien, and E. Monroy
3rd Int. Symposium on the Growth of III-Nitrides (ISGN3). Montpellier, France. July 2010

[5] (Oral) **Study of strain relaxation in GaN/AlGaN superlattices for mid-infrared intersubband absorption**
Y. Kotsar, P. K. Kandaswamy, A. Das, L. Rapenne, E. Sarigiannidou, and E. Monroy
16th Int'l Conference on Molecular Beam Epitaxy (MBE2010). Berlin, Germany. August 2010

[6] (Oral) **Growth and characterization of polar (0001) and semipolar (11-22) InGaN/GaN quantum dots**
A. Das, P. Sinha, Y. Kotsar, P. K. Kandaswamy, S. Magalhães, K. Lorenz, E. Alves, and E. Monroy
16th Int'l Conference on Molecular Beam Epitaxy (MBE2010). Berlin, Germany. August 2010

[7] (Poster) **InGaN quantum dot superlattices grown by plasma assisted MBE**
T. Koukoula, Th. Kehagias, A. Lotsari, A. Das, E. Monroy, G. P. Dimitrakopulos, and Ph. Komninou
Extended Defects in Semiconductors. Brighton, UK. September 2010

[8] (Oral) **Plasma-assisted MBE growth of semipolar (11-22) InGaN layers and GaN/InGaN quantum dots**
A. Das, A. Lotsari, S. Magalhães, P. Sinha, G. P. Dimitrakopulos, Th. Kehagias, Ph. Komninou, K. Lorenz, E. Alves, and E. Monroy
Int'l Workshop on Nitride Semiconductors (IWN-2010), Tampa, USA. September 2010

[9] (Oral) **GaInN quantum dots as optochemical transducers**
J. Teubert, S.Koslowski, A. Das, E. Monroy, and M. Eickhoff
19th European Workshop on Heterostructure Technology (HETECH'10), Crete, Greece. Nov. 2010

[10] (Poster) **Structural properties of Semipolar III-Nitride Quantum Dots**
G. P. Dimitrakopulos, E. Kalesaki, A. Lotsari, Th. Kehagias, J. Kioseoglou, A. Das, L. Lahourcade, E. Monroy, I. Hausler, H. Kirmse, W. Neumann, Ph. Komninou and Th. Karakostas
19th European Workshop on Heterostructure Technology (HETECH'10), Crete, Greece. Nov. 2010

[11] (Poster) **Nanoscale Structure of InGaN Quantum Dot Superlattices Grown by MBE**
T. Koukoula, Th. Kehagias, A. Lotsari, A. Das, E. Monroy, G.P. Dimitrakopulos, and Ph. Komninou
19th European Workshop on Heterostructure Technology (HETECH'10), Crete, Greece. Nov. 2010

[12] (Poster) **Structure of asymmetric V-defects in semipolar InGaN grown by MBE**
A. Lotsari, G. P. Dimitrakopulos, Th. Kehagias, A. Das, E. Monroy, and Ph. Komninou
4th International Conference on Micro-Nanoelectronics, Nanotechnology and MEMS, NCSR-Democritos, Athens, Greece. Dec. 2010

[13] (Poster) **Polar and Semipolar InGaN Quantum Dots**
A. Lotsari, T. Koukoula, Th. Kehagias, A. Das, E. Monroy, G. P. Dimitrakopulos, and Ph. Komninou
4th International Conference on Micro-Nanoelectronics, Nanotechnology and MEMS, NCSR-Democritos, Athens, Greece. Dec. 2010

[14] (Poster) **Plasma-assisted MBE growth of semipolar quantum dots**
A. Das, L. Lahourcade, P. Sinha, G. P. Dimitrakopulos, Th. Kehagias, Ph. Komninou, and E. Monroy
Photonics West (SPIE), San Francisco, U.S.A. January 2011

[15] (Oral) **Improved luminescence and thermal stability of MBE-grown semipolar (11-22) InGaN quantum dots**
A. Das, Y. Kotsar, A. Lotsari, Th. Kehagias, Ph. Komninou, and E. Monroy
16th European Molecular Beam Epitaxy, Alpe d'Huez, France. March 2011

[16] (Oral) **GaN/AlGaN superlattices grown by PAMBE for intersubband applications in the infrared spectral range**
Y. Kotsar, A. Das, E. Bellet-Amalric, E. Sarigiannidou, H. Machhadani, S. Sakr, M. Tchernycheva, F. H. Julien, and E. Monroy
16th European Molecular Beam Epitaxy, Alpe d'Huez, France. March 2011

[17] (Oral) **Plasma-assisted MBE of GaN/AlGaN multiple-quantum-well structures for intersubband optoelectronics**
Y. Kotsar, S. Sakr, E. Sarigiannidou, H. Machhadani, E. Bellet-Amalric, M. Tchernycheva, A. Das, F. H. Julien, and E. Monroy
E-MRS Spring Meeting, Nice, France. May 2011

[18] (Oral) **Internal Quantum Efficiency of InGaN quantum dots: Polar vs. Semipolar**
A. Das, A. Lotsari, Y. Kotsar, G. P. Dimitrakopulos, Th. Kehagias, Ph. Komninou, and E. Monroy
E-MRS Spring Meeting, Nice, France. May 2011

[19] (Poster) **Plasma-assisted MBE of GaN/AlGaN multiple-quantum-well structures for intersubband optoelectronics**
Y. Kotsar, S. Sakr, E. Bellet-Amalric, H. Machhadani, B. Doisneau, E. Sarigiannidou, M. Tchernycheva, A. Das, F. H. Julien, and E. Monroy
9th International Conference on Nitride Semiconductors (ICNS9), Glasgow, UK. July 2011

[20] (Poster) **InGaN quantum dots as optochemical transducers**
J. Teubert, S. Koslowski, A. Das, E. Monroy, and M. Eickhoff
9th International Conference on Nitride Semiconductors (ICNS9), Glasgow, UK. July 2011

[21] (Oral) **Nanostructure and Strain State of InGaN Quantum Dot Superlattices Grown by MBE**
T. Koukoula, Th. Kehagias, G. P. Dimitrakopulos, A. Lotsari, A. Das, I. Häusler, W. Neumann, E. Monroy, and Ph. Komninou
9th International Conference on Nitride Semiconductors (ICNS9), Glasgow, UK. July 2011

[22] (Poster) **Strain and structure of semipolar (11-22) InGaN quantum dots**
A. Lotsari, G. P. Dimitrakopulos, Th. Kehagias, T. Koukoula, A. Das, E. Monroy, and Ph. Komninou
9th International Conference on Nitride Semiconductors (ICNS9), Glasgow, UK. July 2011

[23] (Poster) **Plasma-assisted MBE of semipolar (11-22)-oriented III-nitrides: 2D layers and nanostructures**
A. Das, Y. Kotsar, L. Lahourcade, G.P.Dimitrakopulos, Th. Kehagias, A. Lotsari, T. Koukoula, Ph. Komninou, and E. Monroy
9th Int'l Conference on Nitride Semiconductors (ICNS9), Glasgow, UK. July 2011

[24] (Poster) **A structural analysis of semipolar (11-22)-GaN layers grown on m-sapphire by MOVPE and MBE**
B. Lacroix, M. P. Chauvat, P. Ruterana, G. Nataf, P. de Mierry, A. Das, and E. Monroy
9th Int'l Conference on Nitride Semiconductors (ICNS9), Glasgow, UK. July 2011

[25] (Oral) **Self-Assembled Quantum Dot Superlattices in Semipolar (11-22) III-Nitrides: Stoichiometry, Strain State and Morphology**
G. P. Dimitrakopulos, A. Lotsari, E. Kalesaki, J. Kioseoglou, Th. Kehagias, L. Lahourcade, A. Das, E. Monroy, I. Häusler, H. Kirmse, W. Neumann, G. Jurczak , T. D. Young, P. Duewski, Th. Karakostas and Ph. Komninou
E-MRS 2011 Fall Meeting, Warsaw, Poland. Sept. 2011

[26] (Poster) **Asymmetric V-defects in semipolar InGaN**
A. Lotsari, G. P. Dimitrakopulos, Th. Kehagias, A. Das, E. Monroy, and Ph. Komninou
E-MRS 2011 Fall Meeting, Warsaw, Poland. Sept. 2011

[27] (Poster) **Nanostructure and Strain State of InGaN Quantum Dot Superlattices Grown by MBE**
T. Koukoula, Th. Kehagias, G. P. Dimitrakopulos, A. Lotsari, A. Das, I. Häusler, W. Neumann, E. Monroy, and Ph. Komninou
E-MRS 2011 Fall Meeting, Warsaw, Poland. Sept. 2011

[28] (Oral) **Opto-chemical sensor system based on InGaN/GaN quantum dots for pH detection**
S. Paul, A. Helwig, A. Das, J. Teubert, E. Monroy, G. Müller, and M. Eickhoff
Int'l Meeting on Chemical Sensors, Nuremberg, Germany. May 2012.

[29] (Poster) **III-N nanostructures for optical pH-detection**
S. Koslowski, S. Lippert, J. Wallys, F. Furtmayr, J. Teubert, A. Das, E. Monroy, G. Dimitrakopulos, P. Komninou, S. Paul, A. Helwig, G. Müller, and M. Eickhoff
Int'l Meeting on Chemical Sensors, Nuremberg, Germany. May 2012.

[30] (Poster) **Anisotropic strain and optical properties of semi-polar (11-22) GaN epilayers grown on m-plane sapphire**
Nirupam Hatui, Aparna Das, E. Monroy, Arnab Bhattacharya
International Conference on the Physics of Semiconductors, Zurich, Switzerland. July 2012.

[31] (Submitted) **Direct Imaging of Single GaN Quantum Dots using Helium Temperature Scanning Transmission Electron Microscopy Cathodoluminescence**
M. Müller, G. Schmidt, F. Bertram, P. Veit, A. Das, E. Monroy, and J. Christen
9th Intl.Symp. on Semiconductor Light Emitting Diodes (ISSLED 2012), Berlin, Germany. Jul. 2012

[32] (Oral) **Highly spatially resolved Cathodoluminescence of Single GaN Quantum Dots directly performed in a Scanning Transmission Electron Microscope**
G. Schmidt, M. Müller, F. Bertram, P. Veit, S. Petzold, A. Das, E. Monroy
Microscopy & Microanalysis 2012 Meeting, Phoenix, US. Aug. 2012.

[33] (Oral) **Evaluating anisotropic structural properties of semi-polar III-Nitride epilayers using high-resolution x-ray diffraction**
Nirupam Hatui, Mahesh Gokhale, Aparna Das, Eva Monroy, and Arnab Bhattachary
The 11th Biennial Conference on High Resolution X-Ray Diffraction and Imaging. Saint-Petersburg, Russia. Sept. 2012

This thesis work has focused on the synthesis of (In)GaN-based quantum dot (QD) structures by molecular-beam epitaxy, deposited in both polar (0001) and semipolar (11-22) crystallographic orientations, for application as optical transducers for chemical sensors for detection of pH levels, and hydrogen or hydrocarbon concentrations in gas or liquid environments.

In the first part of this work, I describe the synthesis of semipolar-oriented two-dimensional layers: binary alloys (AlN, GaN and InN) and ternary alloys (AlGaN and InGaN), which are required for the reference contact of the transducers and set the basic know-how to understand the transition from two-dimensional growth to three-dimensional QD nanostructures. It is particularly relevant the study of indium kinetics and indium incorporation during the growth of InGaN(11-22) layers. Similarly to (0001)-oriented InGaN, optimum growth conditions for this semipolar crystallographic orientation correspond to the stabilization of 2 ML of In on the growing InGaN surface, in excellent agreement with first-principles calculations. The limits of the growth window in terms of substrate temperature and In flux lie at same values for polar and semipolar materials. However, I observe an inhibition of the In incorporation in semipolar layers even for substrate temperatures below the segregation threshold for polar InGaN.

In a second stage, I report the successful fabrication of superlattices (SLs) of GaN/AlN and InGaN/GaN QDs, both in polar and semipolar orientations. Photoluminescence and time-resolved photoluminescence confirmed the reduction of the internal electric field in the semipolar GaN/AlN QDs in comparison with polar structures. On the other hand, semipolar InGaN QDs must face the challenge of In incorporation in this crystallographic orientation. To overcome this problem, the influence of the growth temperature on the properties of the polar and semipolar InGaN QDs has been studied, considering growth at high temperature (T_S = 650–510 °C, where In desorption is active) and at low temperature (T_S = 460–440 °C, where In desorption is negligible). I demonstrate that low-T_S growth conditions are not compatible with polar plane whereas they provide a favorable environment to semipolar plane to enhance the quantum efficiency of InGaN nanostructures.

Finally, I have synthesized a number of GaN/AlN and InGaN/GaN QD optical transducers, grown in polar and semipolar orientations. In each case, the growth conditions to attain the targeted spectral range (emission at 420-450 nm with buffer transparent for wavelengths shorter than 325 nm) were identified. The influence of an external electric field on the luminescence of the transducers confirmed that the best performance (larger variation of the luminescence as a function of bias) was provided by InGaN/GaN QD structures. With this feedback, the specifications of the targeted opto-chemical transducer structures have been established (5 InGaN/GaN QD layers on $Al_{0.35}Ga_{0.65}N$:Si). Then, I have synthesized a number of InGaN/GaN opto-chemical transducers in order to get an insight on the reproducibility, limitations and critical steps in the fabrication process. Using these samples, we have achieved an integrated sensor system based on polar InGaN QD SLs, and the system was useful for monitorization of the pH value of water.

Keywords: Nanostructures, nitrides, molecular beam epitaxy, quantum dot, sensor

---

Ce travail de thèse a porté sur la synthèse de boîtes quantiques (BQs) de semi-conducteurs nitrures orientés (11-22) ou (0001) par épitaxie par jets moléculaires, pour des applications aux capteurs chimiques pour la détection du niveau de pH, d'hydrogène ou des hydrocarbures dans des environnements gazeux ou liquides. Dans la première partie de ce manuscrit, je décri la synthèse des couches bidimensionnelles semi-polaires (11-22) : des couches binaires (AlN, GaN, and InN) et des ternaires (AlGaN et InGaN), qui sont requises pour le contact de référence dans les transducteurs et aussi pour établir une base pour comprendre la croissance des BQs.

Un résultat particulièrement relevant est l'étude de la cinétique de croissance et l'incorporation de l'indium dans les couches d'InGaN(11-22). De même que pour InGaN polaire (0001), les conditions optimales de croissance pour l'orientation cristallographique semi-polaire correspondent à la stabilisation de 2 ML d'In sur la surface, en excellent accord avec des calculs théoriques. Les limites de la fenêtre de croissance en termes de température du substrat et de flux d'In sont les mêmes pour les matériaux semi-polaire et polaires. Cependant, j'ai constaté une inhibition de l'incorporation de l'In dans les couches semi-polaires, même pour une température en dessous du seuil de la ségrégation pour l'InGaN polaire.

Dans une deuxième étape, j'ai fabriqué des super-réseaux de BQs de GaN/AlN et InGaN/GaN, à la fois dans l'orientation polaire et semi-polaire. Les mesures de photoluminescence et de photoluminescence en temps résolu confirment la réduction du champ électrique interne dans les boîtes semi-polaires. D'autre part, les BQs semi-polaires à base d'InGaN doit relever le défi de l'incorporation d'In dans cette orientation cristallographique. Pour surmonter ce problème, l'influence de la température de croissance sur les propriétés des boîtes quantiques InGaN polaires et semi-polaires a été étudiée, en considérant la croissance à haute température (T_S = 650–510 °C, où la désorption d'In est active) et à basse température (T_S = 460–440 °C, où la désorption d'In est négligeable). J'ai démontré que les conditions de croissance à faible T_S ne sont pas compatibles avec le plan polaire, tandis qu'ils fournissent un environnement favorable au plan semi-polaire pour améliorer l'efficacité quantique interne de nanostructures InGaN.

Enfin, j'ai synthétisé un certain nombre de transducteurs à BQs de GaN/AlN et InGaN/GaN selon les axes de croissance polaire et semi-polaire. Dans chaque cas, les conditions de croissance pour atteindre la fourchette spectrale ciblée (420-450 nm d'émission à avec une couche contact transparente pour des longueurs d'onde plus courtes que 325 nm) ont été identifiés. L'influence d'un champ électrique externe sur la luminescence des transducteurs ont confirmé que la meilleure performance (plus grande variation de la luminescence en fonction de la polarisation) a été fournie par des structures à base de BQs d'InGaN/GaN. Avec ces données, les spécifications des transducteurs opto-chimiques ont été fixées : 5 perides de BQs d'InGaN/GaN sur une couche contact d'$Al_{0.35}Ga_{0.65}N$:Si). Puis, j'ai synthétisé un certain nombre de ces transducteurs afin d'obtenir un aperçu sur la reproductibilité, limites et les étapes critiques du processus de fabrication. En utilisant ces échantillons, nous avons réalisé un système capteur intégré qui a été utile pour le suivi de la valeur du pH de l'eau.

Mots clés : Nanostructures, nitrures, épitaxie par jets moléculaires, boîtes quantiques, capteurs